MODELLING DIRECTIONAL SOLIDIFICATION

NAG 8 - 541

Final Report

1 September 1985 to 31 August 1989

CLARKSON UNIVERSITY

Potsdam, New York 13699

Principal Investigator: Dr. William R. Wilcox
School of Engineering
Center for Advanced Materials Processing
315-268-6446; fax 6438

Graduate Student Research Assistants:

Mr. Greg Neugebauer, Ph.D. Candidate in Chemical Engineering

Mr. Ross Gray, Ph.D. Candidate in Chemical Engineering

Mr. Mohsen Banan, Ph.D. Candidate in Materials Processing

SUMMARY

Goals and objectives

The long range goal of this program is to develop an improved understanding of phenomena of importance to directional solidification, to enable explanation and prediction of differences in behavior between solidification on Earth and in space. Emphasis during the period of this grant was on experimentally determining the influence of convection and freezing rate fluctuations on compositional homogeneity and crystalline perfection in the vertical Bridgman-Stockbarger technique. Gregory Neugebauer correlated heater temperature profiles, buoyancy - driven convection, and doping inhomogeneties using naphthalene doped with azulene. Ross Gray is aiming to determine the influence of spin-up / spin-down on compositional homogeneity and microstructure of indium gallium antimonide. Mohsen Banan intends to determine the effect of imposed melting - freezing cycles on indium gallium antimonide.

Results

When the temperature of melts of organic compounds decreased with height near the solid-liquid interface, the convection was vigorous, although frequently asymmetrical. At growth rates of up to 6 mm/hr impurity concentration was uniform in cross sections and the axial concentration profile corresponded to theoretical for complete mixing. At higher growth rates, cross sectional variations in impurity concentration occurred; these variations were nearly always asymmetric. Both the magnitude of the cross sectional variations and their asymmetry tended to increase with decreasing temperature difference, increasing growth rate, and increasing melt depth. When the temperature of the melt increased with height very little convection was observed. Cross sectional variations in impurity concentration were significant at all growth rates, and were usually asymmetric.

Apparatus and techniques were developed for vertical Bridgman growth of InSb-GaSb alloys with ACRT, current interface demarcation, vibration, and temperature measurements inside the melt and solid. When the axial temperature gradient was large during growth cracking occurred in the ingots either during growth or afterwards during metallographic operations. With a smaller axial gradient not only was cracking nearly eliminated, but the grain size was increased as well.

With or without ACRT the axial composition profiles of InSb-GaSb corresponded to well-mixed conditions in the melt during growth. Application of ACRT with a rotation rate of 16 rpm and a cycle time of 26.5 s resulted in less radial variation in composition than growth without ACRT or with ACRT at a rotation rate of 80 rpm and a cycle time of 10 s. An ingot growth with ACRT had fewer twin and grain boundaries than an ingot grown without ACRT under otherwise identical conditions.

A computer model was also developed for radial variations in impurity concentration without convection. Radial segregation was predicted to increase as the interface shape deviates increasingly from planar, as the freezing rate increases, and as the segregation coefficient deviates from unity.

A theoretical analysis revealed the conditions under which composition fluctuations in a solidifying material will diffuse away before the solid cools to room temperature.

Personnel

All together, four doctoral students participated in this research over the 4 years of the grant. Ms. Lorraine Ruggiano dropped out of graduate school just prior to taking her qualifying examination, and so produced no results. Greg Neugebauer completed his Ph.D. in January of 1990. The results sections of his thesis are appended to this report. Pending renewal of this grant, Mohsen Banan is being supported by Clarkson University and is expected to complete his Ph.D. thesis in about one year. During the final year of the present grant Ross Gray was supported almost entirely by NASA Headquarters as a NASA Graduate Student Researcher. He also is expected to complete his Ph.D. thesis in about one year.

Publications

The following papers were published during the grant period:

1. R. Sen and W. R. Wilcox, "Twinning of Dodecanedicarboxylic Acid," J. Crystal Growth 75, 323-328 (1986).

2. R. Sen and W. R. Wilcox, "Behavior of a Non-Wetting Melt in Free Fall: Experimental," J. Crystal Growth 74, 591-596 (1986).

3. R. Sen and W. R. Wilcox, "Behavior of a Non-Wetting Melt in Free Fall: Theoretical," J. Crystal Growth 78, 129-134 (1986).

4. G. T. Neugebauer and W. R. Wilcox, "Convection in the Vertical Bridgman - Stockbarger Technique," J. Crystal Growth 89, 143-154 (1988).

5. R. T. Gray, M. F. Larrousse and W. R. Wilcox, "Diffusional Decay of Striations," J. Crystal Growth 92, 530-542 (1988).

6. W. R. Wilcox, review of book, "Techniques of Melt Crystallization," by G. Sloan and McGhie, J. Am. Chem. Soc. 110, 8272 (1988).

Talks and papers presented

1. W. R. Wilcox, "An Overview of Materials Processing in Space," duPont, Wilmington, DE (September 1985).

2. W. R. Wilcox, "An Overview of Materials Processing in Space," IBM, Yorktown Heights, NY (September 1985).

3. W. R. Wilcox and R. Sen, "Enclosed Liquid Behavior in KC135," AIChE, Chicago (November 1985).

4. G. T. Neugebauer, H. Potts and W. R. Wilcox, "Convection in the Bridgman - Stockbarger Technique," AIChE, Chicago (November 1985).

5. W. R. Wilcox, "Convection in the Bridgman - Stockbarger Technique," A&M University of Alabama (December 1985).

6. W. R. Wilcox and R. Sen, "Behavior of a Non-Wetted Melt in Free Fall," TMS AIME Meeting, New Orleans (March 1986).

7. W. R. Wilcox, "Convection in the Bridgman - Stockbarger Technique," Bulgarian Academy of Science, Sofia (June 1986).

8. R. Sen and W. R. Wilcox, "Liquid Behavior in a Non-Wetted Ampoule in Space," ICCG-8, York, England (July 1986).

9. G. T. Neugebauer, H. Potts and W. R. Wilcox, "Convection in the Bridgman - Stockbarger Technique," ICCG-8 (July 1986).

10. W. R. Wilcox, "Validity of the Burton-Prim-Slichter Equation," ICCG-8 (July 1986).

11. G. T. Neugebauer and W. R. Wilcox, "Convection in the Bridgman - Stockbarger Technique," ACCG/east-1 (October 1986).

12. W. R. Wilcox, "Crystal Growth in Space," Aerojet Electro Systems Division, Azusa (October 1986).

13. W. R. Wilcox, "Convection in the Bridgman - Stockbarger Technique," University of Colorado, Boulder (February 1987).

14. W. R. Wilcox, "Convection in the Bridgman - Stockbarger Technique," Queens University, Kingston, Ontario (February 1987).

15. W. R. Wilcox, "Convection in the Bridgman - Stockbarger Technique," Santa Barbara Research Center, Santa Barbara, California (February 1987).

16. W. R. Wilcox, "Convection in the Bridgman - Stockbarger Technique," Gordon Research Conference on Crystal Growth, Santa Barbara (February 1987).

17. W. R. Wilcox, "Application of Chemical Engineering Principles to Materials Processing," McGill University, Montreal (March 1987).

18. W. R. Wilcox, "Bulk Crystal Growth in Space," Third Pathways to Space Experimentation, Orlando (June 1987).

19. W. R. Wilcox, "Influence of Microgravity on Crystal Growth," Battelle-Columbus (June 1987).

20. R. Gray, M. Larrousse and W. R. Wilcox, "Decay of Compositional Striations," ACCG-7/II-VI-87, Monterey (July 1987).

21. G. T. Neugebauer, H. Potts and W. R. Wilcox, "Buoyancy-driven Convection in the Vertical Bridgman - Stockbarger Technique," ACCG-7/II-VI-87, Monterey (July 1987).

22. G. T. Neugebauer, H. Potts and W. R. Wilcox, "Experimental Observations of Natural Convection and its Relation to Compositional Inhomogeneities in the Bridgman - Stockbarger Technique," AIChE Meeting, NY (November 1987).

23. M. Larrousse, R. Gray and W. R. Wilcox, "Use of Spin-up/Spin-down in Growth of Compound Semiconductor Crystals," AIME Meeting, Phoenix (January 1988).

24. W. R. Wilcox, "Materials Processing Research at Clarkson University," Air Force Materials Lab., Dayton (May 1988).

25. G. T. Neugebauer and W. R. Wilcox, "Segregation and Convection in the Bridgman - Stockbarger Technique," Gordon Research Conference on Crystal Growth (July 1988).

26. G. T. Neugebauer and W. R. Wilcox, "Radial Segregation in the Vertical Bridgman - Stockbarger Technique," ACCG/east-2, Atlantic City (October 1988).

27. W. R. Wilcox, "Materials Processing in Space," Pennsylvania State University (November 1988).

28. W. R. Wilcox, "Research on Crystal Growth in Space in the USA and at Clarkson University," Institute for General and Inorganic Chemistry, Bulgarian Academy of Sciences, Sofia (June 1989).

29. *Ibid*, Space Research Institute, University of Sofia, Bulgaria (June 1989).

30. W. R. Wilcox, "Crystal Growth Experiments under Microgravity in the USA," Japan Space Utilization Project Center, Tokyo, Japan (August 1989).

31. G. Neugebauer and W. R. Wilcox, "Radial Segregation in the Vertical Bridgman-Stockbarger Technique," International Conference on Crystal Growth 9, Sendai, Japan (August 1989).

32. W. R. Wilcox, "Recent Developments and Future Outlook for Crystal Growth under Microgravity in the USA," ICCG-9 (August 1989).

33. W. R. Wilcox, "Crystal Growth in Space," Shizuoka University, Hamamatsu, Japan (September 1989).

34. W. R. Wilcox, "Transport Phenomena in Bridgman Growth of Semiconductor Crystals," SUNY Binghamton (November 1989).

CONTENTS

I. THE INFLUENCE OF CONVECTION ON COMPONENT SEGREGATION IN THE VERTICAL BRIDGMAN - STOCKBARGER TECHNIQUE

Gregory T. Neugebauer

Summary

The goal of this project was to determine the relationships between longitudinal and circumferential temperature profiles in the furnace, convection patterns, and variations in impurity doping. This was accomplished by fabrication of special furnaces, light streak photography, solidification of naphthalene doped with azulene, and microchemical analysis for azulene concentration throughout the resulting ingots.

When the temperature of the melt decreased with height near the solid-liquid interface, the convection was vigorous, although frequently asymmetrical. At growth rates of up to 6 mm/hr the azulene concentration was uniform in cross sections and the axial concentration profile corresponded to theoretical for complete mixing. At higher growth rates, cross sectional variations in azulene concentration occurred; these variations were nearly always asymmetric. Both the magnitude of the cross sectional variations and their asymmetry tended to increase with decreasing temperature difference, increasing growth rate, and increasing melt depth.

When the temperature of the melt increased with height very little convection was observed. Cross sectional variations in impurity concentration were significant at all growth rates, and were usually asymmetric.

A computer model was also developed for radial variations in impurity concentration without convection. Radial segregation was predicted to increase as the interface shape deviates increasingly from planar, as the freezing rate increases, and as the segregation coefficient deviates from unity.

The research methods and results are given in detail in Appendix A, which is excerpted from Greg Neugebauer's Ph.D. thesis. This thesis was completed in January 1990.

II. INFLUENCE OF SPIN-UP / SPIN-DOWN ON COMPOSITIONAL HOMOGENEITY AND PERFECTION OF DIRECTIONALLY SOLIDIFIED INDIUM GALLIUM ANTIMONIDE

Ross Gray

Summary

The goal of this continuing project is to determine the mechanism by which the application of the accelerated crucible rotation technique (ACRT or spin-up/spin-down) increases the compositional homogeneity and crystalline perfection of alloy semiconductors.

An apparatus was constructed for vertical Bridgman-Stockbarger growth of $In_xGa_{1-x}Sb$ with ACRT applied. Temperature measurements inside the material enabled us to determine the optimal hot and cold-zone temperatures and adiabatic zone thickness for a favorable thermal environment. Techniques were developed for preparing ampoules containing the alloy. In order to avoid oxide, an etching apparatus was designed so that all oxide can be removed from the antimony and indium shot used as starting material. A rocking furnace was designed and constructed for mixing melted In, Ga, and Sb shot into homogenized starting material.

Five ingots were directionally solidified from starting material of composition $In_{0.2}Ga_{0.8}Sb$. Three were grown with application of ACRT and two without. The axial and radial composition profiles of three ingots were determined using energy dispersive X-ray spectroscopy. The axial profiles were compared to theoretical results for well-mixed conditions in the melt during growth. All profiles agree remarkably well with theory. The radial profiles suggest that application of ACRT with a rotation rate of 16 rpm and a cycle time of 26.5 s results in less radial segregation than growth without ACRT or growth with a rotation rate of 80 rpm and a cycle time of 10 s.

The number of grain and twin boundaries was determined in two ingots, one grown with application of ACRT and one without. The ingot grown without ACRT had 3.02 twin boundaries/mm and 0.535 grain boundaries/mm. The ingot grown with ACRT had 2.38 twin boundaries/mm and 0.368 grain boundaries/mm.

A. Introduction

Bulk single crystals of the alloy system $In_xGa_{1-x}Sb$, which is being used in this research, would have applications for opto-electronic devices such as photodetectors and microwave oscillators [1-3]. Unfortunately no one has succeeded in routinely growing single crystals of concentrated III-V and II-VI alloys, of which $In_xGa_{1-x}Sb$ is representative.

Free convection, which often can be time-dependent [4], has proven to be a large obstacle to obtaining compositionally homogeneous crystals. Previous experimenters attempted to eliminate the adverse effects of free convection by applying a magnetic field to the melt in order to suppress the convection [5] and by growth in the reduced-gravity environment of space where buoyancy effects are much less [6-9]. Both techniques improved the quality of the resulting crystals.

In the vertical Bridgman-Stockbarger (VBS) growth technique, the charge is sealed in a growth ampoule. This ampoule is then lowered at a slow rate through a temperature gradient created by a furnace on top of a cooler. This set-up allows one to independently control the interface shape, growth rate, and temperature gradient. While this arrangement with the heater on top is said to be thermally stable, natural convection is always present on earth due to unavoidable radial temperature gradients and variations in composition. This convection is often time-dependent [4]. The result is variations in temperature and flow velocity near the interface, causing growth rate fluctuations. An inhomogeneous composition profile with striations parallel to the interface can develop.

One method of eliminating free convection problems is to introduce regular, forced convection on a scale that overwhelms any buoyancy effects. Using forced convection offers the additional advantage of keeping the melt well-mixed, thereby eliminating cross-sectional compositional variations. Spin-up/spin-down [11,12], often referred to as the accelerated crucible rotation technique (ACRT) when applied to crystal growth [10,13-16], is a method by which effective mixing can be achieved without making physical contact with the melt. Mixing is achieved by periodically varying the rotation rate of the ampoule. Capper et al. [10] at Mullard in Southampton, England applied ACRT during the vertical Bridgman growth of $Hg_xCd_{1-x}Te$. They achieved a dramatic improvement in compositional homogeneity and crystalline perfection over ingots grown without ACRT. While improved homogeneity is expected, the reason for increased grain size is not known.

Recent research by Larrousse [17] at Clarkson University suggests that ACRT leads to large fluctuations in freezing rate and segregation. Meltback of the grown solid would be expected to occur during each spin-up/spin-down cycle. This periodic melting and freezing could have enhanced grain selection and eliminated twins in the solidification of $Hg_xCd_{1-x}Te$ at Mullard. The benefit of periodic melting and freezing was demonstrated by Jackson and Miller [18] using the organic compound salol. Another possible explanation for the improved crystalline perfection of the ingots grown with ACRT is that ACRT causes the interface to be less concave (more convex) [19,20]. This would enhance grain selection by causing grains not aligned with the direction of growth to grow out as solidification proceeds. In conjunction with this research, Mohsen Banan is performing experiments that will produce periodic melting and freezing without the added convection present with ACRT (see next section in this report). It is hoped that this will allow one to distinguish between the stirring and the periodic remelting effects of ACRT.

B. Progress

An $In_{0.2}Ga_{0.8}Sb$ ingot was solidified in the VBS apparatus at 8 mm/day. The high-temperature zone of the furnace was set at 800°C, the low-temperature zone was at 100°C, and the length of the adiabatic zone was 2.54 cm. These settings were chosen using the conditions Sen [5] used to grow the same material as a guideline. The resulting ingot was highly twinned and contained many small grains. The poor crystal quality is thought to have been caused by the extremely high temperature gradient (150°C/cm) across the adiabatic zone of the furnace. This gradient was determined by placing a thermocouple in an empty quartz ampoule and translating it through the apparatus. Sen stated in her thesis [5] that a gradient above 40°C/cm results in a poor crystal with many microcracks due to the high thermal stress. We concluded that the thermal characteristics of Sen's apparatus were much different than those of the present VBS apparatus, so that her temperature settings produced an unreasonably large temperature gradient in our apparatus.

In order to reduce the temperature gradient in our VBS apparatus, the constant-temperature circulating bath with a range of -30°C to 150°C used to cool the low-temperature zone was replaced by a resistance heater capable of sustaining temperatures from 200°C to 1000°C within 0.5°C. The adiabatic region was increased in length from 2.54 cm to 5.08 cm. These changes allow the gradient to be reduced to 40°C/cm when temperatures of 760°C and 480°C are used in the high and low-temperature zones, respectively.

An improved method for the preparation of the materials for solidification was devised. The antimony and indium shot purchased for this research had layers of oxide on their surfaces. An etching apparatus was designed to remove this oxide. The material is etched in a mixture of 1 HCl:1 H_2O, rinsed in water, and then rinsed in methanol. All of these steps are carried out in a dry nitrogen atmosphere. The sealed etching vessel is removed from the etching apparatus and placed in a glove box filled with dry nitrogen, where it is weighed. By using this procedure, the clean antimony and indium are not reintroduced to an oxygen environment. This greatly improved the quality of the ingots grown, since the presence of oxide tends to result in the sticking of the grown ingot to the ampoule wall.

A rocking furnace for mixing the elements was designed and constructed. The rocking furnace is mounted horizontally on a shaft that allows it to alternately tilt by 15 degrees to the vertical in either direction when it is driven by a cam and shaft assembly. The rocking motion enables us to mix the individual elements (six nines grade In, Ga, and Sb shot) to produce homogenized starting material for the directional solidification experiments. Some black residue forms on the material during the rocking process. This is removed by sandblasting with 220 grit silicon carbide particles followed by ultrasonic cleaning in electronic grade methanol. By following this procedure, all grown ingots are clean, shiny, and slide easily from the ampoule after growth.

Five ingots of $In_{0.2}GaD_{0.8}Sb$ were directionally solidified (three with application of ACRT and two without). The radial and axial composition profiles were determined for four of these ingots, and the number of grain and twin boundaries was counted in two ingots. The composition of the ingots at various axial and radial locations was determined using energy dispersive X-ray spectroscopy (EDX). The spectral data was

collected using a Tracor Northern model TN-2000 and then transferred to floppy disk. The data were then analyzed using a program developed at the NASA Marshall Space Flight Center, which is described in detail by Gillies [22]. This program compares the unknown spectrum to the spectra of two standards and determines the mass fraction of InSb in the unknown sample. The program ignores any atomic number, absorbance, and fluorescence (ZAF) corrections that might be necessary and assumes that the ingot is stoichiometric.

The axial composition profiles of three ingots were analyzed. Figure 1 shows mole fraction of InSb in the solid versus mole fraction of ingot solidified. The mole fraction solidified g is the ratio of number of moles solidified when the interface is at a specific axial location to the total number of moles in the entire ingot. The results for each ingot are practically identical and agree extremely well with the theoretical curve for well-mixed conditions in the melt, assuming no solid-state diffusion and equilibrium at the melt-solid interface. This suggests that even without ACRT there is enough mixing present to create a completely stirred melt. Since the growth rate is very low (8 mm/day), the convection need not be intense. Diffusion and free convection are sufficient to keep InSb from accumulating at the growing interface. Due to the presence of well-mixed conditions without forced convection, application of ACRT does not affect the axial composition profile.

Figure 2 shows percent radial segregation obtained from the radial composition profiles of three ingots analyzed. Percent radial segregation is defined as the maximum mole fraction of InSb across the radial slice minus the minimum, divided by the average. Crystal E1 was grown without ACRT, ingot E2 was grown with an ACRT rotation rate of 80 rpm and a cycle time of 10 s (10 s with rotation, 10 s without), and ingot E3 was grown with a rotation of 16 rpm and a cycle time of 26.5 s. The two ingots grown with ACRT (E2 and E3) had much less radial segregation than ingot E1. However, it should be noted that ingot E1 had a large oxide patch near top (last to freeze end). This oxide patch caused a large void in the top of the ingot that occupied about 50% of its cross-sectional area. This void could have been present in the liquid phase as well. This would have resulted in asymmetry in the heat transfer, leading to an asymmetric interface shape and large radial segregation. For this reason, it is impossible to conclude, without analysis of more ingots, that the application of ACRT was responsible for the reduction in radial segregation. It appears from Figure 2 that the combination of ACRT parameters used in growing ingot E3 were better for reducing radial segregation than those used in growing ingot E2.

The microstructure of the grown ingots was analyzed under optical and scanning electron microscopes. No second phase precipitates or voids were observed in any of the ingots. The numbers of grain and twin boundaries were determined in ingots E1 and E2 (E2 grown with application of ACRT and E1 without). Ingot E2 had 3.02 twin boundaries/mm and 0.535 grain boundaries/mm, while ingot E1 had 2.38 twin boundaries/mm and 0.368 grain boundaries/mm. These numbers were determined by counting the number of boundaries intersected when scanning radially across longitudinal sections of the ingots at 2 mm intervals. Although the ACRT grown ingot had fewer number of boundaries, the difference is not significant enough to allow firm conclusions to be made until more ingots are analyzed.

C. Plans

Now that the experimental apparatus and techniques seem to have been perfected, many more ingots will be solidified during the remainder of this research project. More ACRT rotation rates and cycle times will be investigated; two ingots will be solidified for each set of conditions. Quenching studies will be done to determine the influence of ACRT and its parameters on the liquid-solid interface shape of the growing crystals.

D. References

1. J.C. McGroddy, M.R. Lorenz and T.S. Plaskett, Solid State Communications 7, 901-903 (1969).

2. T.S. Plaskett and J.F. Woods, J. Crystal Growth 11, 341-344 (1971).

3. A. Joullie, J. Allegre, and G. Bougnot, Mater. Res. Bull. 7, 1101-1108 (1972).

4. H. Potts and W.R. Wilcox, J. Crystal Growth 74, 443-445 (1986).

5. S. Sen, PhD thesis, University of Southern California (1976).

6. J.F. Yee, M. Lin, K. Sarma, and W.R. Wilcox, J. Crystal Growth 30, 185-192 (1975).

7. K. Sarma, PhD thesis, University of Southern California (1976).

8. R.A. Lefever, W.R. Wilcox, and K.R. Sarma, Mater. Res. Bull. 13, 1175-1180 (1978).

9. J.F. Yee, S. Sen, K. Sarma, M. Lin, and W.R. Wilcox, in "Proceedings of the Third Space Processing Symposium - Skylab Results" (1974).

10. P. Capper, J.J.G. Gosney, and C.L. Jones, J. Crystal Growth 70, 356-364 (1984).

11. H.P. Greenspan, "The Theory of Rotating Fluids," Cambridge University Press (1968).

12. E.R. Benton and A. Clark, Jr., Ann. Rev. of Fluid Mech. 6, 257-280 (1974).

13. E.O. Schulz-DuBois, J. Crystal Growth 12, 81-87 (1972).

14. H.J. Scheel and E.O. Schulz-DuBois, J. Crystal Growth 8, 304-306 (1971).

15. H.J. Scheel, J. Crystal Growth 13/14, 560-565 (1972).

16. A. Horowitz, D. Gazit, and J. Makovsky, J. Crystal Growth 61, 323-328 (1983).

17. M.F. Larrousse, PhD thesis, Clarkson University (1987).

18. K.A. Jackson and C.E. Miller, J. Crystal Growth 42, 364-369 (1977).

19. P. Capper, W.G. Coates, C.L. Jones, J.J. Gosney, C.K. Ard and I. Kenworthy, J. Crystal Growth 83, 69-76 (1987).

20. P. Capper, J.C. Brice, C.L. Jones, W.G. Coates, J.J.G. Gosney, C. Ard and I. Kenworthy, J. Crystal Growth 89, 171-176 (1988).

21. A.L. Fripp, R.K. Crouch, W.J. Debnam, Jr. and I.O. Clark, J. Crystal Growth 73, 304-310 (1985).

22. D.C. Gillies, J. Electr. Mater. II, 689-697 (1982).

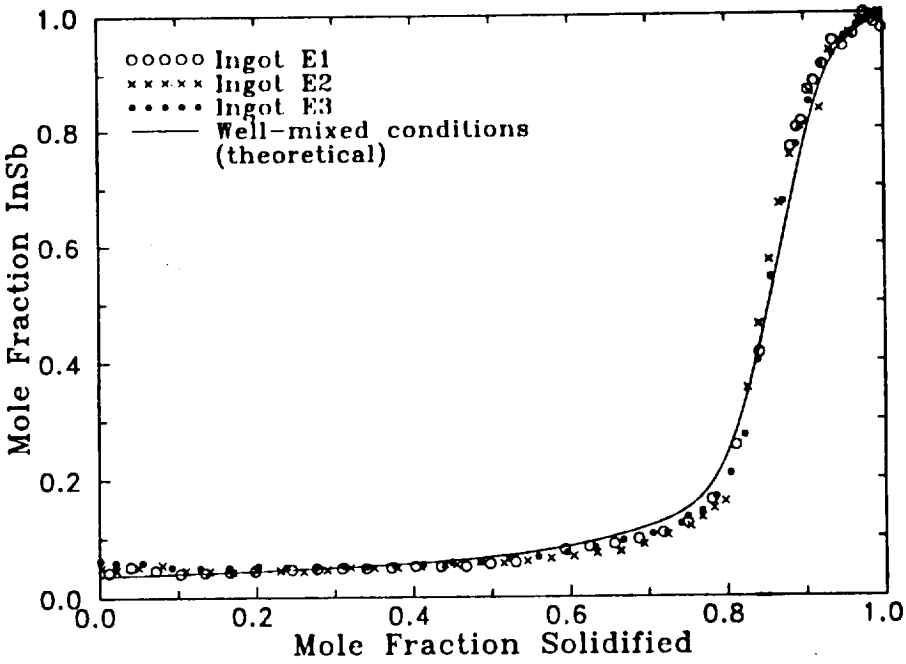

Figure 1: Axial composition profiles for ingots E1, E2, and E3.

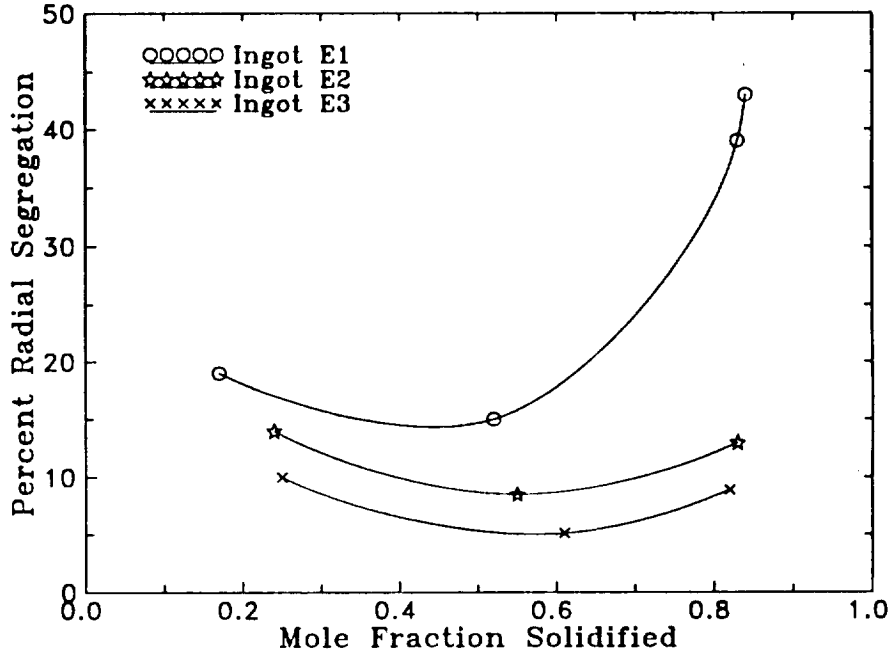

Figure 2: Percent radial segregation vs. fraction solidified for crystals E1, E2, and E3.

III. INFLUENCE OF IMPOSED FREEZING RATE FLUCTUATIONS ON THE MICROSTRUCTURE AND COMPOSITIONAL HOMOGENEITY OF INDIUM GALLIUM ANTIMONIDE

Mohsen Banan

Summary

The long term goal of this project is to develop techniques allowing one to routinely grow single crystal semiconductors uniform in composition. The objective is to determine the influence of imposed freezing rate fluctuations on compositional homogeneity, twinning, and grain size of directionally solidified indium gallium antimonide. This research complements that described in the preceding section. Together these should enable us to determine the mechanism by which spin-up / spin-down reduces polycrystallinity in solidification of mercury cadmium telluride. Passage of current pulses through the material during solidification will produce alternate melting - freezing cycles without significantly influencing convection in the melt.

A technique was developed to measure the radial and axial temperature profiles using three thermocouples; one inside the charge and two attached to the ampoule wall. The thermal perturbation in the melt during application of current pulses was measured *in-situ*. A cyclic temperature variation in the melt was observed during on-off current pulsation. Application of a continuous current resulted in re-establishment of a new steady state temperature in the melt.

Two ingots with 20% InSb composition were grown at 8 mm/day and 12 mm/day with 80 to 110°C/cm axial temperature gradient across the adiabatic zone, corresponding to heater and cooler settings of 770 and 75°C. The ingots consisted of large number of small grains and twins with scattered microcracks near the upper parts, presumably due to thermal stress.

To lower the temperature gradient in the ampoule, the heat exchanger cooler in the apparatus was replaced with a Kanthal resistance heater. The height of the adiabatic zone also was increased. Two ingots with 20% InSb feed composition were grown in the modified furnace at 7.9 mm/day ampoule lowering rate and 25 to 35°C/cm interfacial temperature gradient, corresponding to heater and cooler settings of 800 and 475°C. A significant improvement in the microstructure of this ingot was observed as compared to ingots grown with a larger temperature gradient. In addition there were no microcracks. In the first experiment, power to the heaters were turned off after solidification of half of the ingot, in order to reveal the solid-liquid interface shape at that time.

A new procedure was developed for preparation of the electroded ampoules. Two solidification experiments with current pulse were performed. Electrical continuity across the electrodes was not achieved due to leakage of melt at the bottom electrode. The leakage problem was resolved. A periodic growth experiments was carried out with $In_{0.2}Ga_{0.8}Sb$ feed composition. DC square-wave curent pulses 10 amp in amplitude

(15.7 amp/cm^2 current density) and 26.5 s on and off time (corresponding to the spin-up / spin-down duration performed by Gray) were passed from solid to melt. The heater and cooler settings were 800^{o}C and 475^{o}C, yielding a temperature gradient of 35^{o}C/cm.

A vibration unit was added to the solidification apparatus. The vibrator is used for homogenizing the melt prior to initiation of solidification. It may also be utilized to investigate the effect of axial vibration on the solidification of materials. An attempt was made to measure the temperature fluctuations in the melt during application of axial vibration to the ampoule. Recording of the temperature fluctuations was not feasible due to slow response time of the thermocouple as compared to the frequency of vibration (1 HZ to 20 HZ). An ingot with 20% InSb composition was directionally solidified at a lowering rate of 7.9 mm/day with application of axial vibration to the ampoule at 2 HZ and 0.1 cm amplitude. The liquid-solid interface was revealed by rapid freezing of the melt. The interface was slightly convex.

A. Introduction

Solid solutions of semiconducting III-V and II-VI systems, such as indium gallium antimonide and mercury cadmium telluride, exhibit the advantage of composition - dependent properties. By selecting a suitable composition, particular properties can be produced to suit different purposes and applications, such as optoelectronic and infrared sensing devices. For example, a solid solution of $In_xGa_{1-x}Sb$ is a promising material for photodetectors, Gunn devices, and three level oscillators [1-4].

In spite of considerable interest, the production of large homogeneous single crystals of concentrated alloys has not been feasible due to two basic problems associated with alloy growth, i.e. compositional inhomogeneity and polycrystallinity. The origin of the polycrystallinity is not understood despite the extensive research done in this field.

When concentrated alloy melts are frozen, extensive segregation readily occurs to produce an inhomogeneous solid and morhological breakdown due to constitutional supercooling [5-7]. Such growth behavior may also be the cause of formation of twins, grains, precipitates, dislocations, etc. While constitutional supercooling may be avoided by use of a low growth rate and a large temperature gradient at the freezing interface, twinning and polycrystallinity persist nonetheless. It has been speculated that freezing rate fluctuations may lead to momentary constitutional supercooling with accompanying nucleation of twins and grains even when the average freezing rate is sufficiently low that constitutional supercooling is not expected.

Application of ultrasonic vibration during Czochralski growth of $In_xGa_{1-x}Sb$ (x~0.01) seeded with GaSb resulted in single crystals, whereas ingots grown without vibrations were polycrystalline [8]. The stirring induced by ultrasonic vibration was thought to enhance mixing and to reduce the build-up of the rejected solute at the liquid-solid interface. However, as the feed composition was increased from 1% to 3% and 7% InSb, increasing difficulty was experienced in achieving single crystallinity even with application of ultrasonic vibrations. The polycrystallinity was attributed to morphological breakdown due to a high growth rate.

Buoyancy induced convection is always present in the melt during solidification on Earth because of the unavoidable thermal and compositional gradients. Steady state flows may be desirable since they reduce the buildup of compositional variations at the interface due to segregation and reduce the sensitivity of the growth to small fluctuations in growth rate. However, unsteady flows are undesirable because they result in temperature fluctuations, flow velocity variations and freezing rate fluctuations. The microscopic distribution of components at the interface is often extremely sensitive to changes in convection, temperature and freezing rate. In addition to causing compositional striations, these fluctuations may also lead to nucleation of grains and twins.

A "thermally stable" VBS configuration, with the heater situated above cooler, may be used for minimizing convective problems. However, due to unavoidable radial temperature gradients and variations in composition of the melt at the interface, some convection is always expected [9,10]. One way to eliminate the effect of free convection during solidification is to perform the experiments in space. The directional solidification of InGaSb ingots aboard Skylab [11-13] resulted in a reduction in the number of twins and grain boundaries as compared with the corresponding ingots solidified on Earth under otherwise identical conditions. A similar reduction in the number of twins was also observed in InGaSb ingots solidified with a magnetic field applied to the melt to inhibit free convection [14]. Such an improvement was attributed to the suppression of temperature fluctuations in the melt due to application of the magnetic field.

As pointed out in the preceding section by Gray, another approach to overcome free convection is to introduce regular, forced convection on a scale that will overwhelm any buoyancy effects. Mullard in England produces homogeneous large grain HgCdTe ingots by use of accelerated crucible rotation (ACRT) during Bridgman growth. Quenching studies [16] of the HgCdTe ingots grown under application of ACRT revealed the solid-liquid interface was less concave than without ACRT. Also a region ahead of the interface in ACRT grown ingots were found to consist of alternating cadmium enriched and depleted zones, which was taken to be evidence of periodic meltback. The marked grain size enlargement might have been due to a less concave interface, periodic meltback and growth, and/or ACRT-induced stirring removing nuclei formed on the ampoule wall adjacent to the interface.

Recent electrochemical measurements by Larrousse [17] of mass transfer during ACRT of a vertical tube showed large fluctuations. Temperature measurements during the top seeded flux growth of YIG with ACRT revealed temperature oscillations of 2 to 8°C near the interface [18]. We conclude from these observations that it is likely that there is periodic meltback and growth during solidification with ACRT. Meltback and regrowth have been shown to greatly accelerate grain selection during solidification of films of salol [19]. The dislocation density of GaP was reduced by a factor of 3 as result of one meltback cycle during LPE growth [20].

As shown in the preceding section, Gray is studying the effect of ACRT on the compositional homogeneity and crystallographic perfection of InSb-GaSb solid solutions. Indium gallium antimonide was chosen as a model substance representing II-VI and III-V alloy systems. For example, it has a phase diagram similar to mercury cadmium telluride, but with a low melting temperature and vapor pressure. It exhibits

the same sort of solidification problems, i.e. twinning, grain formation, and inhomogeneities.

To differentiate the effect of stirring from that of backmelting effect with ACRT, here we grow InGaSb ingots with and without application of current pulses during directional solidification. The passage of current results in a thermal perturbation at the solid-liquid interface due to the Peltier effect [22]. Joule and Thomson effects also occur in the melt and the solid. The combination of these effects induces periodic melting and growth at the interface without enhancing convection.

For comparison, the experimental parameters of the ACRT solidification runs and the current induced growth variation runs are similar. Ingots are grown with the same feed composition (20% InSb) and 8 mm/day ampoule translation rate. The interfacial temperature gradients are nearly the same. The frequency of current pulsation corresponds with the frequency of ACRT.

B. Experimental methods

In this section we discuss the experimental apparatus, thermal characterization of the furnace, growth materials and ampoule preparation techniques, and in-situ temperature measurements in the melt during application of current. The experimental apparatus is shown in Figures 1 and 2. It consists of a vertical Bridgman-Stockbarger assembly with provisions for passing electric current and vibrations through the ampoule. The VBS furnace is fabricated from two tubular furnaces (9" OD, 3" ID and 6" long) made of Kanthal heating elements embedded in Fibrothal insulation. The maximum operating temperature of the furnaces is 1100^{o}C. The heater and cooler are separated by an adiabatic zone with adjustable height of 0.5" to 4". Two microprocessor based controllers with PID are used to control the heater and cooler temperatures.

A translation unit, held vertically, is utilized to translate the ampoule down the furnace. The translation unit was modified to achieve an ampoule lowering rate as low as 4 mm/day. (Low translation rates are required to avoid constitutional supercooling in the InSb-GaSb solid solution system [15].)

The current interface demarcation system consists of an electroded ampoule, shown in Figure 3, connected to a Keithley voltage/current pulse generator with a maximum output of 10 amp and 100 W with a 1000 s dwell time. The graphite electrodes are machined from UF-4S graphite rods made by Ultra Carbon to proper dimensions, rinsed in an ultrasonic bath with de-ionized water and methanol, and dried in a furnace under a vacuum of 10^{-5} torr. To attach the molybdenum leads to the graphite electrodes, a graphite cement, made by Dylon Industry, is used. The graphite cement is cured at 120^{o}C for 4 hours and followed by another 4 hours at 320^{o}C, preferably under vacuum. The pulse generator operates in either constant current or constant voltage modes. If the ratio of the voltage setting to the current setting is greater than the load resistance, the generator operates in a constant current mode. The voltage is adjusted automatically to compensate for an increase or decrease in the load resistance. Since, melt and solid have different electrical resistivity, as solidification advances the resistance between two electrodes varies. During periodic growth runs, the voltage and current outputs of the

pulse generator are recorded to calculate the relative ampoule resistance. The resistance versus ampoule lowering time and distance into the furnace allows one to determine the time when solidification has been initiated and its position relative to the furnace axial location.

A vibrating unit, manufactured by Bruel and Kjaer Instruments and connected to a power amplifier and function generator, was also installed on the moving platform of the translation unit. The ampoule containing growth materials can be attached to the vibrating unit and be axially vibrated during solidification at different frequencies and amplitudes. The vibrating unit is also used to homogenize the growth materials prior to solidification.

Thermal characterization of the VBS furnace utilized to grow ingots is essential to determine appropriate heater and cooler temperature settings to achieve a desired axial temperature gradient. Temperature profiling of the furnace was performed by measuring the temperature at different axial positions in the furnace. Due to different thermophysical properties, an ampoule with charge has different thermal coupling with the furnace as compared with an empty ampoule. Therefore it was considered desirable to profile the furnace with a thermocouple placed in an ampoule with charge. Due to the erosive nature of the metallic melt, a sheathed thermocouple must be used, or the thermocouple must be coated with a protective high temperature ceramic cement. To avoid oxidation of the molten materials, the ampoule must be evacuated (or filled with an inert gas) and sealed.

A technique was developed to measure the radial and axial temperature profiles. Figure 4 is a schematic diagram of the thermocouples-ampoule arrangements used for temperature profiling. One sheathed thermocouple was situated at the center of the ampoule and two thermocouples were cemented to the ampoule wall at the same lateral position the as the center thermocouple. The ampoule was loaded with prehomogenized $In_{0.2}Ga_{0.8}Sb$, sealed under a vacuum of 10^{-3} torr, and placed in the VBS furnace. The thermocouples were connected to three digital readouts for simultaneous monitoring. Results of the profiling are given in the results section.

A technique was developed to measure the temperature in the melt during current pulsing. A schematic diagram of the experimental apparatus is shown in Figure 5. This arrangement consisted of a vacuum sealed ampoule containing the growth material in contact with graphite electrodes and molybdenum leads. An ungrounded 304 stainless steel sheath thermocouple was situated in the charge. The leads were connected to a Keithly programmable voltage/current pulse generator. The thermocouple output and the voltage proportional to the applied current were recorded simultaneously on a strip-chart recorder.

Two experiments were performed. In the first experiment a K-type thermocouple passing through a double-hole ceramic tubing was used. The thermocouple junction was covered with a high temperature ceramic cement. The experiment failed due to failure of the cement covering the thermocouple bead. Exposure of the thermocouple junction to the current resulted in exessive overshooting of the thermocouple output voltage. In the second experiment, a 0.081 cm diameter ungrounded type K sheath thermocouple, shown in Figure 6, was placed in the charge. The electroded ampoule, 0.9 cm ID and 1.1 cm OD, was loaded with prehomogenized $In_{0.2}Ga_{0.8}Sb$. The height of the

charge was 5 cm. The tip of the thermocouple was positioned 2.5 cm above the bottom electrode. The pre-alloyed charge was melted and allowed to reach thermal equilibrium with the surroundings over a 24 hour period. A series of pulsing experiment were performed. Results are discussed in later.

In order to prepare experimental ampoules, we used a new cryo-vacuum unit equipped with argon, nitrogen, and methane gas inlets. This eliminated the moisture in the ampoule (as observed previously when the former vacuum unit was used) and also provides a 10^{-6} torr vacuum. A proper amount of 99.9999% purity growth materials In, Ga, and Sb (purchased from Cerac and Johnson & Mathey) were weighed and loaded into a precleaned 8 in long ampoule. The ampoule was purged with argon three times, sealed under a 10^{-6} torr vacuum, and then placed in a rocking furnace. The growth materials were homogenized and alloyed in the rocking furnace for 8 hours at 850°C. The resulting melt was rapidly solidified by shutting off the rocking furnace. The alloyed materials were chemically polished in 1 HF: 9 HNO_3: 10 H_2O solution for 10-20 s to remove any scum on the surface of the ingot. The polished materials were kept in a desicator.

The fused silica ampoules were cleaned according to the procedure obtained from Rockwell International. The ampoule was soaked in Micro-cleanser overnight, rinsed with de-ionized water three times, rinsed with methanol, soaked in trichlorethane for 1 hour, rinsed with acetone and methanol, soaked in 5% HF for 10 min, rinsed with de-ionized water, soaked in aqua regia for 1 hour, and rinsed thoroughly with de-ionized water. Afterward, the cleaned ampoules were dried and baked in a furnace at 900°C for 3 hours.

For directional solidification runs the pre-alloyed materials were loaded into a pre-cleaned quartz ampoule. The ampoule was purged with argon three times and sealed under a vacuum of 10^{-6} torr. For current pulsing experiments the pre-alloyed materials were solidified in a constricted-tip ampoule. The shaped ingot was placed in between two electrodes in a quartz ampoule, as shown in Figure 3. The ampoule was purged with argon and sealed under a vacuum of 10^{-6} torr.

The loaded ampoule was attached to the ampoule holder of the translation unit. The ampoule was lowered into the VBS furnace. The bottom of the ampoule was situated 1 cm above the adiabatic zone. The heater temperature was set above the melting temperature of the growth materials (about 710°C). The growth material was allowed to melt and to equilibrate over 24 hours prior to initiation of the ampoule translation. To measure the average macroscopic growth rate, the ampoule position was recorded as a function of time during the growth run. Thus far an ampoule lowering rate of 8 mm/day, feed composition of 20% InSb, and ingot dimensions of 0.9 cm in diameter and 7-8 cm long were employed for all growth experiments. (A temperature gradient greater than 20°C for a growth rate of 8 mm/day is required to avoid constitutional supercooling in the $In_{0.2}Ga_{0.8}Sb$ system, Figure 7.)

After termination of a growth run, the heater and cooler temperatures were decreased at 30°C/hr to room temperature. The ampoule was removed from furnace and broken to retrieve the ingot. The ingot was sandblasted using 220 grid industrial SiC to reveal the grains and twins. Afterward, the ingot was sectioned axially and mounted in epoxy. The ingot samples were mechanically polished using 320, 420, and 600 grid size SiC

polishing papers. The final polish was achieved by using 5 and 1 micron micropolish alumina and polishing cloth. The samples were cleaned with de-ionized water in an ultrasonic bath between each step. After mechanical polishing, the samples were etched chemically to reveal the microstructure. The etchant contained HF, HNO_3, and H_2O or HAc. The volumetric fractions of etchant's components were varied from one ingot to another depending on the effect of the etchant on the ingot.

The microstrcture of the ingots was examined using optical and scanning electron microscopy. When this grant period ended last summer we had arranged with NASA/MSFC in Huntsville to use their EDX and FTIR facilities to analyze our ingots.

C. Progress

The original furnace consisted of a Kanthal resistance tubular heater, 2.54 cm adiabatic zone, and a heat-exchanger used as cooler attached to a circulating constant temperature bath with operating temperature range of -20°C to 100°C. Axial temperature profiling of the VBS furnace was performed for heater settings of 800°C and 850°C and cooler settings of 10°C to 70°C using a thermocouple in an empty ampoule. The axial temperature gradients across the adiabtic zone corresponding to the above mentioned settings were about 110 to 150°C/cm.

To measure the axial and radial temperature profiles, a type K sheath thermocouple was placed 3 cm into a prehomogenized $In_{0.2}Ga_{0.8}Sb$ charge. Two K-type thermocouples were cemented onto the outerwall of the ampoule at the same lateral position as the thermocouple inside the charge. The ampoule was sealed under a vacuum of 10^{-3} torr. The ampoule was situated in the heater such that the thermocouple junctions were 3 cm above the adiabatic zone. The temperature settings of the heater and cooler were 770°C and 75°C, respectively. The height of the adiabatic zone was 2.54 cm. The charge was melted and allowed to equilibrate over 24 hours. The thermocouple readings were recorded at 0.2 cm intervals as the ampoule was moved slowly downward into the furnace. Figure 8 shows the resulting temperature profiles. The freezing temperature of the melt varied from 695 to 550°C depending on the fraction that had solidified. Referring to Figure 8, the freezing temperature range was from 1 cm above the adiabatic zone to 1 cm into the adiabatic zone, meaning that the liquid-solid interface might be near-convex to planar. Figure 9 shows that the axial temperature gradient across the adiabatic zone varied from 75 to 150°C/cm. The highest gradient was near the center of the adiabatic zone. The interfacial temperature gradient at the beginning of growth was about 75°C/cm. As solidification proceeded, the temperature gradient also increaseed. Near the end of the growth the temperature gradient approached 140°C/cm. The G/V ratio was in the stable region of Figure 7 for an $In_{0.2}Ga_{0.8}Sb$ alloy.

Figure 10 shows the radial isotherms versus the corresponding axial position of the ampoule in the furnace. The origin is the center of the adiabatic zone. The shape of the isotherms changed from convex to concave as the ampoule was moved from the heater into the cooler.

Two ingots with 20% InSb composition were directionally solidified. DS12-1 was solidified at 12 mm/day with heater and cooler settings of 770°C and 75°C. DS8-2 was

solidified at an ampoule lowering rate of 8 mm/day ampoule lowering rates with the same heater and cooler settings. Prior to initiating the growth, the materials were melted and homogenized for 4 days by application of ACRT to the ampoule at 30 rpm (the rocking furnace had not been fabricated yet). The dome shaped end of ingot DS12-1 in Figure 11a could have been due to insufficient mixing of the elements. Figure 13 shows the results of differential scanning calometery (DSC) analysis of samples taken from four different sections of the dome material. The melting temperature was between 500 and 510^{o}C, which corresponds to the melting temperature of InSb.

Figure 11b shows the microstructure of ingot DS12-1 after mechanically polishing and chemically etching with 1HF:1HNO_3:1H_2O for 20 s to reveal the microstructure. A large number of microcracks and a few voids were in the upper portion of the ingot. The microcracks were possibly caused by thermal stress due to the high temperature gradient. Figure 14 shows a SEM micrograph of a cross sectional sample taken from halfway along the DS12-1. The dislocation pits were about 30 microns in diameter. In DS8-2, as shown in Figure 12, the overall microstructure was not improved as compared to the other ingot. Twins mostly started from the ampoule wall and propagated inward. There were many bubbles on the surface of DS8-2. The surface of the ingot was partially covered with a scumy film similar to that on the surface of DS12-1. The shape of the interface, near the end of growth, was slightly convex as revealed in the last part to freeze. Microcracks were also observed in this ingot. The larger cracks occurred during etching. In DS8-2 the number of curved boundaries was less but the number of twins was greater than in DS12-1.

To reduce the temperature gradient, there were two options; increase the cooler temperature and increase the length of the adiabatic zone. The heat-exchanger cooler (maximum temperature about 100^{o}C) in the VBS furnace was replaced by a Kanthal resistance furnace, similar to the one used for the top heater with an operating temperature up to 1100^{o}C. The height of the adiabatic zone was increased to 2.5". The insulation at both ends of the VBS furnace was increased by 2" to suppress the temperature variations near the ends of the furnace. A quartz liner was placed all the way through the heater-adiabatic-cooler configuration.

Figures 15 and 16 show the temperature profile of the modified VBS furnace, measured with a thermocouple in an ampoule without a charge, for different heater and cooler settings. An axial temperature gradient of 30^{o}C/cm to 40^{o}C/cm across the adiabatic zone was achieved. For the growth runs mentioned in the following, the growth ampoules were prepared using the new cleaning procedure obtained from Rockwell, loaded with 20%InSb feed materials pre-alloyed in the rocking furnace for 8 hours at 850^{o}C. The ampoule was purged with ultra pure argon and evacuated at 10^{-6} torr.

Ingot DS8-3 was solidified with an 8 mm/day ampoule lowering rate with temperature settings of 800 and 450^{o}C for heater and cooler. Translation was terminated after solidification of 65% of the melt; the remaining melt was rapidly solidified by lowering the heater temperature from 800 to 500^{o}C. The cooler temperature was held at 475^{o}C to avoid exessive thermal stress on the already grown portion. After solidification of the remaining melt, the heater and cooler temperatures were lowered at 30^{o}C/hr to the room temperature. Figure 17a is a photograph of DS8-3 after sandblasting. During sandblasting it cracked into two pieces along the rapidly frozen region. The boundary between the two regions was convex. The surface of the ingot was shiney and free of

voids and bubbles. Figure 17b illustrates the axially sectioned ingot after being polished mechanically and chemically etched using 1HF:1HNO_3:1HAc for 15-20 s. (The etchant used for ingots DS12-1 and DS8-2 was not effective on ingot DS8-3.)

There were no microcracks in the directionally solidified portion of DS8-3. The number of columnar grains diminished to four in the middle of the ingot. The overall microstructural quality of DS8-3 was improved as compared to DS12-1 and DS8-2, previously grown at larger temperature gradients.

DS8-4, shown in Figure 18, was directionally solidified at 7.8 mm/day translation rate and 800 and 475 ^{o}C heater and cooler settings with an adiabatic zone of 5.08 cm (2"). The surface of the ingot was fairly shiney and free of bubbles and voids. A crack occurred near the end of the ingot at the time of removal from the ampoule.

VDS8-5 was directionally solidified at 7.9 mm/day translation rate with axial vibration of 2 Hz and 0.1 cm amplitude. The heater and cooler settings were 800 and 475^{o}C. Figure 19a is a photograph of VDS8-5 after being sandblasted. The ingot cracked during sandblasting. A large number of bubbles and voids were on the surface of the ingot, specially at its beginning. VDS8-5 was axially sectioned and sandblasted to reveal the microstructure, Figure 19b. After solidification of half of the ingot, the heater temperature was lowered from 800 to 710^{o}C by shutting off the furnace for few minutes. Afterward the heater was reset to its initial setting of 800^{o}C. Referring to figure 19b a distinct variation in microstructure was observed at this perturbation, marked by an arrow, indicating a near convex liquid-solid interface shape. Afterward directional solidification at 8 mm/day was resumed. The melt was rapidly frozen after solidification of half of the ingot. The cooler was held at 475^{o}C to avoid stressing the already solidified region. The boundary between the two regions was convex. A few twins started from the prephiery, near the outer surface of the ingot adjacent to the ampoule wall.

Four growth runs were performed with electroded ampoules. The first experiment was performed with the ampoule design shown in Figure 3c. Despite the bottom electode fitting tightly against the ampoule wall, during heating up some molten material leaked down into the bottom of the ampoule and rapidly froze. This broke the ampoule. The ampoule design was modified to a double-wall ampoule design as shown in Figure 3b. In the first growth run with the new ampoule design, melt again leaked between the bottom electrode inner wall and the ampoule wall. The leakage problem was resolved by filling the gap between the bottom electrode and the ampoule wall with high temperature ceramic cement, manufactured by Omega Engineering, cured at 120^{o}C for 4 hours.

CIDS8-6, Figure 20a, was grown at 7.9 mm/day translation rate. The heater and cooler settings were and 475^{o}C. The bottom of the ampoule was positioned 1 cm above the adiabatic zone. After 40 hours of ampoule translation, corresponding to 1.3 cm of translated distance, passage of current through the growth system was initiated. An on-off 10 amp dc current pulse with 53 s period was passed from solid to melt (i.e. solid + and melt -) during the entire run. The duration of the pulses, 26.5 s on and 26.5 s off, corresponds to the period used in the ACRT growth experiment described earlier in this report. The variation in the voltage and current settings was recorded to permit calculation of the relative ampoule resistance. Figure 21 ampoule resistance versus

time. During the first 80 hours of pulsation the resistance was nearly constant and stable. Then the resistance increased linearly. Such a change in the resistance can be attributed to the progression of solidification.

Figure 20b shows CIDS8-6 after sanblasting. The axially sectioned ingot is shown in Figure 20c. A crack appeared during cutting. A large number of scattered curved boundary grains were present in the first-to-freeze region of the ingot. The number of columnar grains diminished in the middle of the ingot. A few twins started near the prephiery of the ingot and grew parallel to the direction of growth. No new twins were generated during growth. One half of the sectioned ingot was mounted in epoxy, mechanically polished and chemically etched. No striations were detected even at 5000X under SEM.

To determine temperature and freezing rate variations with current pulsing, an electroded ampoule was prepared with 20% InSb feed composition material doped with 1000ppm Te (0.03 g). Due to a 3 hour power outage, the ampoule broke. (The available backup power source for the VBS ingot growth apparatus, on the bottom rack in Figure 2, provides 2400 W for 40 min.)

In-situ temperature measurements during pulsations were performed in the melt prior to the onset of solidification. Figures 21 and 22 show the temperature measurements in the melt of $In_{0.2}Ga_{0.8}Sb$ during 30 s aqnd 60 s pulsations. The steady temperature prior to pulsation in the melt was 812.3°C. The temperature of the melt increased to maximum values of 815.0 and 816.1°C, for the 60 s and 30 s pulsation times, respectively. After the termination of the current pulse, the melt was allowed to cool to the initial steady state temperature for 220 to 250 s. The temperature continued to rise for 10 s after the current was switched off and then began to decay. This extended temperature rise probably reflects the response time of the thermocouple. (Similar behavior was observed by Silberstein et al. [24] in studying the effect of pulsations on the directional solidification of the Bi-Mn eutectic.) Passage of a square-wave 10 amp current, 60 s on and 30 s off, through the melt resulted in a periodic temperature variation in the melt, as shown in Figure 23. However, alternating current pulses of 10 amp with 60 s duration, i.e. 30 s + and 30 s -, resulted in restablishment of a new steady state temperature in the melt during each application of current.

The ampoule was then lowered into the furnace to promote solidification. The thermocouple reading was monitored to position the thermocouple junction in the vicinity of the liquid-solid interface (in reference to the freezing temperature of the material, about 695°C). The objective was to measure the temperature variations due to Peltier heating or cooling generated at the interface. At 716.1°C, passage of the current resulted in a sudden jump of the thermocouple output, Figure 24. This jump, from 716 to 737°C, at the time of pulsation was due to exposure of the junction to the melt during pulsation. The experiment was terminated.

D. Plans

First on the agenda is to analyze the already grown ingots using EDX and FTIR. The axial and radial composition profiles of the ingots will be determined. Compositional

profiling of the ingots will provide information on the effect of current-induced growth rate fluctuations and axial vibrations on the homogeneity of the ingots as compared with the ingots directionally solidified under no external disturbance. A transient one dimensional heat transfer model, already formulated using a finite element Galerkin method with roof function, will be programmed for the computer. The model will be used to predict the variation in the interfacial growth rate due to Peltier heating/cooling and Joule heating.

Two *in-situ* thermal transient measurements will be performed; one with GaSb, whose thermophysical properties are well known and another with $In_{0.2}Ga_{0.8}Sb$ feed composition. The emphasis will be on measuring the temperature fluctuations near the interface due to the Peltier effect. Temperature measurents in the melt during pulsation will be implemented into a lumped capacity model to determine the heat transfer coefficient between the charge and the furnace. The value of heat transfer coefficient will be used in the heat transfer model.

One current-induced growth run will be performed with $In_{0.2}Ga_{0.8}Sb$ feed composition doped with Te (100 ppm). The ojective of this experiment will be to demarcate the interface by passage of current across the interface. The demarcation striations will reveal the shape of the interface. Also, by measuring the distance between consecutive demarcations and knowing the frequency of pulses, the microscopic growth rate can be determined. The heater and cooler settings will be 800 and 475^{o}C, and translation rate will be 8mm/day. One ingot with 20% InSb composition will be grown with alternative current pulses of 10 amp amplitude. Different pulse durations will be tried during growth, e.g. 3 days of growth with 60 s + and 60 s - ; 3 days of 120 s + and 120 s - , etc. This experiment will provide information on the effect of pulse duration on the microstructure and composition of the ingot. One ingot with 20% InSb will be grown with on and off squarewave 10 amp current pulses. The pulse durations will be similar to the previous experiment for comparison.

E. References

1. T.S. Plaskett and J.F. Woods, J. Crystal Growth 11, 341 (1971).

2. A. Joullies, J. Allegre and G. Bougnot, Mater. Res. Bull. 7, 1101 (1972).

3. J.C. McGoody, M.R. Lorenz, and T.S. Plaskett, Solid State Comm. 7, 901 (1961).

4. G. Hilsum and H.D. Rees, Electronics Lettr. 9, 277 (1970).

5. W.A. Tiller, K.A. Jackson, J.W. Rutter and B. Chalmers, Acta Met. 1, 428 (1953).

6. J.W. Rutter and B. Chalmers, Can. J. Phys. 31, 15 (1953).

7. W.W. Mullins and R.F. Sekerka, J. Applied Phys. 34, 323 (1963).

8. T. Tsuruta, Y. Hayakawa and M. Kumagawa, Jap. J. Appl. Phys. 27 (1988) Supplement 27-1 p. 47.

9. G. Neugebauer and W.R. Wilcox, J. Crystal Growth 89, 143-154 (1988).

10. G. Neugebauer, Private Communication, Clarkson University (1989).

11. J.F. Yee, M. Lin, K. Sarma, and W.R. Wilcox, J. Crystal Growth 30, 185 (1975).

12. K. Sarma, Ph.D. Thesis, University of Southern California (1978).

13. R.A. Lefever, W.R. Wilcox and K. Sarma, Mater. Res. Bull. 13, 1175 (1978).

14. S. Sen, Ph.D. Thesis, University of Southern California (1976).

15. P. Capper, J.J.G. Gosney and C.L. Jones, J. Crystal Growth 70, 356 (1984).

16. P. Capper, J.J. Gosney, C.L. Jones and M.J.T. Quelch, J. Crystal Growth 63, 154-164 (1983).

17. M. Larrousse, Ph. D. Thesis, Clarkson University (1987).

18. S. Durock and E. Pollert, J. Crystal Growth 82, 501-508 (1987).

19. K.A. Jackson and C.E. Miller, J. Crystal Growth 42, 364 (1977).

20. M. Schieber, p. 279 in "Crystal Growth and Materials," Eds. E. Kaldis and H.J. Scheel, North Holland, Amsterdam (1977).

21. R. Gray, Private Communication, Clarkson University (1989).

22. R.D. Barnard, "Thermoelectricity in Metals and Alloys," John Wiley and Sons, New York (1973) Ch. 1.

23. S.P. Silberstein, D.J. Larson and B. Dressler, Met. Trans. A15, 2147 (1984).

Figure 1. Schematic diagram of vertical Bridgman - Stockbarger ingot growth apparatus and current interface demarcation system.

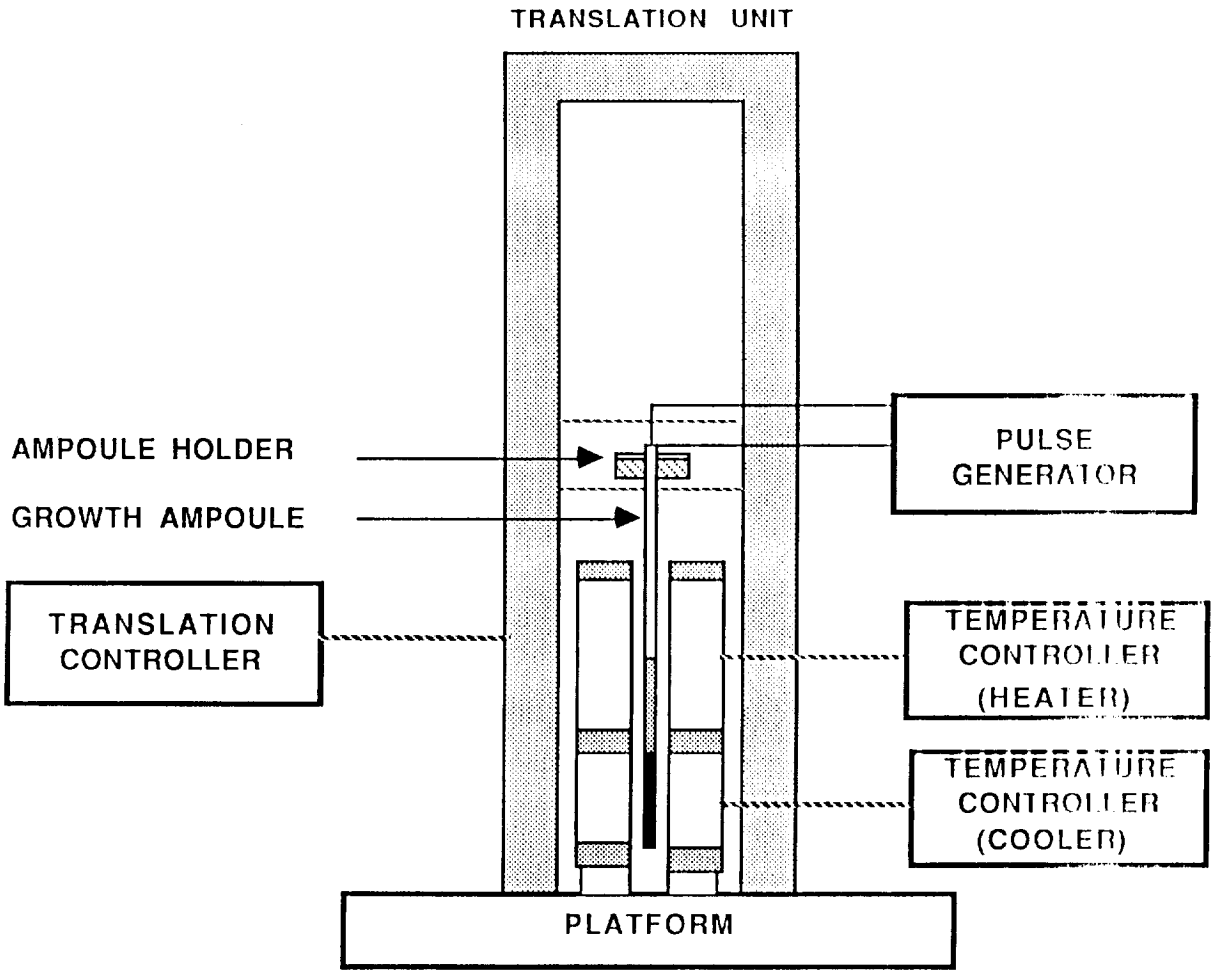

Figure 2. Experimental setup.

ORIGINAL PAGE
BLACK AND WHITE PHOTOGRAPH

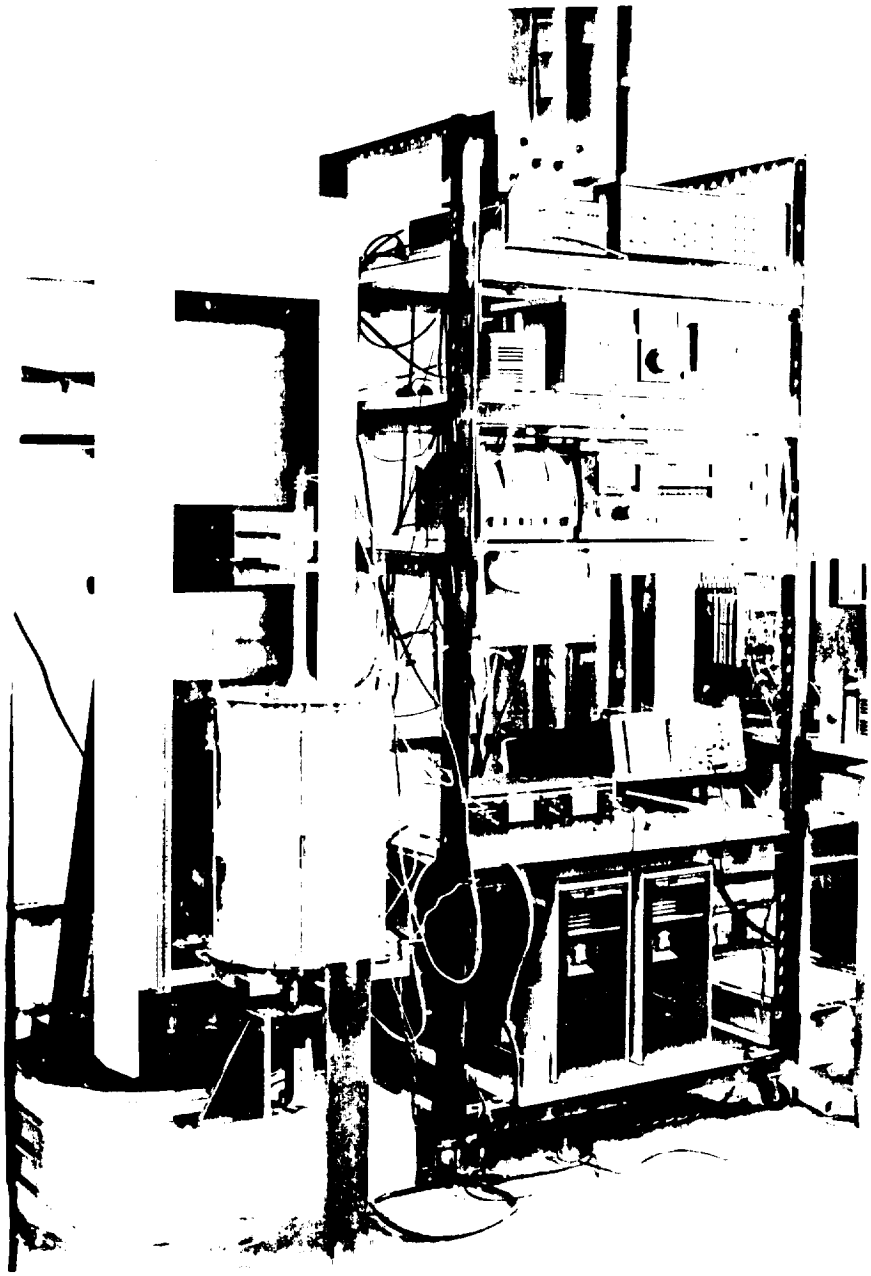

Figure 3. Electroded ampoule for current interface demarcation.

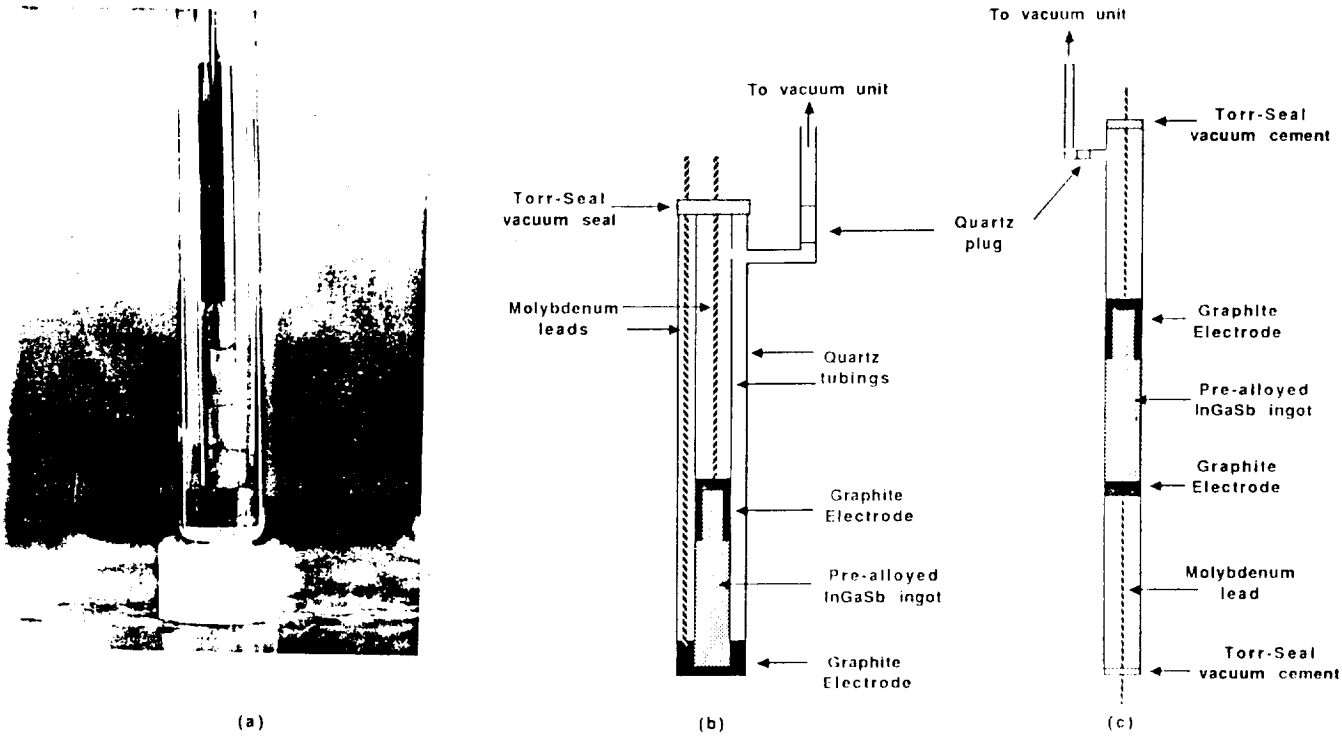

Figure 4. Thermocouple - ampoule arrangement for radial and axial temperature profiling in the VBS furnace.

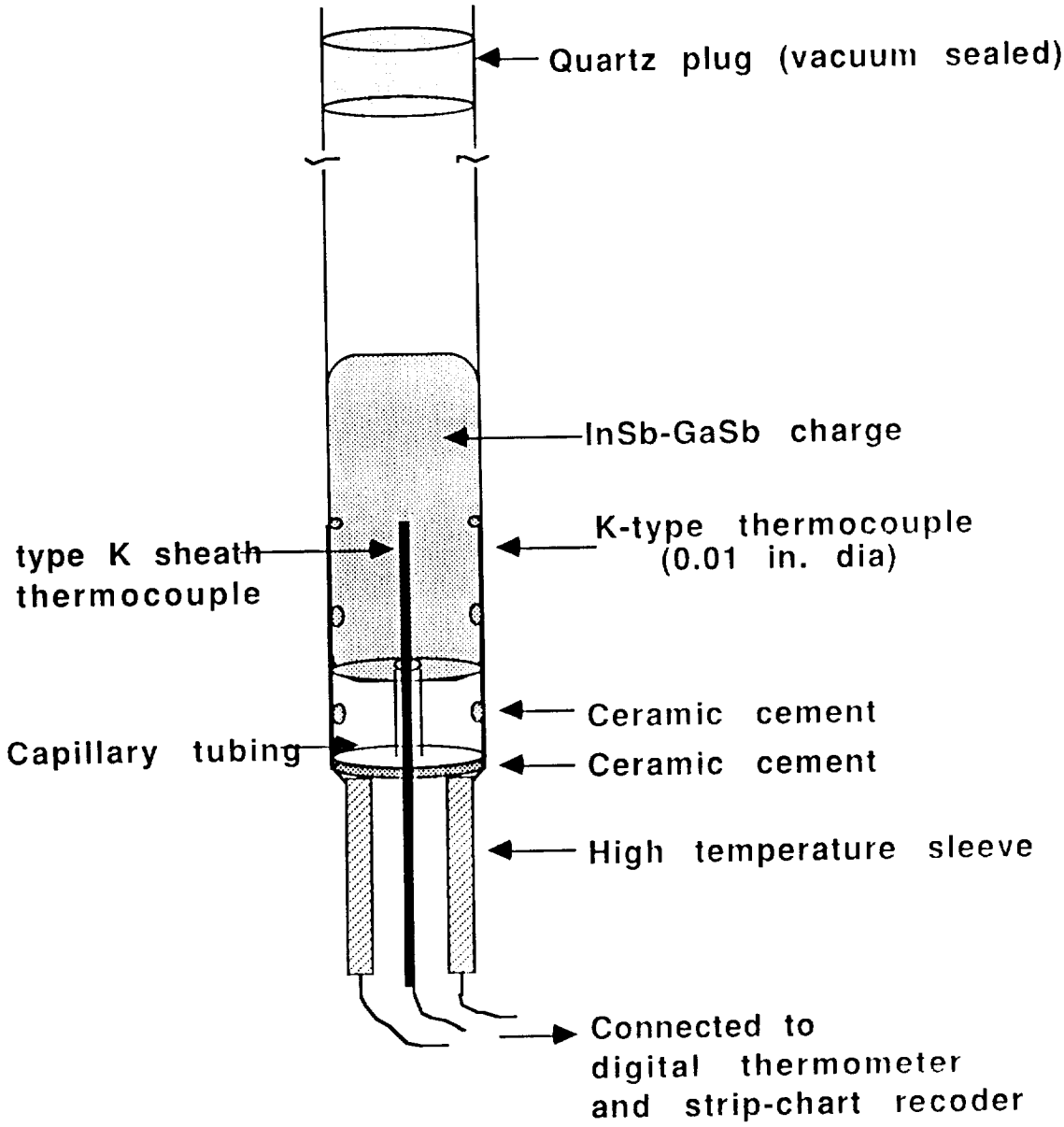

Figure 5. Experimental setup for *in-situ* temperature measurements in the charge during application of current pulse.

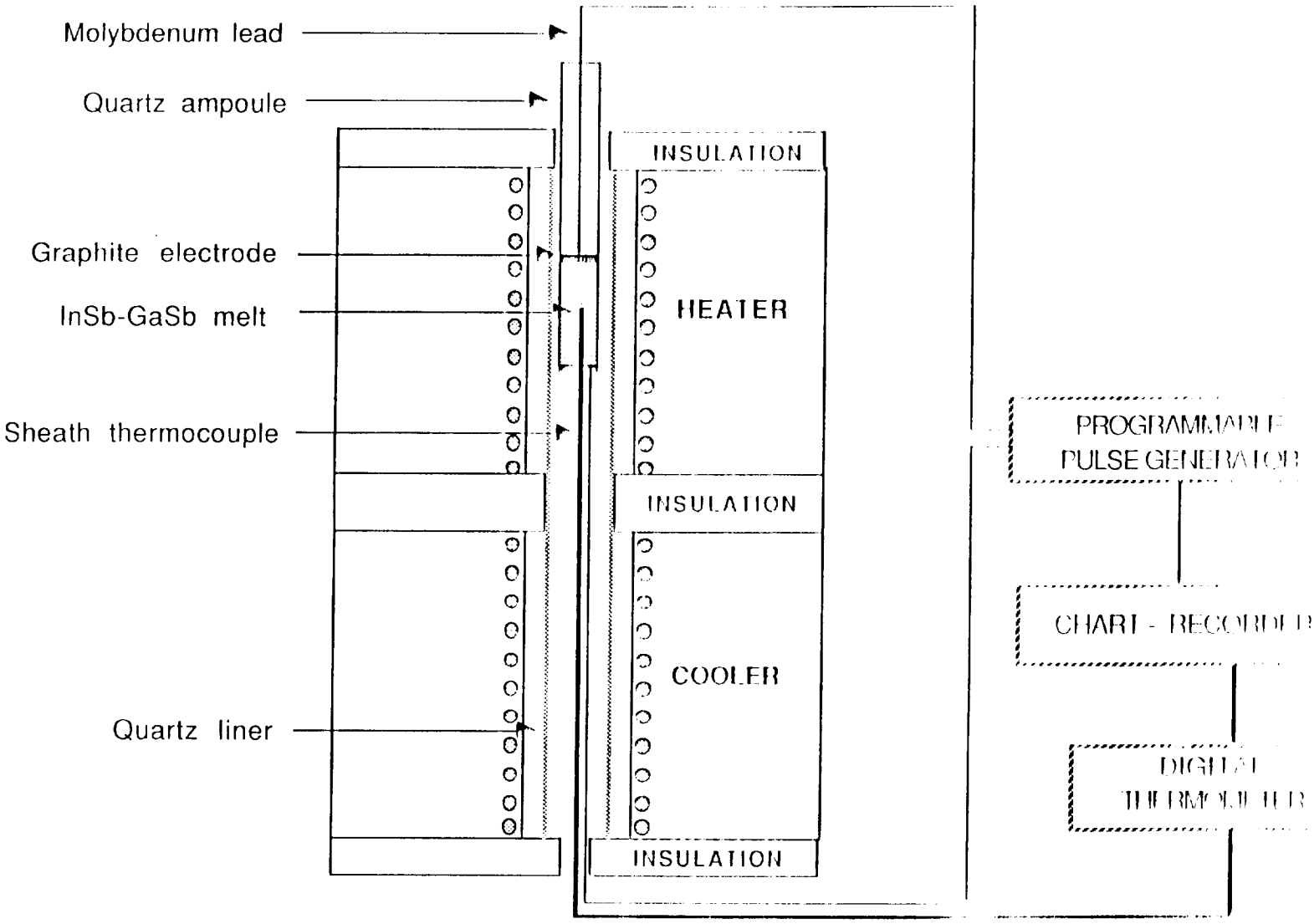

Figure 6. Ampoule design for in-situ thermal transient measurements during current pulsation.

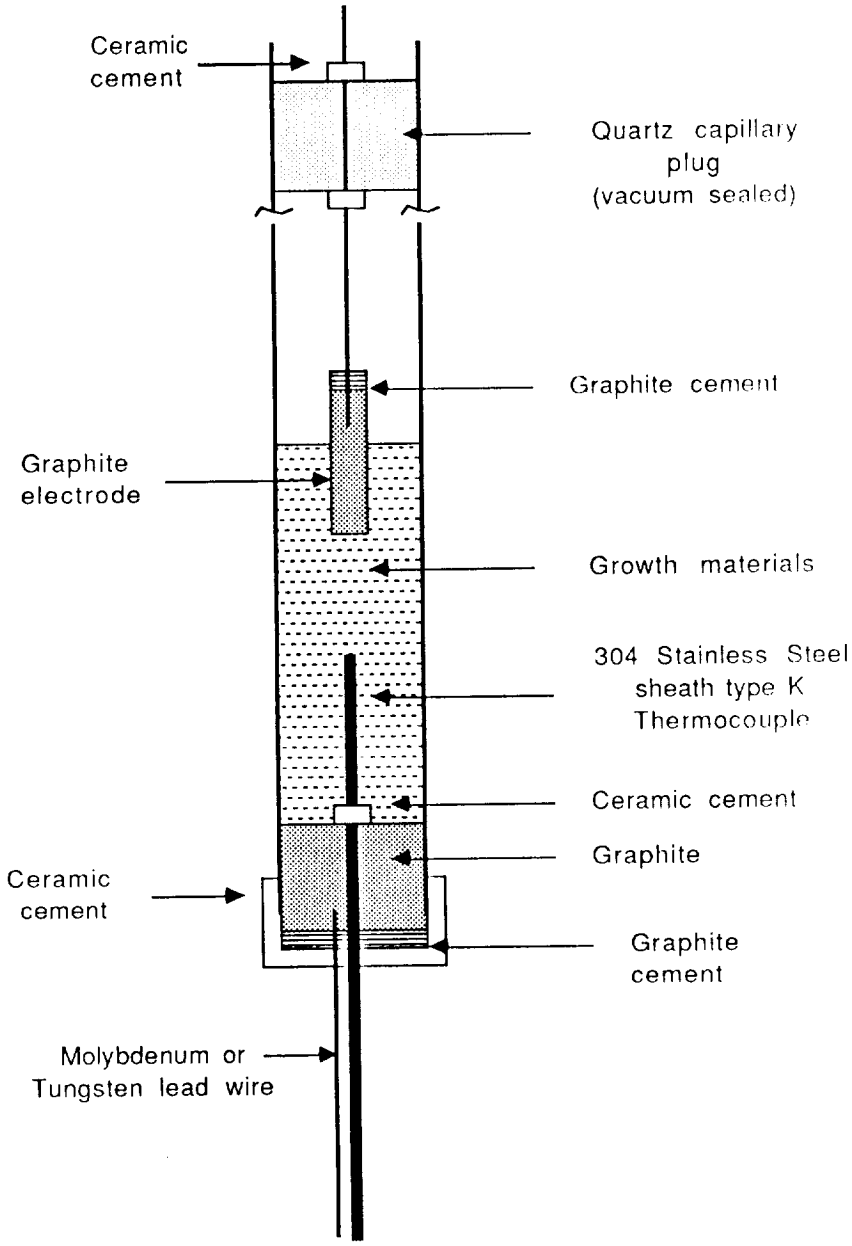

Figure 7. Critical G/V for contitutional supercooling in $In_xGa_{1-x}Sb$ [14].

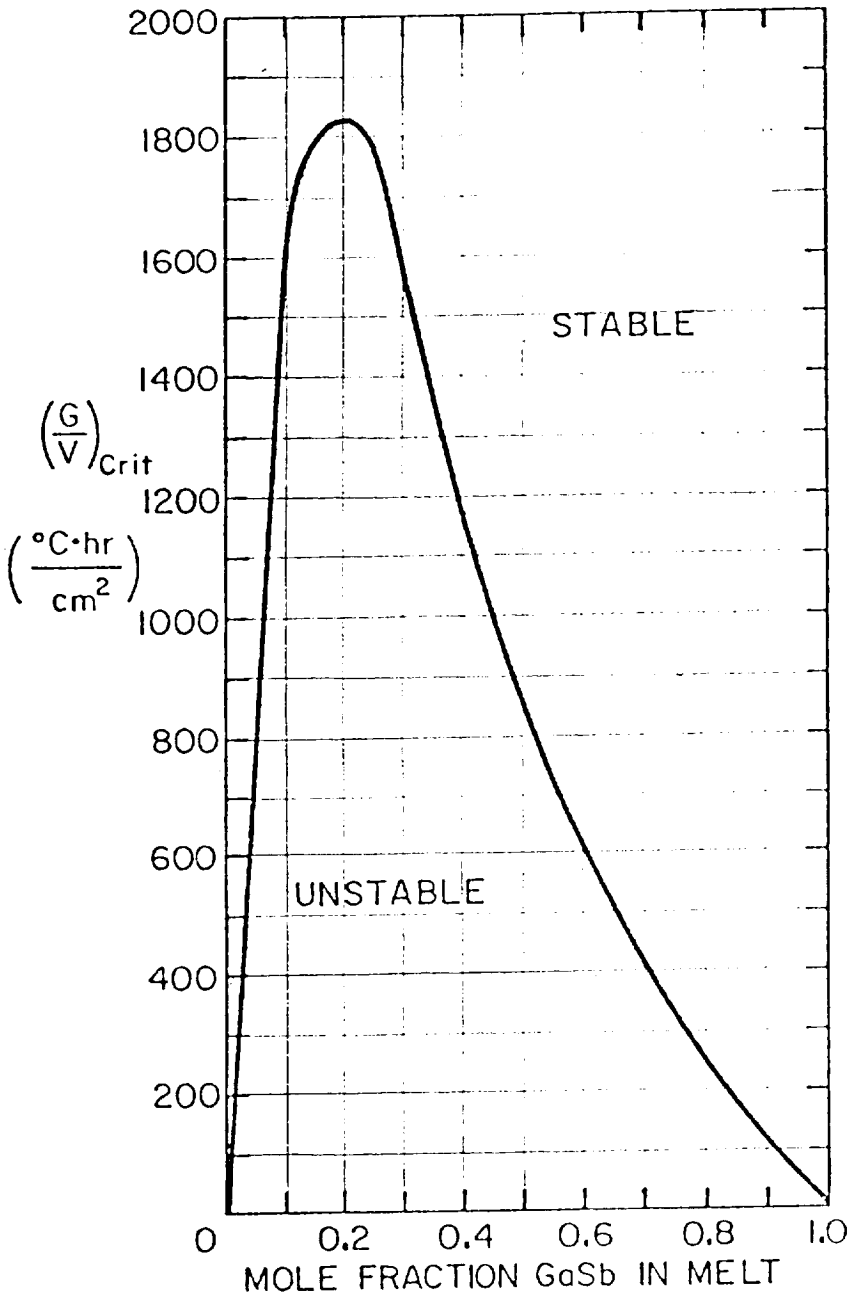

Figure 8. Thermocouple readings in the charge and on the ampoule wall in the VBS furnace for heater and cooler settings of 770 and 75°C, respectively, and 2.54 cm (1") adiabatic zone.

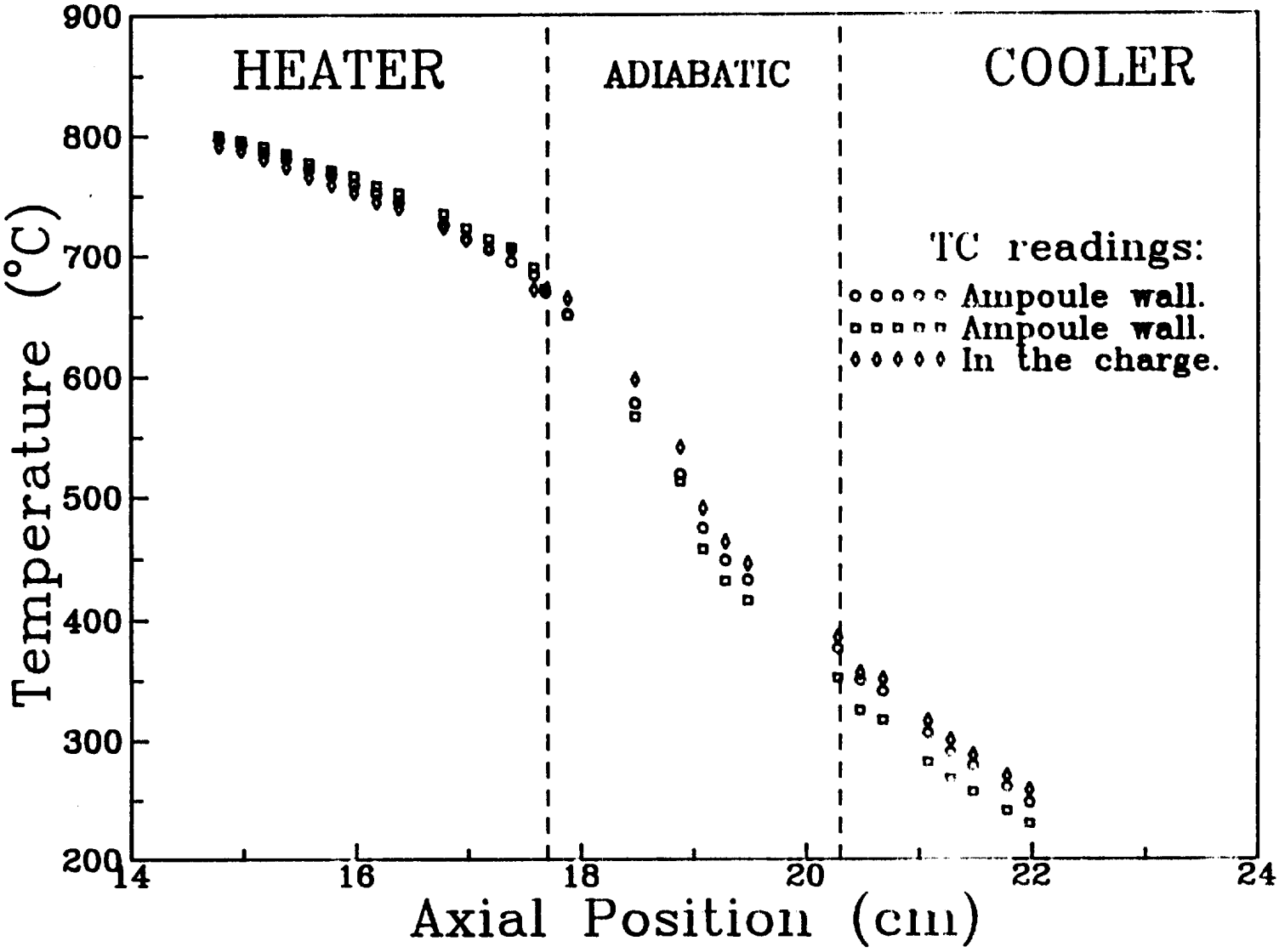

Figure 9. Temperature gradient versus axial position in the furnace, from the data in Figure 8.

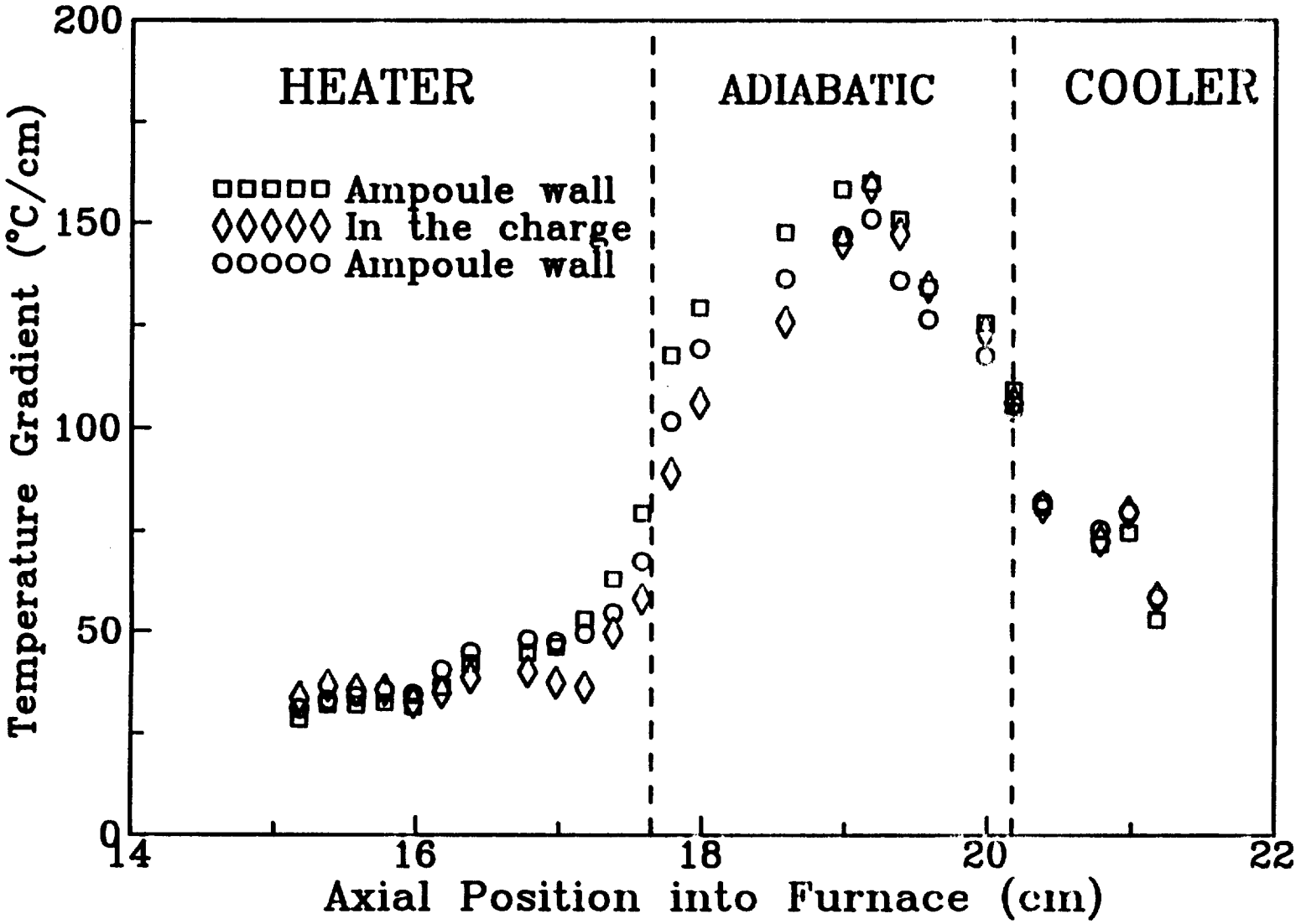

Figure 10. Radial isotherms versus axial position in the furnace. The origin is the center of the adiabatic zone.

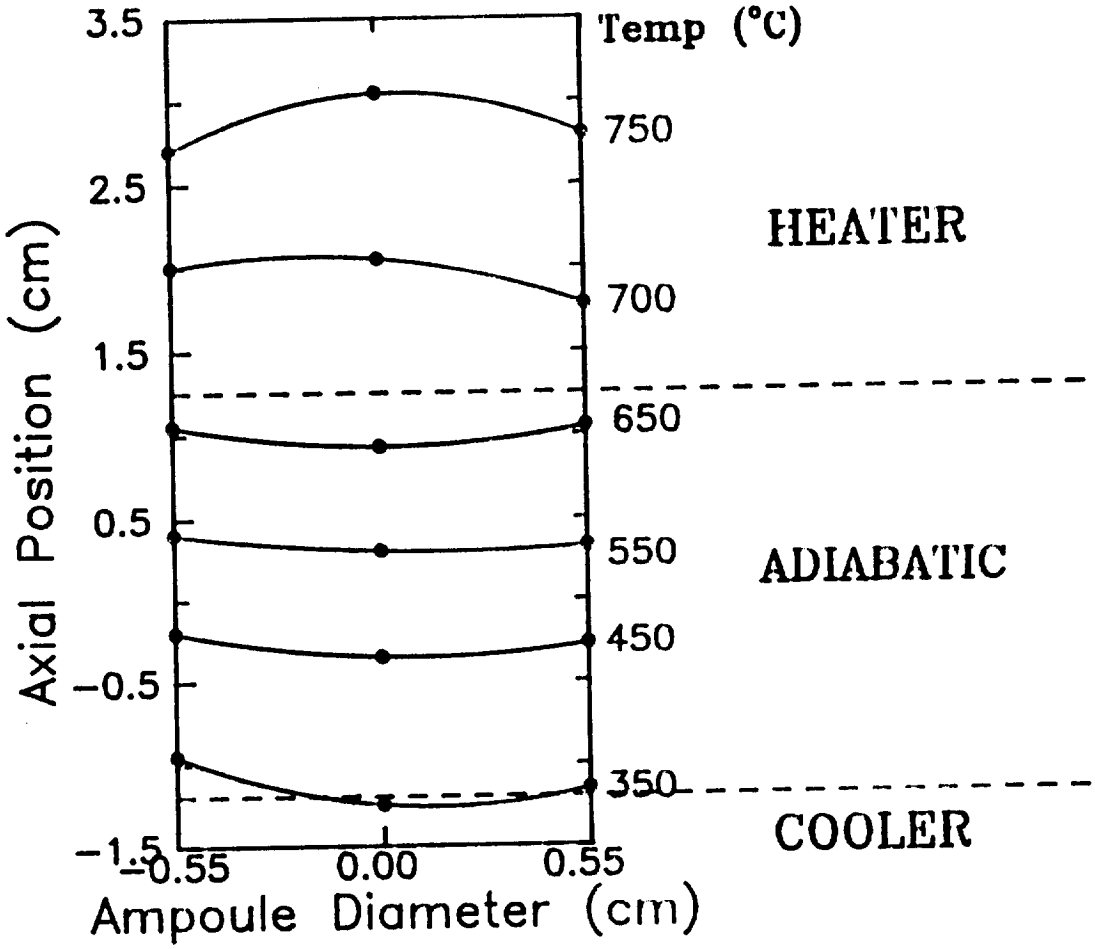

Figure 11a. Photograph of ingot DS12-1 with $In_{0.2}Ga_{0.8}Sb$ feed composition grown at 12 mm/day ampoule lowering rate and temperature gradient of 80 to 110°C/cm. The growth direction is from left to right.

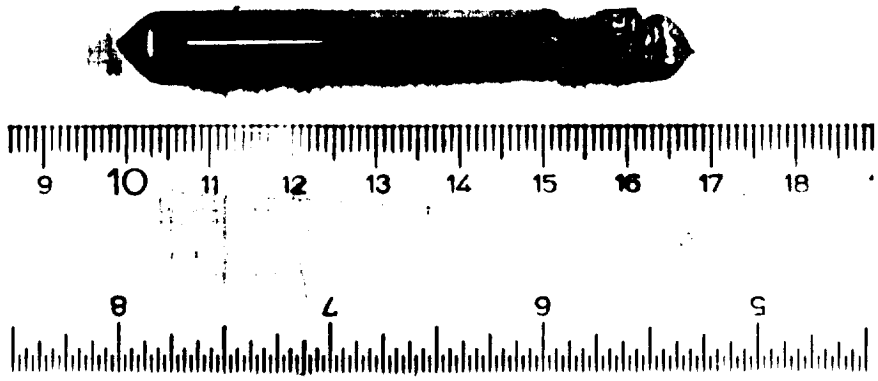

Figure 11b. Photograph of axially sectioned ingot DS12-1 mounted in an epoxy mold. The ingot was mechanically polished and chemically etched in $1HF:1HNO_3:1H_2O$ for 15 to 20 s to reveal the microstructure. Arrows indicate the direction of growth.

Figure 12. Photograph of axially sectioned DS8-2 mounted in epoxy. The ingot was directionally solidified at 7.9 mm/day and 90 to 110°C/cm temperature gradient. The growth direction was from left to right. The ingot was mechanically polished and chemically etched in $1HF:1HNO_3:1H_2O$ for 15 to 20 s to reveal the microstructure. Large microcracks occurred during etching the sample. The liquid-solid interface was near convex, as seen in the last-to-freeze section.

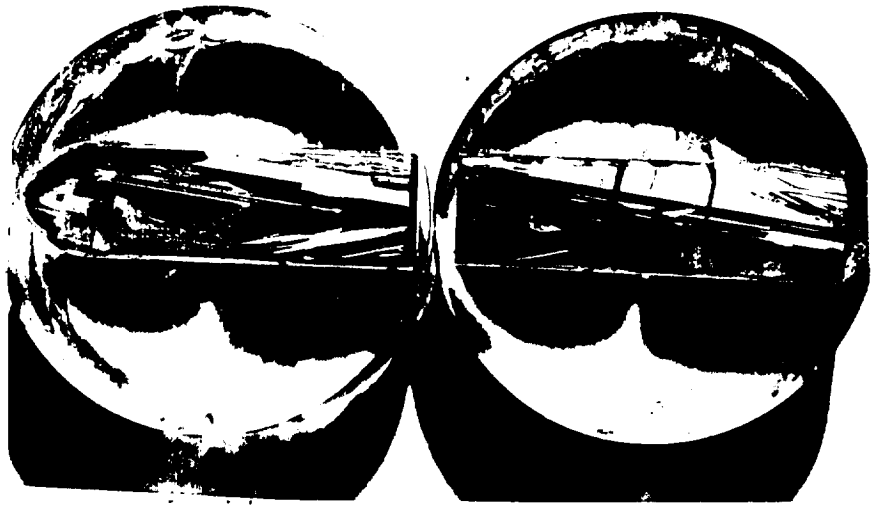

Figure 13. DSC heating thermogram of the dome material accumulated at the end of ingot DS12-1. Aluminum was used for calibration of Perkin-Elmer DSC.

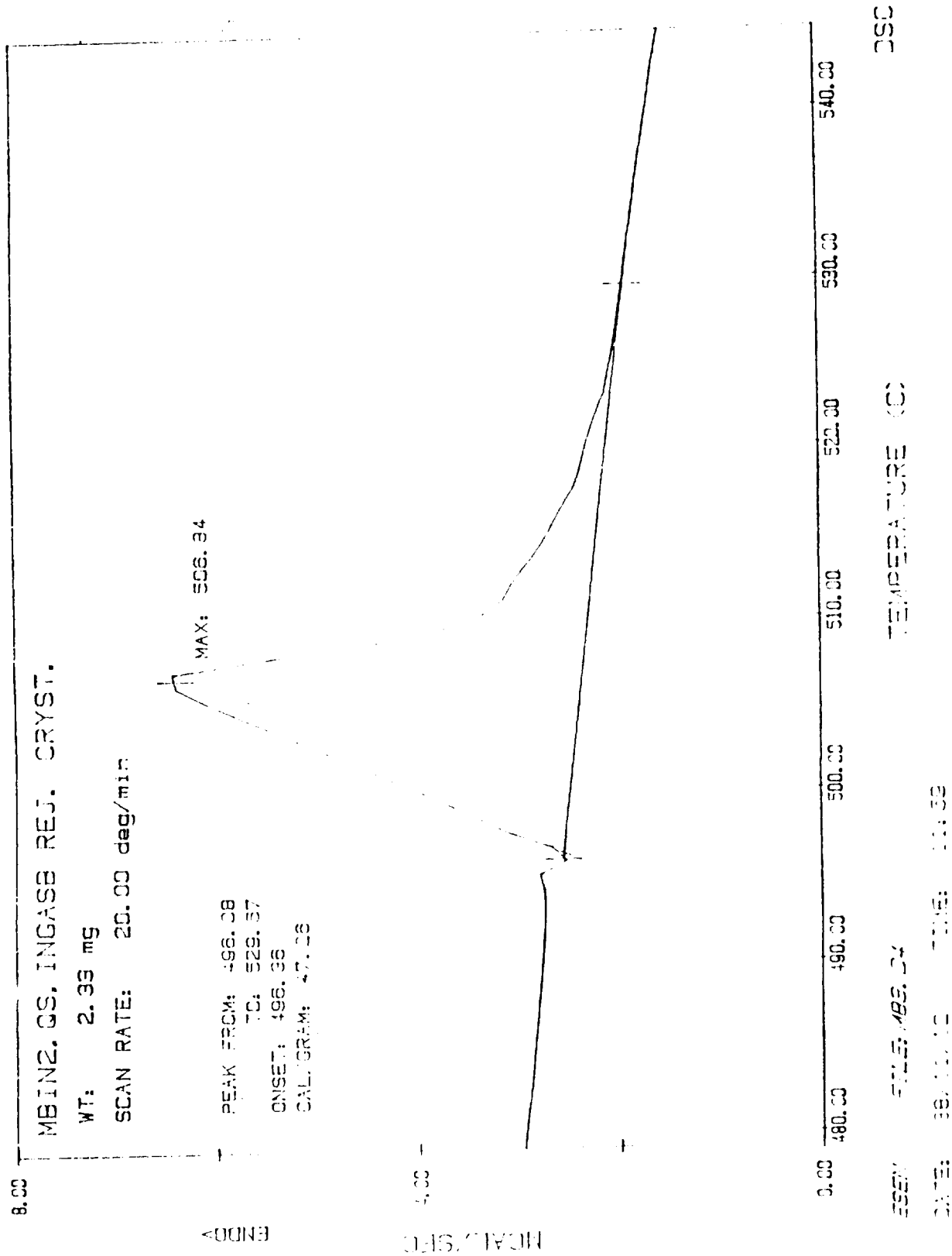

Figure 14. SEM micrograph of a cross section of DS12-1 showing dislocation pits. The long marking line is 100 microns.

Figure 15. Temperature profile in the VBS furnace measured in an empty ampoule using a K-type thermocouple at a heater setting of 800°C and cooler settings of 450 and 490°C. The height of the adiabatic zone was 2.5".

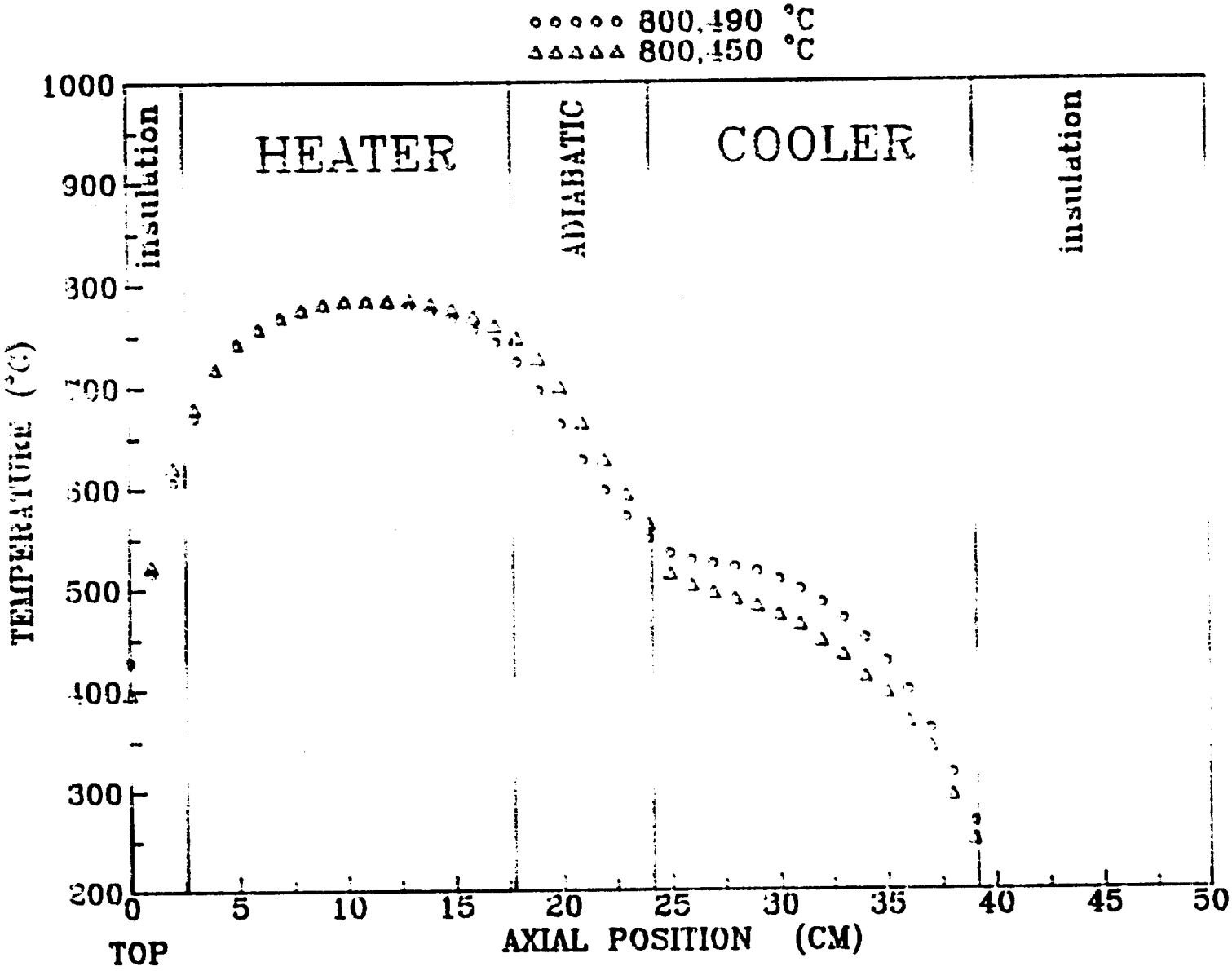

Figure 16. Temperature profile and temperature gradient in the VBS furnace measured using a K-type thermocouple in an ampoule without a charge for heater settings of 825 and 850°C and a cooler setting of 500°C, with a 6.35 cm (2.5") adiabatic zone.

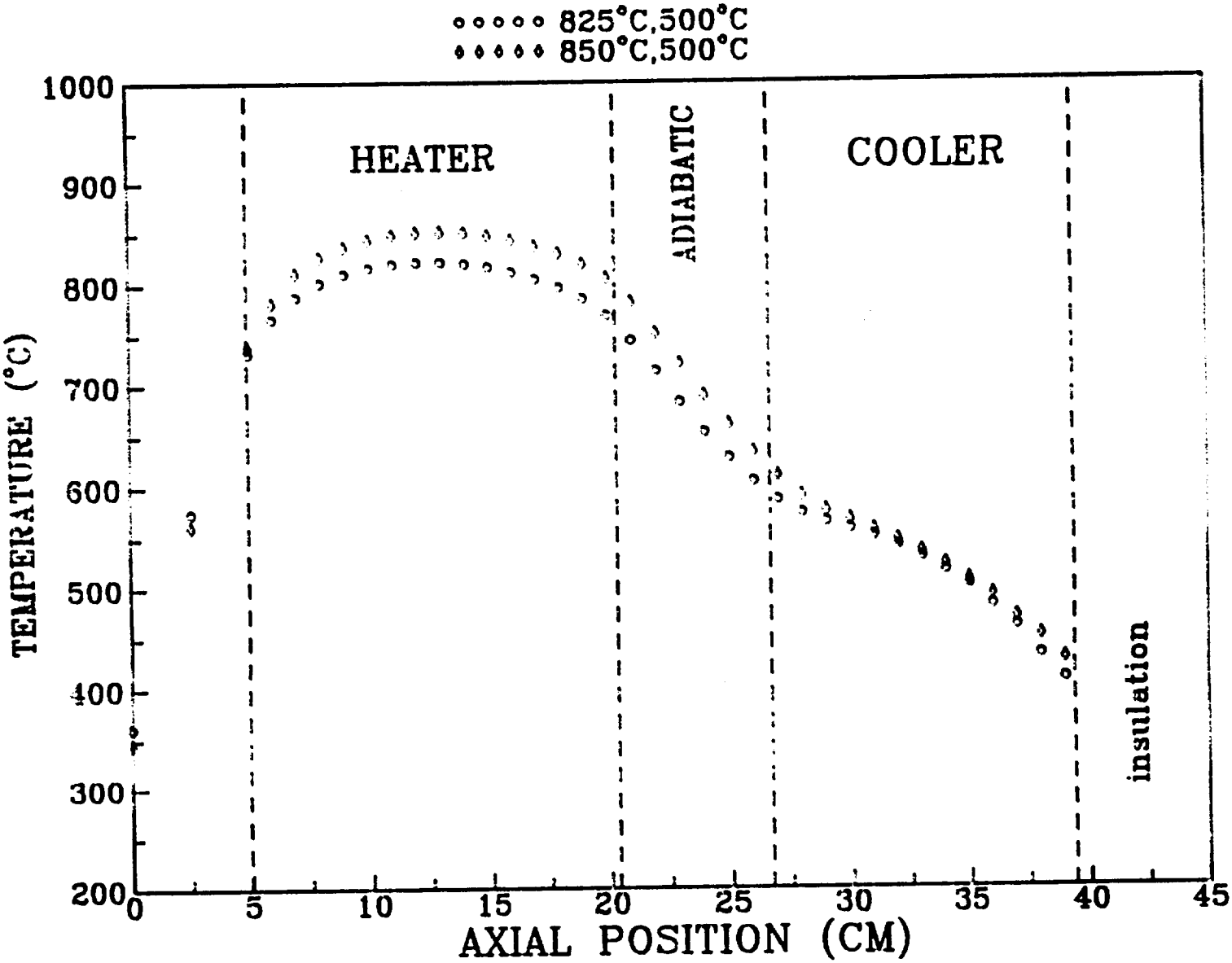

Figure 17a. Photograph of DS8-3, $In_{0.2}Ga_{0.2}Sb$ feed composition, grown at 7.9 mm/day ampoule lowering rate, and 25-30°C/cm temperature gradient. The growth direction is from left to right. The ingot was sandblasted to reveal the grains. Half of the melt was rapidly solidified to reveal the liquid-solid interface.

Figure 17b. Photograph of axially sectioned ingot of Figure 17a mounted in epoxy. The ingot was mechnically polished and chemically etched in 1HF:1HNO_3:1HAc for 20 to 25 s to reveal the microstructure. Arrows indicate the direction of growth.

Figure 18. Photograph of DS8-4; $In_{0.2}Ga_{0.8}Sb$ feed composition directionally solidified at 8 mm/day ampoule lowering rate and temperature gradient of 35°C/cm. The growth direction was from left to right.

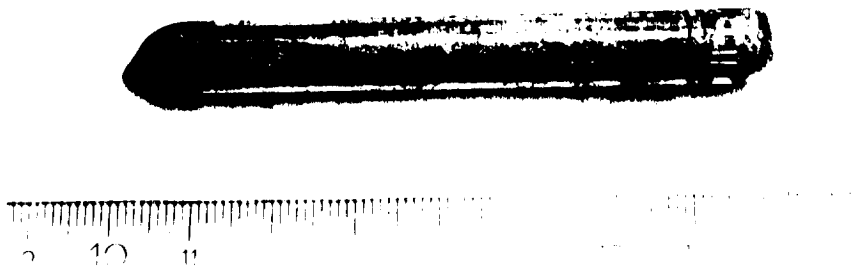

Figure 19a. Photograph of VDS8-5; $In_{0.2}Ga_{0.8}$ feed composition, directionally solidified at 7.9 mm/day and 35°C/cm temperature gradient under application of axial vibration to the ampoule at 2 Hz and 0.1 cm amplitude. Growth direction was from left to right.

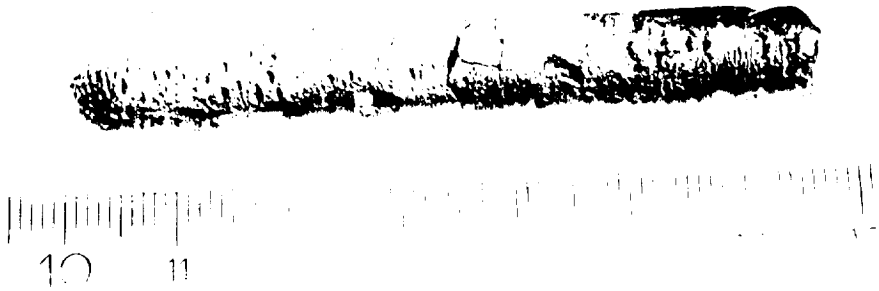

Figure 19b. Photograph of axially sectioned VDS8-5 after sandblasting. The markers indicate the liquid-solid interface.

Figure 20a. Photograph of CID8-6; $In_{0.2}Ga_{0.8}Sb$ feed composition, directionally solidified under application of 10 amp square-wave dc current (15.7 amp/cm^2 current density) for 26.5 s on and 26.5 s off. Current was passed from solid to melt (i.e. solid [+] pole and melt [-] pole).

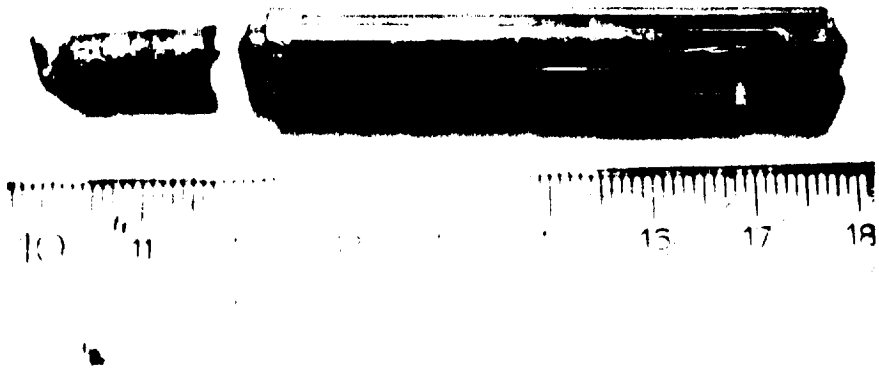

Figure 20b. Photograph of CID8-6 after sandblasting to reveal grains and twins. Growth direction was from right to left.

Figure 20c. Photograph of axially sectioned and sandblasted CID8-6. Growth direction was from left to right.

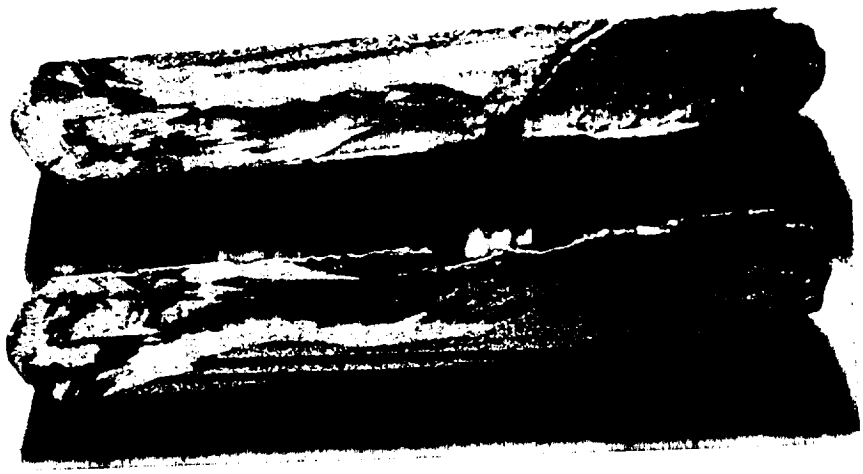

Figure 21. Ampoule resistance versus time. Pulsation was initiated after 40 hours of translation.

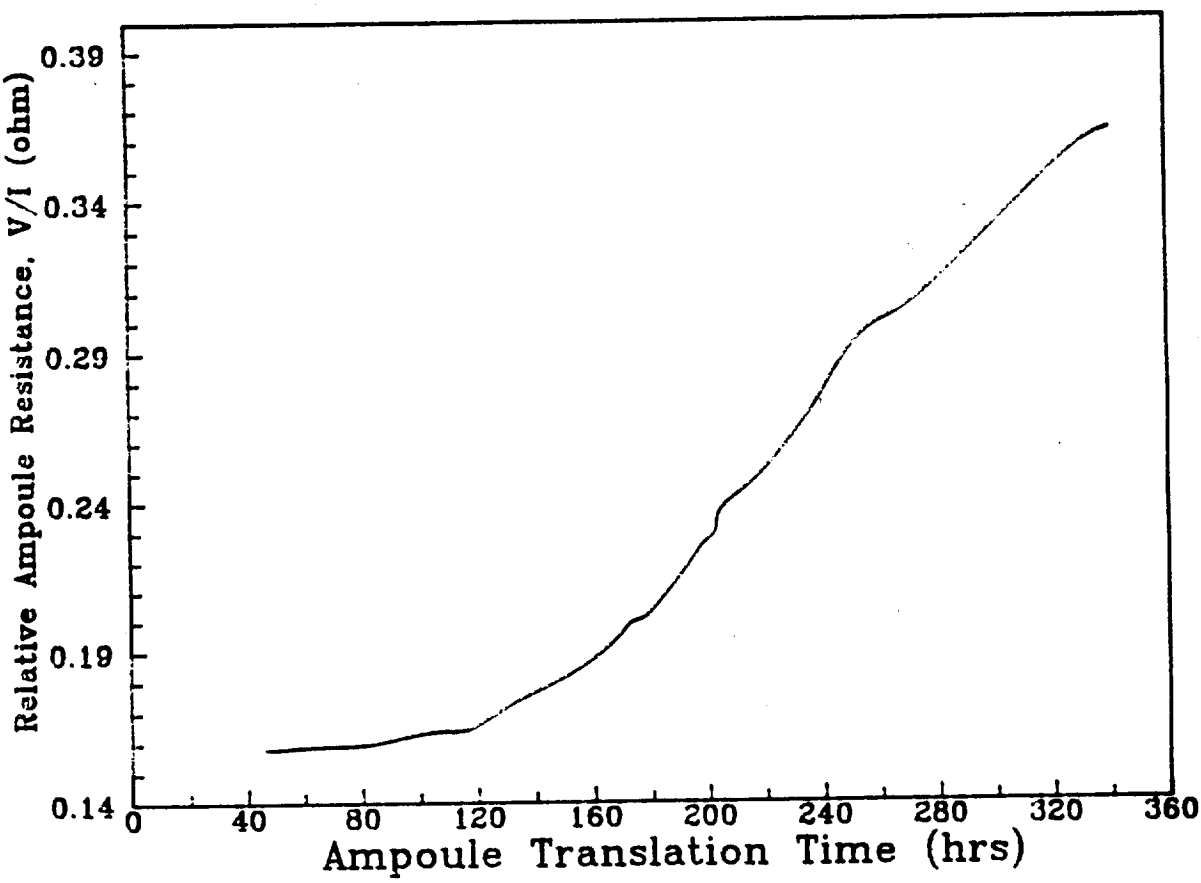

Figure 22. Thermocouple readings in a melt of $In_{0.2}Ga_{0.8}Sb$ during and after application of a 10 amp dc current pulse for 30 s.

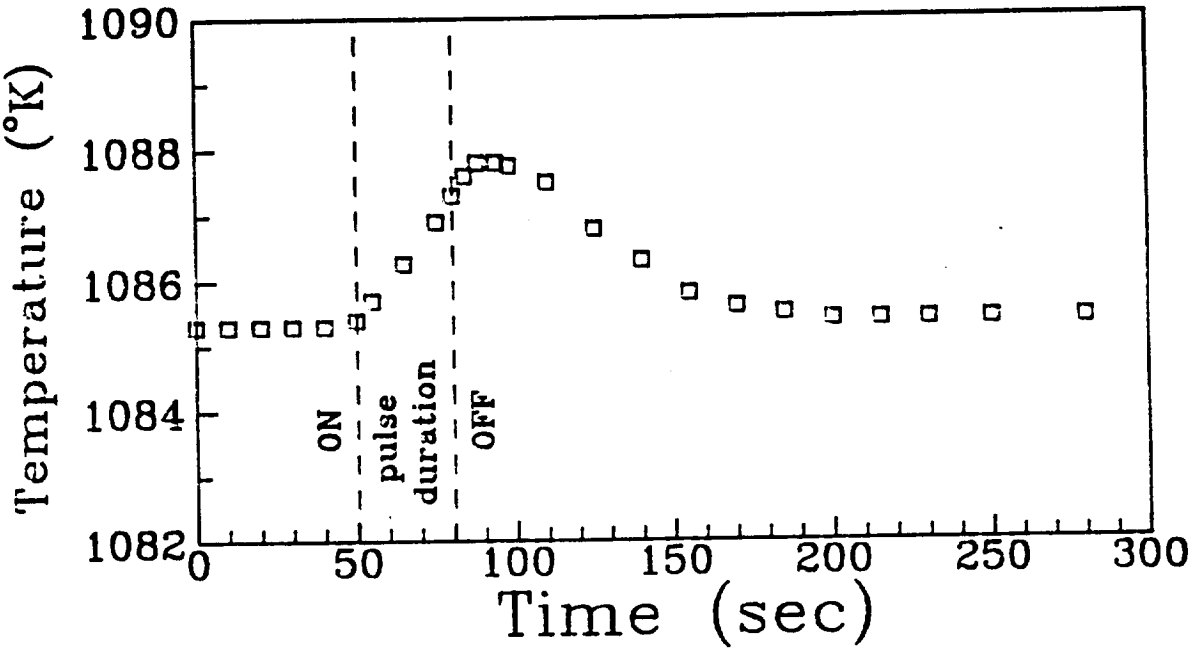

Figure 23. Thermocouple readings in a melt of $In_{0.2}Ga_{0.8}Sb$ during and after application of a 10 amp dc current pulse for 60 s.

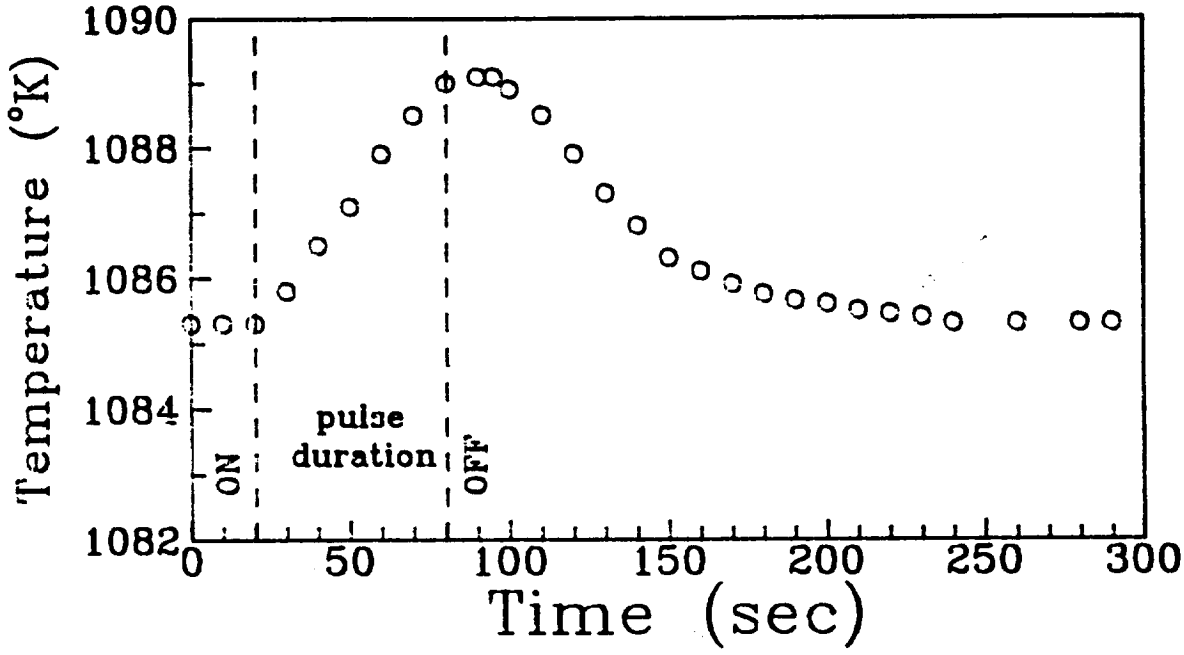

Figure 24. Thermocouple readings in a melt of $In_{0.2}Ga_{0.8}Sb$ during passage of square-wave 10 amp dc current (15.7 amp/cm^2 current density) through the melt.

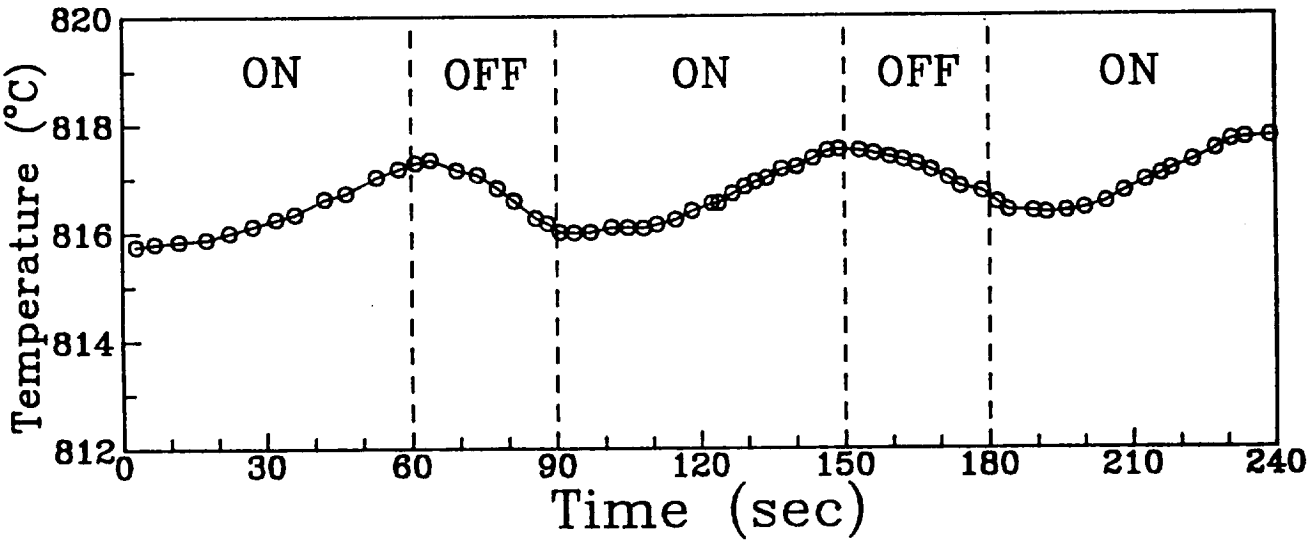

Figure 25. Thermocouple readings in a melt of $In_{0.2}Ga_{0.8}Sb$ during and after application of 10 amp alternating dc current pulses for a duration of 60 s, over 240 sec. pulsation range. (Steady state temperature in the melt before passage of the pulse = 808.9°C. Maximum temperature in the melt during pulsation = 811.5°C).

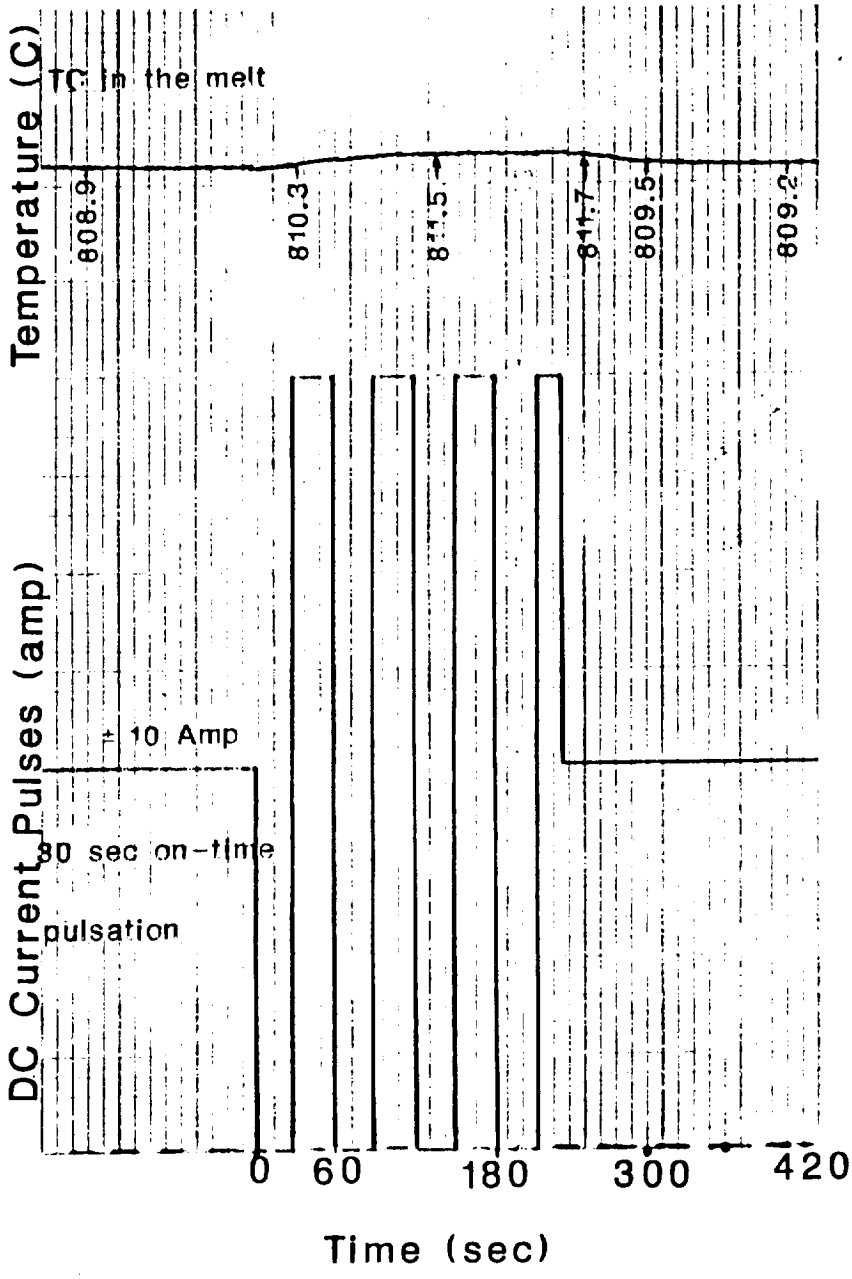

Figure 26. Jump in thermocouple reading (from 716.3 to 737.1°C) in a melt of InSb-GaSb during application of a 5 amp current pulse. This jump is attributed to exposure of the thermocouple junction to the melt at the time of current passage.

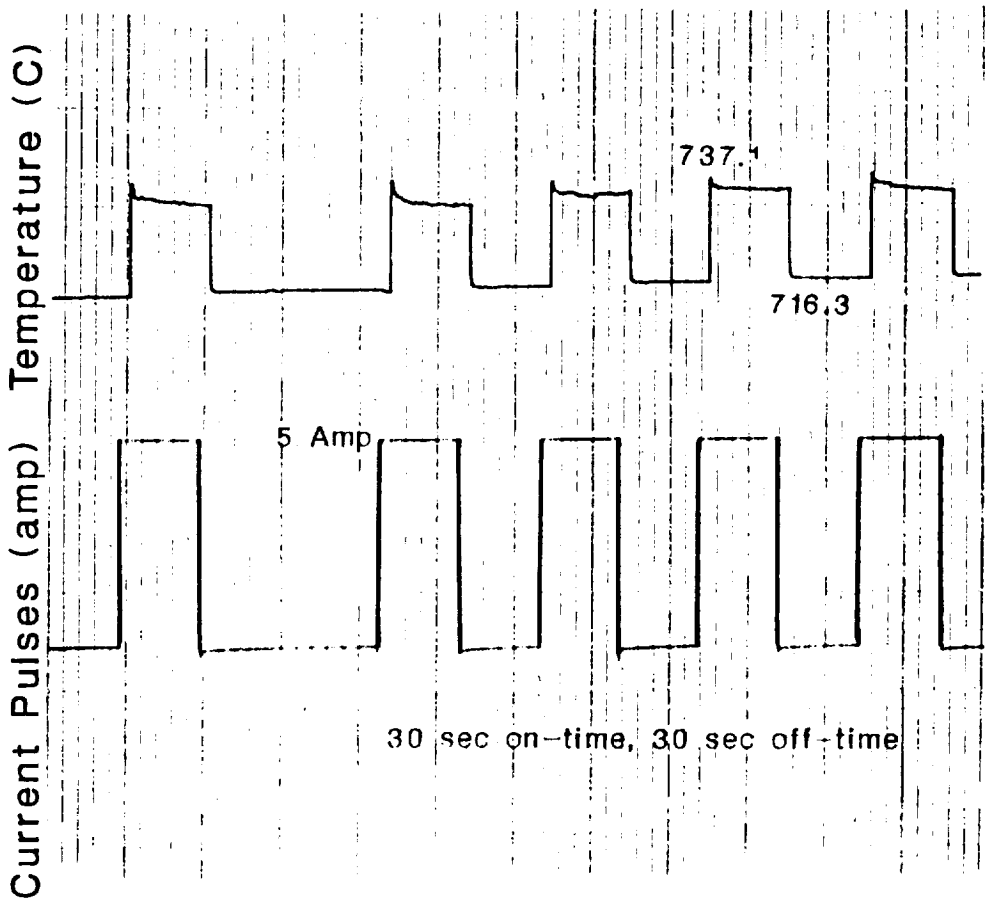

3 Diffusion Controlled Conditions – A Numerical Model

3.1 Background

The non-dimensional equation that describes the concentration distribution in the melt is:

$$\frac{\partial^2 C}{\partial R^2} + \frac{1}{R}\frac{\partial C}{\partial R} + \frac{\partial^2 C}{\partial Z^2} + Pe\frac{\partial C}{\partial Z} = 0, \tag{3.1}$$

where

$$Pe = \frac{RV}{D}. \tag{3.2}$$

Essentially two strategies have been used to solve this equation: finite element analysis and finite difference methods coupled with a coordinate transformation. Given the recent advances in memory, speed, and software for personal computers, the finite element method may become the dominant method to solve any problem for a non-rectangular domain, no matter how simple that domain may be.

The curved melt/solid interface poses a problem for finite-difference schemes. If a regularly spaced grid used, interpolation is required at the interface. This makes programming a nuisance. To avoid interpolation, a coordinate transformation is often used. The classical transformation for this problem was used by Landau (33) for the heat conduction equation and later for diffusion by Duda et al. (34). If the interface is described by $H(R)$ the following substitution is made into the diffusion equation:

$$\epsilon = Z/H(R) \tag{3.3}$$

$$\lambda = R \tag{3.4}$$

This transforms the domain into a unit square. Using these substitutions, it is easy, although tedious, to obtain new equations for the differentials:

$$\frac{\partial C}{\partial R} = \frac{\partial C}{\partial \epsilon}\frac{\partial \epsilon}{\partial R} + \frac{\partial C}{\partial \lambda} \tag{3.5}$$

$$\frac{\partial^2 C}{\partial R^2} = \frac{\partial C}{\partial \epsilon}\frac{\partial^2 \epsilon}{\partial R^2} + \left(\frac{\partial \epsilon}{\partial R}\right)^2 \frac{\partial C^2}{\partial \epsilon^2} + 2\frac{\partial \epsilon}{\partial R}\frac{\partial C^2}{\partial \epsilon \partial \lambda} + \frac{\partial C^2}{\partial \lambda^2} \tag{3.6}$$

$$\frac{\partial C}{\partial Z} = \frac{\partial C}{\partial \epsilon}\frac{\partial \epsilon}{\partial Z} \tag{3.7}$$

$$\frac{\partial C^2}{\partial Z^2} = \frac{\partial C^2}{\partial \epsilon^2}\left(\frac{\partial \epsilon}{\partial Z}\right)^2 \tag{3.8}$$

After making the appropriate substitutions into the original diffusion equation, a linear, homogeneous, partial differential equation with variable coefficients is produced. A banded coefficient matrix is produced in the discrete problem. In the previous discretization scheme a "five-point star" was used in the bulk melt, and a "seven-point star" was used near the interface. In this discretization, the mixed partial derivatives generate a "nine point star" that is used throughout the entire melt.

Other more sophisticated transformations stretch the solutal boundary layer in addition to transforming the domain into a square (35). Stretching transformations have the benefit of reducing the truncation error associated with the discretization in regions where the concentration in the melt changes rapidly with distance.

3.2 Discretization Used Here

The discretization in this work uses constant radial and axial step sizes in the bulk of the melt. Near the interface the radial step size is maintained, and the axial step size is adjusted so that all grid points are either on or within the domain. The discretization used near the interface is shown in Figure 3.1.

The non-dimensional equation that describes the concentration distribution in the melt is given by equation 3.1. The boundary conditions follow:

At the top of the ampoule, $Z \approx 2$, a fictitious inlet is used. This inlet is placed sufficiently far from the interface to satisfy $\frac{\partial C}{\partial R} = 0$ for all R. Conservation of mass at the inlet yields

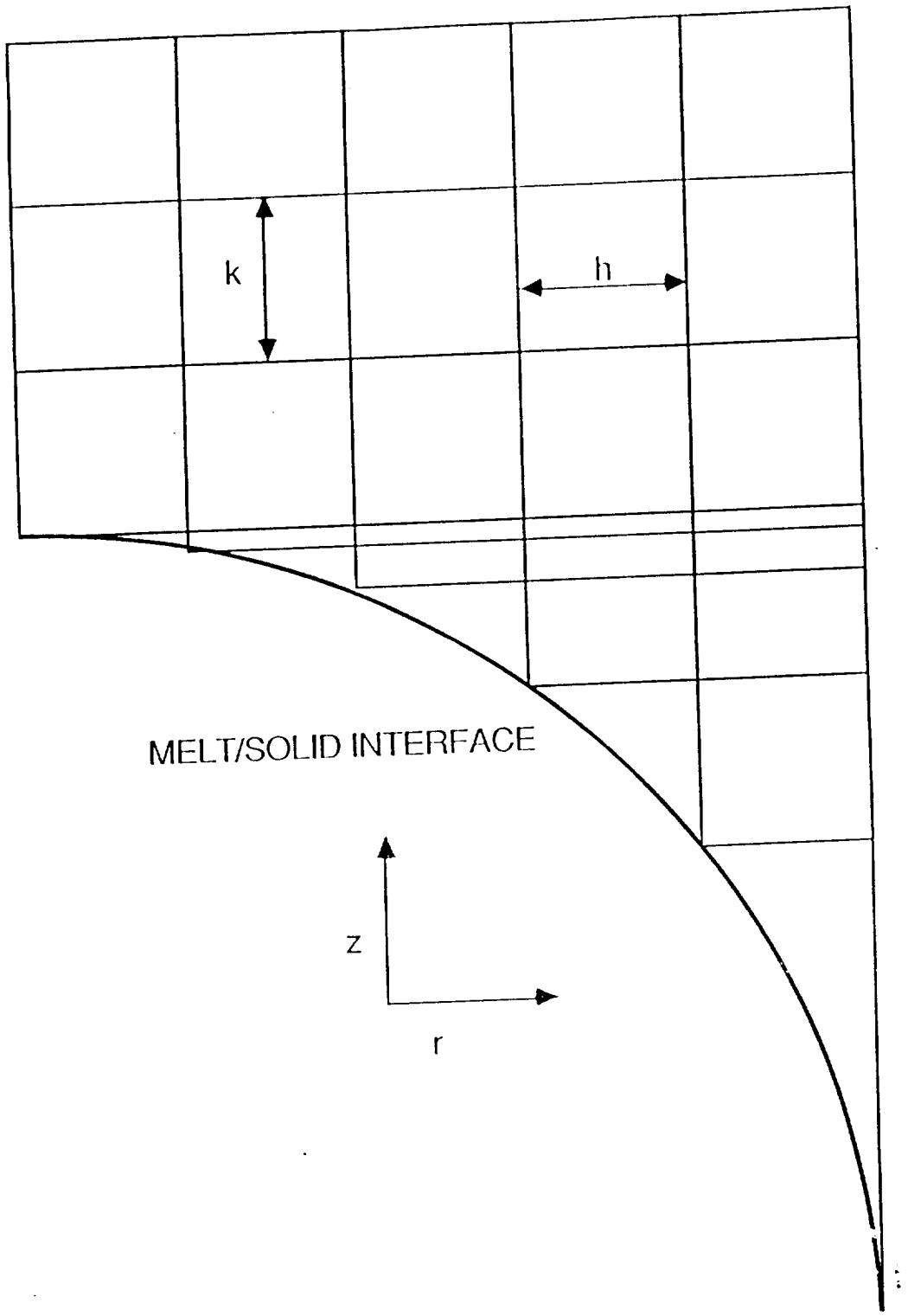

Figure 3.1: Discretization scheme for interfacial region.

the following equation:

$$\frac{\partial C}{\partial Z} = Pe(1 - C). \tag{3.9}$$

Radial symmetry is assumed, so that at the wall and at the center of the ampoule:

$$\frac{\partial C}{\partial R} = 0. \tag{3.10}$$

Assuming constant volumetric properties in the solid and the liquid, a mass balance at the melt/solid interface yields:

$$D\frac{\partial C}{\partial n} + V_n C = V_n k C, \tag{3.11}$$

where V_n is normal crystal growth rate. The normal derivative of concentration at the interface is:

$$\frac{\partial C}{\partial n} = \hat{N} \bullet \vec{\nabla} C \tag{3.12}$$

Where the unit normal vector $\hat{N}$ is:

$$\hat{N} = \frac{\hat{e}_Z - h_R \hat{e}_R}{(1 + h_R^2)^{1/2}}. \tag{3.13}$$

Here $\hat{e}_Z$ and $\hat{e}_R$ are the unit vectors in the axial and radial directions, and h_R is the slope of the interface.

From these equations, the boundary condition at the interface can be expressed as:

$$-\frac{\partial H}{\partial R}\frac{\partial C}{\partial R} + \frac{\partial C}{\partial Z} = Pe(k_{eq} - 1)C. \tag{3.14}$$

The finite difference approximations of the derivatives are found using Taylor series expansions about the i_{th} and j_{th} points. In the bulk melt the finite difference equations for the first and second derivatives and their corresponding truncation errors (TE) are:

$$\frac{\partial C_{i,j}}{\partial R} = \frac{C_{i+1,j} - C_{i-1,j}}{2h} + TE \tag{3.15}$$

$$TE \leq \frac{h^2}{3}\left\|\frac{\partial^3 C(\rho_1)}{\partial R^3}\right\|_\infty, \quad R_{i-1} \leq \rho_1 \leq R_{i+1} \tag{3.16}$$

$$\frac{\partial^2 C_{i,j}}{\partial R^2} = \frac{C_{i+1,j} - 2C_{i,j} + C_{i-1,j}}{h^2} + TE \tag{3.17}$$

$$TE \leq \frac{h^2}{12}\left\|\frac{\partial^4 C(\rho_2)}{\partial R^4}\right\|_\infty, \quad R_{i-1} \leq \rho_2 \leq R_{i+1}. \tag{3.18}$$

$$\frac{\partial C_{i,j}}{\partial Z} = \frac{C_{i,j+1} - C_{i,j-1}}{2k} + TE \tag{3.19}$$

$$TE \leq \frac{k^2}{3}\left\|\frac{\partial^3 C(\varrho_1)}{\partial Z^3}\right\|_\infty, \quad Z_{i-1} \leq \varrho_1 \leq Z_{i+1} \tag{3.20}$$

$$\frac{\partial^2 C_{i,j}}{\partial Z^2} = \frac{C_{i,j+1} - 2C_{i,j} + C_{i,j-1}}{k^2} + TE \tag{3.21}$$

$$TE \leq \frac{k^2}{12}\left\|\frac{\partial^4 C(\varrho_2)}{\partial Z^4}\right\|_\infty, \quad Z_{i-1} \leq \varrho_2 \leq Z_{i+1}. \tag{3.22}$$

The finite difference approximations are substituted into the continuous problem (Eq. 3.1). One then solves for $C_{i,j}$. The equation for $C_{i,j}$ in the bulk melt is:

$$\begin{aligned} C_{i,j} = \frac{1}{2}\left(\frac{1}{h^2} + \frac{1}{k^2}\right)^{-1} \Bigg\{ & \left(\frac{1}{h^2} + \frac{1}{2hR}\right) C_{i+1,j} + \left(\frac{1}{h^2} - \frac{1}{2hR}\right) C_{i-1,j} \\ & + \left(\frac{1}{k^2} + \frac{Pe}{2k}\right) C_{i,j+1} + \left(\frac{1}{k^2} - \frac{Pe}{2k}\right) C_{i,j-1}. \Bigg\} \end{aligned} \tag{3.23}$$

The boundary condition at the wall and the center of the ampoule, $\frac{\partial C}{\partial R} = 0$, yields $C_{i+1,j} = C_{i-1,j}$. The appropriate substitution is made in the equation for $C_{i,j}$ at the wall or the center.

At the top of the ampoule, a backward difference approximation is used for $\frac{\partial C}{\partial Z}$. This is done so that all the grid points in the discrete problem lie within the domain. Unlike at the interface, this is done merely for convenience. At the interface, as explained below, programming considerations require that all the grid points lie within the domain. The equation for $C_{i,j}$ at the fictitious inlet of the ampoule is:

$$C_{i,j} = \left(\frac{3}{2k} + Pe\right)^{-1}\left\{Pe + \frac{2}{k}C_{i,j-1} - \frac{1}{2k}C_{i,j-2}\right\}. \tag{3.24}$$

In the region near the melt/solid interface, the axial step size is varied to to avoid interpolation. Again, Taylor series expansions are used to determine the finite difference

approximations. Near the interface, the axial step size is some fraction α of the radial step size h.

The first and second derivatives in the axial direction are:

$$\begin{aligned}\frac{\partial C_{i,j}}{\partial Z} &= \frac{\alpha_2}{h\alpha_1(\alpha_1+\alpha_2)}C_{i,j+1} \\ &\quad - \frac{\alpha_1}{h\alpha_2(\alpha_1+\alpha_2)}C_{i,j-1} - \frac{\alpha_2-\alpha_1}{h\alpha_1\alpha_2}C_{i,j} + TE \end{aligned} \tag{3.25}$$

$$TE \le \frac{\alpha_2\alpha_1^2 - \alpha_1\alpha_2^2}{\alpha_1+\alpha_2}\,\frac{h^2}{6}\left\|\frac{\partial^3 C(\zeta_1)}{\partial Z^3}\right\|_\infty, \quad Z_{j-1} \le \zeta_1 \le Z_{j+1}. \tag{3.26}$$

Note that α_1 and α_2 are weakly dependent on both the curvature of the melt-solid interface and on the radial position.

For $H(R) = -R^2$,

$$TE \le \frac{h^2}{30}\left\|\frac{\partial^3 C(\zeta_1)}{\partial Z^3}\right\|_\infty. \tag{3.27}$$

$$\begin{aligned}\frac{\partial^2 C_{i,j}}{\partial Z^2} &= \frac{2}{h^2}\left\{\frac{\alpha_2\alpha_1(\alpha_1-\alpha_2)+\alpha_4\alpha_3(\alpha_3+\alpha_4)}{\alpha_1\alpha_2\alpha_3\alpha_4[(\alpha_1-\alpha_2)-(\alpha_3+\alpha_4)]}C_{i,j}\right. \\ &+ \frac{\alpha_1-\alpha_2}{\alpha_4(\alpha_4-\alpha_3)[(\alpha_1-\alpha_2)-(\alpha_3+\alpha_4)]}C_{i,j+3} \\ &- \frac{\alpha_1-\alpha_2}{\alpha_3(\alpha_4-\alpha_3)[(\alpha_1-\alpha_2)-(\alpha_3+\alpha_4)]}C_{i,j+2} \\ &- \frac{\alpha_3+\alpha_4}{\alpha_1(\alpha_1+\alpha_2)[(\alpha_1-\alpha_2)-(\alpha_3+\alpha_4)]}C_{i,j+1} \\ &- \left.\frac{\alpha_3+\alpha_4}{\alpha_2(\alpha_1+\alpha_2)[(\alpha_1-\alpha_2)-(\alpha_3+\alpha_4)]}C_{i,j-1}\right\} + TE, \end{aligned} \tag{3.28}$$

$$TE \le \frac{(\alpha_1^2-\alpha_2^2)(\alpha_3^3+\alpha_4^3)+(\alpha_3^2-\alpha_4^2)(\alpha_1^3+\alpha_3^3)}{(\alpha_1^2-\alpha_2^2)(\alpha_3+\alpha_4)+(\alpha_3^2-\alpha_4^2)(\alpha_1+\alpha_2)}\,\frac{h^2}{12}\left\|\frac{\partial^4 C(\zeta_2)}{\partial Z^4}\right\|_\infty, \tag{3.29}$$

where

$$Z_{j-1} \le \zeta_2 \le Z_{j+3}. \tag{3.30}$$

Again, α_1 to α_4 are weakly dependent on interfacial curvature and radial position.

For $H(R) = -R^2$,

$$TE \leq \frac{5h^2}{12} \left\| \frac{\partial^4 C(\zeta_2)}{\partial Z^4} \right\|_\infty . \tag{3.31}$$

The important thing to recognize is that the truncation error is not only bounded, but is also second order for all interfacial curvatures. For the case of the planar interface, $\alpha_1 = \alpha_2$ and the finite difference equations reduce to those used in the bulk melt.

In the melt in the interfacial region the expression for $C_{i,j}$ is:

$$\begin{aligned} C_{i,j} \;=\; & \left\{ \frac{2}{h^2} + Pe\frac{\alpha_2 - \alpha_1}{h\alpha_2\alpha_1} - \frac{2}{h^2}\left(\frac{\alpha_2\alpha_1(\alpha_1 - \alpha_2) + \alpha_4\alpha_3(\alpha_3 + \alpha_4)}{\alpha_1\alpha_2\alpha_3\alpha_4[(\alpha_1 - \alpha_2) - (\alpha_3 + \alpha_4)]} \right) \right\}^{-1} \times \\ & \left\{ \frac{C_{i+1,j} + C_{i-1,j}}{h^2} + \frac{1}{R}\frac{C_{i+1,j} + C_{i-1,j}}{2h} \right. \\ & + \frac{2}{h^2}\frac{\alpha_1 - \alpha_2}{\alpha_4(\alpha_4 - \alpha_3)[(\alpha_1 - \alpha_2) - (\alpha_3 + \alpha_4)]} C_{i,j+3} \\ & - \frac{2}{h^2}\frac{\alpha_1 - \alpha_2}{\alpha_3(\alpha_4 - \alpha_3)[(\alpha_1 - \alpha_2) - (\alpha_3 + \alpha_4)]} C_{i,j+2} \\ & - \left(\frac{2}{h^2}\frac{\alpha_3 + \alpha_4}{\alpha_1(\alpha_1 + \alpha_2)[(\alpha_1 - \alpha_2) - (\alpha_3 + \alpha_4)]} - Pe\frac{\alpha_2}{h\alpha_1(\alpha_1 + \alpha_2)} \right) C_{i,j+1} \\ & \left. - \left(\frac{2}{h^2}\frac{\alpha_3 + \alpha_4}{\alpha_2(\alpha_1 + \alpha_2)[(\alpha_1 - \alpha_2) - (\alpha_3 + \alpha_4)]} + Pe\frac{\alpha_1}{h\alpha_2(\alpha_1 + \alpha_2)} \right) C_{i,j-1} \right\} \end{aligned} \tag{3.32}$$

Figure 3.2 shows the values of C used at each grid point near the interface.

It is important to recognize that the coefficients in the above equation are a function of h and axial position only. In other words, for a given Z the values of the coefficients are constant for all r. This feature can be taken advantage of in the algorithm used to solve the problem. When an iterative procedure is used, such as Jacobi or Gauss-Seidel, the coefficients need only be calculated on the first iteration. Once their values are known, they are stored as a one dimensional array. This property of the discretization significantly decreases the time needed to solve the problem. The total number of grid points is given by:

$$M(N+1) + \sum_{i=1}^{N+1} i. \tag{3.33}$$

Here M is the number of axial steps and N is the number of radial steps.

If central difference approximations are used at the interface, some mesh points will be outside of the domain. Points that lie outside of the domain are often referred to as

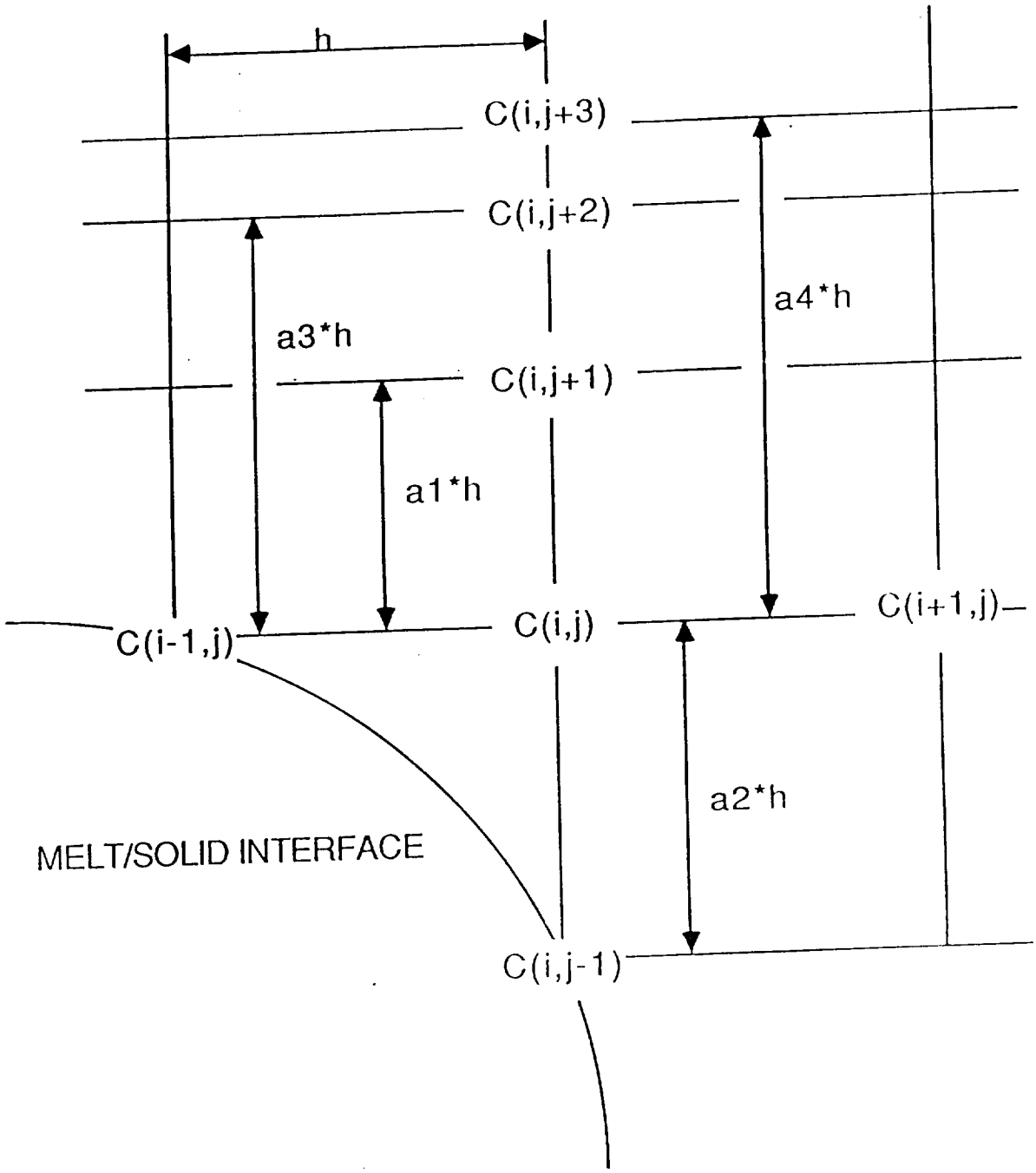

Figure 3.2: Values of C used at each grid point in discretization near the interface.

"fictitious points." Normally this isn't a problem, as expressions for these points are derived from the boundary conditions. However, because of the unique discretization scheme used here the fictitious points pose a problem.

Figure 3.1 shows that in the interfacial region the number of mesh points in a row is one fewer than the row above it. This seemingly innocuous feature causes each fictitious point to be a function of all fictitious points above it. This destroys the banded structure of the coefficient matrix, and makes it extremely difficult to solve the discretized equations directly. This problem is shown through the following example.

Consider any point which is on the interface but not at the wall or center. This point is shown schematically Figure 3.3. Two fictitious points are directly associated with this point. C_D is the external point created by the central difference approximation for $\frac{\partial C}{\partial R}$. C_E is the external point created by the central difference approximation for $\frac{\partial C}{\partial Z}$. An expression for C_E is found using the interfacial boundary equation (3.14):

$$\begin{aligned} C_E = & \frac{-h\alpha_2(\alpha_1+\alpha_2)}{\alpha_1}\left(\frac{\alpha_2-\alpha_1}{h\alpha_2\alpha_1}+Pe(k_{eq}-1)\right)C_{i,j}+\left(\frac{\alpha_2}{\alpha_1}\right)^2 C_{i,j+1} \\ & -\frac{h_r\alpha_2(\alpha_1+\alpha_2)}{2\alpha_1}C_{i+1,j}+\frac{h_r\alpha_2(\alpha_1+\alpha_2)}{2\alpha_1}C_D \end{aligned} \tag{3.34}$$

The problem with this discretization can now be seen. Just as C_E is a function of C_D, C_D is a function of C_C, C_C a function of C_B, and finally C_B is a function of the very first fictitious point C_A. The latter point is found using the boundary equation at the interface coupled with the boundary condition at the center at the ampoule:

$$\frac{\partial C}{\partial Z} = Pe(k_{eq}-1)C \tag{3.35}$$

From whence,

$$C_A = \frac{-h\alpha_2(\alpha_1+\alpha_2)}{\alpha_1}\left(\frac{\alpha_2-\alpha_1}{h\alpha_2\alpha_1}+Pe(k_{eq}-1)\right)C_{i,j}+\left(\frac{\alpha_2}{\alpha_1}\right)^2 C_{i,j+1} \tag{3.36}$$

For completeness the final fictitious point, C_Z, which is associated with the interface at the ampoule wall, is specified by:

$$\frac{C_{i,j+1}-C_Z}{2h\alpha_1} = Pe(k_{eq}-1)C \tag{3.37}$$

$$C_Z = -2h\alpha_1 Pe(k_{eq}-1)C_{i,j}+C_{i,j+1} \tag{3.38}$$

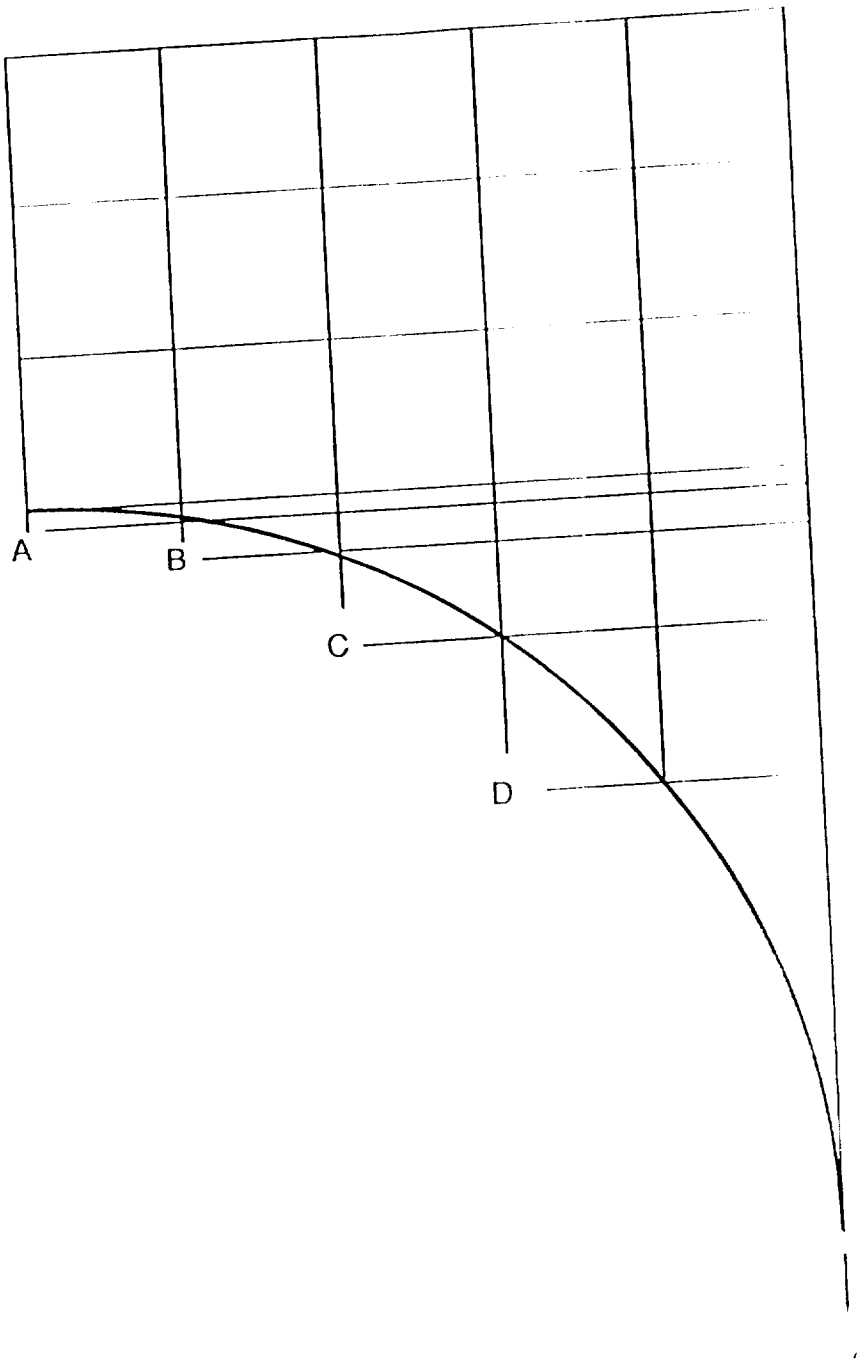

Figure 3.3: Fictitious points that are generated when central difference approximations are used at the interface. The fictitious points lie outside of the domain

The above problems are avoided by using forward finite difference approximations to the interfacial boundary equation:

$$\frac{\partial C}{\partial R} \cong -3C_{i,j} + 4C_{i+1,j} - C_{i+2,j} \tag{3.39}$$

$$\begin{aligned}\frac{\partial C}{\partial Z} &= \frac{1}{h}\left\{\frac{\alpha_1}{\alpha_3(\alpha_1-\alpha_3)}C_{i,j+2} - \frac{\alpha_3}{\alpha_1(\alpha_1-\alpha_3)}C_{i,j+1}\right. \\ &\left. - \frac{\alpha_1+\alpha_3}{\alpha_1\alpha_3}C_{i,j}\right\} + TE \end{aligned} \tag{3.40}$$

$$T.E \leq \alpha_1\alpha_3\frac{h^2}{6}\left\|\frac{\partial^3 C(\varrho_3)}{\partial Z^3}\right\|_\infty \tag{3.41}$$

$$Z_j \leq \varrho_3 \leq Z_{j+2} \tag{3.42}$$

Using the above difference equations and the boundary condition at the interface (3.14) an expression for $C_{i,j}$ is found:*

$$\begin{aligned}C_{i,j} &= \frac{1}{h}\left\{\frac{-3h_r}{2h} + \frac{\alpha_1+\alpha_3}{h\alpha_1\alpha_3} + Pe(k_{eq}-1)\right\}^{-1}\left\{-\frac{\alpha_1}{\alpha_3(\alpha_1-\alpha_3)}C_{i,j+2}\right. \\ &\left. - \frac{\alpha_3}{\alpha_1(\alpha_1-\alpha_3)}C_{i,j+1} - \frac{h_r}{2}(4C_{i+1,j} - C_{i+2,j})\right\}\end{aligned} \tag{3.43}$$

In this project, three methods were used to solve the system of discrete equations: two were direct methods, and one was iterative. In one method finite difference equations are written so that all points are within the domain. This generates a banded coefficient matrix. The matrix is inverted using Gaussian elimination. Although the matrix isn't diagonally dominant, pivoting was not necessary.

In the second case, central finite difference equations were used on the boundaries. This process, as explained above, generates fictitious points which change the banded coefficient matrix into a sparse square matrix. This increases the computer time needed to solve the problem greatly since the time needed to invert a square matrix is proportional to its order cubed. (For a banded matrix the time to invert it is proportional to its order squared.)

*This equation needs to adjusted when the point $r = 1 - h$ is reached. At that point $C_{i+2,j}$ is outside of the domain. This is accomplished by noting that:

$$\left.\frac{\partial C}{\partial R}\right|_{r=1} = 0.$$

From this relation one obtains $C_{i+2,j} = C_{i,j}$. The appropriate substitution is made in the equation at the interface.

A highly efficient Successive Over Relaxation SOR method is the third technique used to solve the discrete problem. In this method, the discrete equations are rearranged to the form $C_{i,j} = \ldots$. The equation for $C_{i,j}$ is solved at each mesh point in the domain and its value is "corrected" using the following procedure:

$$C_{i,j}^{k} = (1-\omega)C_{i,j}^{k-1} + \omega C_{i,j}^{k} \tag{3.44}$$

Where k is the iteration number.

The speed with which any iterative method converges is directly related to how well the initial guess approximates the actual solution. In the SOR method used, the concentration field is initialized using the one-dimensional diffusion equation. Then several thousand iterations are performed using a coarse axial and radial step size of 0.1. When 5000 iterations are performed or when the maximum residual falls below 10^{-6}, the procedure is stopped. The axial and radial step sizes are quartered. The values of concentration at the new grid points are estimated with linear interpolation, and the SOR is continued until the previous stopping requirements are met. Three to six hours on a Zenith Z-248 computer (with an 80287 math co-processor) is usually enough time to obtain a solution.

The accuracy of the results can be checked by comparing the mass flux at $Z = \infty$ to the flux through the interface (defined by $Z = H(R)$). For steady-state conditions the two fluxes must be equal since mass is conserved at the interface. At $Z = \infty$, the axial mass flux is given by:

$$\bar{C}VA \tag{3.45}$$

where A is the cross-sectional area of the ampoule. At the melt/solid interface, the axial mass flux is given by:

$$Vk_{eq}\int_0^1 C(R)dA \tag{3.46}$$

For steady-state condtions the two fluxes are equal and the expression for $\bar{C}$ is given by:

$$\begin{aligned} \bar{C} &= k_{eq}\int_0^1 C(R)RdR\Big|_{Z=H(R)} \\ &= 1 \end{aligned} \tag{3.47}$$

The error in the mass balance is always below 5%, and usually below 1%.

The speed of convergence was found to be extremely sensitive to small changes in ω; $\omega = 1.7$ was usually used. Any factor which increases radial segregation (interfacial curvature, higher Peclet number, k_{eq} different from 1) necessitates the use of a slightly smaller value of ω. However, in all cases $1.65 \leq \omega \leq 1.75$.

4 Experimental Procedure

In this project naphthalene crystals that were doped with approximately 0.3% azulene were grown using the vertical Bridgman-Stockbarger technique. After the solidification process was completed, the axial and radial distribution of azulene in the naphthalene matrix was measured using gas chromatography. Convection in the melt was observed through a transparent furnace under the same thermal conditions used to grow the crystals. (For details of the visualization procedure refer to references 25,26.) In Chapter 5 the nature of the convection is correlated with the segregation in the crystal.

Scintillation grade naphthalene and sublimated azulene were obtained from Aldrich Chemical Co. The physical properties of naphthalene are summarized in Table 4.1. The phase diagram for this system is given in Figure 4.1 (36).

Physical Property	Value	Reference
Thermal Expansion, β	$7.758*10^{-4}$ K^{-1}	(15)
Dynamic Viscosity, μ	$8.25*10^{-3}$ g/cm.s	(15)
Melt Density, ρ_l	0.977 g/cm^3	(15)
Solid Density, ρ_s	1.15 g/cm^3	(15)
Diffusion Coef., D	$2.0*10^{-5}$ cm^2/s	(37)
Segregation Coef., k_{eq}	0.3	(36)
Schmidt Number, Sc	422	
Grashof Number, Gr	$5012\Delta T$ K^{-1}	

Table 4.1: Physical properties of the azulene/naphthalene system

The diffusion coefficient of azulene in molten naphthalene was calculated using a correlation that is based on the Stokes-Einstein equation. For small concentrations of A in B the diffusion coefficient D_{AB} in cm^2/s is given by (37):

$$D_{AB} = 7.4 * 10^{-8} \frac{(\psi_B M_B)^{1/2} T}{\mu V_A^{0.6}}. \qquad (4.1)$$

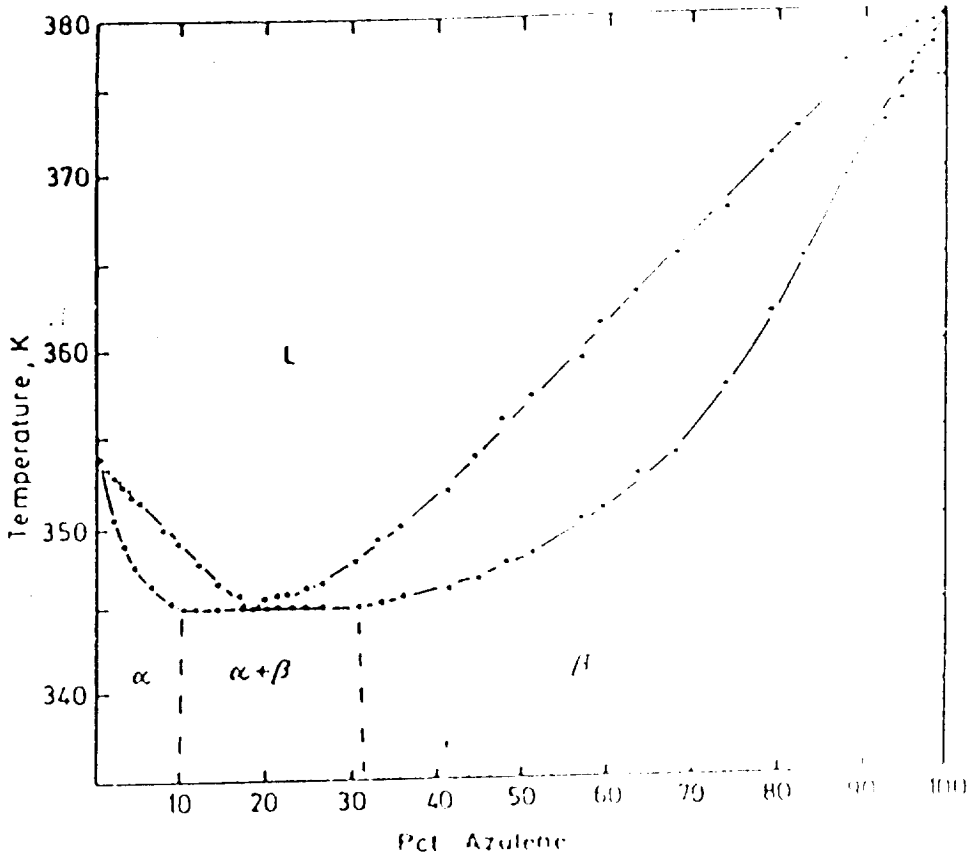

Figure 4.1: Phase diagram for the azulene/naphthalene system (36). The azulene concentration is given in weight percent.

Here $\tilde{V}_A$ is the molar volume of the solute in cm^3 g $mole^{-1}$ as a liquid at its normal boiling point (the molar volume of naphthalene was used as an approximation for the molar volume of azulene), μ is the viscosity of the solution in centipoise, ψ_B is an "association parameter" (for this system it is 1), and T is the absolute temperature. For dilute solutions of nondissociating solutes this correlation is usually good to within 10%.

A photo of the experimental set-up is shown in Figure 4.2. The heating section was made using large diameter Pyrex tubing and Nichrome wire. The main portion of the heater consisted of a tube 23 cm long. nichrome wire was wound on the outside of this tube at a pitch of 3.4 turns/cm. Inside this tube was placed another which fit snugly in place. This was done to distribute the helical heat source. This entire construction was slid inside a third tube. The latter tube served to reduce the hazards of electrical shock and to decrease radial thermal asymmetries at the ampoule.

A short booster heater 6 cm long was constructed by winding nichrome wire on the outside of the third tube at its base. A Pyrex tube 6 cm long was placed over the booster section. In all, the main section of the heater was constructed from three concentric Pyrex tubes and the booster section from four. By changing the power to the booster heater the axial temperature profile in the heater could be changed along with the convection in the melt.

Anti-freeze was circulated through the cold zone with a heater/pump. When temperatures below room temperature were desired, the anti-freeze was cooled with a flow-through refrigerator that was connected in series with the pump. With this system a range of cooler temperatures of $-40°C \leq T_c \leq 50°C$ could be achieved. A temperature range of $20°C \leq T_c \leq 40°C$ was commonly used. This proved to be cold enough to maintain a steep temperature gradient and prevent constitutional supercooling in the melt. When temperatures below 20 °C were desired, thermal stress caused cracking of the crystal.

The ampoules used to grow the crystals were Pyrex with an inner diameter of 1.56 cm and an outer diameter of approximately 18 mm. In order to favor selection of a single grain during crystal growth, the ampoule had a narrow constriction at one end. The constriction was typically 6 cm long with a uniform outer diameter of 0.5 cm over approximately 3 cm

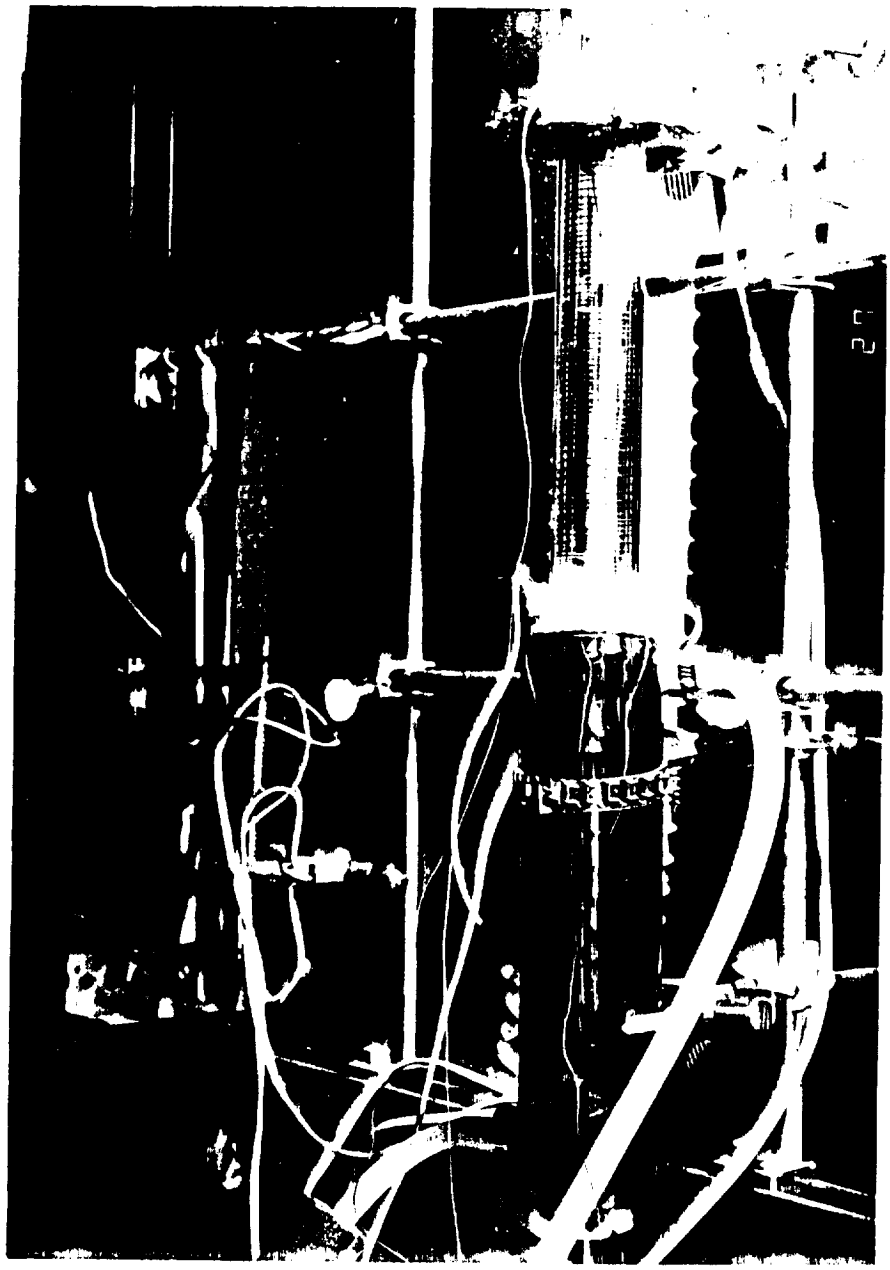

Figure 4.2: Photo of set-up used to grow crystals. It was taken prior to the addition of the booster heater.

of its length. The constriction began approximately 3 cm from the bottom of the ampoule. The ampoules were typically about 60 cm long. A schematic of the ampoule is shown in Figure 4.3. During crystal growth, the ampoules were sealed at the top with a size "0" rubber stopper.

The degree of crystallinity of a material is often hard to judge by visual inspection alone. However, N. Karl reported that a tapered ampoule, such as the one that was used here, caused a single grain to be selected in the great majority of organic crystals that he grew (36). He also reported that low angle grain boundaries appeared as striations in the crystal. Most of the crystals that were grown here were free from striations. They were transparent through-out except for the final few millimeters at the end. At the end, the boule was opaque, and very small grains characteristic of supercooling were observed. When grain boundaries were observed, they ran parallel (or nearly parallel) to the growth direction. In such occasions, the crystal would break apart at the grain boundary if handled to any degree. A discontinuity in azulene concentration was observed in only one crystal, but a grain boundary could not be seen.

The ampoules were rinsed several times with deionized water to clean them. They were then soaked overnight in a solution containing equal parts by volume of deionized water, concentrated HCl , and concentrated HNO_3. After this they were again rinsed several times with deionized water followed by several rinses with spectrophotometric grade acetone. The ampoules where then stoppered until used.

Prior to growth, 20 g of naphthalene and approximately 0.05 grams of azulene were added to the ampoule. The material was melted with a heat gun and shaken in order to homogenize the melt. The ampoule was placed in a preheated furnace, and was allowed to equilibrate for approximately 6 hr before growth began. After the growth process was completed the ampoule was cut a few centimeters above the top of the crystal. The crystal was removed from the ampoule by carefully heating the ampoule with a heat gun, causing the outside surface of the crystal to melt, thereby allowing it to slide out of the ampoule.

The crystals were sliced with a small fine-toothed saw. If necessary, the crystal was gently sanded with fine-grit emory paper to make the surface of the crystal smooth. Sam

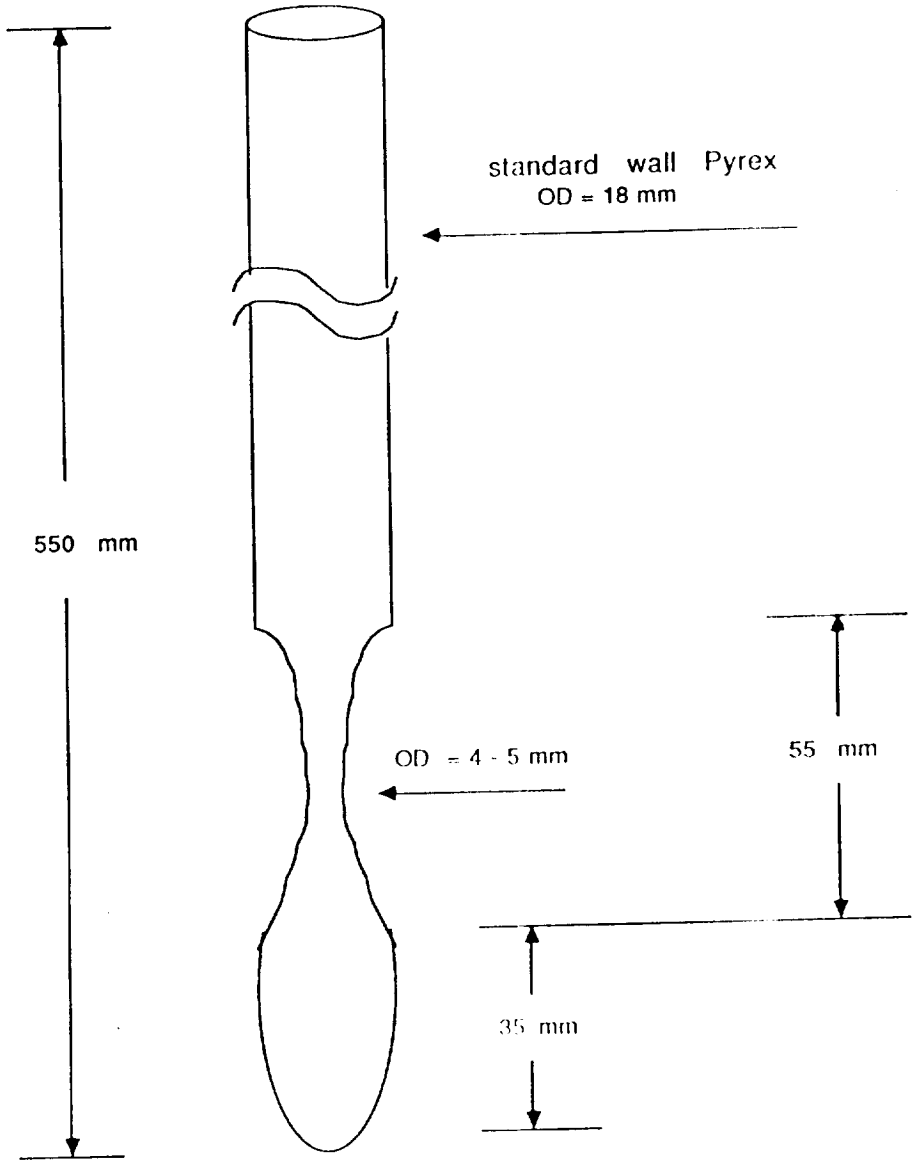

Figure 4.3: Schematic of the ampoule used to grow crystals. The constriction near the bottom favored selection of a single grain.

ples were prepared by scratching the crystal with a melting point capillary tube in order to gather approximately 0.1mg of material. The tip of the tube was then dipped into spectrophotometric grade acetone. Capillary action drew approximately 10 to 20 microliters of acetone into the tube. After the sample dissolved completely, 0.8 microliter was withdrawn from the capillary and injected into the gas chromatograph (GC). Samples were gathered along a diameter of the crystal at five nearly equally spaced positions. In several crystals, two additional samples were taken near the edge of the crystal perpendicular to the line formed by the five samples.

The GC used was a Perkin-Elmer Sigma 2000 gas chromatograph equipped with a flame ionization detector. The column used was 6 ft (1.8 m) by 1/8 in (3.25 mm) ID stainless steel . It was packed with 10% Carbowax 20M on Chromosorb W-HP 80/100. Eleven minutes was required to completely elute the sample using a column temperature of 190 ^oC. Nitrogen was the carrier gas.

A chromatogram of a typical sample is shown in Figure 4.4. It is a plot of the response of the detector, measured in voltage, versus elution time in minutes. The elution times for the components were approximately: 1 minute for acetone, 4 minutes for naphthalene, and 9 minutes for azulene. In Figure 4.4, only the naphthalene and acetone peaks can be seen. In Figure 4.5 the full-scale height has been reduced approximately 500 times. In this figure, the azulene peak is visible. Note the excellent separation of the naphthalene and azulene peaks. The peak areas were calculated automatically by the instrument.

The GC results were converted to mass fraction using:

$$x_1 = f(m)\frac{A_1}{A_1 + \frac{\mu_2}{\mu_1}A_2}, \tag{4.2}$$

where A is area in the chromatogram (determined numerically by the instrument) and μ_i is the detector's flame ionization yield for component i. Detector nonlinearities caused by interactions between components are contained in the term $f(m)$. Provided the variation in the total mass injected is small, and x_1 is less than 1%, $f(m)$ can be set equal to 1 (38). The ionization yield factors were found by calibrating the instrument using standard solutions of azulene and naphthalene in acetone. (The ratio of the ionization yield factors and the data from the GC for each run are given in Appendix A.)

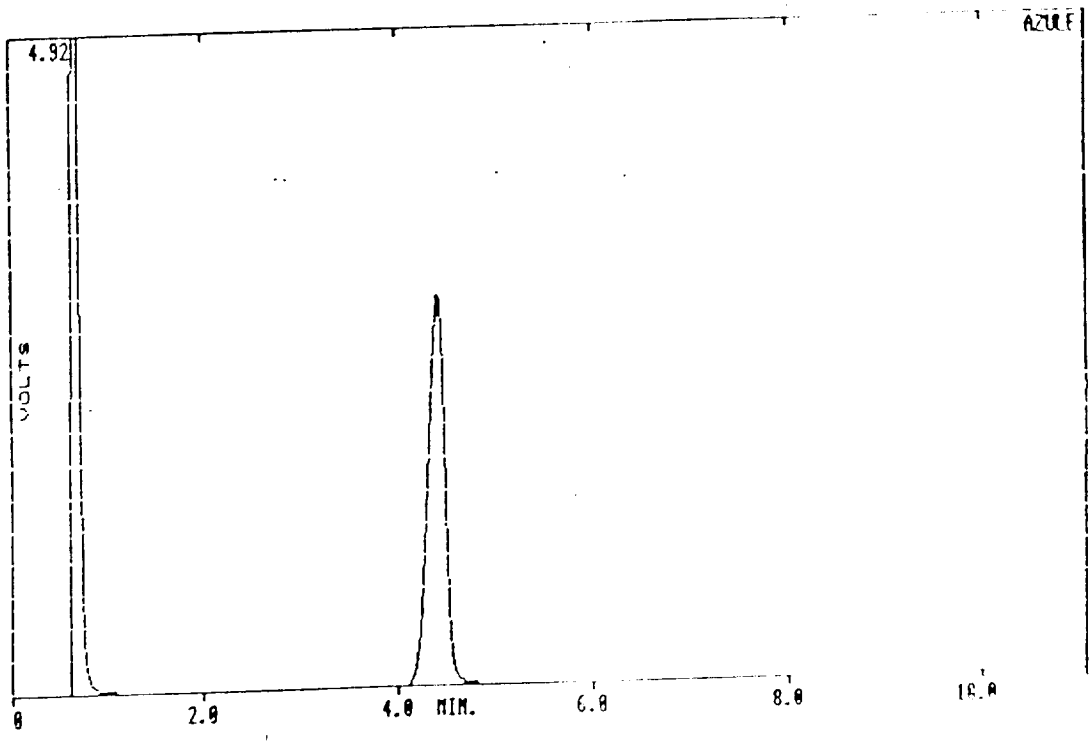

Figure 4.4: Chromatogram of a typical naphthalene-azulene sample. The acetone peak is at 1 min and the naphthalene is at 4 min. The azulene peak, which can't be seen at this scale, is at 9 minutes.

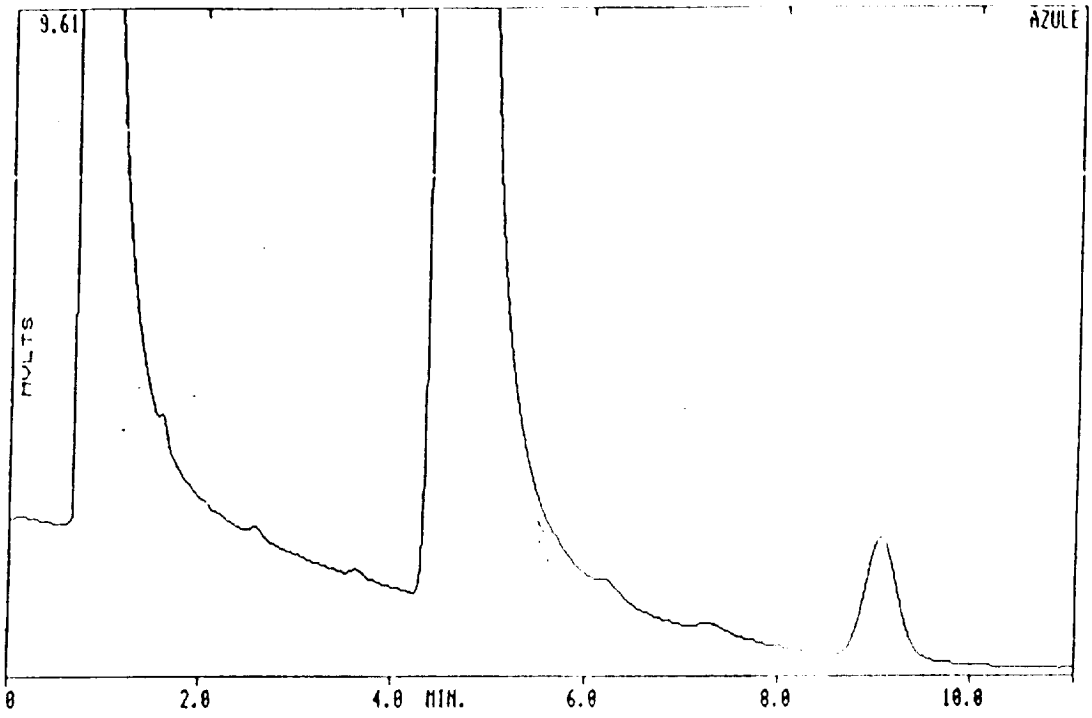

Figure 4.5: Chromatogram of a typical naphthalene-azulene sample with a full-height scale of 10mV. Note the good separation between azulene and naphthalene.

Run	Naphthalene Area	Azulene Area	Azulene Mass Frac.
1	197000	1070	$6.74*10^{-3}$
2	171000	951	$6.92*10^{-3}$
3	199000	1090	$6.82*10^{-3}$
4	191000	1070	$7.02*10^{-3}$
5	197000	1100	$6.96*10^{-3}$
6	195000	1110	$7.09*10^{-3}$

Table 4.2: Determination of the relative error in procedure by repeatedly analyzing the same solution.

An estimate was obtained of the relative error of the chromatographic procedure, i.e. the variation in the results when the same sample is analyzed repeatedly. To approximately 20 ml of acetone was added enough naphthalene and azulene to produce a solution similar in total mass dissolved and in relative concentrations to that obtained from a typical experimental run. 0.8 micro-liters of this solution were repeatedly injected and the chromatograms obtained. The results are noted in Table 4.2. The total naphthalene area, $A_{Naph.}$, was 1150000, and the total azulene area, $A_{Az.}$, was 6390. From these results the mean azulene mass fraction was given by:

$$\begin{aligned} \bar{x}_{Az.} &= \frac{A_{Az.}}{A_{Az.} + 0.796 * A_{Naph.}} \\ &= 6.93 * 10^{-3} \end{aligned}$$

Twice the maximum deviation from the mean in these runs was 5% of the mean. This is taken as a conservative estimate of the relative error in this procedure. In other words, the mass fraction and its error were calculated using:

$$x_1 = \frac{A_1}{A_1 + \frac{\mu_2}{\mu_1} A_2} \pm 0.05 * \left(\frac{A_1}{A_1 + \frac{\mu_2}{\mu_1} A_2} \right) \tag{4.3}$$

The absolute error, the error in the calculated mass fraction versus the actual mass fraction (also called systematic error), depends on the calibration procedures used. When

using quantitative GC analysis, internal standards should be used. Two solutes of known concentration should be added to the acetone. Their properties with respect to gas chromatography, e.g. flame ionization yield, mobility on the column and chemical stability at high temperatures, must be the same as naphthalene and azulene. However their retention times must be sufficiently different so that no two peaks overlap in the chromatogram. Using this method, a negligible experimental error is obtainable. Unfortunately, the enormous mass of naphthalene in the samples precluded this method.

Assuming the flame ionization yields in equation 4.1 could be precisely determined by calibration of the instrument, the GC analysis used here would be the same as the internal standard method. The reason one calibration wasn't enough is because the column ages with use, and the mobility of materials on the column changes. Therefore, it should be recalibrated before every analysis. This proved to be impossible since the GC had an intermittant electrical problem that worsened as the instrument warmed up. Precious runs couldn't be spared for recalibration.

For this reason all radial composition profiles were scaled by the measured mean concentration of each crystal. In this way, moderate systematic errors were eliminated and the actual error in the results, when scaled, was a conservative 5% of the calculated value. If no calibration procedure was used, the azulene concentration would be calculated by,

$$x_1 = \frac{A_1}{A_1 + A_2} \tag{4.1}$$

The difference between equations 4.4 and 4.3 represents an upper bound on the absolute error of the determination of the azulene concentration in the crystal.

5 Results

5.1 Diffusion Controlled Conditions – Numerical Results

The calculation of the amount of radial variation in composition in a crystal (also called radial segregation) during solidification under diffusion controlled conditions is straightforward. The diffusion coefficient and k_{eq} are the only physical properties that influence segregation. As shown in Section 4, these values are accurately known for the naphthalene/azulene system. When the shape of the melt/solid interface and the growth rate are known, the shape of the radial concentration profile in the crystal can be calculated. However, the effects of these parameters may be difficult to separate using composition data, especially since segregation is also influenced by convection in the melt.

Without a strong magnetic field or low gravity, diffusion controlled conditions are difficult to produce in the vertical Bridgman-Stockbarger crystal growth technique. The geometry of the Bridgman setup insures that radial temperature gradients, and therefore convection, are nearly always present in the melt. Because of this, the distribution of dopants in the crystal is usually influenced by convection in the melt. However, the degree to which convection in the melt played a role in concentration variations in a grown crystal can, to some extent, be estimated by calculating the radial segregation that would have occurred had convection in the melt not been present.

Figure 5.1 shows the influence of Peclet number on the radial concentration profile for a convex interface having a dimensionless amplitude of 0.25 with $k_{eq} < 1$ and no convection. The dimensionless amplitude of the interface is defined:

$$|H(R = 1) - H(R = 0)| \tag{5.1}$$

where R is the radial position nondimensionalized by the ampoule's radius. In all results presented, the mass balance at the melt/solid interface is satisfied to within 1%. As shown in Figure 5.1, the radial variation in composition increases with Peclet number. As the Peclet number becomes large, the change in composition at the interface, near the center, is reduced, and most of the change in the radial composition profile is at the ampoule wall. The is because the axial concentration profile in the melt is steepest at the wall when the

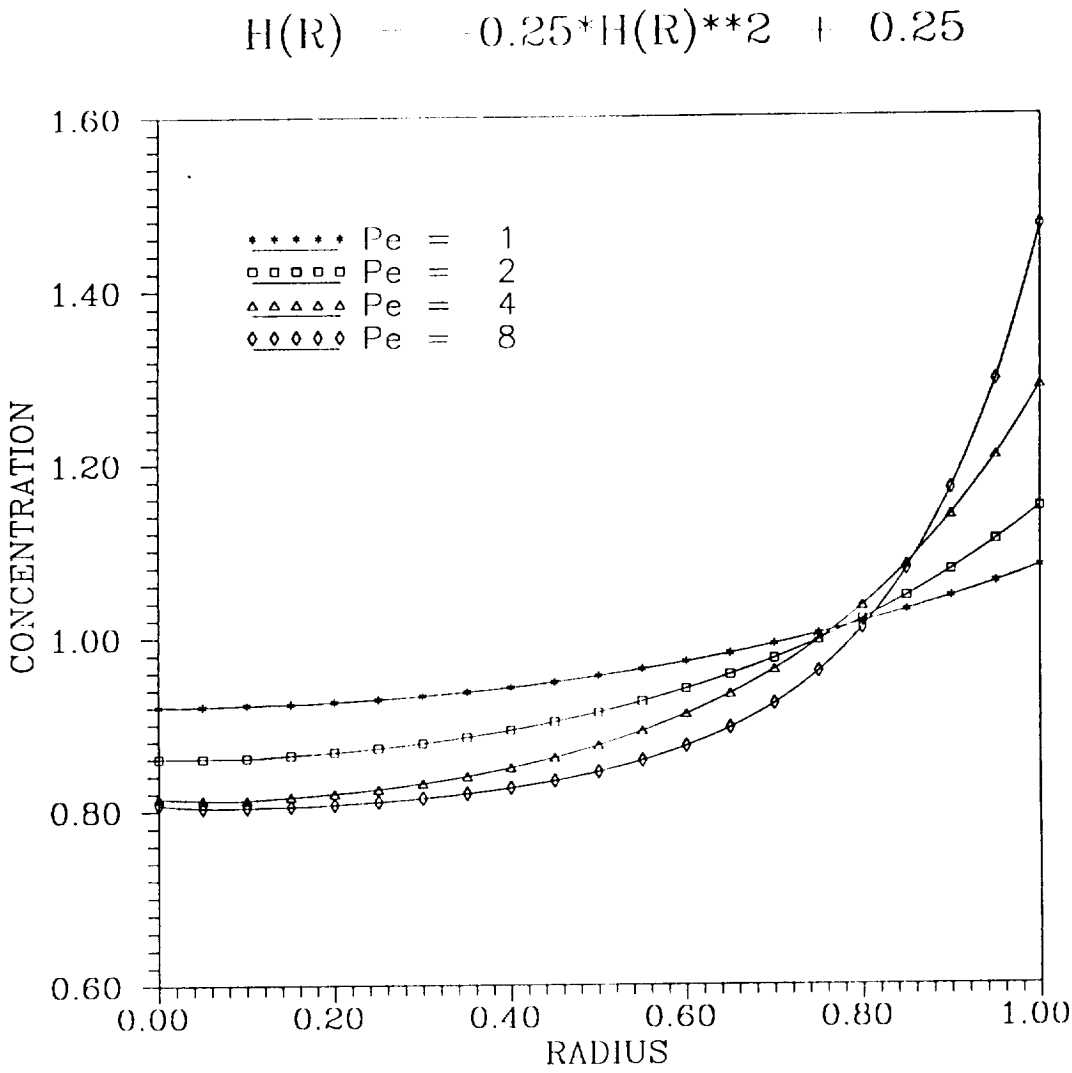

Figure 5.1: The influence of Peclet number on the radial composition at the melt/solid interface. $k_{eq} = 0.3$. The interface is convex with an amplitude of 0.25.

interface is convex.

For sufficiently low Peclet number, there is no radial segregation, regardless of interfacial curvature. Under these conditions the results of this model have little to do with an actual crystal growth situation. When the growth rate is very small, an extremely long ampoule is needed to achieve steady-state conditions in the melt. For very slow growth rates in a real growth system, e.g. as with HgCdTe or InGaSb, the transport phenomena are always transient and the axial concentration profile is identical to that obtained under well mixed conditions. For well-mixed conditions, or diffusion controlled conditions when the growth rate is small, there is no radial segregation for any interfacial curvature.

Figure 5.2 shows the influence of Peclet number on the radial variation in composition for a concave interface with $k_{eq} < 1$. The results for the concave interface are essentially identical to those in the previous case, except the shape of the concentration profile is inverted.

A useful feature of the discretization used here is that it can be easily adapted to any interfacial curvature. Figures 5.3 to 5.5 show the radial concentration variation for a cosine shaped interface. This interface shape is somewhat unusual in that it changes concavity in the domain. Also, its first derivative with radial position is zero at both the center and the ampoule wall. This type of interfacial curvature could occur if the melt/solid interface intersects the ampoule in the insulation zone.

Figure 5.6 shows the radial concentration profile for an interface described by $H(R) = -0.5 * R^N + 0.5$ for different values of N. As the order of the polynomial that describes the shape of the interface increases, the interface becomes flatter in the center and changes more steeply near the edges. This effect is seen in the radial concentration profiles of Figure 5.6. The same thing is observed in Figure 5.7, which shows the radial concentration profile for an interface described by $H(R) = 0.5 * R^N$.

Figure 5.8 shows the effect of the equilibrium segregation coefficient on radial segregation. The further k_{eq} changes from 1, the larger the segregation. Because of the behavior of the truncation error in the finite difference scheme, the smallest value of k_{eq} that could be studied was 0.1. There was no limitation on the value of k_{eq} when $k_{eq} > 1$.

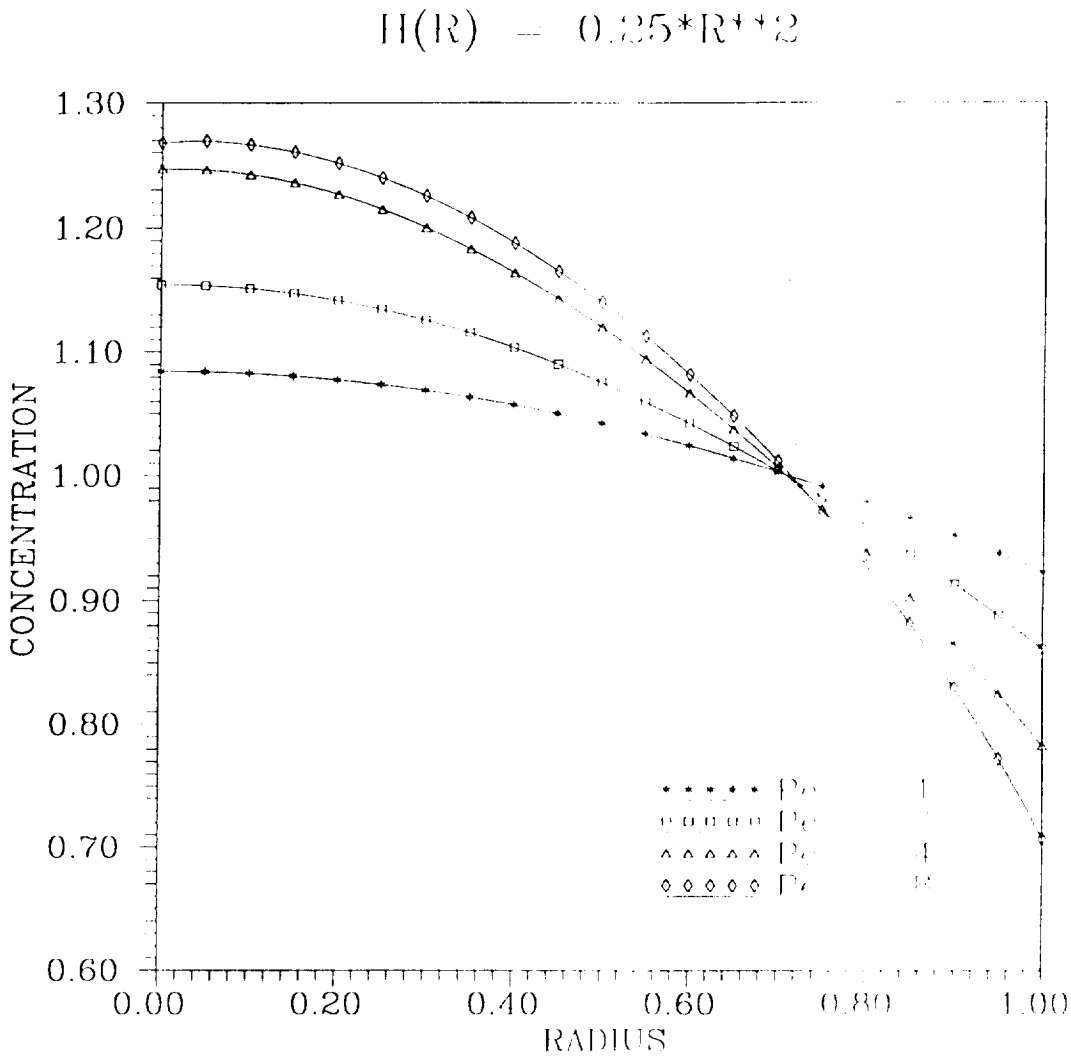

Figure 5.2: The influence of Peclet number on the radial concentration profile. $k_{rq} = 0.3$.

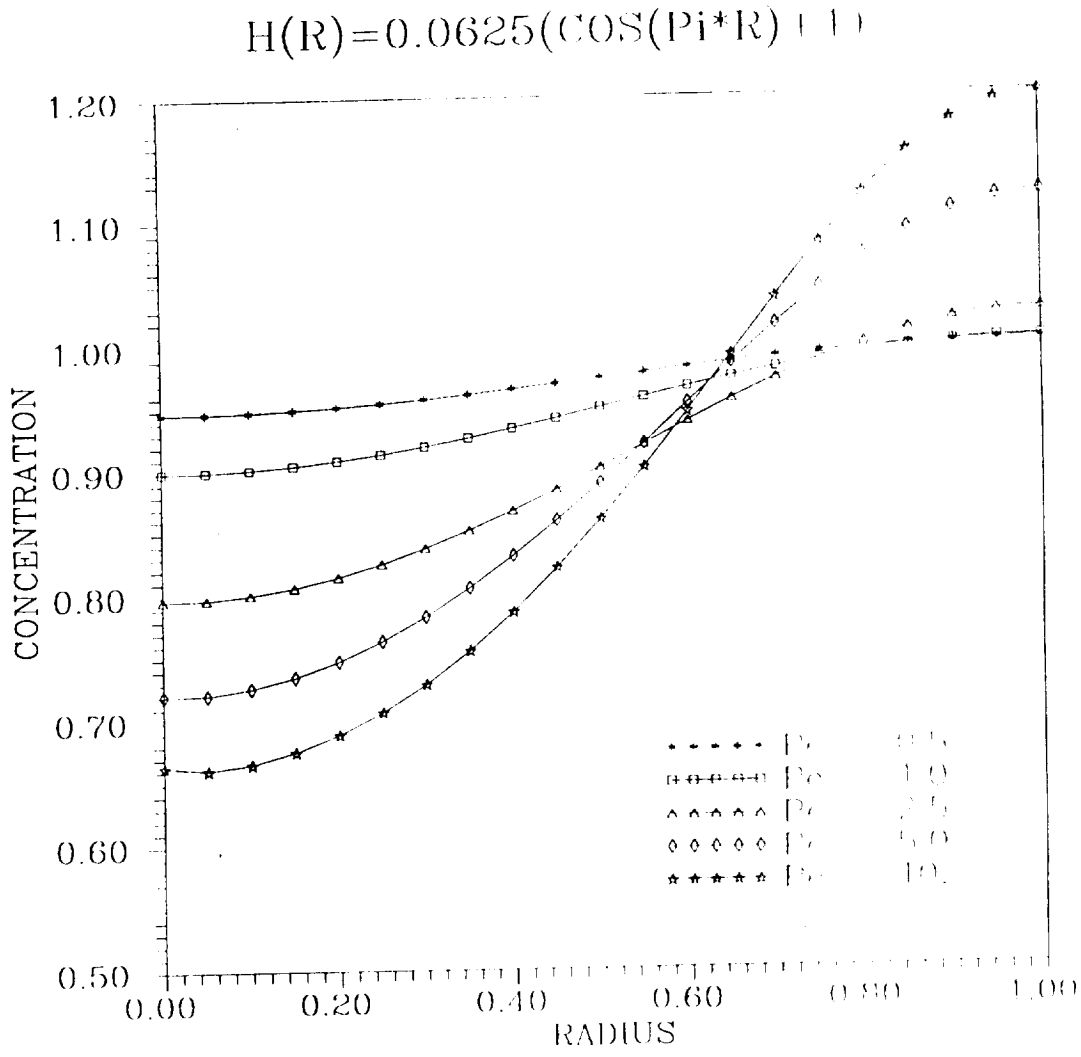

Figure 5.3: The effect of Peclet number on the radial concentration profile for a cosine shaped interface. The interface's dimensionless amplitude is 0.125.

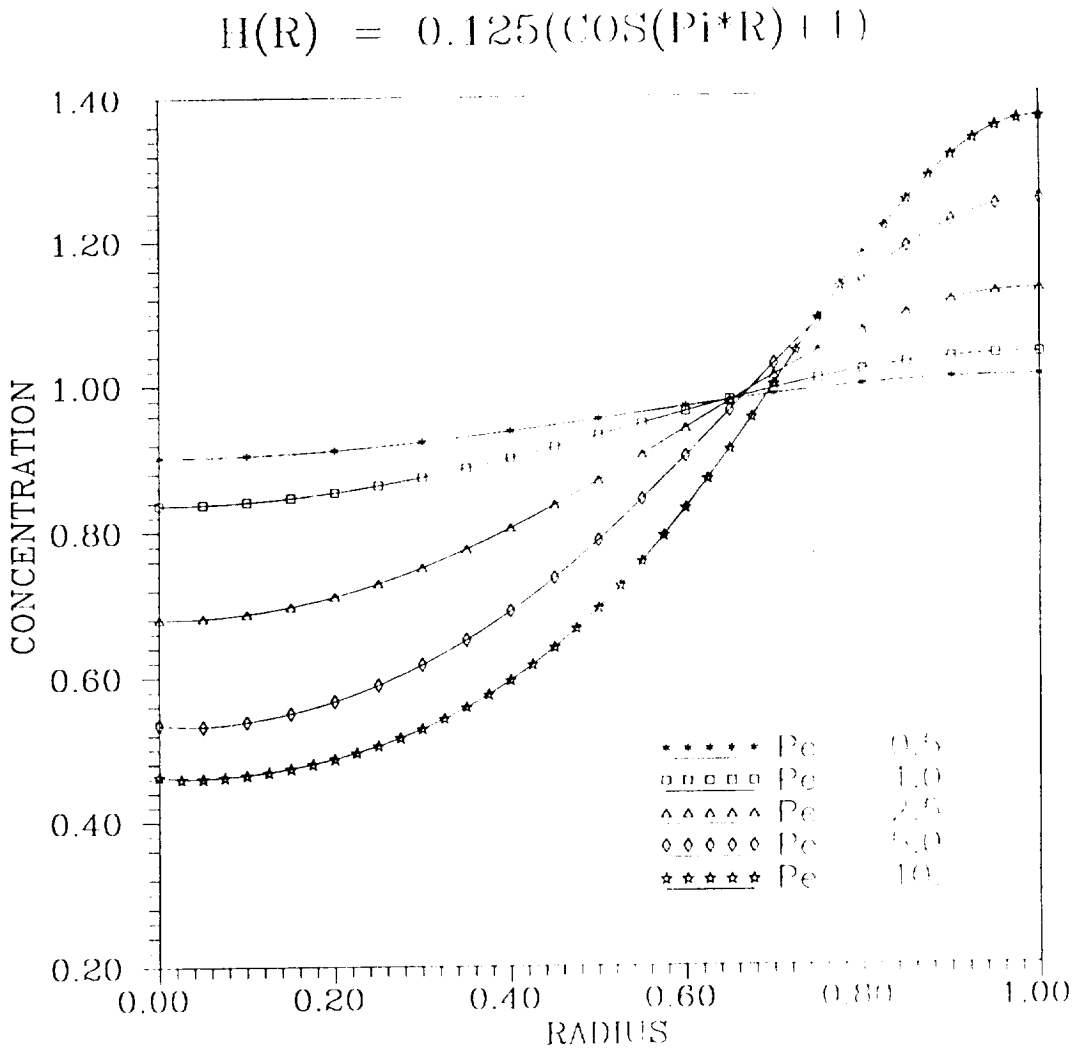

Figure 5.4: The influence of Peclet number on the radial concentration profile for a cosine-shaped interface. The interface's dimensionless amplitude is 0.25. k_{eq} = 0.3.

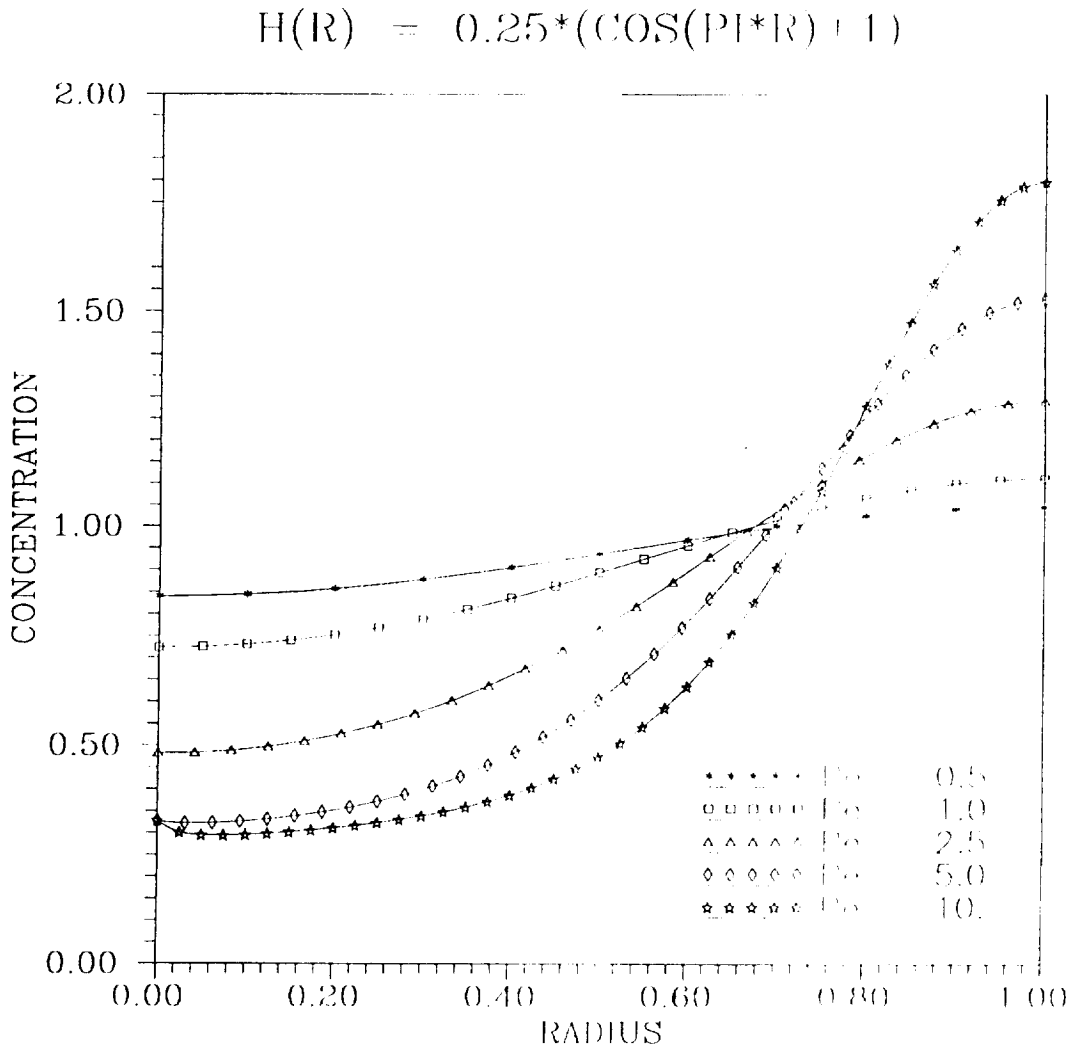

Figure 5.5: The influence of Peclet number on the radial concentration profile for a cosine-shaped interface. The interface's dimensionless amplitude is 0.5. k_{r_0} = 0.3

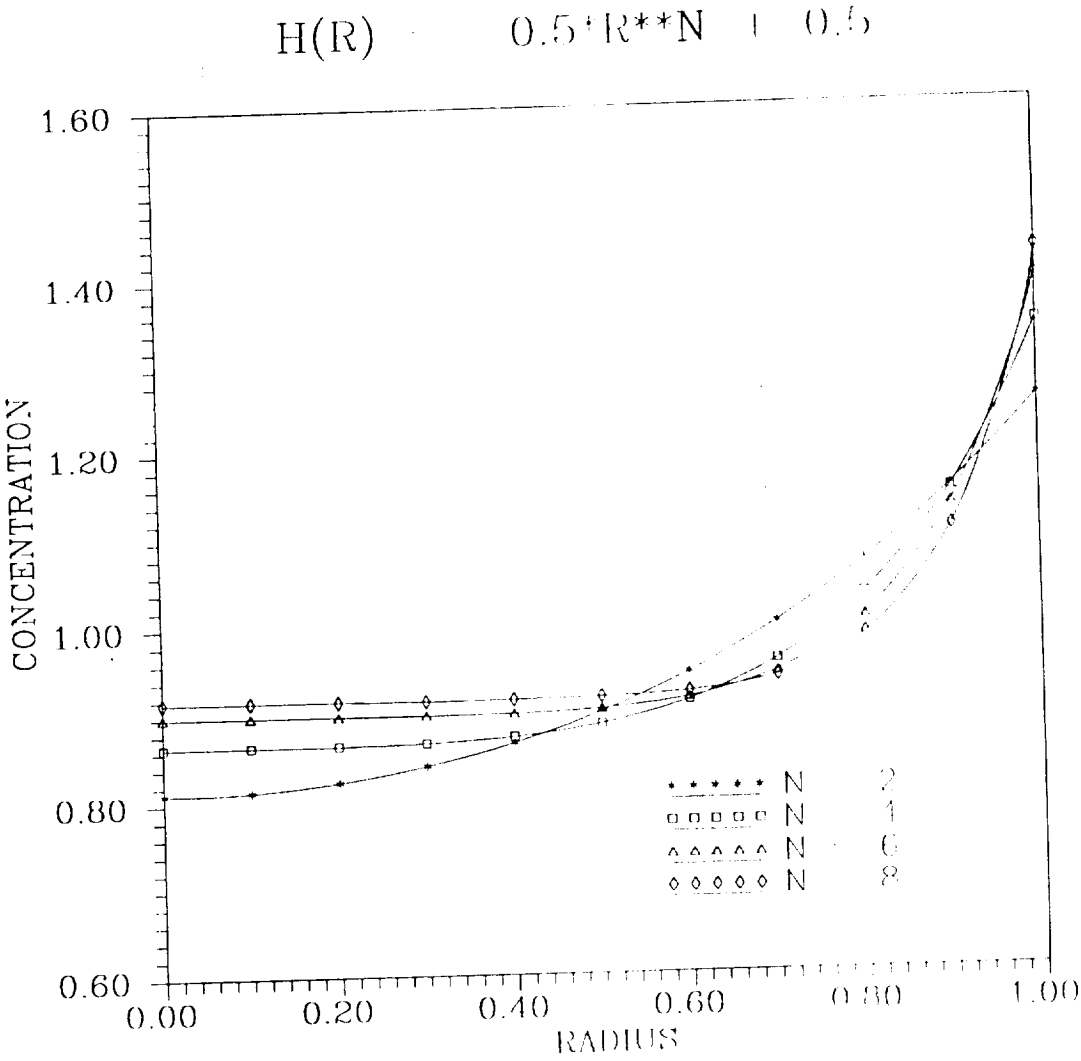

Figure 5.6: Radial concentration profile for $H(R) = -0.5 * R^N + 0.5$, $P_e = 1$, and $k_{eq} = 0.1$.

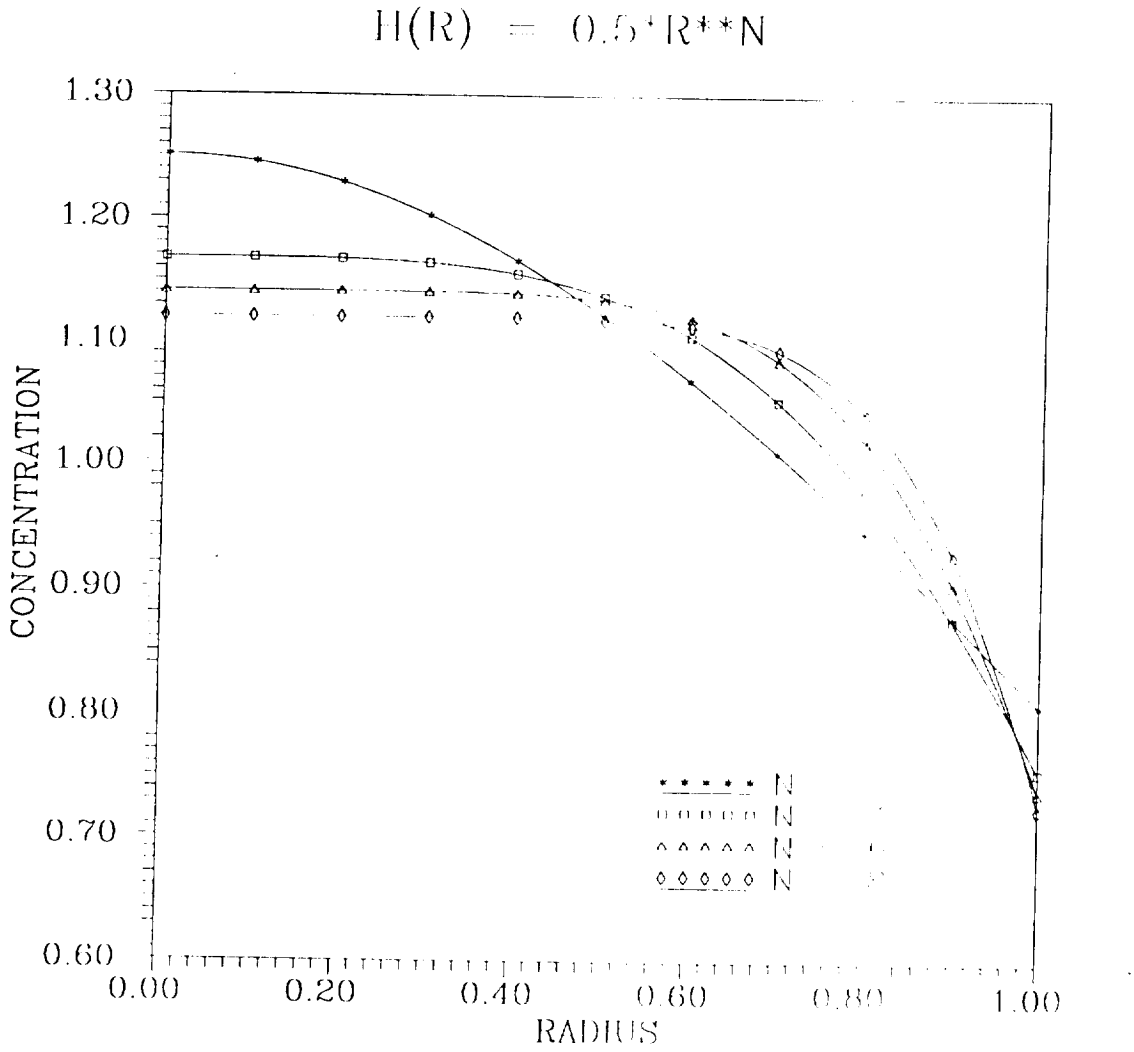

Figure 5.7: Radial concentration profile for $H(R) = 0.5 * R^N$, Pe = 1, and $k_{eq} = 0.1$.

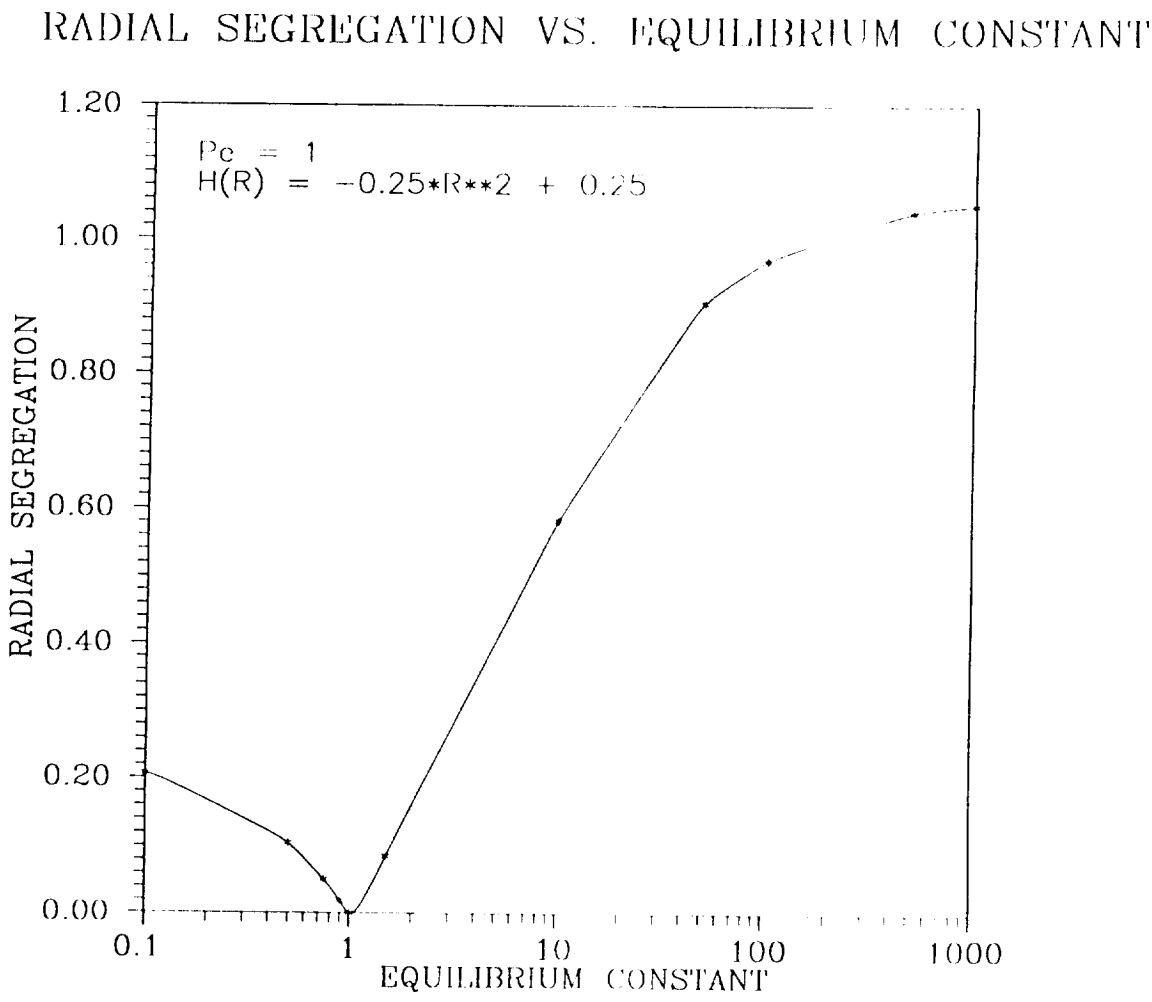

Figure 5.8: Effect of k_{eq} on radial segregation. Radial segregation is defined as the maximum deviation in scaled concentration at the interface from 1.

Figures 5.9 to 5.12 summarize the radial concentration profiles calculated for the growth conditions typical of azulene doped naphthalene. The Peclet numbers most often used in the experimental portion of this project were 3.2, 5.6, and 8.6. The equilibrium segregation coefficient for this system is 0.3 when the concentration is azulene in the melt is below 5%. The parameter with the most uncertainty in the experiments was the shape of the melt/solid interface. Because of the transparent heater used to grow the crystals, the interface could be seen when the ampoule was illuminated from behind with a bright light. (Azulene is very dark blue.) Under all growth conditions the interface appeared to be flat. Nevertheless, the possibility exists that an interfacial amplitude on the order of 1 mm could have escaped detection. When scaled by the radius of the ampoule this would correspond to a dimensionless amplitude of 0.125. An interfacial amplitude twice this value is probably is an upper limit for the amount of curvature obtained in these experiments. The radius of the crystal was approximately 8 mm, and a curvature of 2 mm over this distance would surely have been noticed. Therefore, 0.25 is used as the likely maximum interfacial amplitude for this project.

Figure 5.9 shows the computed radial concentration profile of material when the dimensionless amplitude of a convex melt/solid interface is 0.125. At high Peclet number the solutal boundary layer (i.e. the region in the melt where the solute concentration goes from its interfacial value to near its bulk melt value) begins to conform to the shape of the melt/solid interface. This causes the radial concentration profile to become flatter near the center. This effect is more clearly seen in Figure 5.10, which shows the results for an interfacial amplitude of 0.25. In this case, the radial concentration profile is not only flatter for the highest Peclet number, but the concentration of azulene near the center is actually closer to one. For very high Peclet numbers, i.e. $Pe \simeq 40$, there would be no radial segregation because the solutal boundary layer would conform exactly to the shape of the melt/solid interface Unfortunately, this model can't be used for such large values of Peclet number.

Figure 5.11 shows the calculated radial concentration profile when the dimensionless amplitude of a concave melt/solid interface is 0.125. Figure 5.12 shows the radial concen

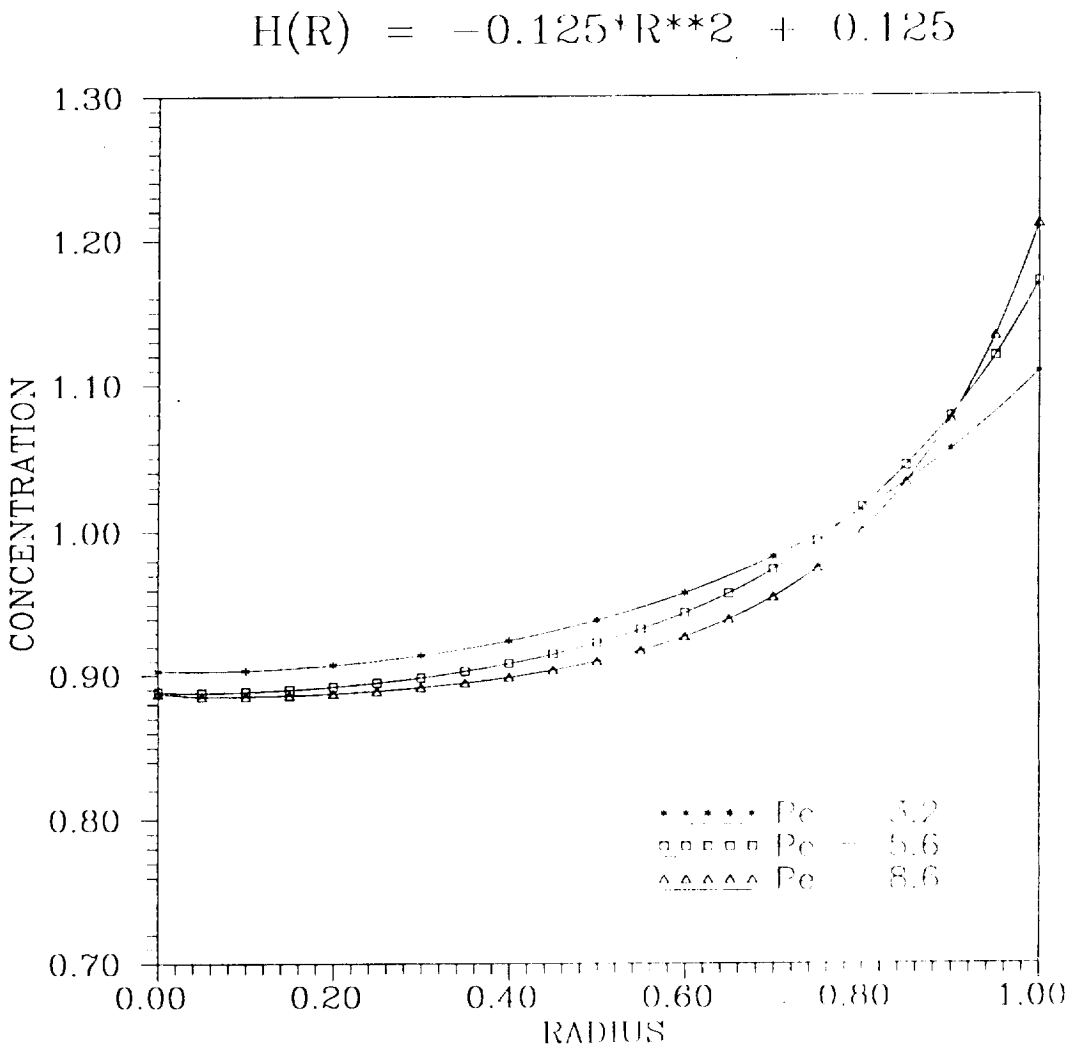

Figure 5.9: Radial concentration profile as a function of Peclet number for a convex interface with an amplitude of 0.125 and $k_{eq} = 0.3$. The parameters reflect those typically used here for the growth of azulene-doped naphthalene.

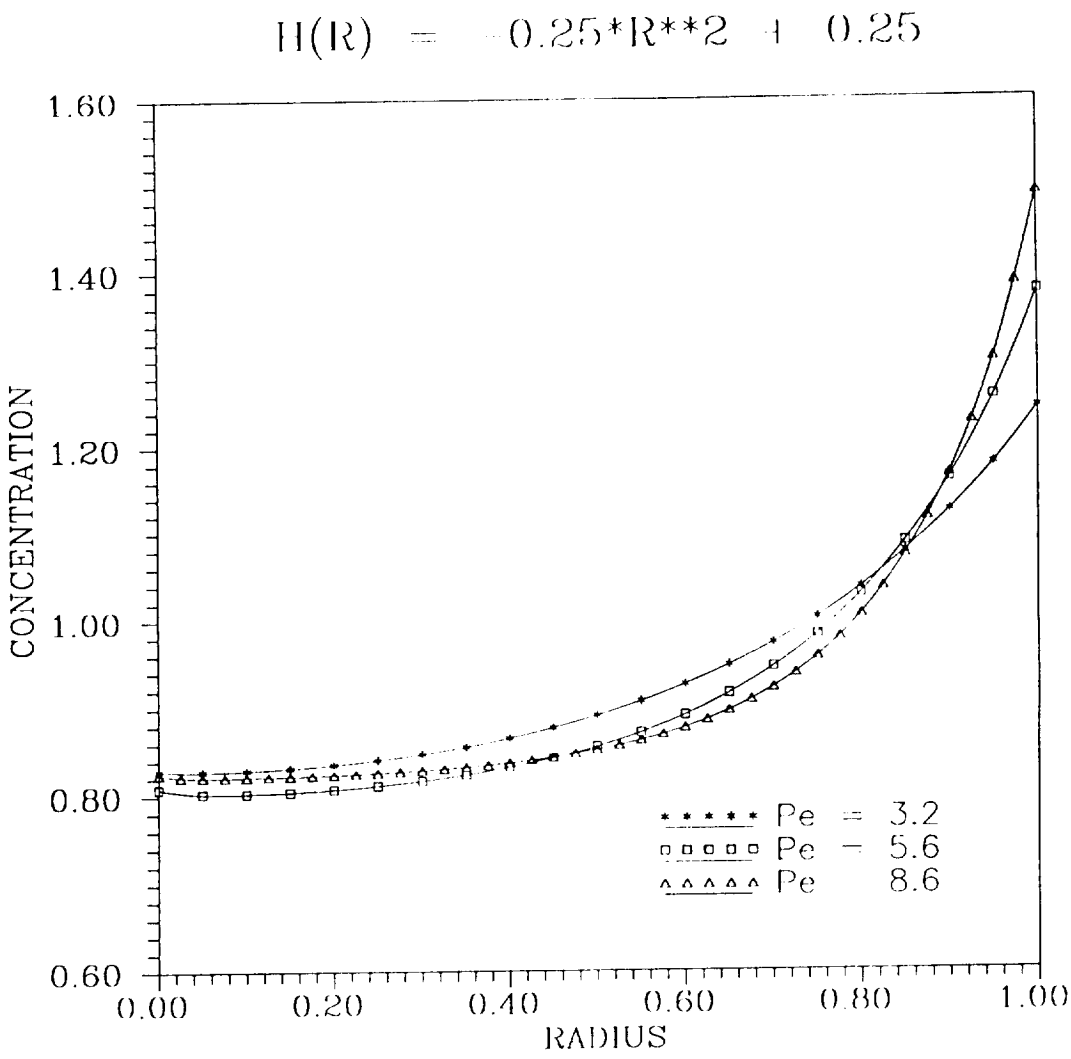

Figure 5.10: Radial concentration profile as a function of Peclet number for a convex interface with an amplitude of 0.25 and $k_{eq} = 0.3$. The amplitude of the interface represents an upper limit for that actually used the growth of azulene-doped naphthalene.

tration profile when the dimensionless amplitude of a concave melt/solid interface is 0.25. Unlike the results for the convex interface, the decrease in concentration near the center of the crystal at high Peclet number is more pronounced for an interface curvature of smaller amplitude.

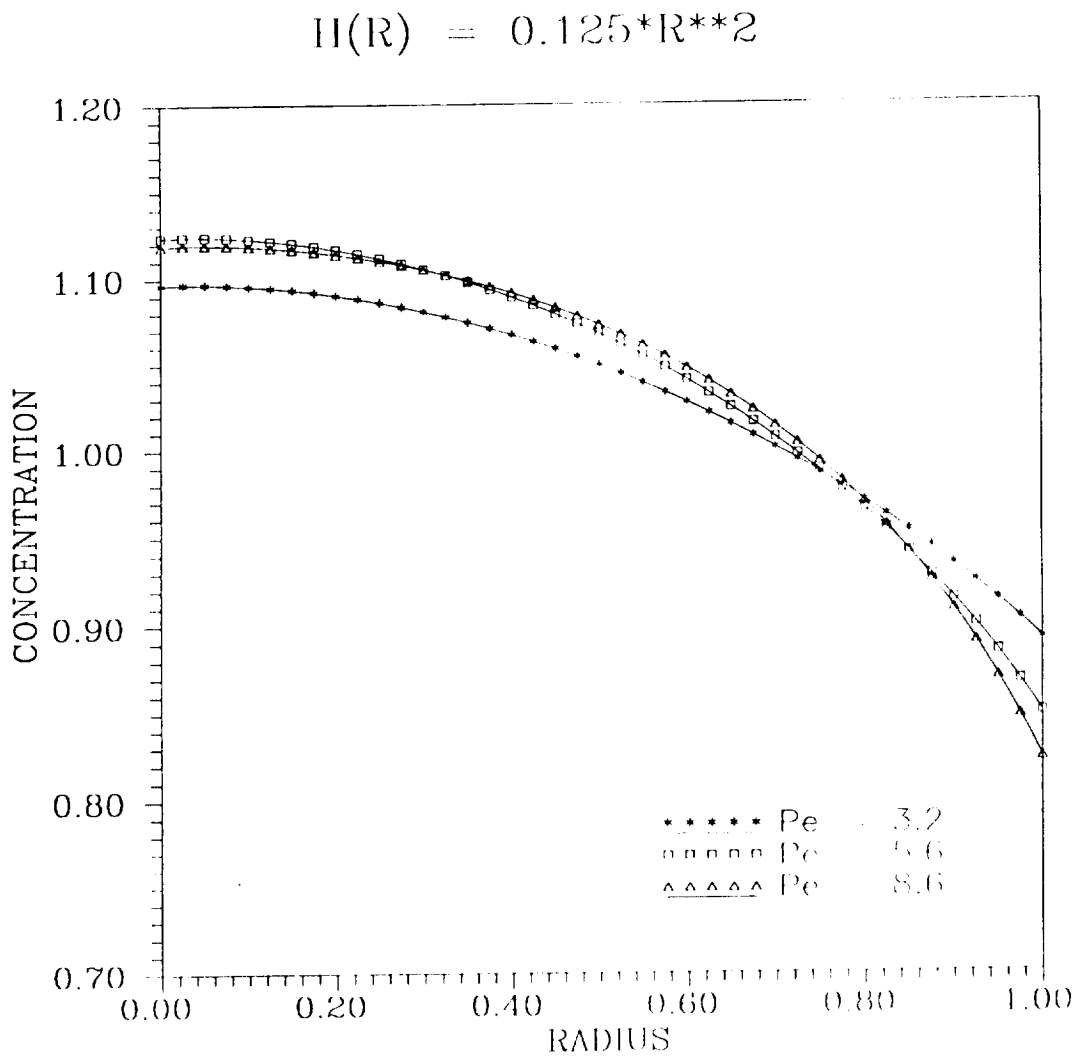

Figure 5.11: Radial concentration profile as a function of Peclet number for a concave interface with an amplitude of 0.125 and $k_{eq} = 0.3$. The parameters reflect those typically used here for growth of azulene-doped naphthalene.

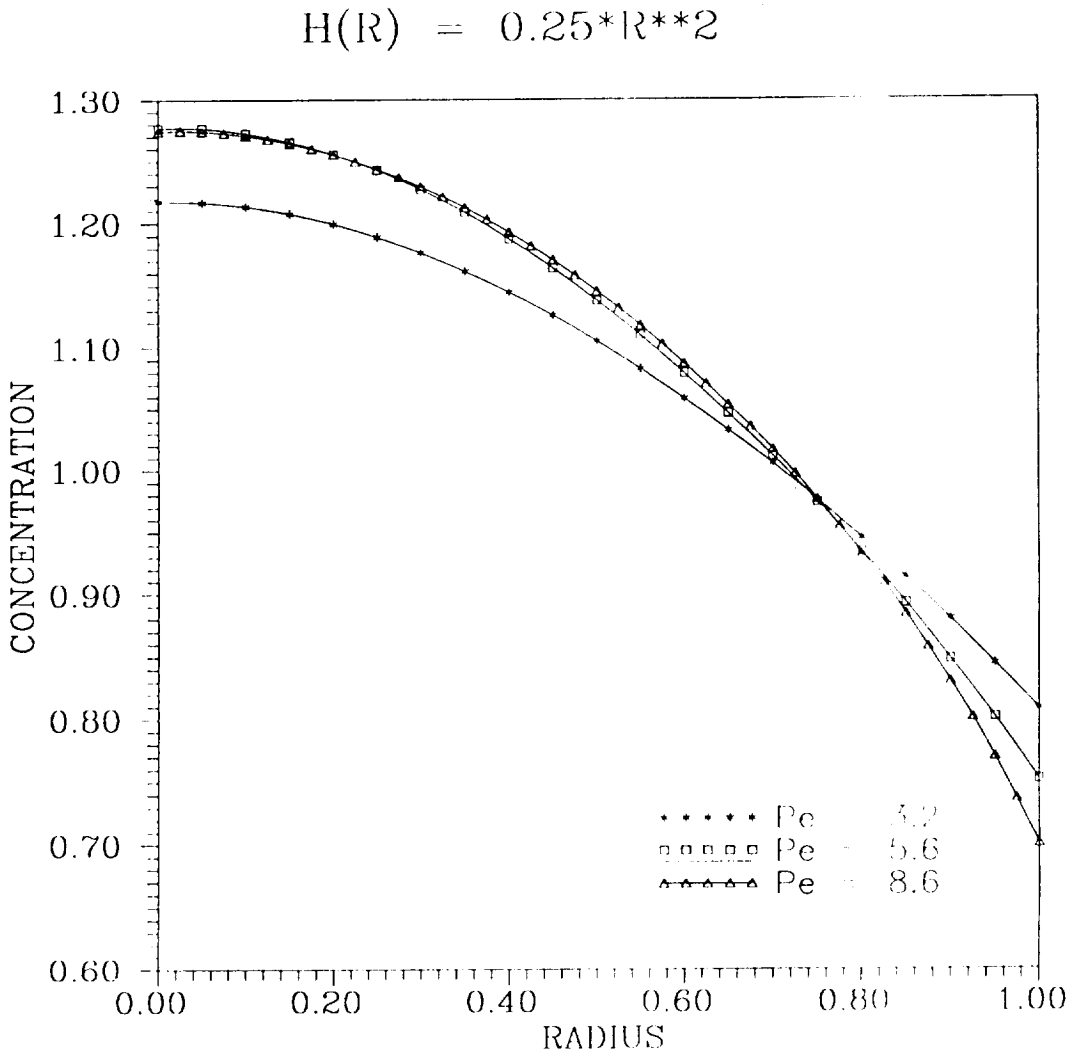

Figure 5.12: Radial concentration profile as a function of Peclet number for a concave interface with an amplitude of 0.25 and $k_{eq} = 0.3$. The amplitude of the interface represents an upper limit for that used here for the growth of azulene-doped naphthalene.

C-2

5.2 Convection

This section summarizes the relationship between the temperature profile of the heater and buoyancy-driven convection in the melt. Flow visualization in naphthalene is difficult because of the unavailability of a suitable neutrally buoyant tracer particle. Flow visualization is particularly difficult in the vertically stabilized condition in which convective velocities are extremely small. In a destabilized condition, in which convective velocities are much larger, the flow field is much easier to visualize because the viscous forces on the tracer particles are much larger. For this reason, salol, with sulfur as a tracer, was used for most of the experiments leading to the following figures.

The heater for these experiments was made from a polycarbonate tube. Its inner diameter was 22.3 mm. Grooves were carved in the outer wall of the tube using a lathe. Within the grooves were mounted nichrome wires at a uniform pitch of 3.2 turns/cm. The heater consisted of three zones: a 3.5 cm booster, a 16.2 cm main heater, and 32.0 cm heater on top. The diameter of the Pyrex tube containing the salol was 15.6 mm. Below the heater, the ampoule was cooled by the surrounding air. Thermocouples were glued to the outer wall of the Pyrex tube at regularly spaced axial intervals. The standard flow visualization technique was used (25,26).

Figure 5.13 shows the axial temperature profile in a destabilized condition. In this run, the power to the booster heater was large. This generated a maximum in temperature in the melt just above the melt/solid interface. The power to the upper zone of the furnace was turned down. This caused the temperature to drop off sharply near the top of the melt. In this destabilized condition the axial temperature gradient above the melt/solid interface and near the top of melt generated convection. The convection associated with Figure 5.13 is shown in Figure 5.14. Strong convection existed throughout the entire melt. The convective cell near the top of the melt was generated by the temperature roll-off at the top of the heater. Strong convection existed near the interface due to the maximum in temperature caused by the booster heater.

Figure 5.15 shows the temperature profile when the power to the booster heater was decreased. The axial temperature gradient near the interface did not promote convection.

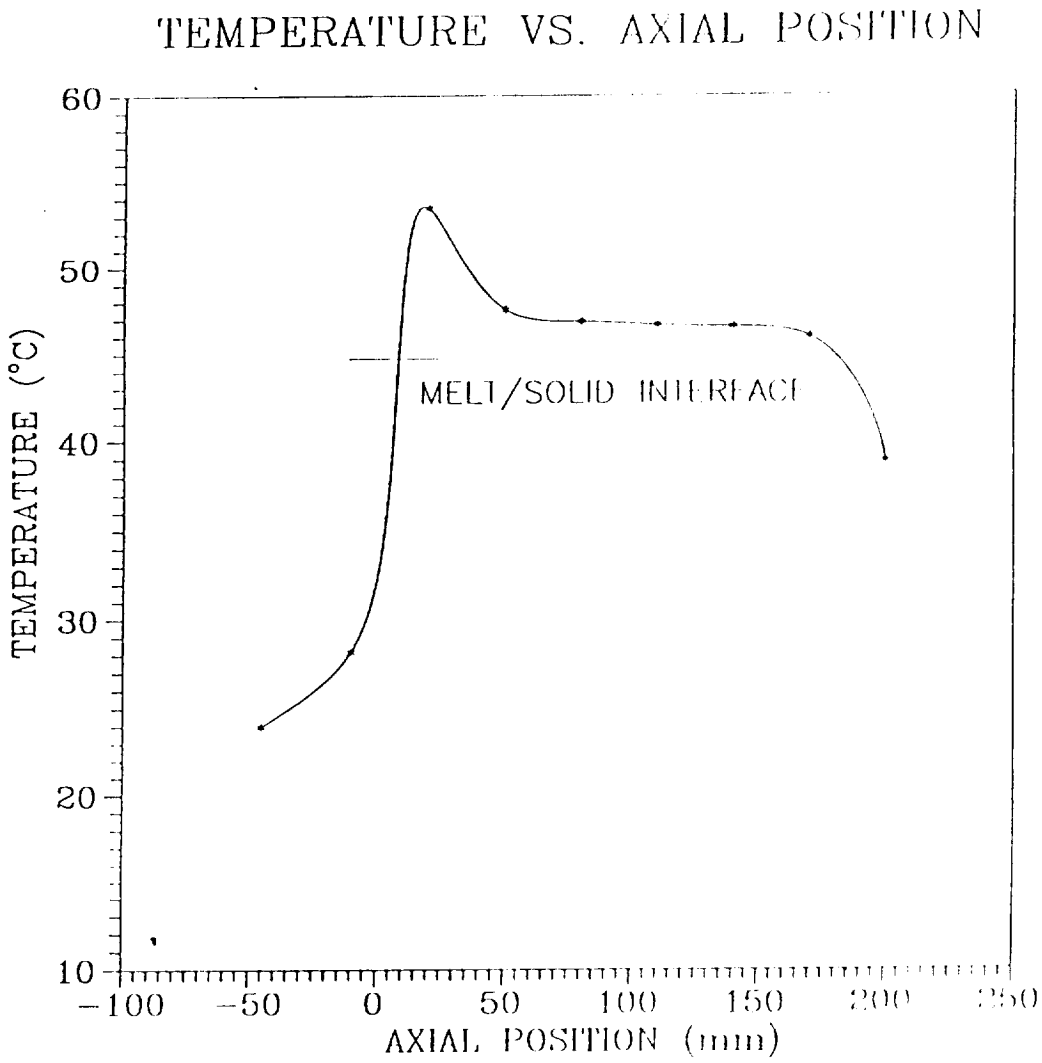

Figure 5.13: Axial temperature profile for a destabilized condition. The short line indicates the position of the melt/solid interface. The top of the melt is at 200mm.

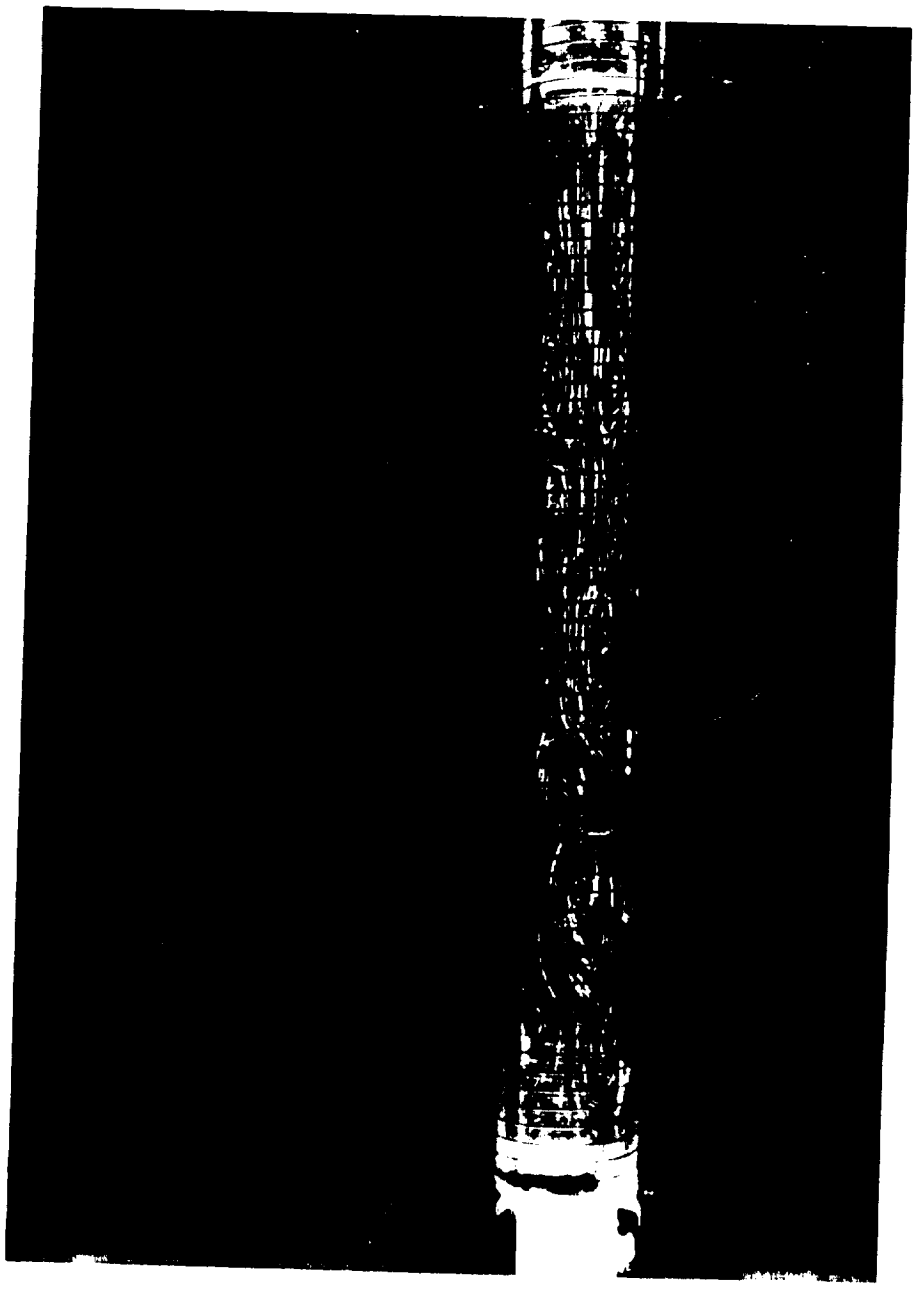

Figure 5.14: Convection for a completely destabilized condition. Strong convection exists throughout the entire melt. A 4 second exposure was used.

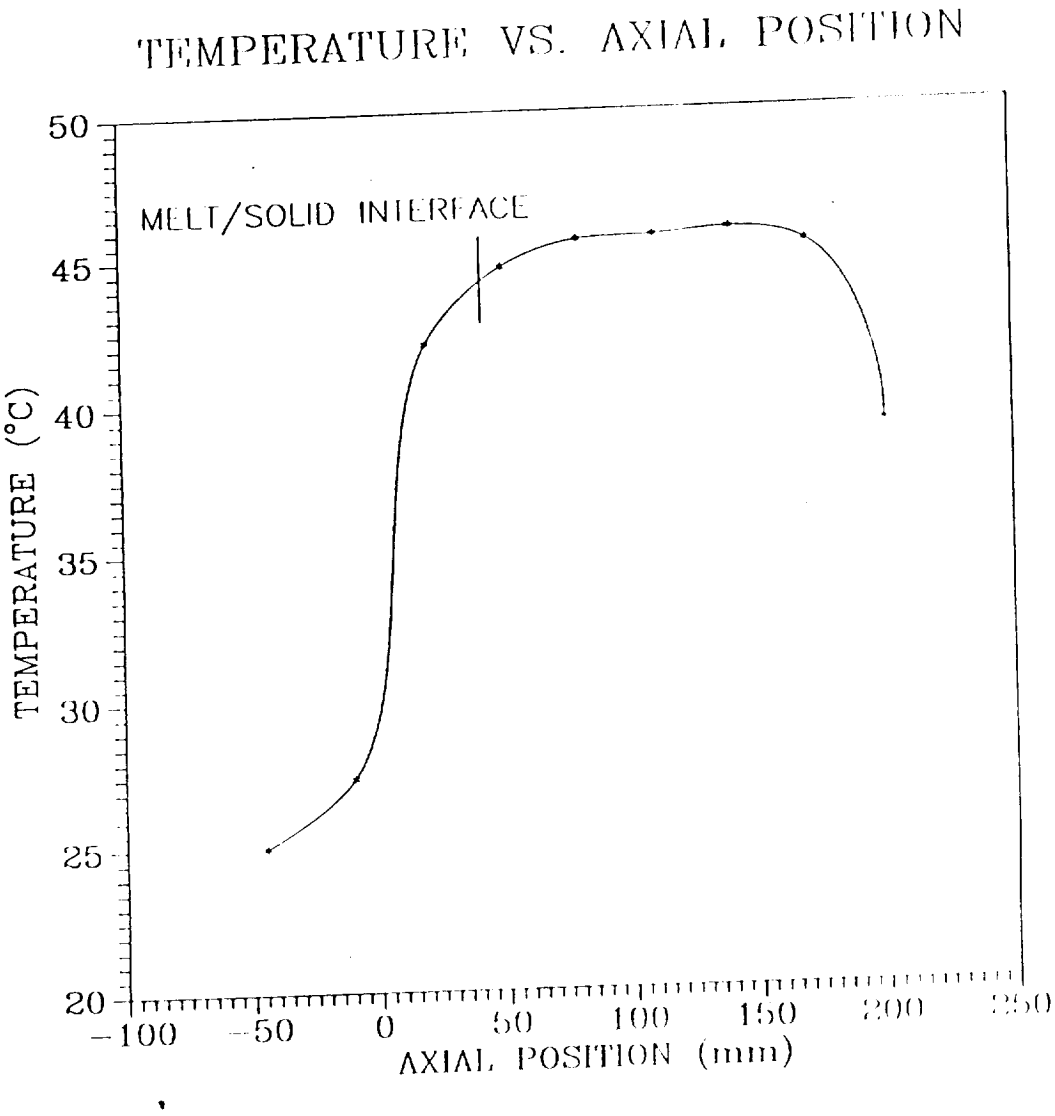

Figure 5.15: Stabilizing temperature gradient near the interface and a destabilizing temperature gradient at the top of the ampoule. The top of the melt is at 200 mm.

The convection associated with this temperature gradient is shown in Figure 5.16. This figure shows that the temperature roll-off at the top of the heater generated convection which was most intense at the top of the melt and decreased in intensity as the interface was approached. There appeared to be very little convection near the interface.

Figure 5.17 shows the axial temperature profile when the power applied to both the booster heater and the top zone of the heater was large. The convection associated with this temperature gradient is shown in Figure 5.18. The maximum in temperature generated intense convection near the interface. The intensity of convection decreased with height. The stabilizing temperature gradient at the top of the melt appeared to retard the convection generated by the booster.

It is very difficult to visualize the convection in a stabilized condition. Since no tracer particle is completely neutrally buoyant, they tend to either float or sink. Very slow convection requires very long time exposures in the flow visualization procedure. In order to prevent over exposure of the film, a multiple exposure technique was used. In this procedure the lens was left open for 3 minutes and every 30 seconds the laser was flashed for approximately 5 seconds. This generated a photo of the flow field that was three minutes long, but the film was actually exposed for only 30 seconds.

Figure 5.19 shows the axial temperature profile for a stabilized condition. Under these conditions, the axial temperature gradient did not promote convection. However, convection in the melt was generated by radial temperature gradients.

The convection associated with these conditions is shown in Figure 5.20. Although the sulfur tended to sink, evidence of convection in the melt was clear. The streaks traced by the sulfur as it settled were very curved, indicating convection was present in the melt. The radial component of the convective velocity can be estimated from the total radial motion of the particle during the three minute period. Figure 5.20 indicates that the maximum radial convective velocity was on the order of 20 micron/s. This is of the same order of magnitude as the growth rate used in the naphthalene/azulene system, 3 to 9 micron/s.

Figure 5.21 shows the axial temperature profile for a stabilized condition under the conditions used to grow naphthalene crystals. Under these conditions, sulfur particles tended

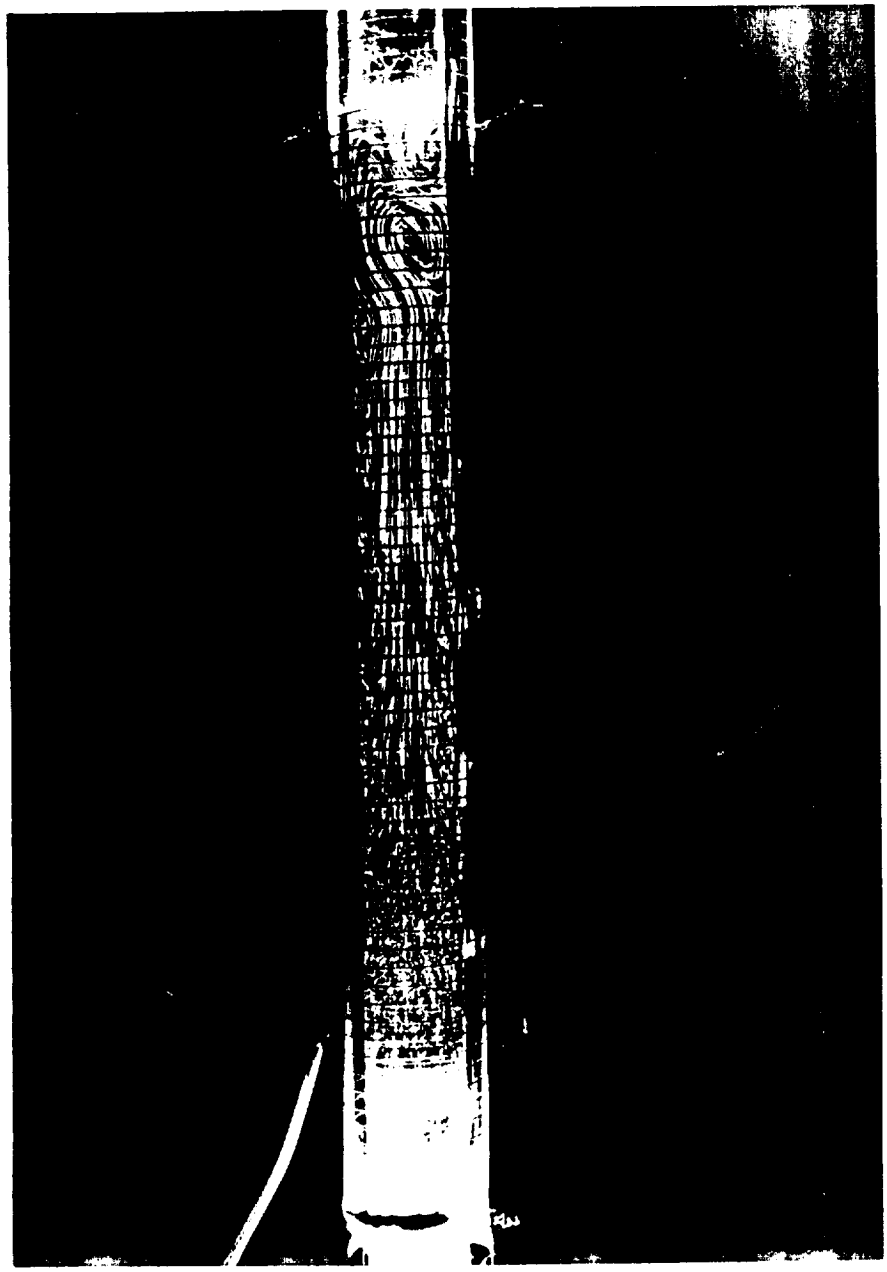

Figure 5.16: Convection caused by the temperature roll-off at the top of the heater. An 8 second time exposure was used.

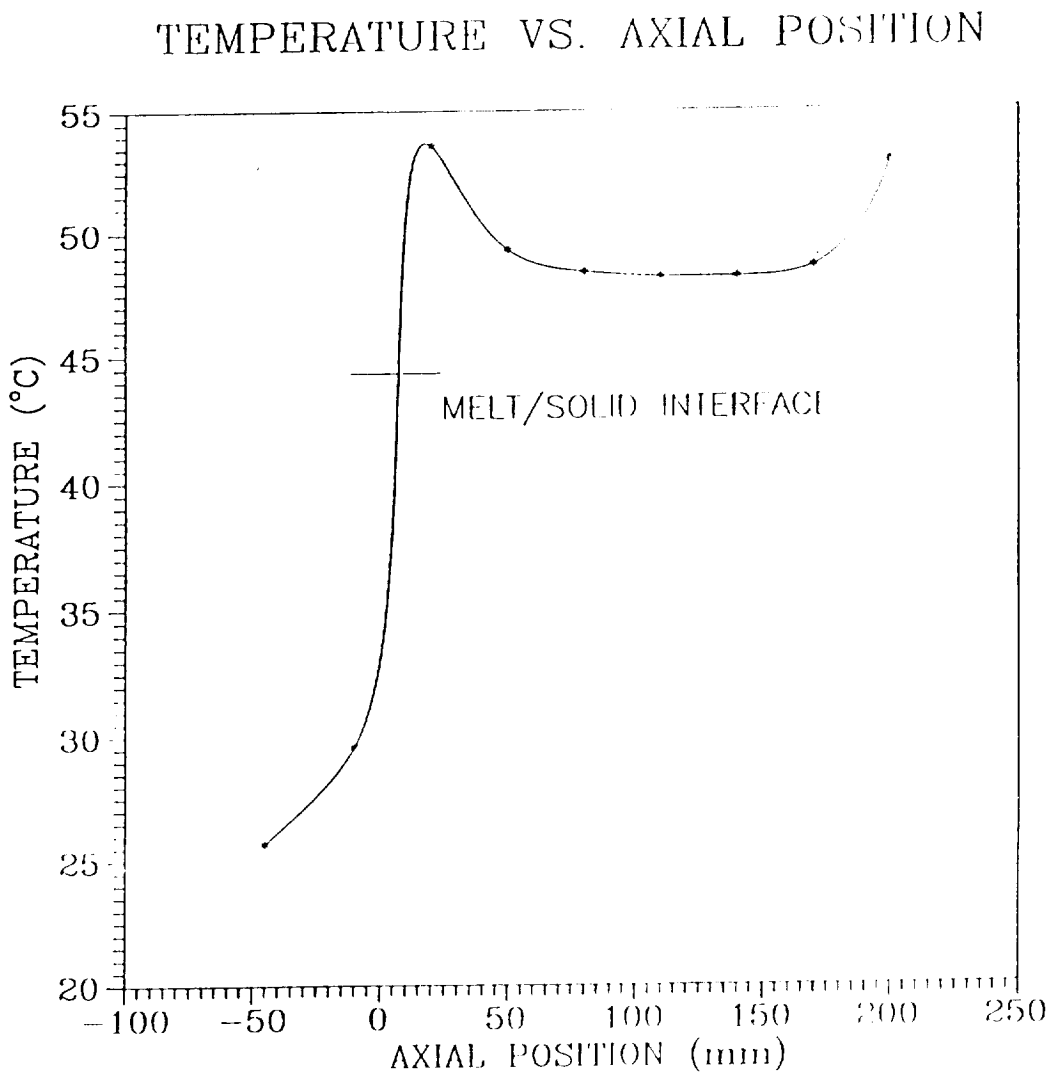

Figure 5.17: Destabilizing temperature gradient near the interface and a stabilizing temperature gradient at the top of the ampoule. The top of the melt is at 200 mm.

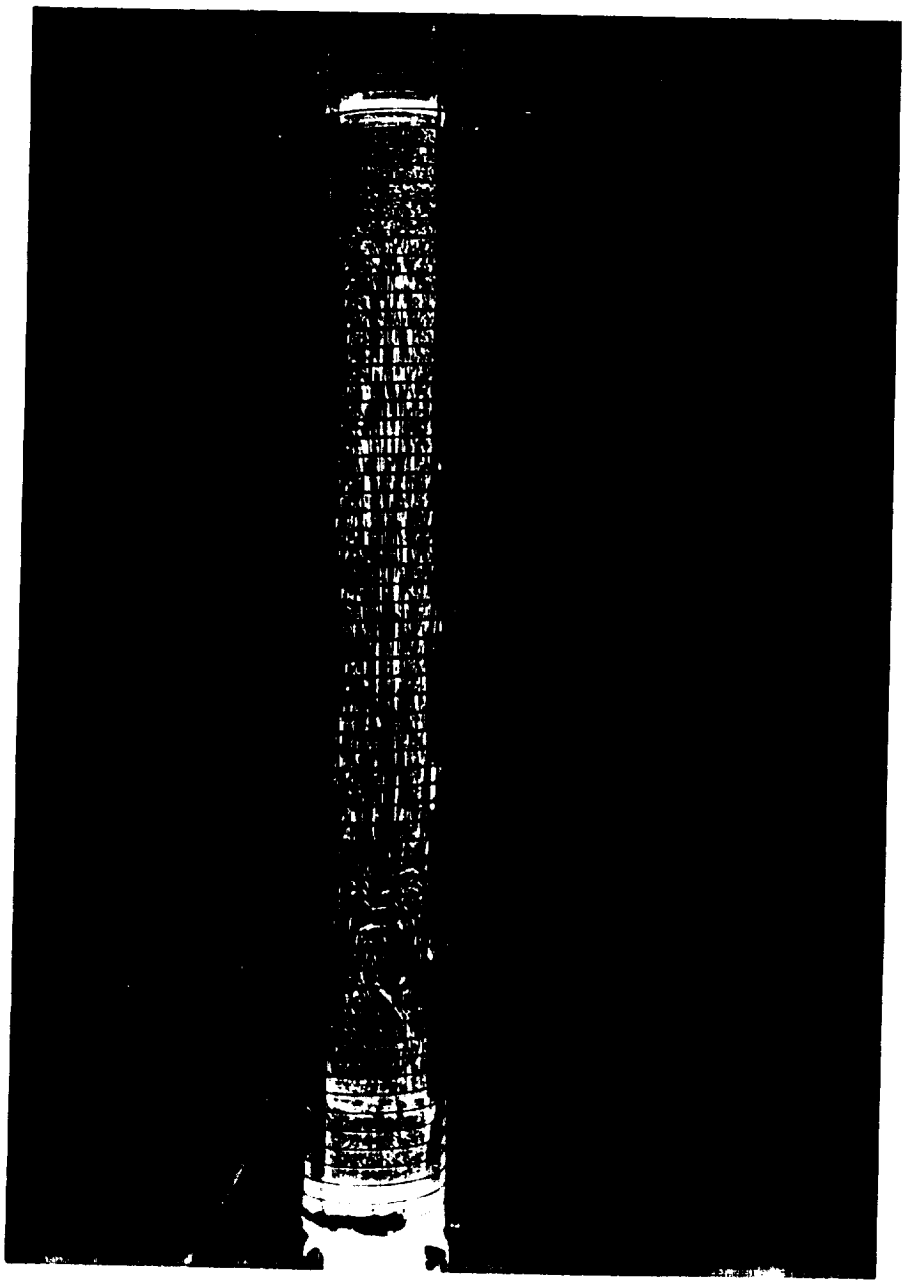

Figure 5.18: Convection caused by a maximum in temperature near the interface. A 4 second time exposure was used.

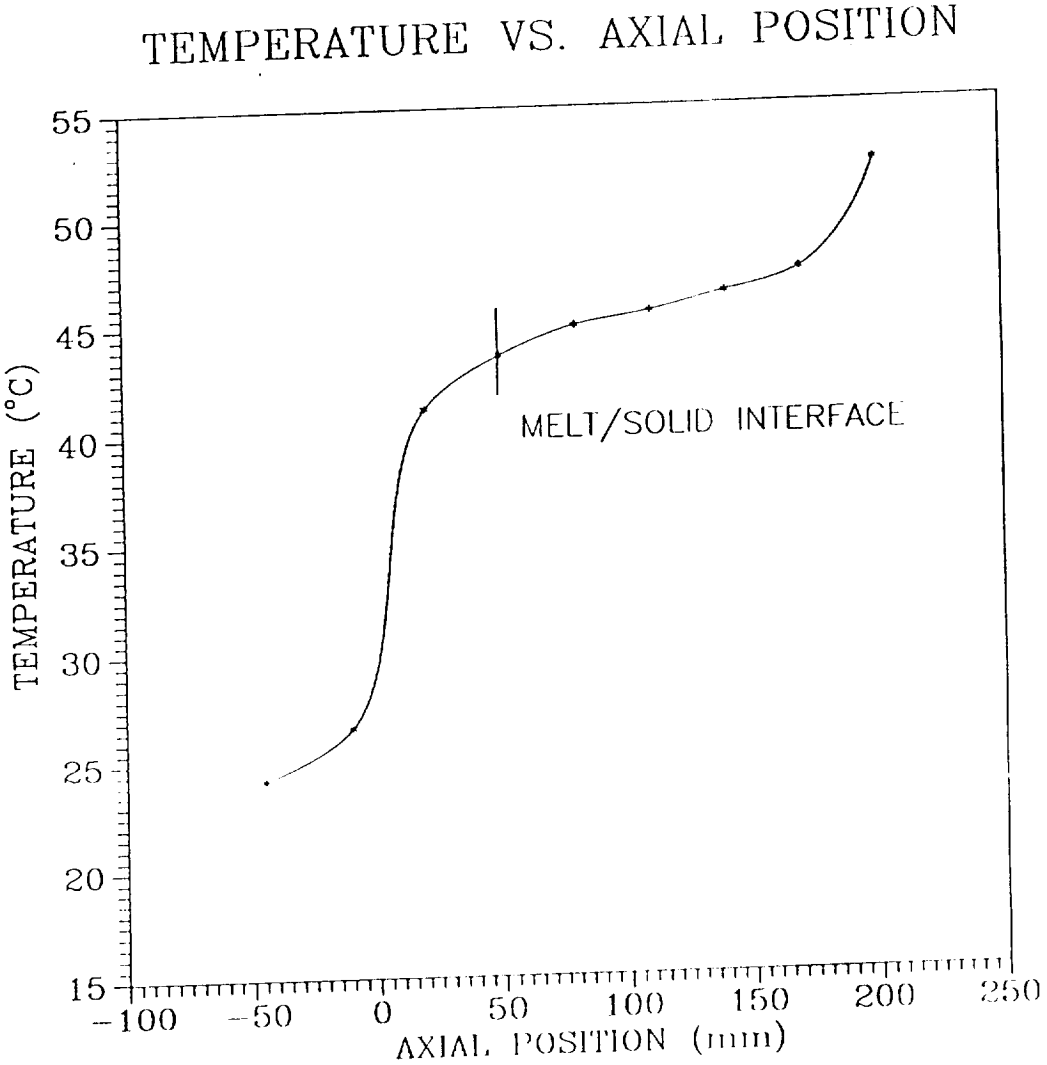

Figure 5.19: Axial temperature profile for a stabilized condition. The top of the melt is at 200mm.

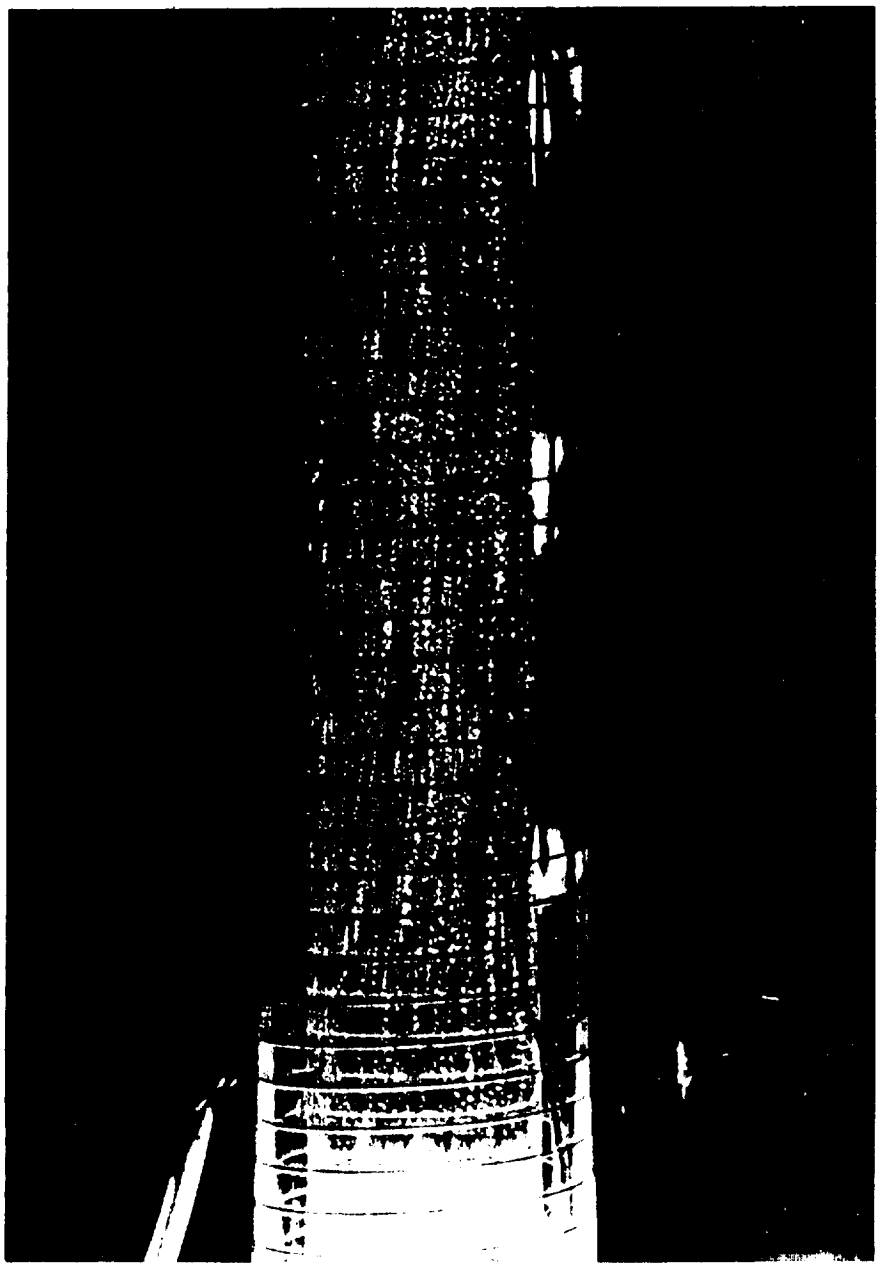

Figure 5.20: Convection for a stabilizing temperature profile. Very little convection existed throughout the entire melt. A 3 minute multiple exposure was used.

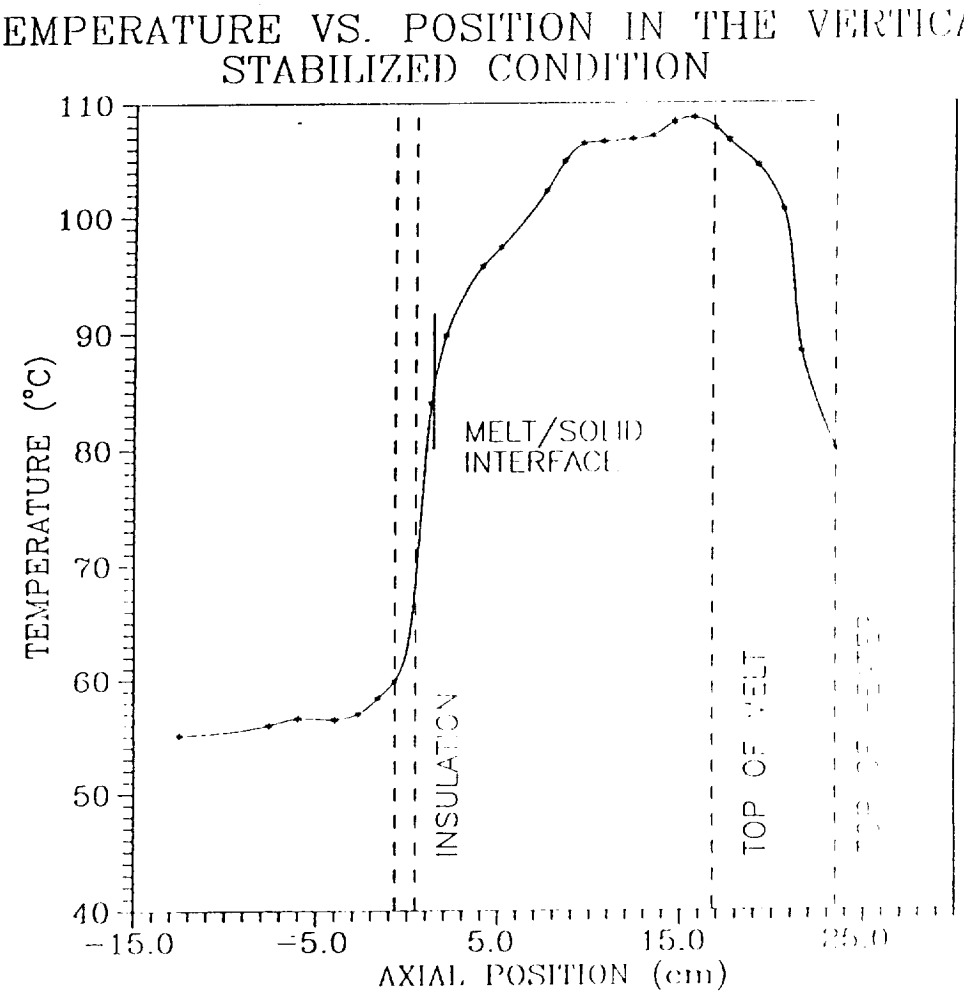

Figure 5.21: Axial temperature profile used to grow naphthalene crystals in a stabilized condition

to sink almost immediately. Nevertheless, the amount of convection in the melt was estimated using azulene as a tracer dye. (Note that one must be cautious in interpreting the results when tracer dyes are used to visualize convection since the dye itself can generate solutal convection.) To the naphthalene melt was added a few milligrams of azulene. The two photos in Figure 5.22 were taken 10 minutes apart. While some mixing was apparent in the left side of the melt, it is consistent with the results obtained in the salol experiments. Convection in a stabilized condition is extremely gentle.

Figure 5.23 is an interesting photo taken during solidification of pure naphthalene in a stabilizing temperature gradient. This time exposure photo shows the streaks caused by a stream of bubbles that were being ejected from the melt/solid interface during solidification. As the bubbles rose, they broke into smaller ones. The spots in the melt are sulfur particles, which appear motionless in this photo. Evolution of gases at the melt/solid interface can contribute to mixing in the melt. Marangoni convection caused by the bubble at the melt/solid interface may also influence segregation.

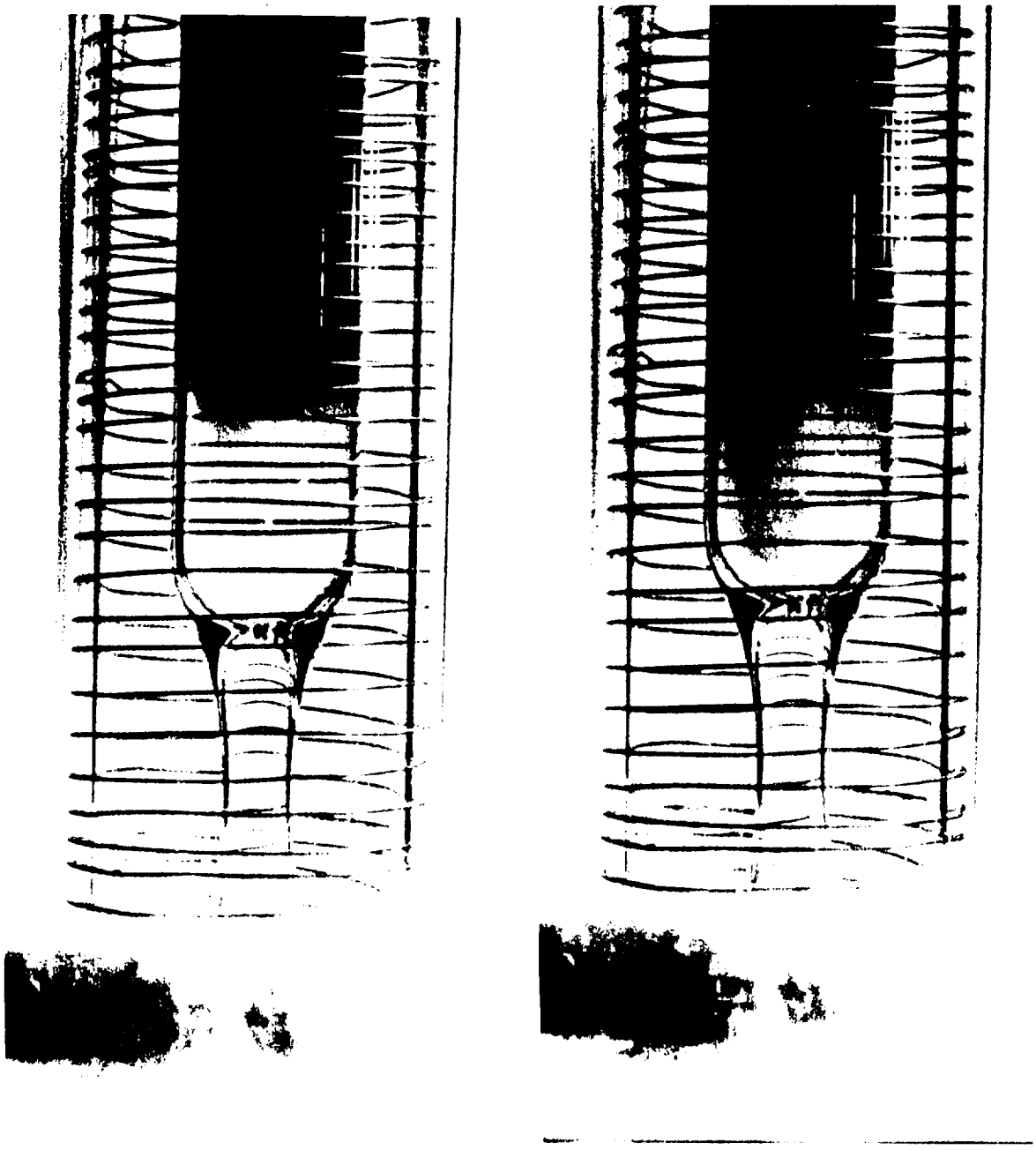

Figure 5.22: Azulene is being used as a tracer-dye to visualize convection. The two photos were taken 10 minutes apart.

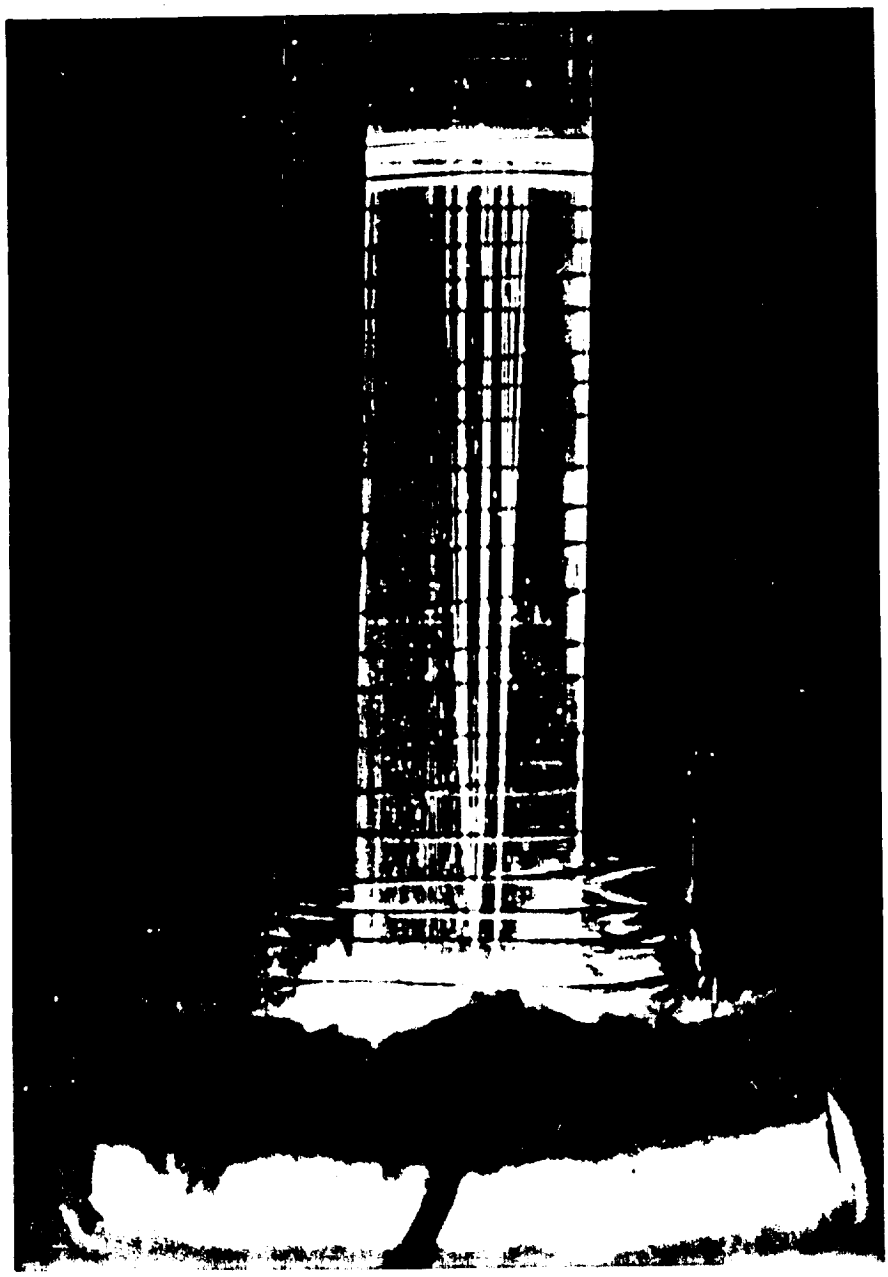

Figure 5.23: Streaks caused by the evolution of gas bubbles from the melt/solid interface during solidification. The photo is a 4 sec exposure.

5.3 Radial Segregation – Stabilized Conditions

A stabilized condition is defined as one in which the temperature near the interface increased with height. The temperature profile used to grow all the crystals in a stabilized condition is given in Figure 5.21

Figure 5.24 shows the axial composition profile of azulene for a typical crystal grown under the vertically stabilized condition shown in Figure 5.21 with a dimensionless growth rate, Pe, equal to 3.2. This axial concentration profile is characteristic of that produced by solidification from a well mixed melt. The temperature difference in the melt near the interface was measured and found to be approximately 0.2^oC. This corresponds to a Grashof number of approximately 10. Although the radial temperature gradient was very small, there was a significant amount of convection in the melt.

Radial composition data associated with Figure 5.24 are given in Figure 5.25. The radial concentration profile was scaled by the mean mass fraction of azulene. This figure gives the radial concentration of azulene for various axial locations along the same crystal. Axial locations along the crystal were measured in terms of the mass fraction of the crystal, g. The radial concentration profile was very asymmetric. For mass fractions 0.2 and 0.4 the radial concentration profile was characteristic of an asymmetric convex interface or asymmetric convection, or both. The concavity of the interface at mass fraction 0.7 is difficult to judge. Figure 5.25 suggests that temperature field in the melt was asymmetric. However, the thermal field at the interface was measured at the outer wall of the sample ampoule, and it was found to be symmetric to within 0.1^oC.

The amount of variation in the radial concentration profile of the azulene is referred to here as the segregation. The segregation is defined as the maximum deviation in scaled concentration from 1. For example the segregation of the concentration profile at $g = 0.7$ in Figure 5.25 is 0.45 (or equivalently 45%). Also, the asymmetry of a radial concentration profile is quantified through an asymmetry index. The asymmetry index is the maximum ratio of the scaled concentration at $\pm R$ ($R \neq 0$) to the scaled concentration at $\mp R$. (Interpolation is used if necessitated by the spacing of the data.) From the ratio 1 is subtracted so that a perfectly symmetric interface has an asymmetry index of zero. The asymmetry

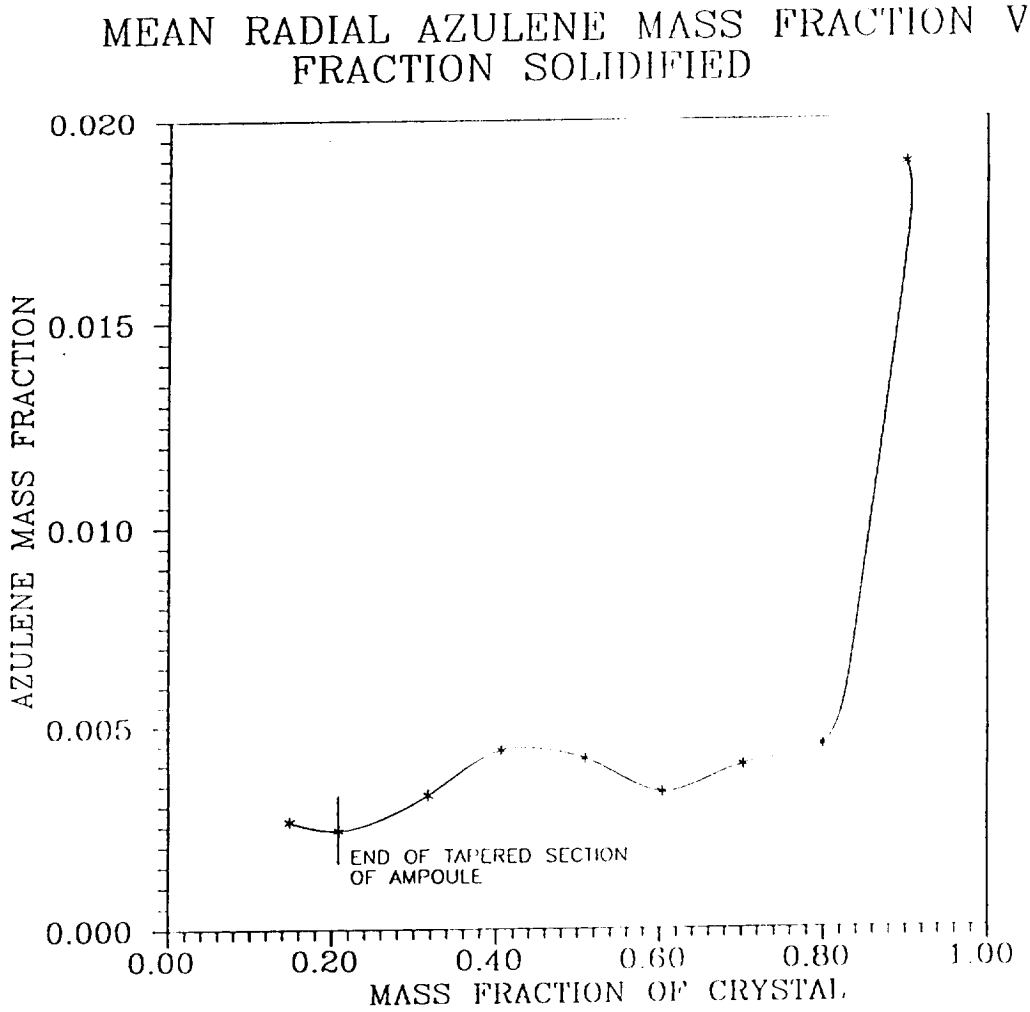

Figure 5.24: Axial concentration profile for stabilized condition

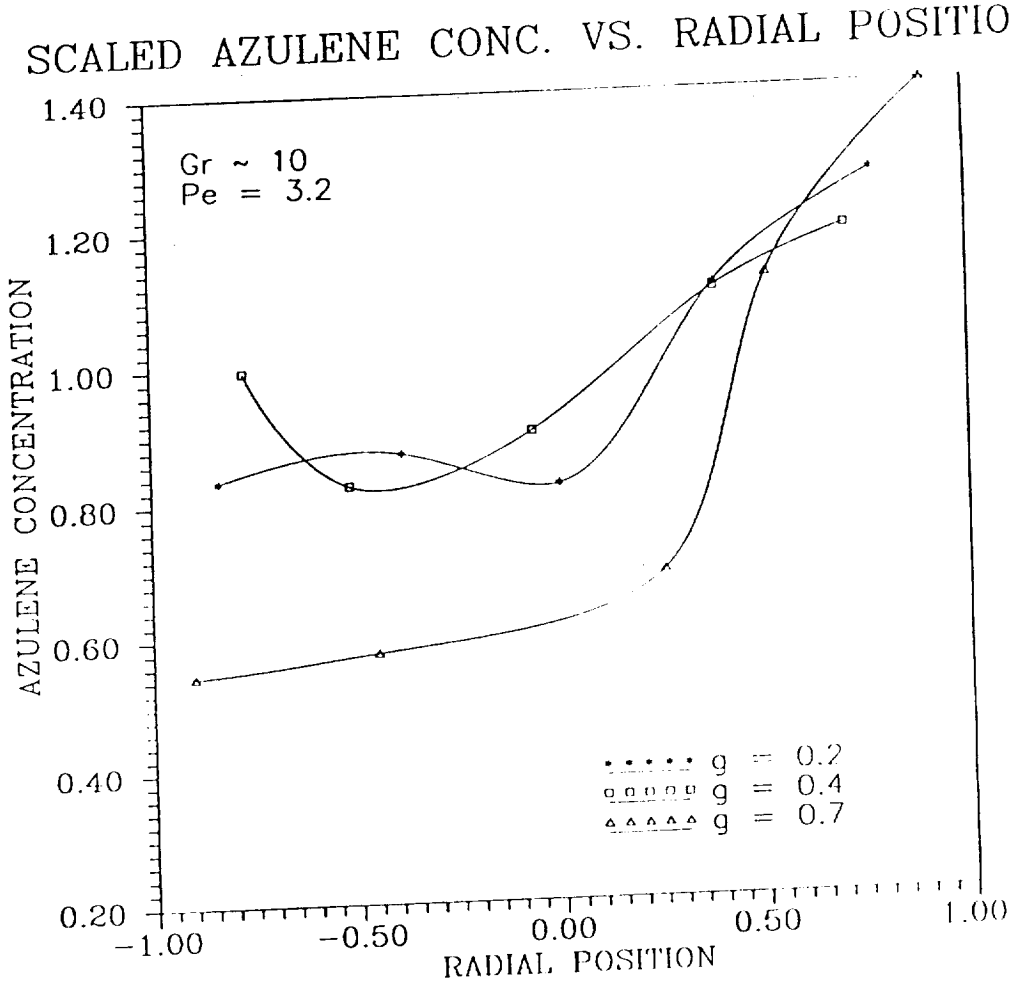

Figure 5.25: Radial concentration profile for a stabilized condition, Pe = 3.2

index of the composition profile at $g = 0.7$ in Figure 5.25 is 1.56.

The segregation and the asymmetry index of each run for a stabilized condition are listed in Tables 6.1 and 6.2 in Section 6. The results for solidification under destabilized conditions are summarized in Table 6.3 in Section 6.

In order to investigate the effect of thermal asymmetry on radial segregation, an asymmetry was deliberately induced by insulating the left half of the heater. This induced a thermal asymmetry across the ampoule at the interface of approximately 6.4°C. The radial segregation induced by the above asymmetry is shown in Figure 5.26. The insulated side of the ampoule was at $R = 1$. For all length fractions the radial concentration profile was somewhat sinusoidal, with an increase in composition near the hot side of the ampoule. Surprisingly, the magnitude of the radial segregation was unchanged by the thermal asymmetry.

Figure 5.27 shows the radial concentration profile for a crystal that was solidified at the same rate as the one described in Figure 5.25. Again the radial concentration profile was concave and asymmetric. When convection is not axi-symmetric, the cross sectional composition is not accurately revealed by composition measurements along only one diameter. In order to more accurately characterize the cross-sectional variation in the concentration profile, the concentration of azulene in the crystal described in Figure 5.27 was measured along two diameters at $g = 0.5$. The results are shown in Figure 5.28. The azulene concentration was measured along one diameter at 5 points and then at 2 points along a line perpendicular to the first 5. The concentration was scaled by the mean of the seven values. Figure 5.28 indicates that although a radial concentration profile may be very symmetric in one direction, this does not guarantee that the radial composition profile will be symmetric in another direction. The curve consisting of five points shows a sinusoidal variation typical of that showed in Figure 5.26, the strongly asymmetric thermal profile.

When composition was measured along two diameters, the same convention was always used to describe radial position. The concentration measurements go from left to right and back to front (facing the crystal as grown) along the two perpendicular diameters. For the curve described by five points, $R = 1$ refers to the right side of the crystal. For the curve

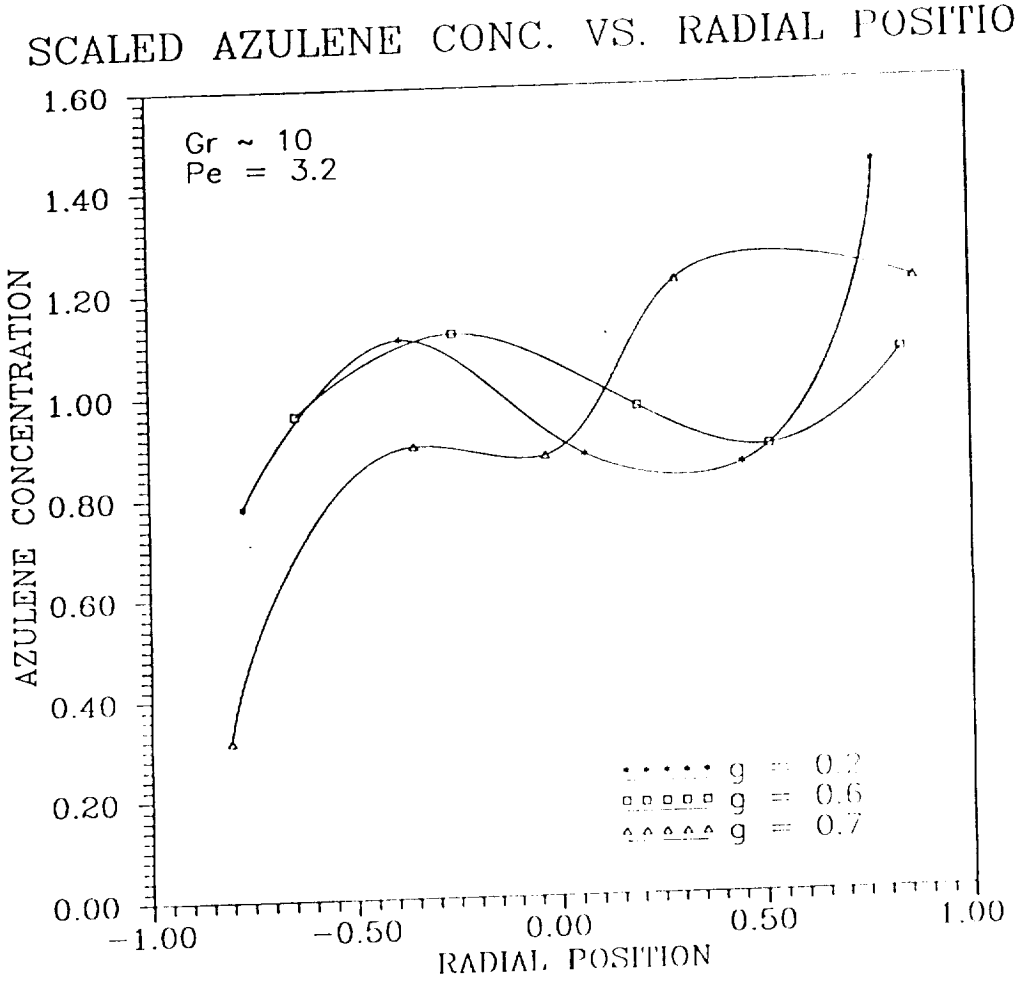

Figure 5.26: Radial concentration profile under asymmetrical thermal conditions. The temperature at $R = 1$ was $6.4°C$ hotter than at $R = -1$. The Peclet number was 3.2.

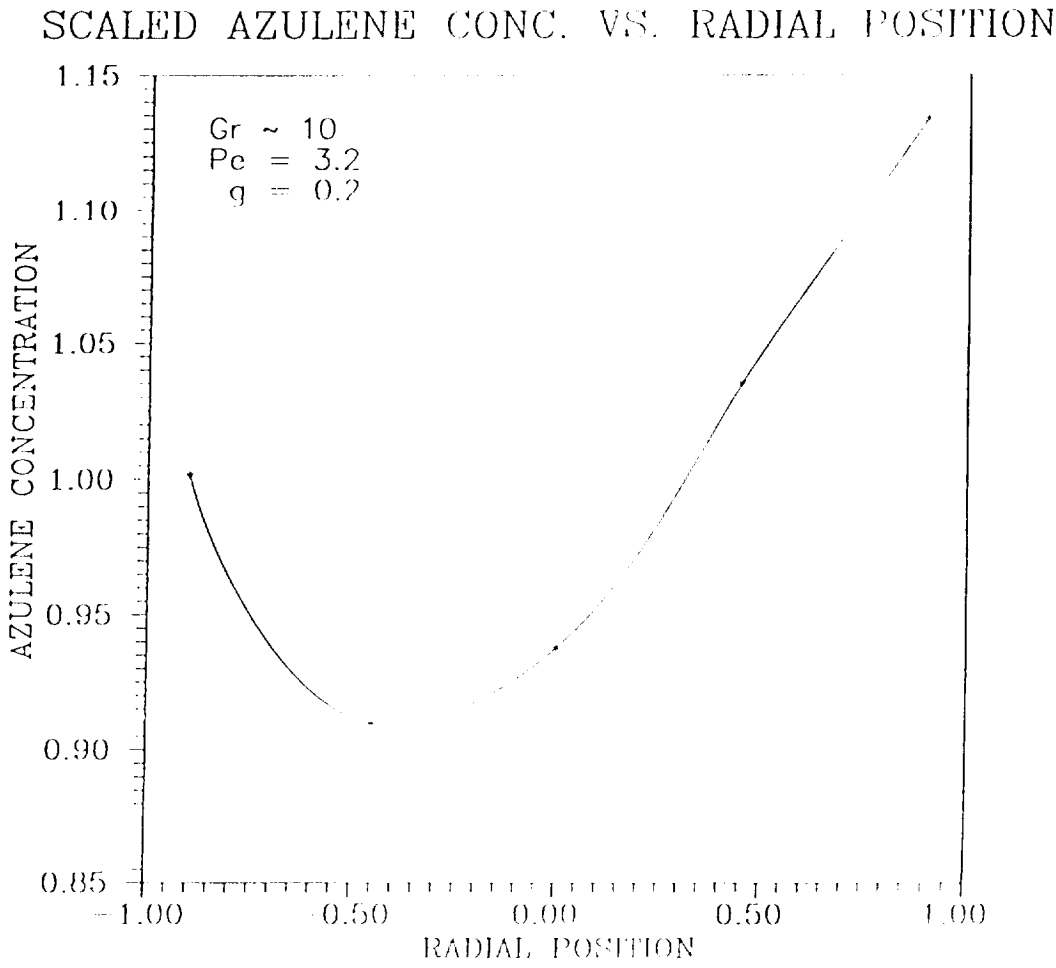

Figure 5.27: Radial concentration profile for a stabilized condition, $Pe = 3.2$ at $g = 0.2$.

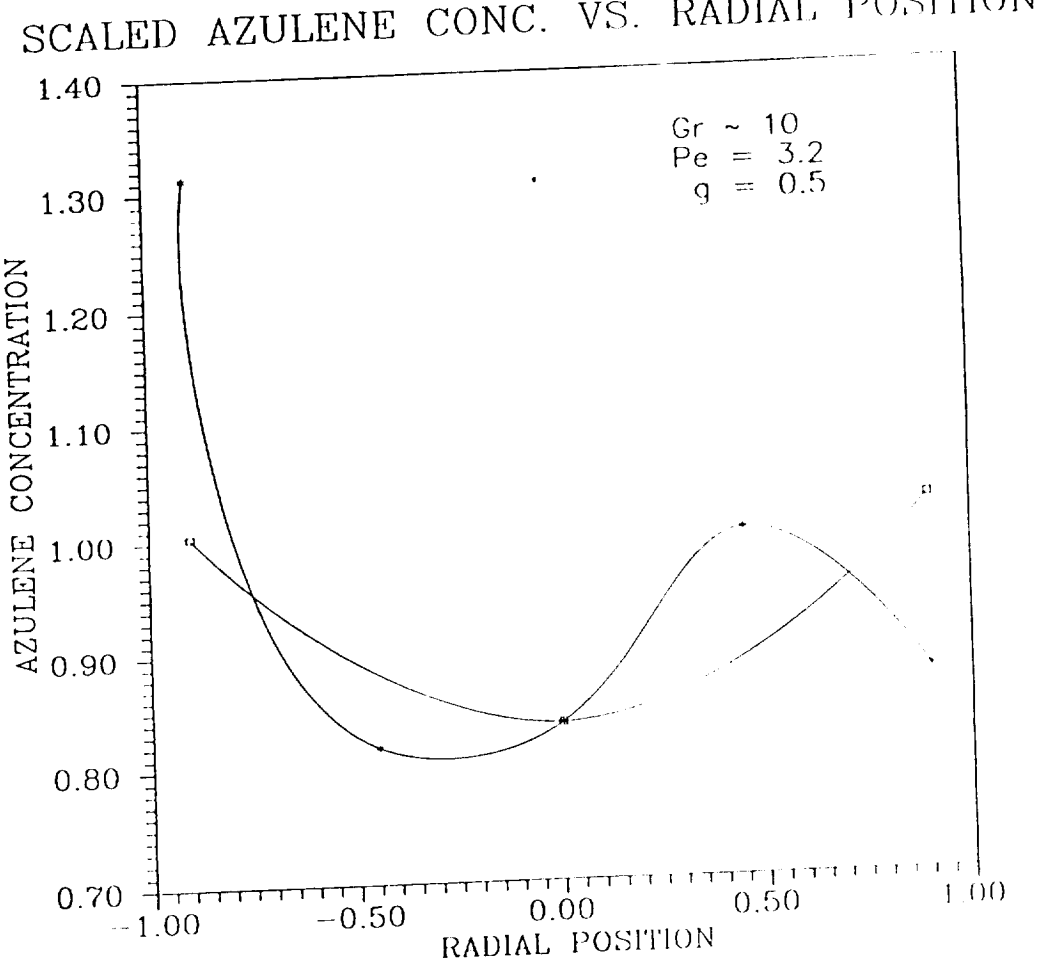

Figure 5.28: Radial concentration profile for a stabilized condition measured along two diameters. The radial concentration of azulene was measured at five points along one diameter and then at two points along another diameter perpendicular to the first.

described by three points, $R = 1$ refers to the front of the crystal.

Figure 5.29 shows the radial composition profile for a crystal grown at a higher growth rate of 5.23 mm/hr Pe = 5.6. (Note that in these experiments the Peclet number equals the growth rate in mm/hr times 1.0726 hr/mm.) The radial concentration profile of azulene was concave and appeared to be more symmetrical than the previous cases. The measurements were taken at a crystal mass fraction of $g = 0.6$.

Figure 5.30 shows the results for another crystal that was grown at a rate that corresponded to Pe = 5.6. The radial concentration profile was measured along two perpendicular diameters at approximately the same mass fraction as the crystal described in Figure 5.29. Along both diameters the segregation and asymmetry of the concentration profile were much greater for this crystal than for that in Figure 5.29, even though both crystals were grown under the same conditions.

An attempt was made to improve the radial homogeneity of the crystal by slowly rotating the ampoule at 2/3 rpm. The results are shown in Figure 5.31. The radial homogeneity did not improve. In fact, it became slightly worse. Both the radial segregation and the asymmetry of the concentration profile increased.

Figures 5.32 and 5.33 show the results for a crystal that was grown at a rate corresponding to $Pe = 7.4$. The figures each show two perpendicular radial concentration profiles in the same crystal but at different axial locations. Figure 5.32 shows the results at the axial location that corresponded to $g = 0.2$. Along both diameters the concentration profile was convex. Unlike the crystals described above, the two perpendicular profiles were similar in shape. The segregation and the asymmetry were greater along the diameter described by five points.

The same results were obtained when the radial concentration profile was measured farther down the crystal at $g = 0.5$, Figure 5.33. The shapes of the curves in Figures 5.33 and 5.32 are very similar. The curves that consist of three points are concave and symmetric, while the curves that consist of five points are concave and more asymmetric.

The segregation results along the length of this crystal proved to be reproducible. The same results were obtained again when a crystal was grown under the same conditions,

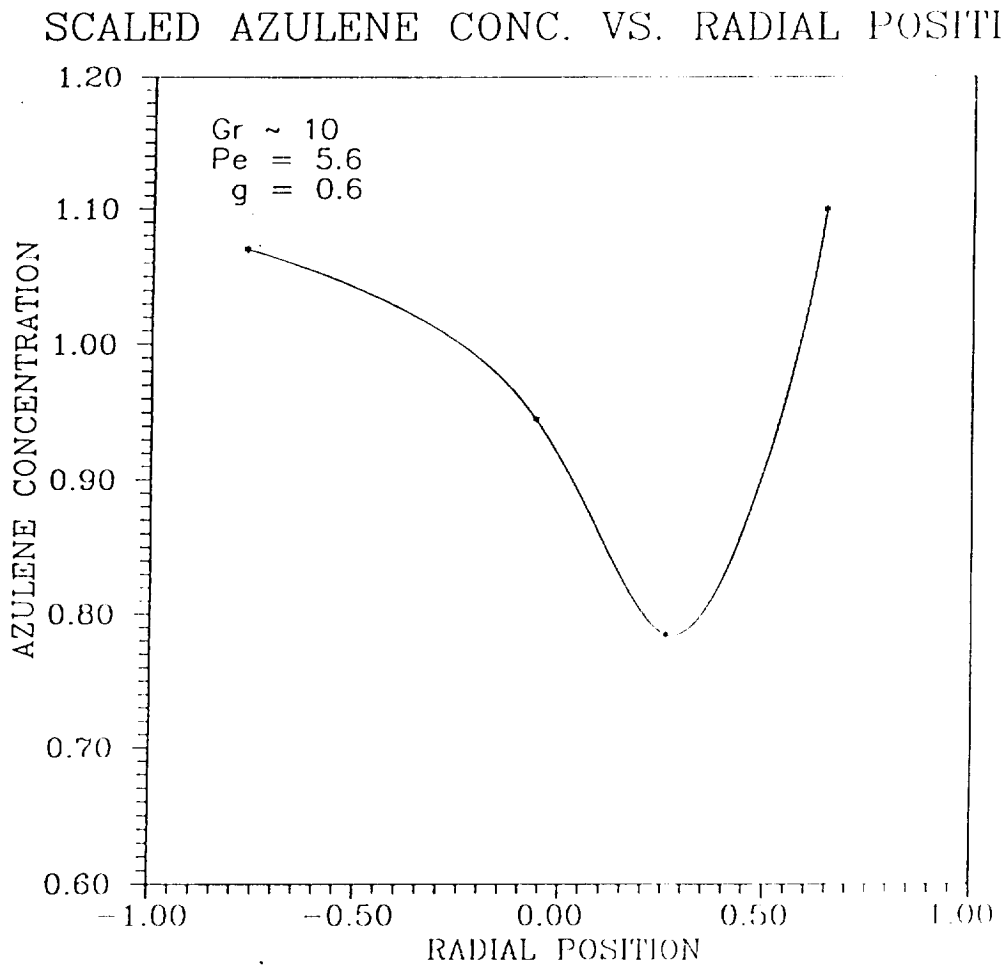

Figure 5.29: Radial concentration profile for $Pe = 5.6$ and $g = 0.6$.

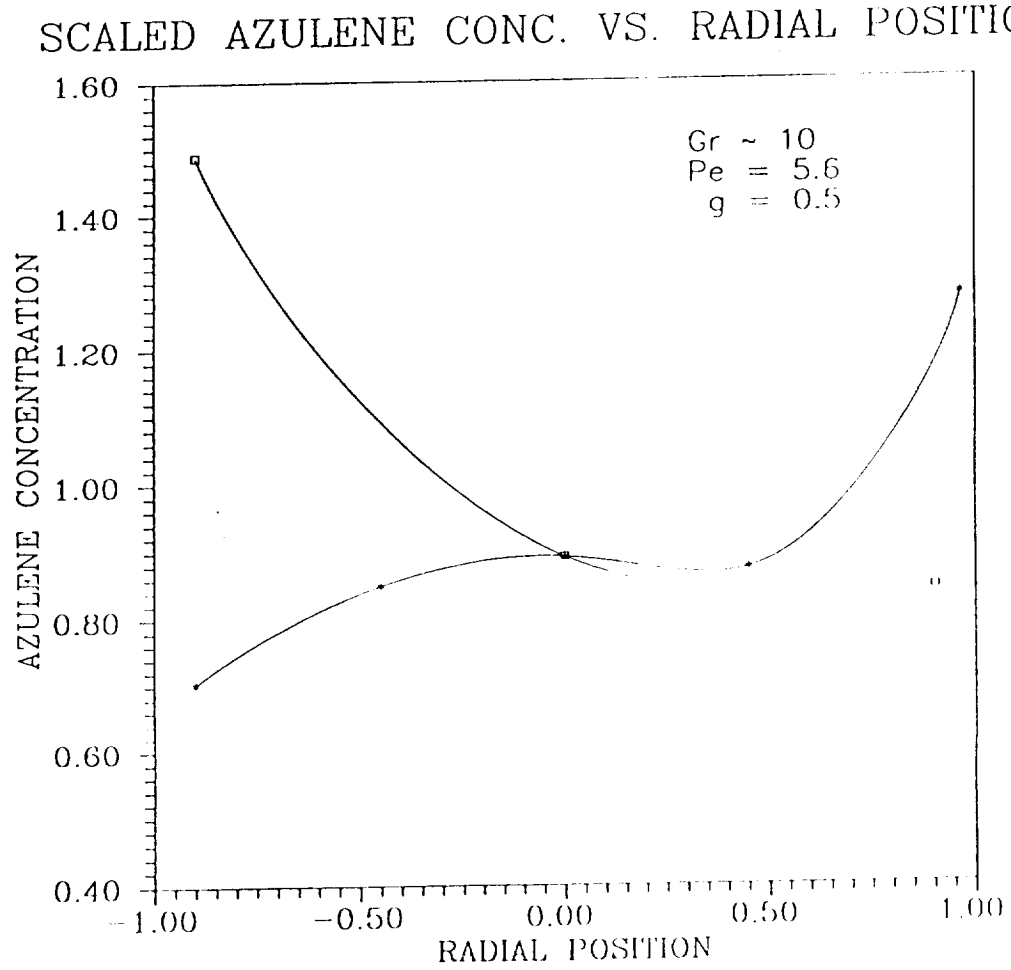

Figure 5.30: The concentration was measured along two perpendicular diameters at the axial position that corresponded to $g = 0.5$.

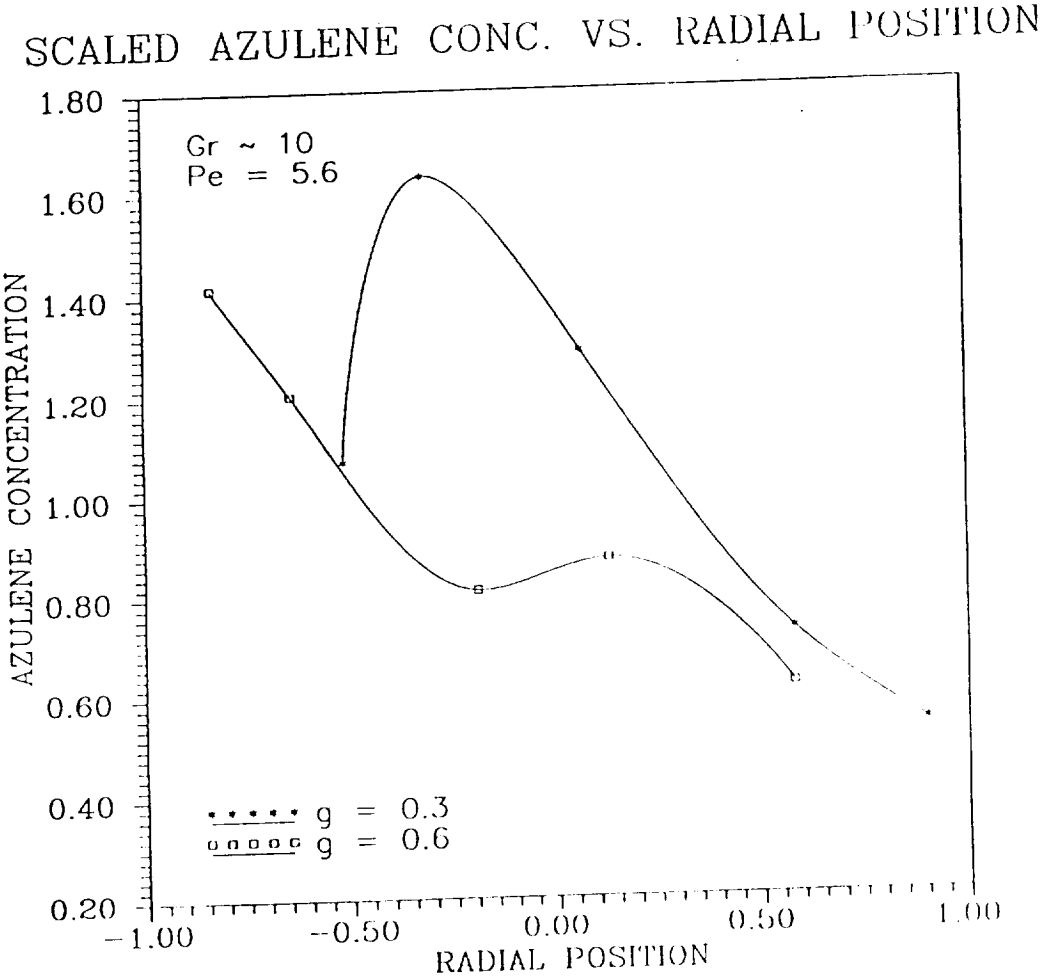

Figure 5.31: Radial concentration profile when the ampoule was rotated at 2/3 rpm during growth. The concentration was measured at two different axial locations.

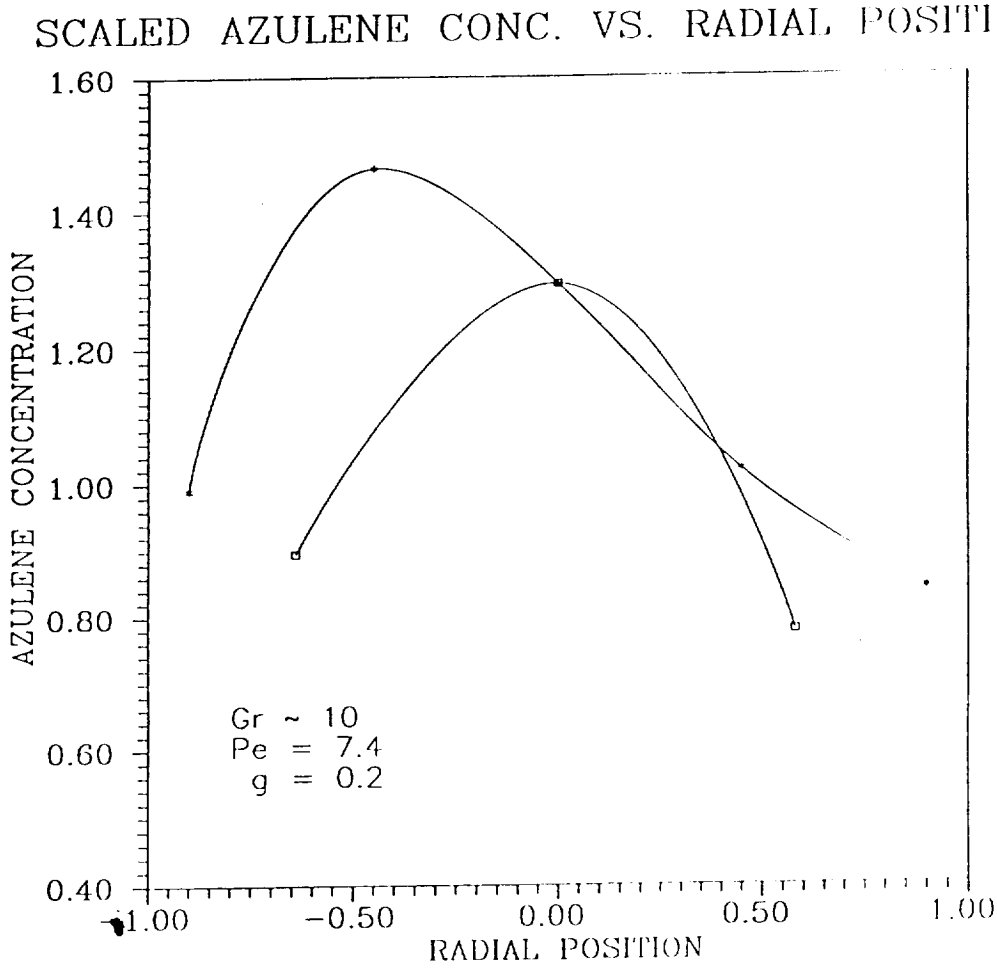

Figure 5.32: Radial concentration profile at $g = 0.2$ when the crystal was grown at a dimensionless rate $Pe = 7.4$. The concentration was measured along two perpendicular diameters.

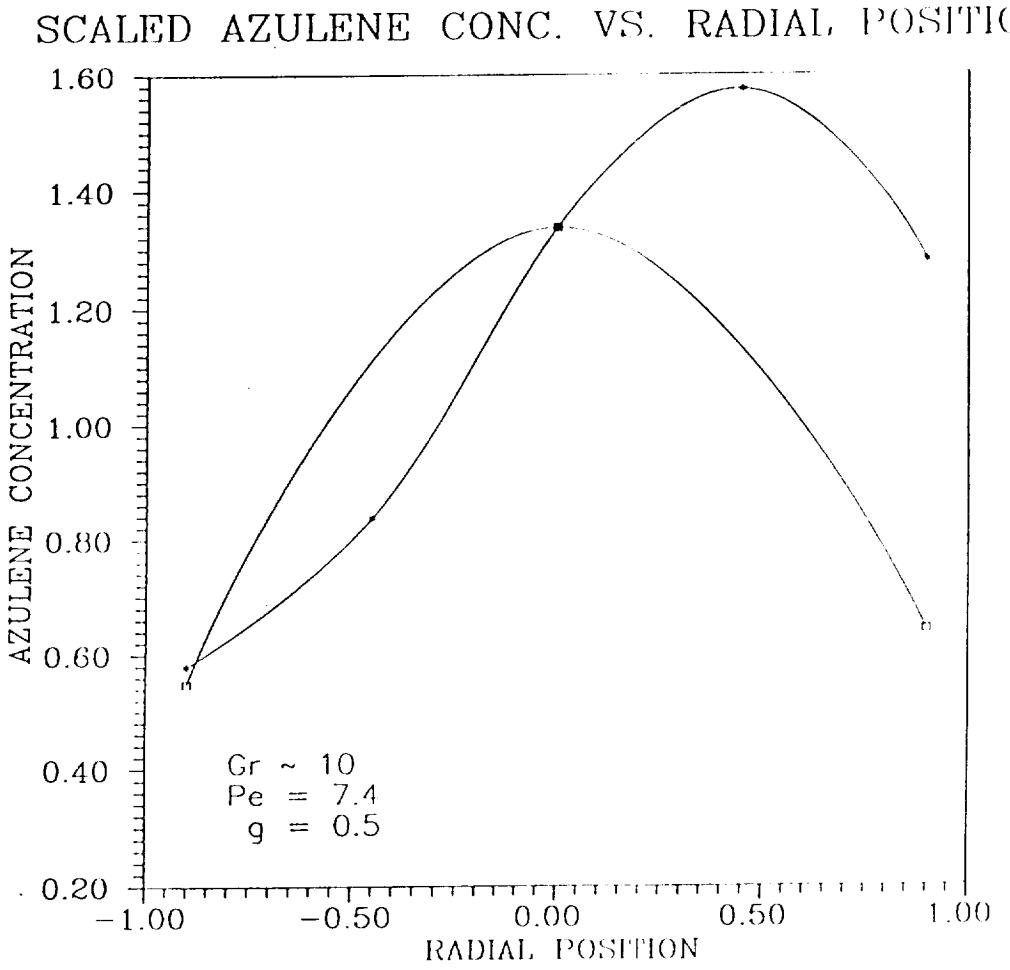

Figure 5.33: Radial concentration profile at $g = 0.5$ when the crystal was grown at a dimensionless rate $Pe = 7.4$. This is the same crystal as described in Figure 5.32. The concentration was measured along two perpendicular diameters.

$Pe = 7.4$. These results are shown in Figure 5.34. The concentration profiles were measured along two diameters at $g = 0.5$. The segregation was the same along both diameters, but the curve consisting of three points was more asymmetric. The segregation and the asymmetry for this crystal were nearly the same as that obtained in the previously described case.

Figure 5.35 shows radial concentration profiles for a crystal grown at 7.96 mm/hr ($Pe = 8.6$). The profiles are given for two different axial locations along the same crystal. In both cases the concentration profiles were convex and fairly symmetric.

Figures 5.36 and 5.37 show the radial concentration profiles for a crystal grown under the same conditions as that described in Figure 5.35. Shown in Figure 5.36 is the concentration profile measured along two perpendicular diameters at $g = 0.2$. Both curves have the same shape and are very symmetric. Figure 5.37 shows the radial concentration profiles farther down the same crystal at $g = 0.5$. The radial concentration profile for this case was very symmetric in one direction, but skewed in the other. In this way this result is similar to that shown in Figures 5.32 and 5.33 for $Pe = 7.4$.

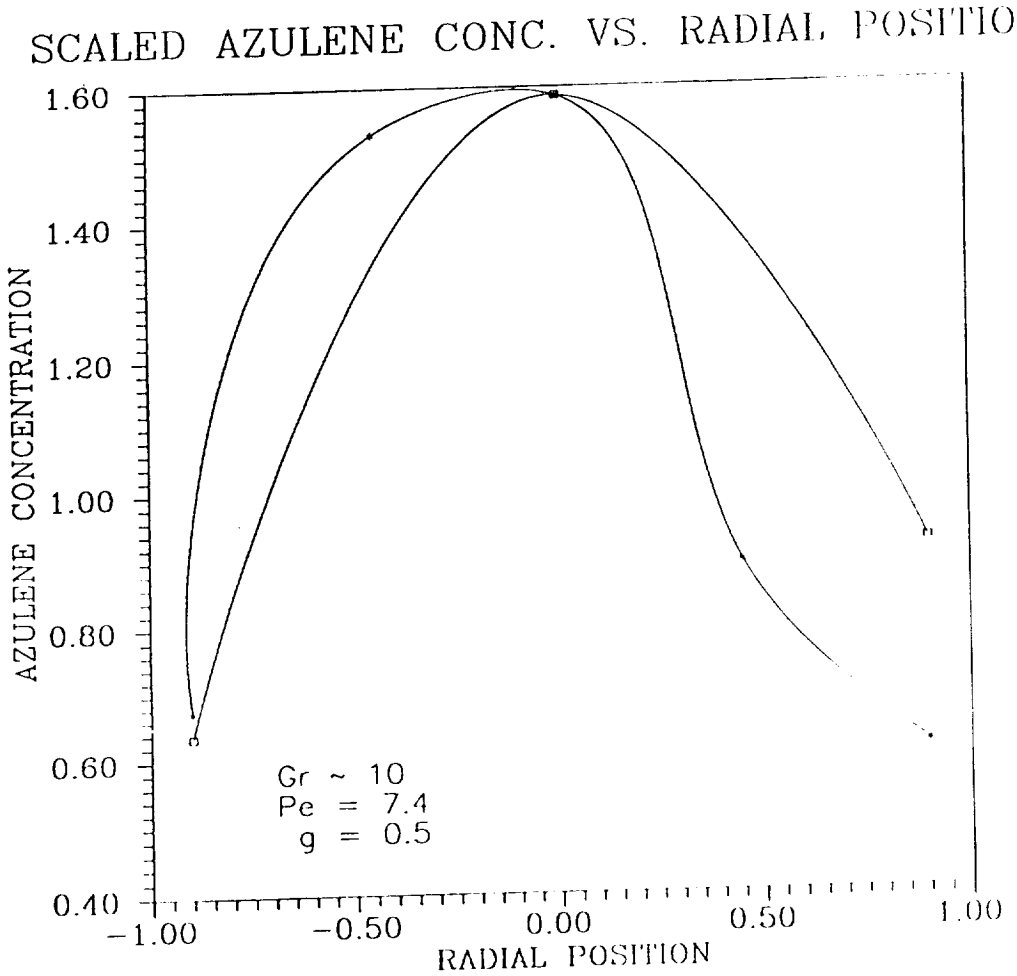

Figure 5.34: Radial concentration profile at $g = 0.5$ for $Pe = 7.4$. This was the same growth conditions as for the crystal described in Figure 5.33. The concentration was measured along two perpendicular diameters.

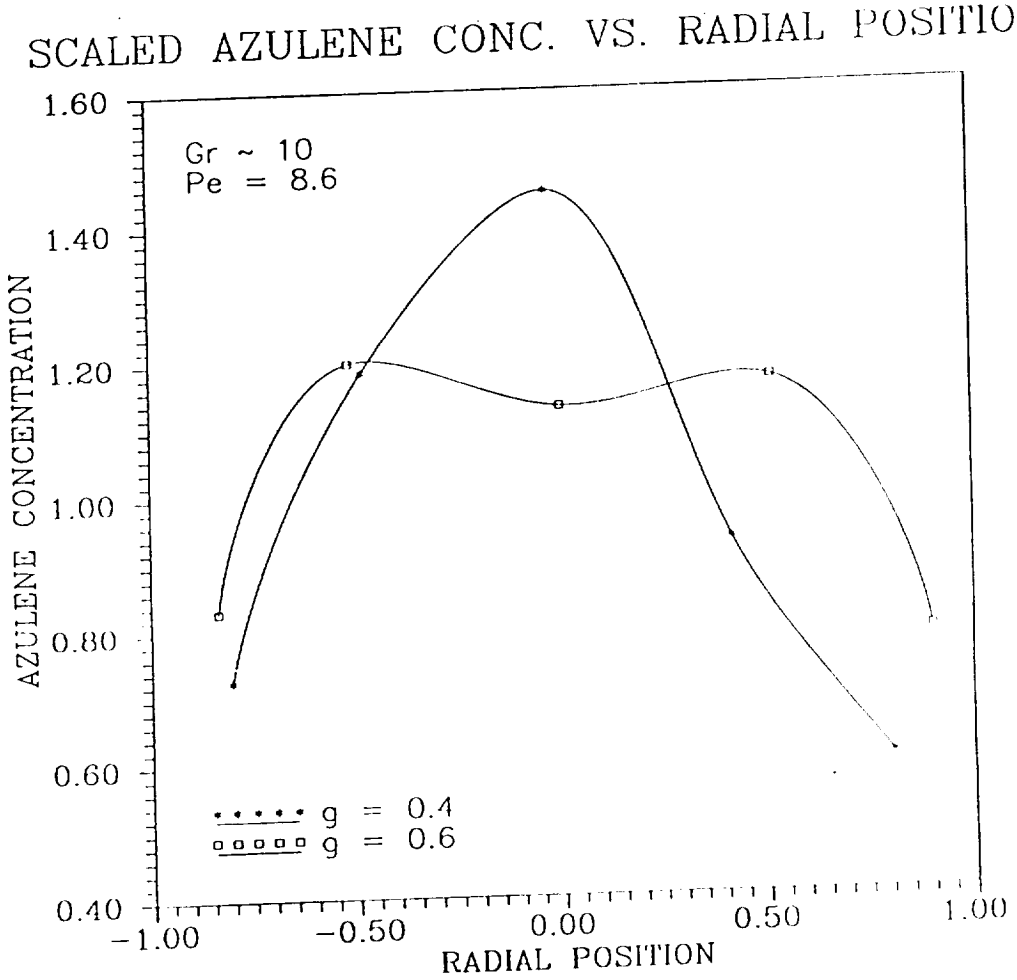

Figure 5.35: Radial concentration profile when the crystal was grown at a rate that corresponded to $Pe = 8.6$.

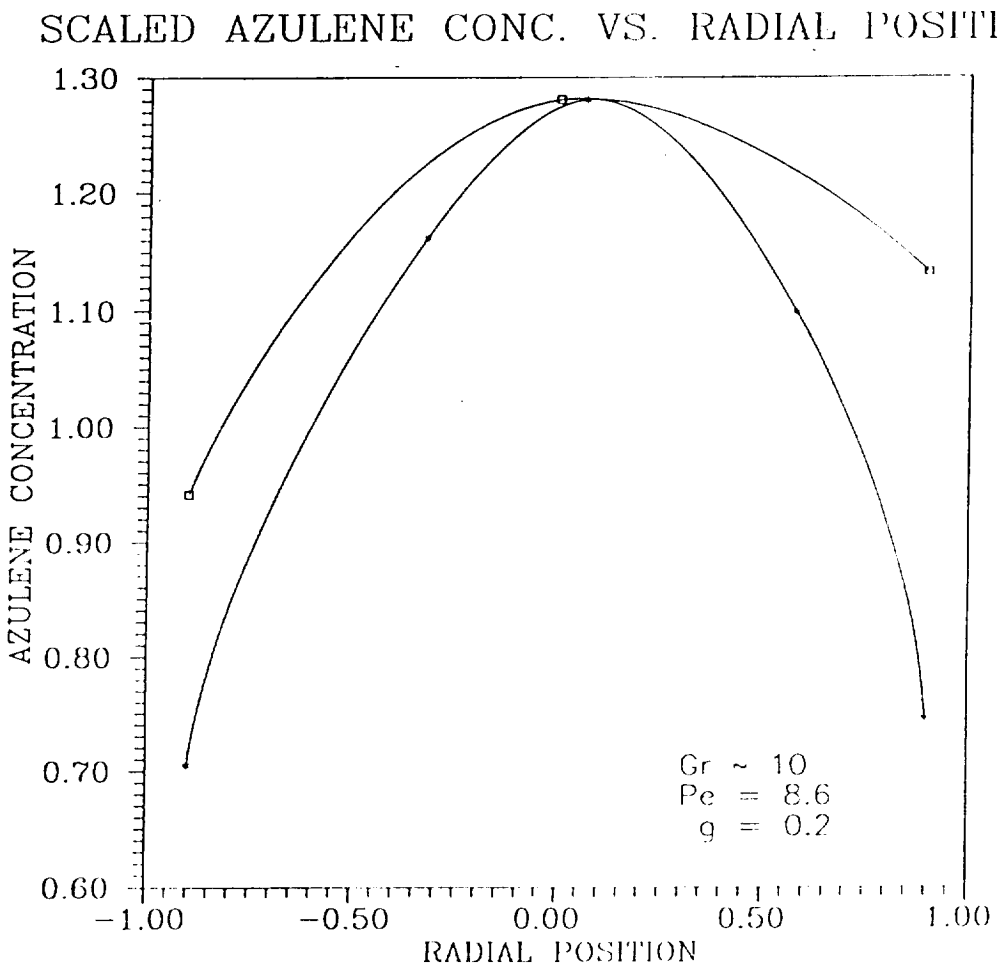

Figure 5.36: Radial concentration profile at $g = 0.2$ when the crystal was grown at a rate that corresponded to $Pe = 8.6$. The concentration was measured along two perpendicular diameters.

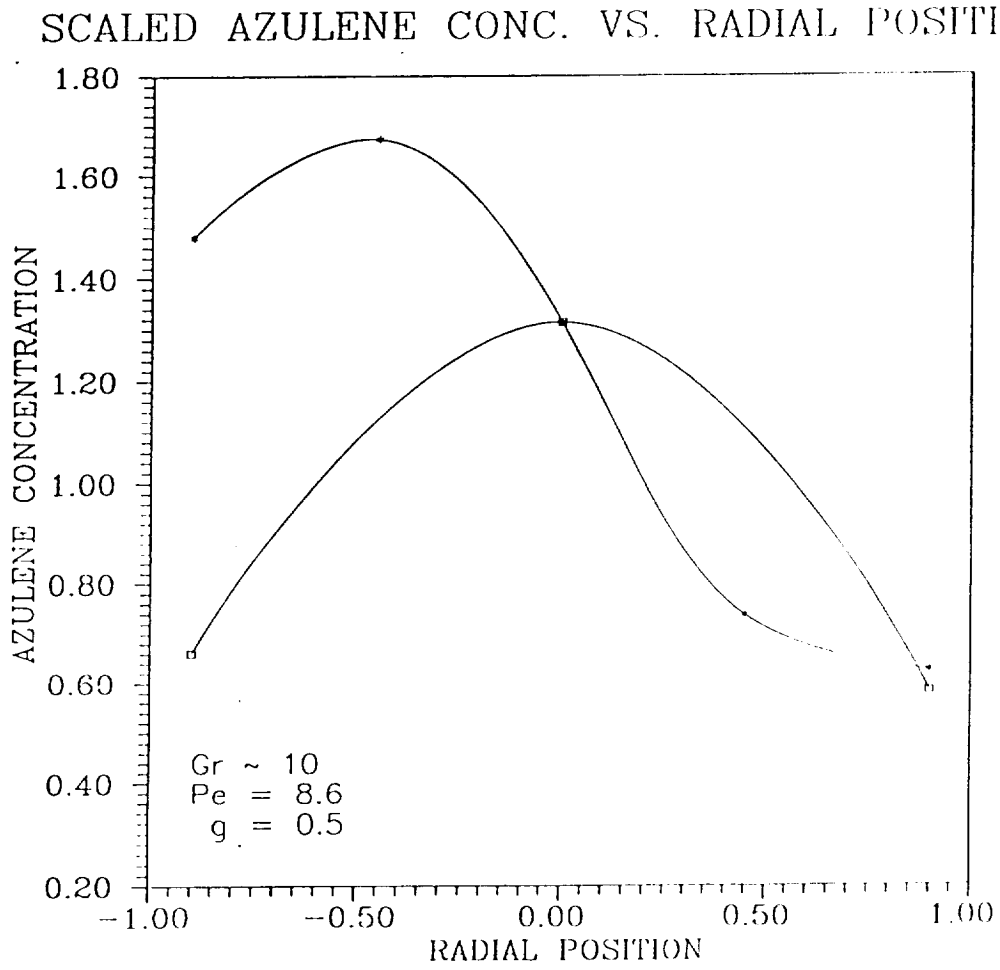

Figure 5.37: Radial concentration profile at $g = 0.5$ when the crystal was grown at a rate that corresponded to $Pe = 8.6$. This is the same crystal as described in Figure 5.36. The concentration was measured along two perpendicular diameters.

5.4 Radial Segregation – Destabilized Conditions

Figures 5.38 to 5.40 show three axial temperature profiles that are characteristic of a destabilized condition. The maximum in temperature near the interface was controlled by the power supplied to the booster heater. When the power to the booster was increased, the maximum in temperature above the melt became greater and broader. In all cases the axial temperature profiles for a destabilized condition had nearly the same shape. For this reason, only Figures 5.38 to 5.40 are given as representative temperature profiles.

The characteristic temperature difference used to calculate the Grashof number was the maximum temperature in the melt minus the temperature at the top of the melt. In order to provide maximize reproducibility in the determination of the Grashof number, the characteristic temperature difference was always measured when the top of the melt was 10.5 cm above the center of the insulation zone. This corresponded to the point during solidification when the mass fraction of the material solidified was 0.2.

The radial concentration profile for a destabilized condition associated with $Gr = 55600$ and $Pe = 3.2$ is shown in Figure 5.41. The radial homogeneity for this crystal was very good, the segregation was only 5%. The radial concentration profile was also very symmetric.

Figure 5.42 shows the radial concentration profiles for a run when the power to the booster heater was increased to yield $Gr = 88500$. Figure 5.42 shows two perpendicular concentration profiles that were measured at a mass fraction of 0.2. This was the only crystal in which a discontinuity in radial composition was observed. Six points had nearly the same azulene concentration, but the concentration in the center of the crystal was larger by nearly an order of magnitude. Perhaps the anomalous results were caused by the constriction in the ampoule used to promote single grain selection.

The mass fraction $g = 0.2$ corresponded to the point during growth when the melt/solid interface emerged from the constriction and entered the main body of the ampoule. Perhaps the transient growth conditions at this point in the growth process caused the interface to be flat near the wall but very concave near the center. Maybe the segregation was associated with a grain boundary, although no boundary was visible at that point. In any case, an order of magnitude jump in concentration between two points was never observed in any

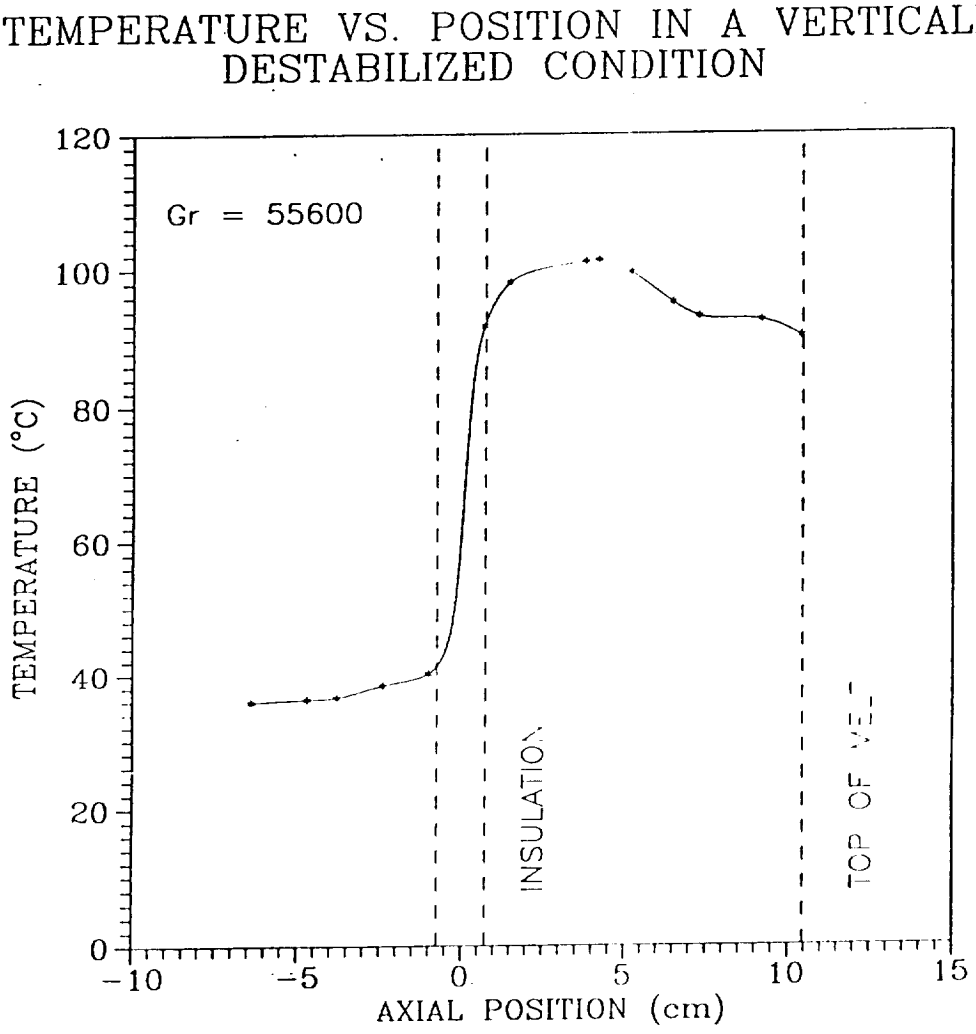

Figure 5.38: Axial temperature profile for a destabilized condition with Gr = 55600.

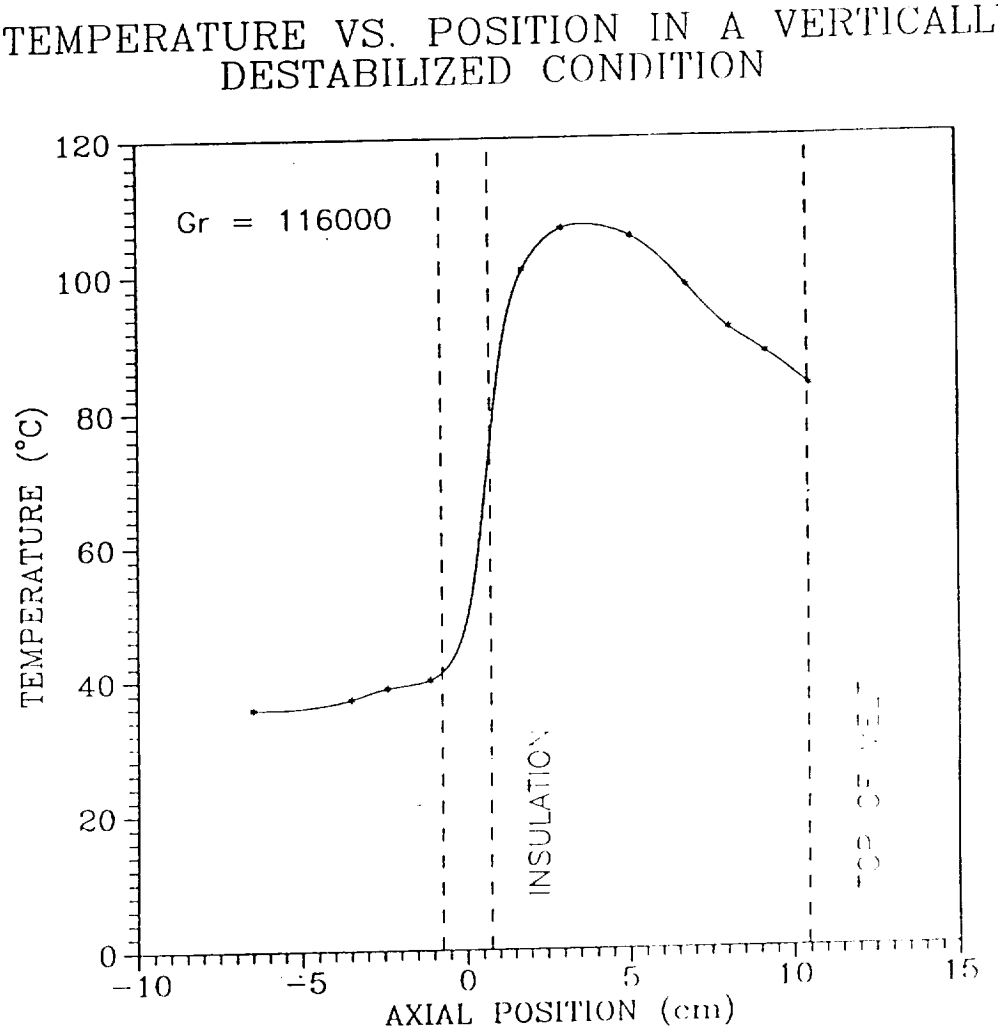

Figure 5.39: Axial temperature profile for a destabilized condition with Gr = 116000.

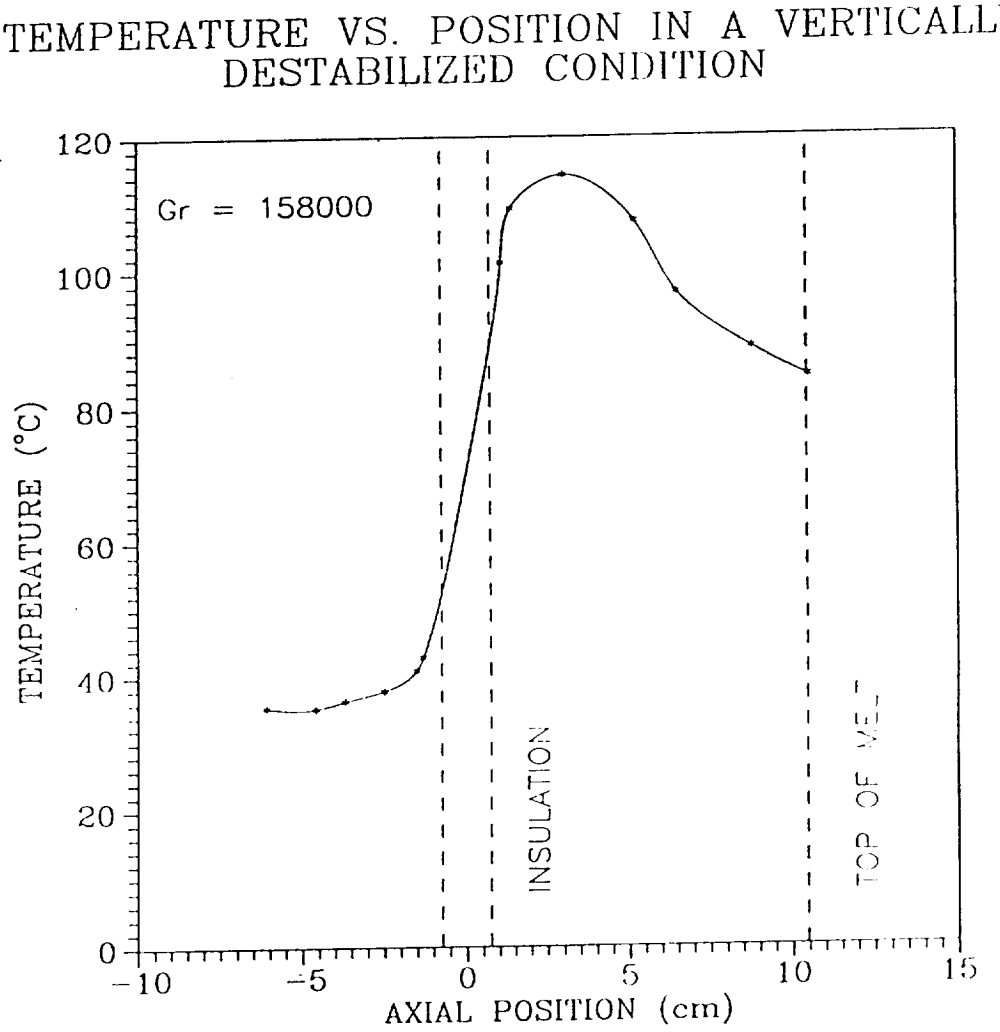

Figure 5.40: Axial temperature profile for a destabilized condition with Gr = 158000.

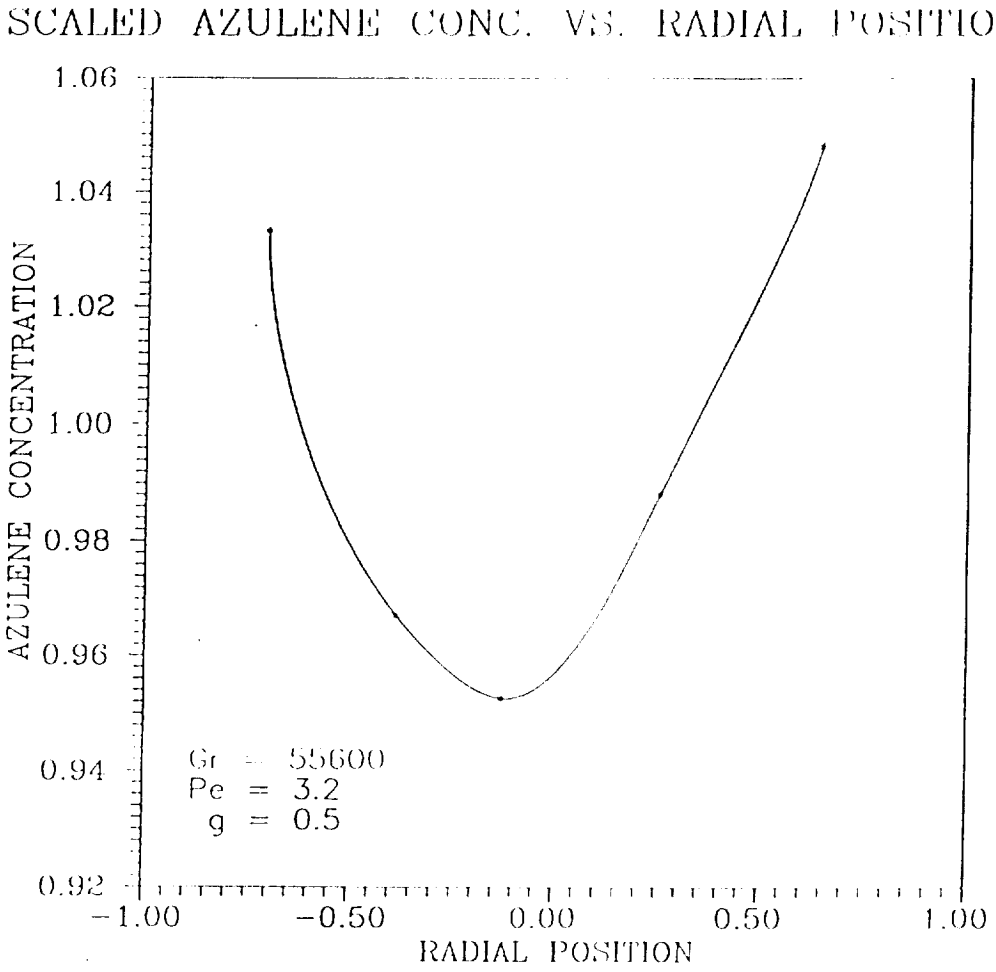

Figure 5.41: Radial concentration profile for a destabilized condition associated with $Gr = 55600$ and $Pe = 3.2$. Figure 5.38 is the temperature profile associated with this run.

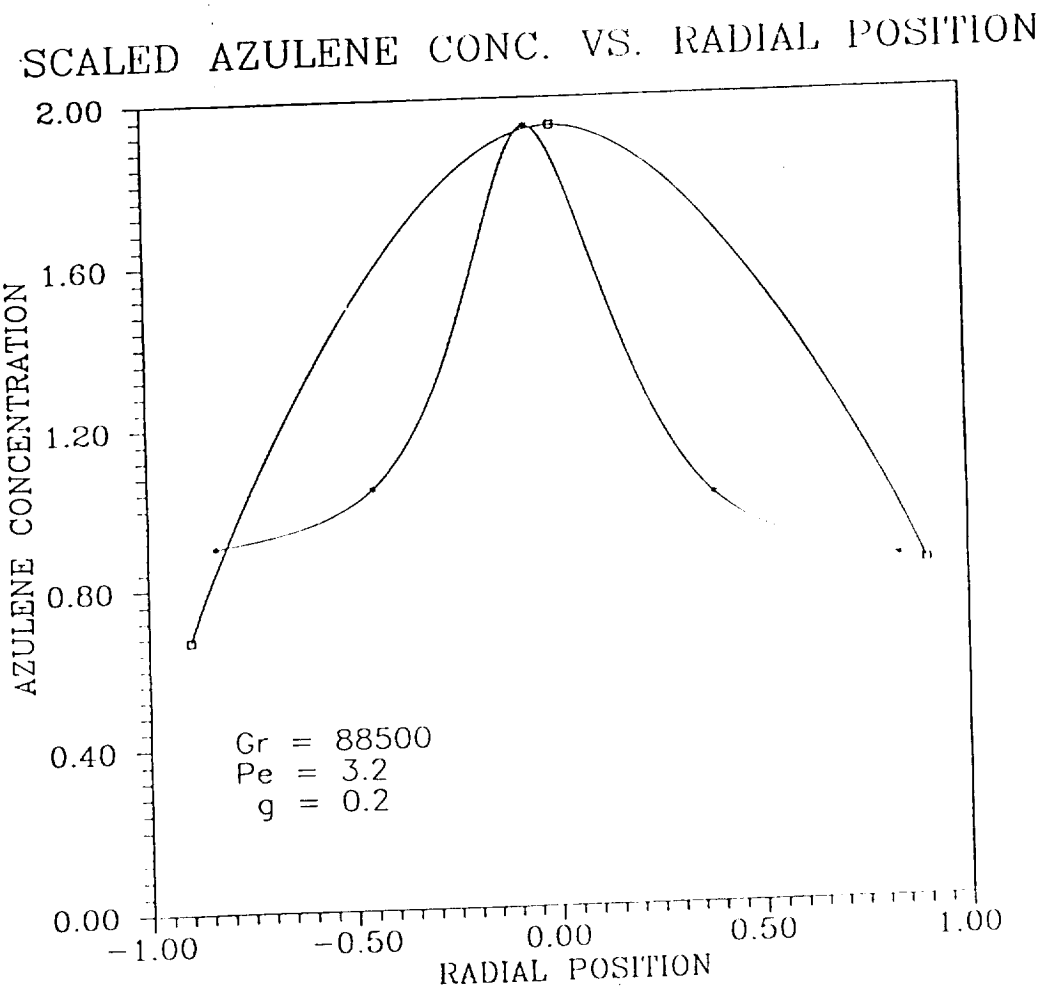

Figure 5.42: Radial concentration profile for a destabilized condition at $g = 0.2$ associated with $Gr = 88500$, $Pe = 3.2$. The composition was measured along two perpendicular diameters.

other crystal.

Figure 5.43 shows the radial concentration profile when this crystal was analyzed at $g = 0.5$. In this case little segregation was observed (4%) and the concentration profile was very symmetric. These results are similar to those shown in Figure 5.41 (i.e. growth condition $Gr = 55600$, $Pe = 3.2$, concentration measured at $g = 0.5$; 5% segregation observed).

Figure 5.44 shows the radial concentration profile at the same growth rate, $Pe = 3.2$, and a higher Grashof number, $Gr = 116000$. Little segregation was observed, 4%. The results shown in Figures 5.41, 5.42, and 5.44 indicate that convection in the destabilized condition (with $Pe = 3.2$) was sufficient to cause the crystals to have very little radial segregation. In fact the amount of segregation might even be called negligible since it was of the same order of magnitude as the error in the technique used to analyze the crystals.

Figure 5.45 shows the radial concentration profile in a destabilized condition with $Gr = 39600$, at a growth rate associated with a Peclet number of 5.6. Significant segregation was measured in this crystal (17%). The concentration profile was also asymmetric. Less radial segregation was observed in another crystal grown at the same rate but with a higher Grashof number, Figure 5.46. The radial concentration profile was measured along two perpendicular diameters at a mass fraction solidified $g = 0.5$. The shape of the profiles were similar to that observed in several stabilized cases, i.e. skewed sinusoidally along one diameter and convex along the other. The profiles were also convex. However, in the destabilized case shown in Figure 5.46 the radial segregation was much less, 7%.

Figures 5.47 and 5.48 show the radial concentration profiles for a crystal that was grown with a dimensionless rate $Pe = 7.4$. Concentration profiles were obtained along two perpendicular diameters at two different axial locations in the crystal. Figure 5.47 shows the results for $Gr = 76200$, $Pe = 7.4$, as measured at $g = 0.2$. For this crystal, the concentration profile was symmetric although the segregation was large (45% in one direction and 25% in the other). Figure 5.48 shows the radial concentration profile measured farther down the crystal at $g = 0.5$. At this location the radial segregation was reduced but the asymmetry had increased. Four concentration profiles were measured for this crystal. A

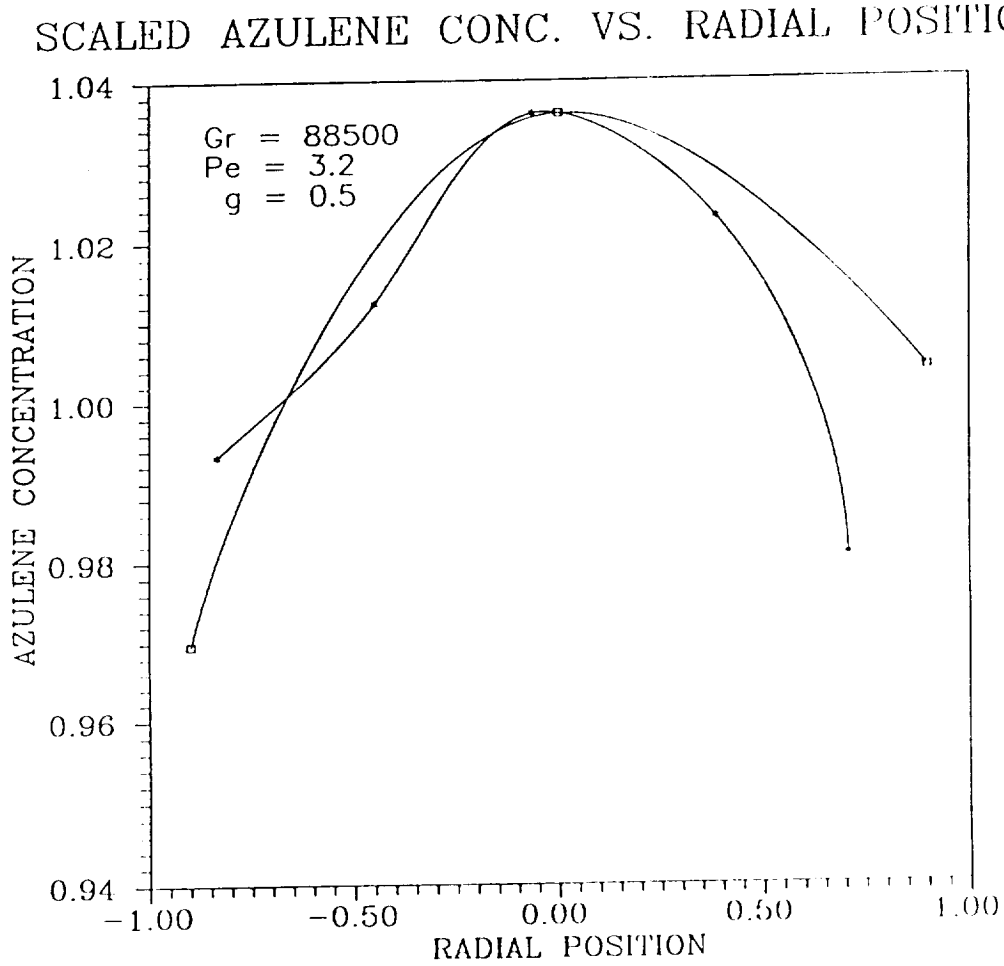

Figure 5.43: Radial concentration profile for a destabilized condition at $g = 0.5$ associated with $Gr = 88500$, $Pe = 3.2$. The composition was measured along two perpendicular diameters.

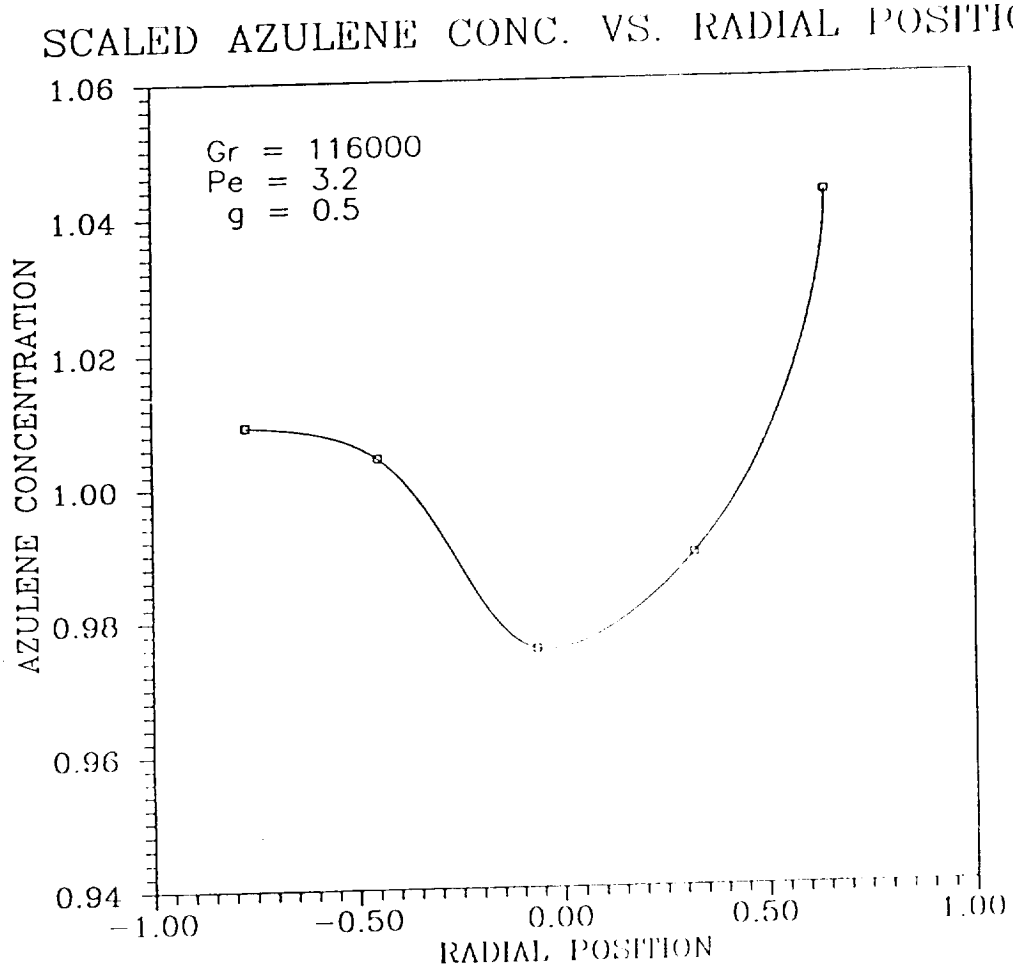

Figure 5.44: Radial concentration profile for a destabilized condition associated with Gr = 116000, Pe = 3.2. (Figure 5.39 is the temperature profile associated with this run.)

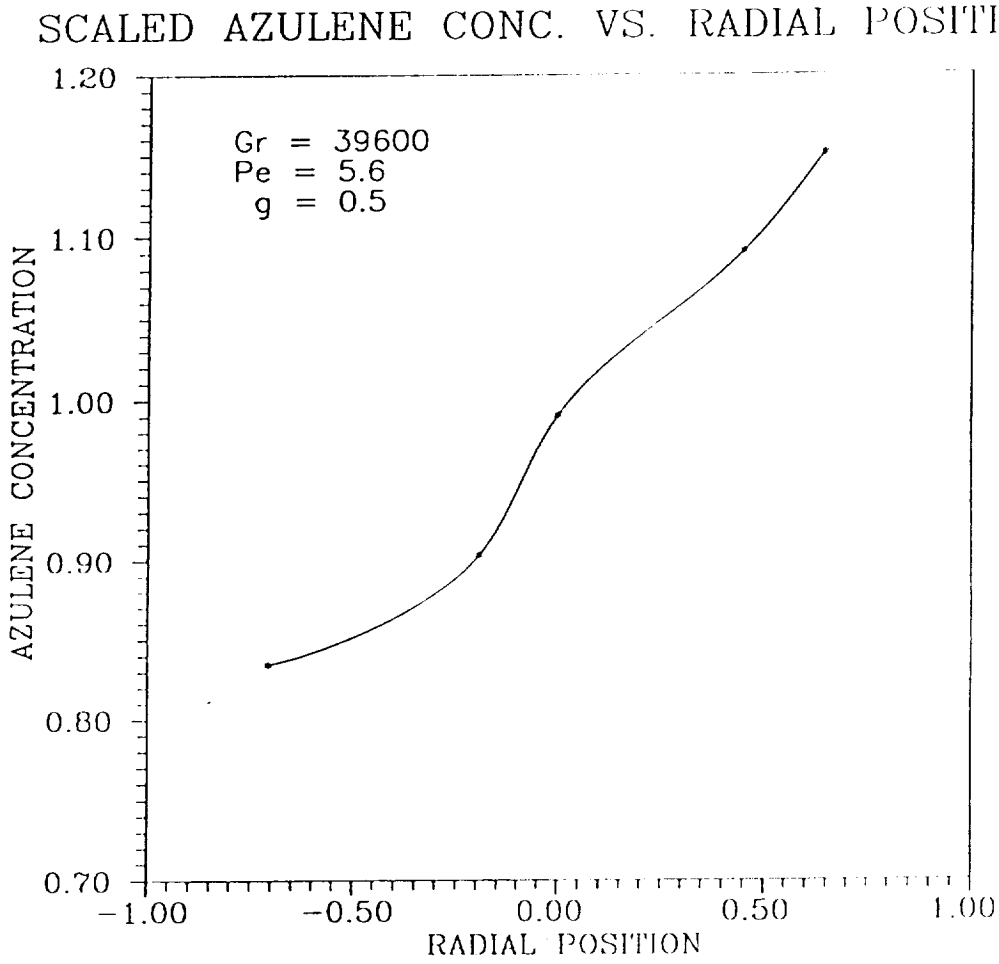

Figure 5.45: Radial concentration profile for a destabilized condition associated with Gr = 39600 and $Pe = 5.6$.

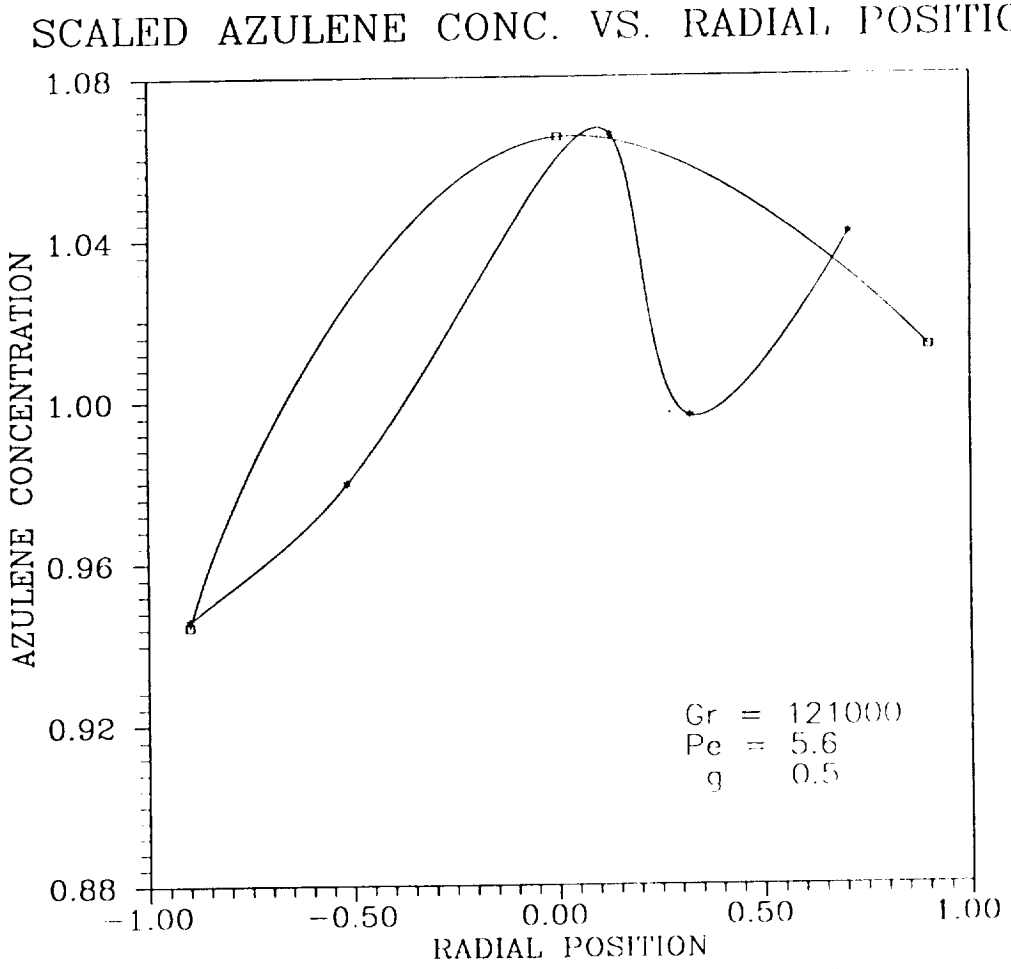

Figure 5.46: Radial concentration profile for a destabilized condition associated with Gr = 121000 and Pe = 5.6.

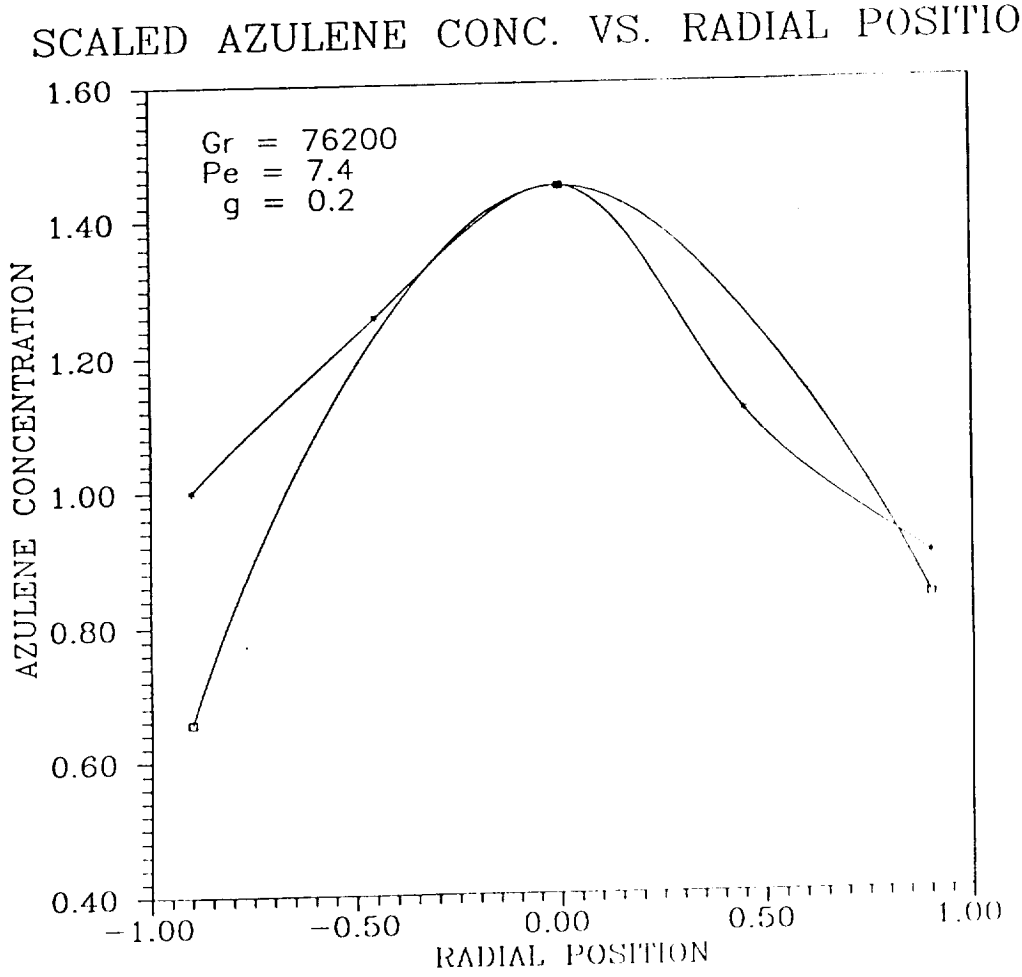

Figure 5.47: Radial concentration profile for a destabilized condition at $g = 0.2$ associated with $Gr = 76200$, $Pe = 7.4$. The composition was measured along two perpendicular diameters.

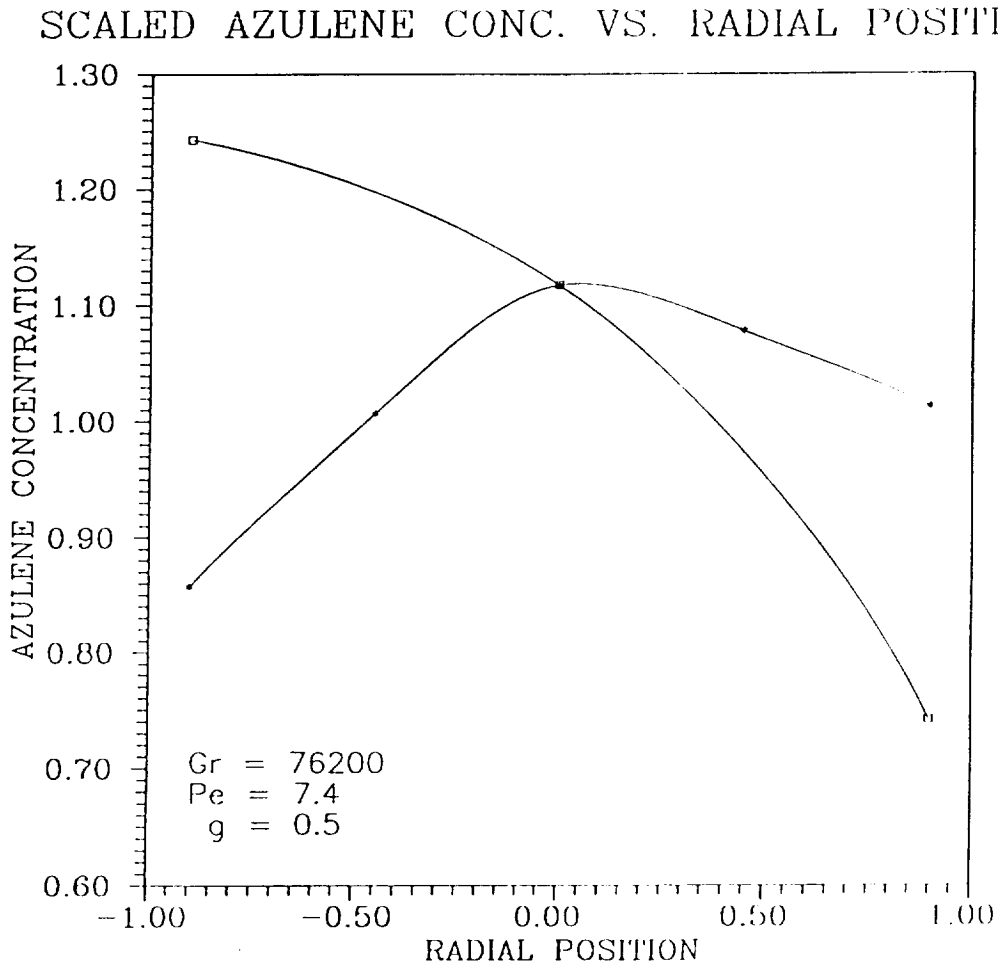

Figure 5.48: Radial concentration profile at $g = 0.5$ for a destabilized condition associated with $Gr = 76200$, $Pe = 7.4$. The composition was measured along two perpendicular diameters. The results are for the same crystal as shown in Figure 5.47.

mean segregation of 28% was observed. Figure 5.49 shows that when the Grashof number was increased to 138000 for this growth rate the mean segregation was reduced to 13%.

Figures 5.50 to 5.53 show the results for a dimensionless growth rate of 8.6 with various Grashof numbers. In Figure 5.50 the results are shown for $Gr = 76700$. The concentration profile was very asymmetric and the segregation was 21%.

Figures 5.51 and 5.52 show the concentration profiles for a crystal grown with $Gr = 109000$ and $Pe = 8.6$. Figure 5.51 shows that the segregation was larger than that in the previous case, which was grown with a lower Grashof number. The segregation was large (47%), as was the asymmetry. Figure 5.52 shows the composition profile measured in the same crystal at $g = 0.5$. Again a large segregation of 50% was measured, although the profiles were more symmetrical. When the Grashof number was increased to 158000 a reduction in segregation was observed (to 15%). As shown in Figure 5.53, the segregation was less than the previous case but the profile was very asymmetric.

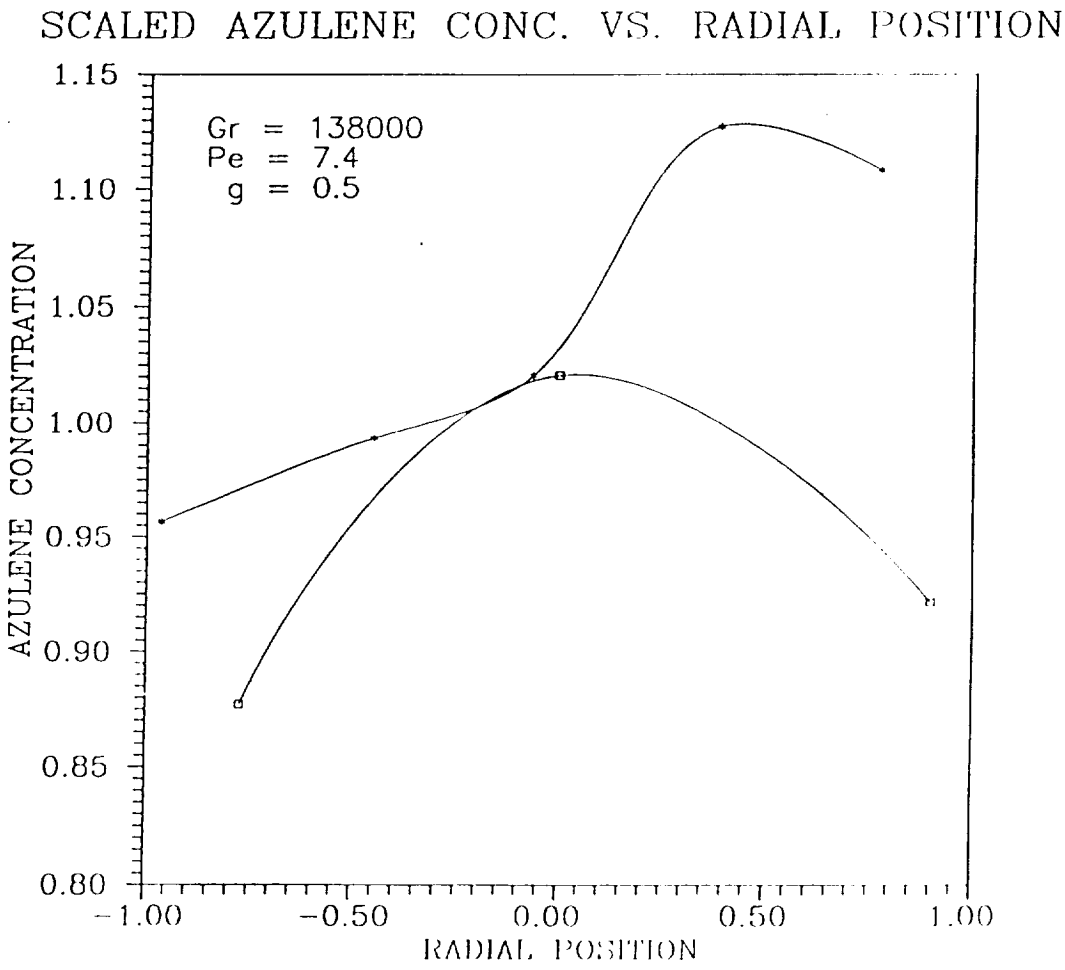

Figure 5.49: Radial concentration profile for a destabilized condition at $g = 0.5$ associated with $Gr = 138000$, $Pe = 7.4$. The composition was measured along two perpendicular diameters.

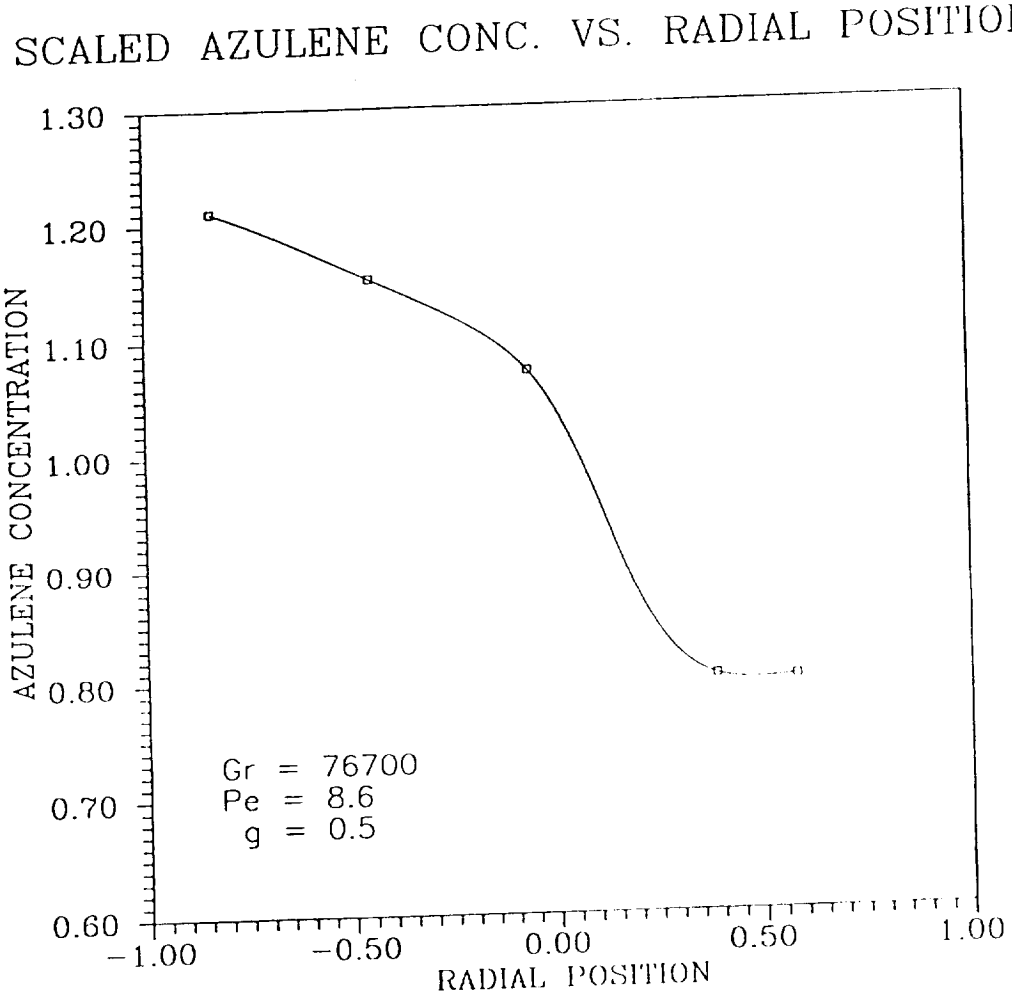

Figure 5.50: Radial concentration profile for a destabilized condition at $g = 0.5$ associated with $Gr = 76700$, $Pe = 8.6$. The composition was measured along two perpendicular diameters.

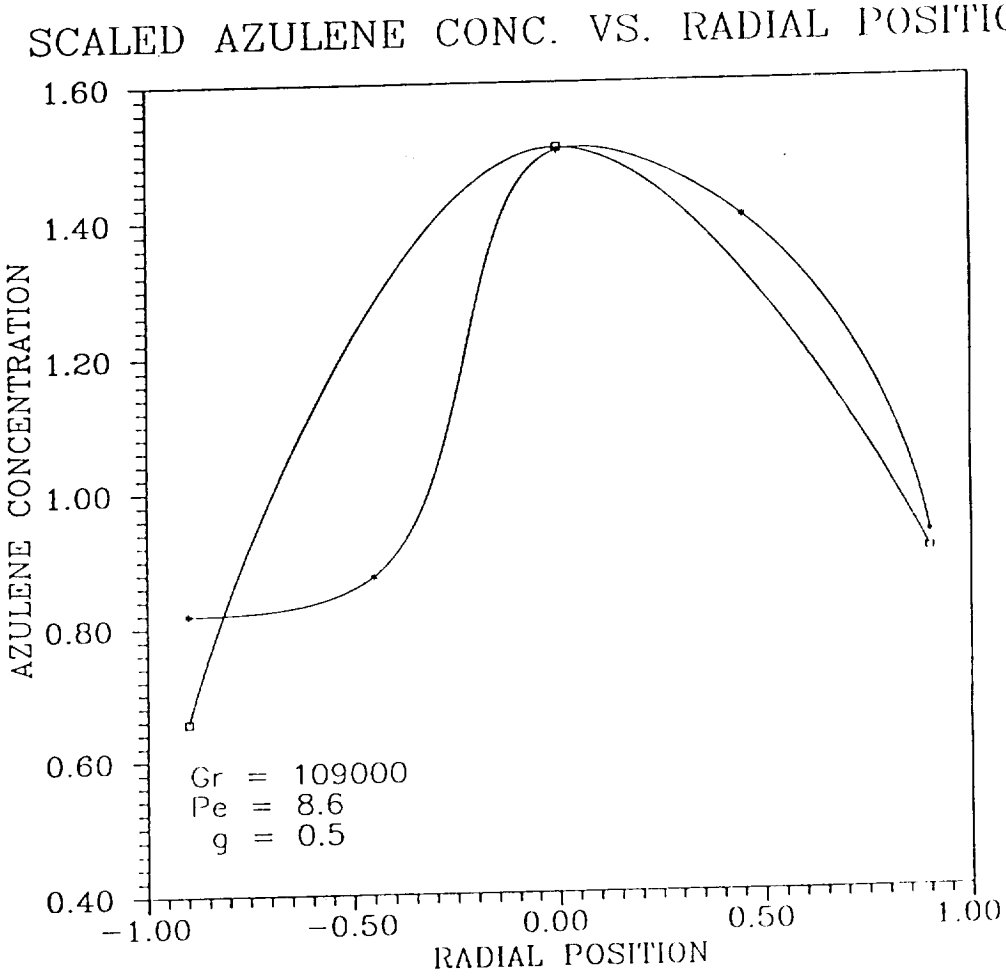

Figure 5.51: Radial concentration profile for a destabilized condition at $g = 0.2$ associated with $Gr = 109000$, $Pe = 8.6$.

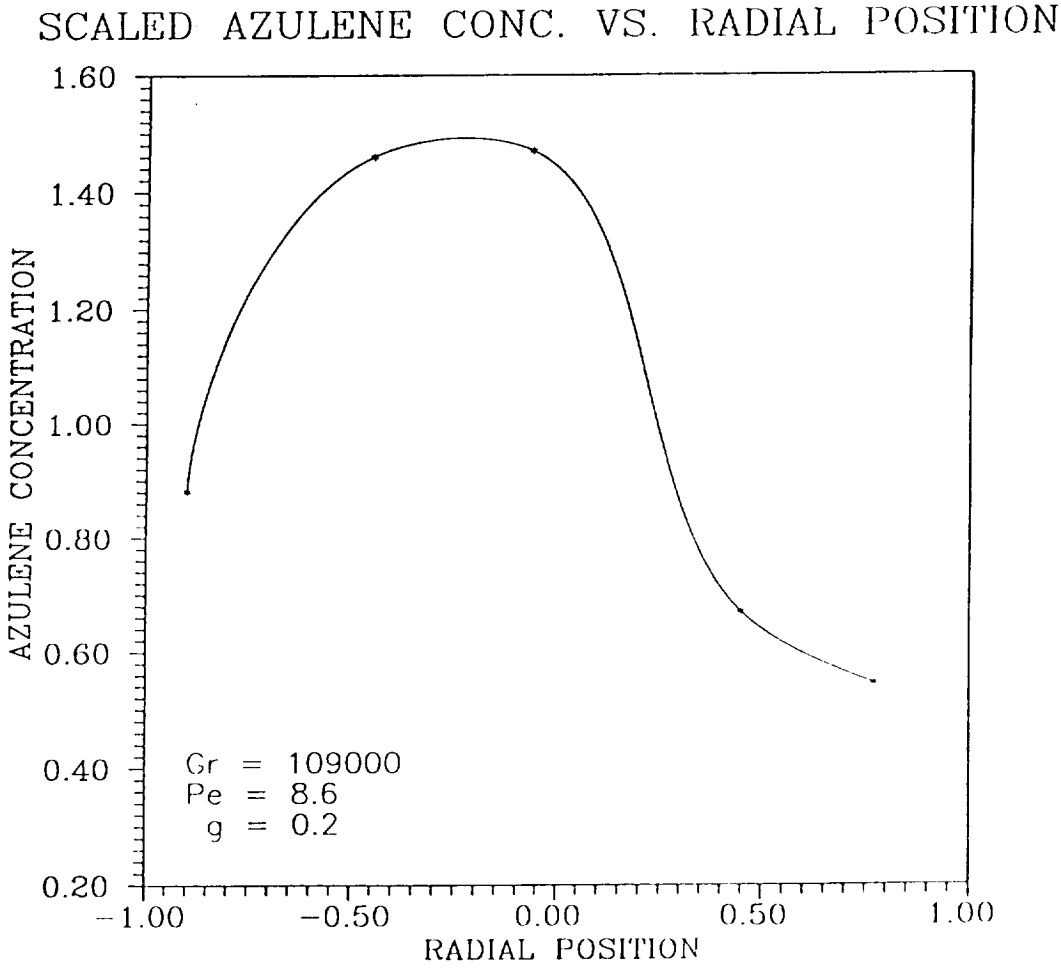

Figure 5.52: Radial concentration profile for a destabilized condition at $g = 0.5$ associated with $Gr = 109000$, $Pe = 8.6$. The composition was measured along two perpendicular diameters. The results are for the same crystal as shown in Figure 5.51.

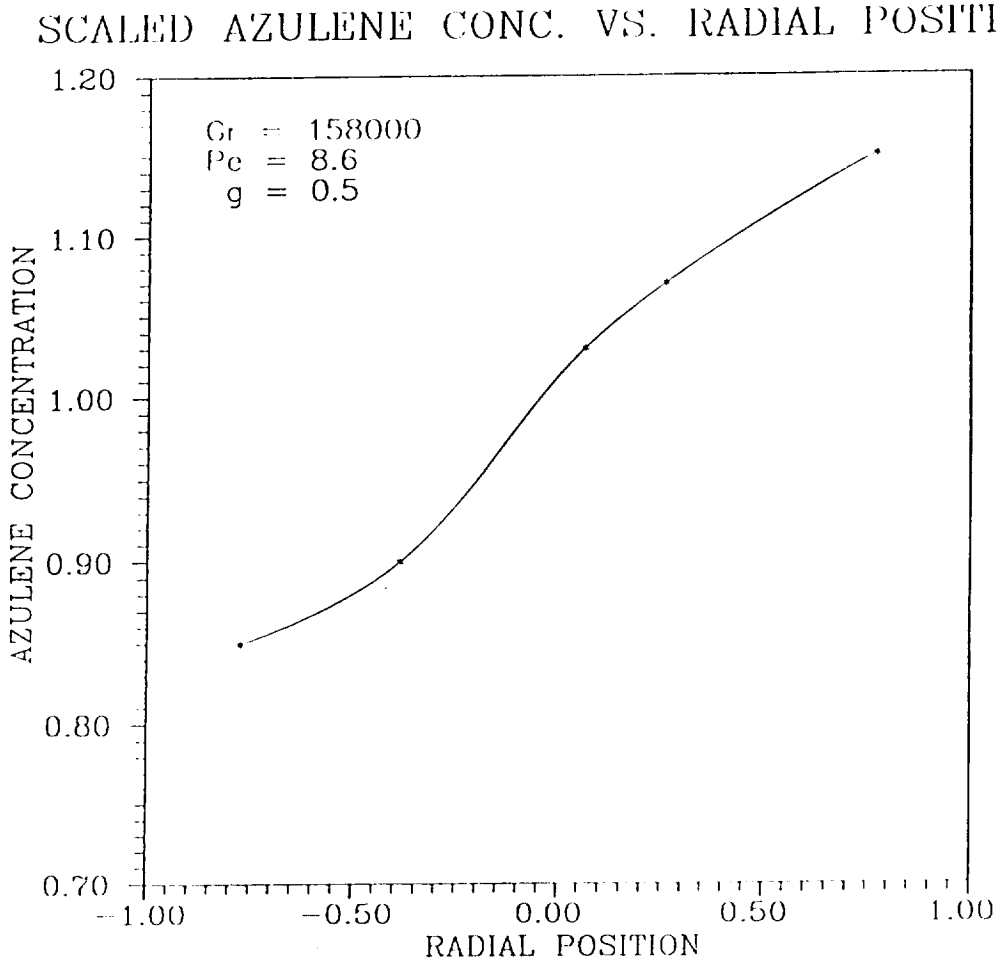

Figure 5.53: Radial concentration profile for a destabilized condition at $g = 0.5$ associated with $Gr = 158000$, $Pe = 8.6$. Figure 5.40 is the temperature profile associated with this run.

6 Discussion and Conclusions

6.1 Stabilized Conditions

The results for solidification under stabilized conditions are summarized in Tables 6.1 and 6.2. Table 6.1 lists the results for $Pe = 3.2$ and $Pe = 5.6$. Table 6.2 lists the results for $Pe = 7.4$ and $Pe = 8.6$. The following example shows how to read the tables: Crystal number 53 was grown with $Pe = 3.2$. (In stabilized conditions the Grashof number was always approximately equal to 10). The radial composition profile was measured at $g = 0.2$ and $g = 0.5$. The segregation was 13% and the asymmetry index was 0.13. At $g = 0.5$ two values are given for the segregation and the asymmetry index because two perpendicular radial concentration profiles were measured. For this and all other entries, the first line lists the results for the profile constructed using five points. The second line lists the results for the profile that consisted of three points.

Figure 6.1 summarizes graphically the results for stabilized conditions. It is a plot of all the measured segregation values versus dimensionless growth rate. (The runs where a deliberate asymmetry was created and the run where the ampoule was rotated were not included.) The error bars in the plot are the standard deviation of the segregation at each Peclet number. A second order polynomial was fitted to that data. The data suggest that there might a maximum in segregation at $Pe = 7.1$. (The correlation coefficient for this figure is very poor, 0.29. If a third order polynomial is used to fit the data, the correlation coefficient is only marginally improved, 0.35; but there is still a maximum at $Pe = 7.1$.)

In stabilized conditions, the buoyancy-driven convective velocity is of the same order of magnitude as the growth rate, $\approx 10\mu$m/s. Convection this gentle does not homogenize the melt effectively. During crystallization, solute is rejected from the melt/solid interface and a solutal boundary layer of δ_S thickness is formed ahead of the interface. Gentle convection near the interface doesn't homogenize the melt, but sweeps the rejected solute along causing its concentration to vary along the melt/solid interface.

Summarized Results – Stabilized Conditions

Peclet #	Crystal	Mass Fraction	Segregation	Asymmetry Index
3.2	30	0.2	0.27	0.51
		0.4	0.19	0.34
		0.7	0.45	1.56
	32[†]	0.2	0.44	0.84
		0.6	0.11	0.17
		0.7	0.68	2.8
	53	0.2	0.13	0.13
		0.5	0.31	0.50
			0.17	0.09
5.6	35	0.6	0.22	0.05
	54	0.5	0.30	0.74
			0.49	0.46
	37[‡]	0.3	0.64	1.1
		0.6	0.42	0.86

Table 6.1: Summarized results for stabilized conditions, $3.2 \leq Pe \leq 5.6$. The table lists the growth conditions for each run, the resulting segregation and the asymmetry index at the axial location in the crystal at which they were measured. (Refer to text for further information.)

[†]A temperature difference of 6.4 °C was imposed across the outside of the ampoule near the melt/solid interface.

[‡]The ampoule was rotated at 2/3 rpm.

Summarized Results – Stabilized Conditions

Peclet #	Crystal	Mass Fraction	Segregation	Asymmetry Index
7.4	50	0.2	0.46	0.41
			0.29	0.20
		0.5	0.57	0.89
			0.45	0.17
	55	0.5	0.59	0.71
			0.59	0.45
8.6	34	0.4	0.45	0.21
		0.6	0.21	0.02
	49	0.2	0.29	0.06
			0.28	0.20
		0.5	0.67	1.3
			0.51	0.13

Table 6.2: Summarized results for stabilized conditions, $7.4 \leq Pe \leq 8.6$. The table lists the growth conditions for a run, the resulting segregation, and the asymmetry index at the axial location in the crystal at which they were measured.

In the absence of convection, and density differences between the solid and the melt, the dependence of the axial composition profile in the melt on growth rate is demonstrated by the following equation, which describes one-dimensional steady-state diffusion in the melt (40).

$$\frac{C}{C_o} = 1 + \frac{1 - k_{eq}}{k_{eq}} \exp^{\frac{zv}{D}} \tag{6.1}$$

For these conditions, the solutal boundary layer is defined:

$$\begin{aligned} \frac{C}{C_o} &= 1 + \frac{1 - k_{eq}}{k_{eq}} \exp^{-\frac{\delta_s v}{D}} \\ &= 1.01 \end{aligned} \tag{6.2}$$

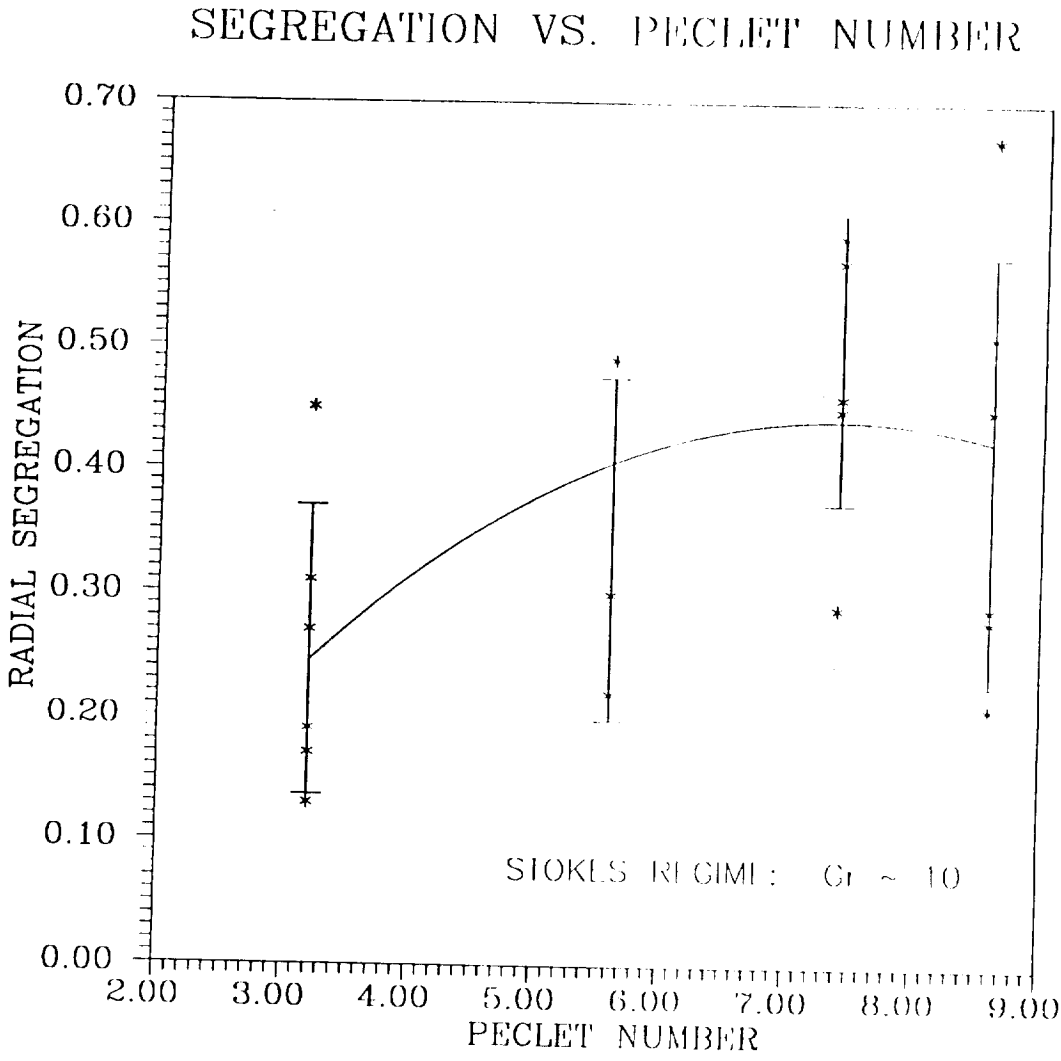

Figure 6.1: Radial segregation versus Peclet number for stabilized conditions. The error bars in the plot represent the standard deviation at each Peclet number.

Rearrangement gives an expression for δ_S:

$$\delta_S = -\frac{D}{V}\ln\left(\frac{0.01k_{eq}}{1-k_{eq}}\right) \tag{6.3}$$

As the growth rate is increased δ_S is decreased. Although the above conditions may seldom be met in practice, Equation 6.3 was derived to introduce the concept of a solutal boundary layer. When there is convection in the melt, the thickness of the solutal boundary layer is reduced, and δ_S refers to the region where the solute concentration in the melt changes from its interfacial value to near its bulk-melt value.

As the growth rate is increased above $Pe = 7.4$, radial segregation might be expected to decrease for the stabilized condition. At high rates of growth $\delta_S \ll \delta_V$ so convection doesn't significantly disturb the concentration field in the melt, i. e. mass transfer in the melt is diffusion controlled even though there is convection in the melt. This explains why there is a maximum in Figure 6.1. At high growth rates the effects of convection and interfacial curvature on radial segregation are decoupled, and only interfacial curvature is expected to influence radial segregation.

The effect of growth rate on the experimental axial concentration profile of azulene is shown in Figure 6.2, which is a plot of $C(g)/C_o$ versus g for three different growth rates. (The data for this plot are at the end of Appendix A.) As the growth rate was increased, the shape of the axial azulene concentration profile changed from that associated with well-mixed to that associated with diffusion controlled conditions. The important feature of Figure 6.2 is the shape of the curves, not exact values of the data, since the data for this figure must be incorrect.

Recall the normal freeze expression:

$$\frac{\tilde{C}_I(g)}{C_o} = k_{eff}(1-g)^{k_{eff}-1} \tag{6.4}$$

If experimental data are available, k_{eff} can be determined by plotting $\ln\left(\frac{\tilde{C}_I(g)}{C_o}\right)$ versus $\ln(1-g)$. For well-mixed conditions, $k_{eff} = k_{eq}$; for steady-state diffusion controlled conditions $k_{eff} = 1$. For any other condition, $k_{eq} < k_{eff} < 1$. In Figure 6.2 for $Pe = 3.2$, k_{eff} was found to be 0.24. In Figure 6.2 for $Pe = 8.6$, the axial composition profile violates conservation of mass. These results are theoretically impossible, the error was probably

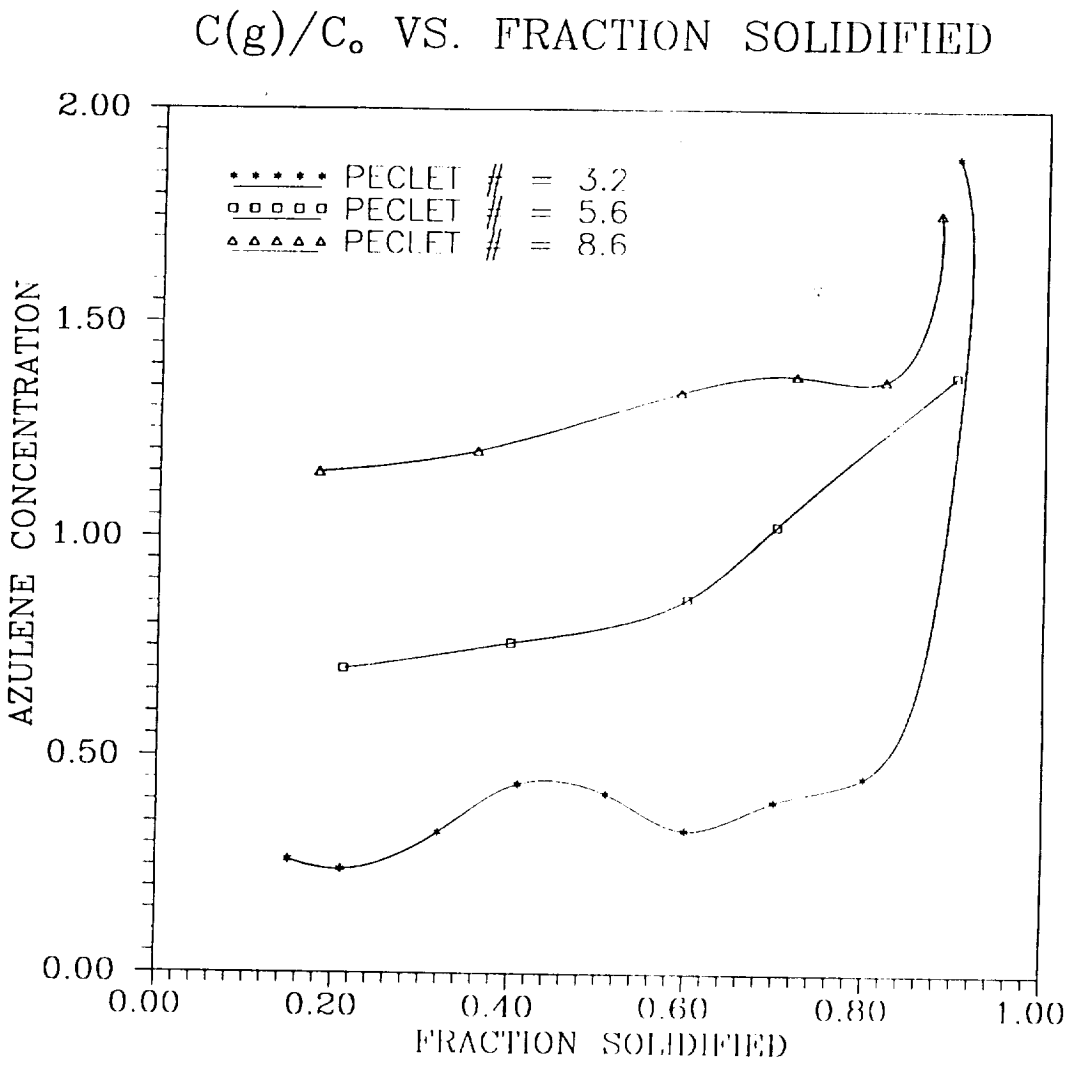

Figure 6.2: A plot of $C(g)/C_o$ versus g for three different growth rates. As the growth rate was increased, the shape of the axial concentration profile of azulene changed from that associated with well-mixed to a shape associated with diffusion controlled.

caused by improper calibration of the gas chromatograph that was used to analyze the crystals. As discussed in Section 4, improper calibration was unavoidable and that was why all radial concentration data in this thesis were scaled by the mean value as measured at a given axial position. Figure 6.2 indicates the the absolute error in the measurement of azulene concentration could be significant, on the order of 20%. Nevertheless, the trend shown in Figure 6.2 is accurate. Figure 6.2 suggests that as the growth rate was increased, k_{eff} increased from approximately k_{eq} to approximately and mass transfer in the melt at the interface became diffusion controlled.

6.2 Destabilized Conditions

The results for all the runs with destabilized conditions are summarized in Table 6.3. This table lists the growth conditions associated with each run, the measured segregation, and the asymmetry index.

Figure 6.3 shows the effects of Peclet number and Grashof number on segregation. This plot was constructed using the minimum segregation observed at each Pe and Gr. The minimum was used rather than an average value because not all runs were replicated the same number of times, and it was felt that an average value would skew the results in favor of the runs which were replicated. (The results for $Pe = 8.6$ and $Gr = 109000$ were not plotted because the radial segregation for that condition was so large it obscured the relative variation in the segregation for the other conditions, i. e. the plot didn't look good.) There is waviness in the plot because a small number of points can't adequately define a surface, particularly when there is scatter in the experimental data. In general, there was little segregation at very low growth rates, but segregation was smallest when the Peclet number was small and the Grashof number was large. For large growth rates, segregation could be decreased by increasing the Grashof number.

For a destabilized condition, buoyancy-driven convection in the melt is intense and the solute distribution in the melt tends to be very homogeneous. As the growth rate is increased, the solutal boundary layer becomes smaller, thereby reducing the effectiveness of convection in promoting radial homogeneity in the crystal.

No axial concentration profiles of azulene were obtained for destabilized conditions since it was assumed that the conditions were characteristic of a well mixed melt. This assumption can be checked using the normal freeze equation. For well-mixed conditions:

$$\frac{\tilde{C}_I(g)}{C_o} = k_{eq}(1-g)^{k_{eq}-1} \tag{6.5}$$

$$\left.\frac{\tilde{C}_I(g)}{C_o}\right|_{g=0.5} = 0.49$$

With the exception of crystals 51 and 48 all crystals grown under destabilized conditions had a concentration of azulene, as described by Equation 6.5 at $g = 0.5$, between 0.50 and 0.63. Considering the error associated with the measurement procedure, these results

Summarized Results – Destabilized Conditions

Peclet #	Crystal	Grashof #	Mass Fraction	Segregation	Asymmetry Index
3.2	41	55600	0.5	0.05	0.05
	42	88500	0.2	0.93	0.07
				0.93	0.22
			0.5	0.04	0.02
				0.04	0.03
	43	116000	0.5	0.04	0.04
5.6	44	39600	0.5	0.17	0.36
	45	121000	0.5	0.07	0.08
				0.07	0.07
7.4	51	76200	0.2	0.45	0.13
				0.25	0.27
			0.5	0.14	0.18
				0.26	0.68
	52	138000	0.5	0.13	0.13
				0.12	0.07
8.6	47	76700	0.5	0.21	0.46
	48	109000	0.2	0.47	1.2
			0.5	0.50	0.61
				0.50	0.38
	46	158000	0.5	0.15	0.35

Table 6.3: Summarized results for solidification under destabilized conditions. The table lists the growth conditions associated with each run, the segregation and asymmetry indexes and the axial location in the crystal where they were measured. (Refer to text for further information.)

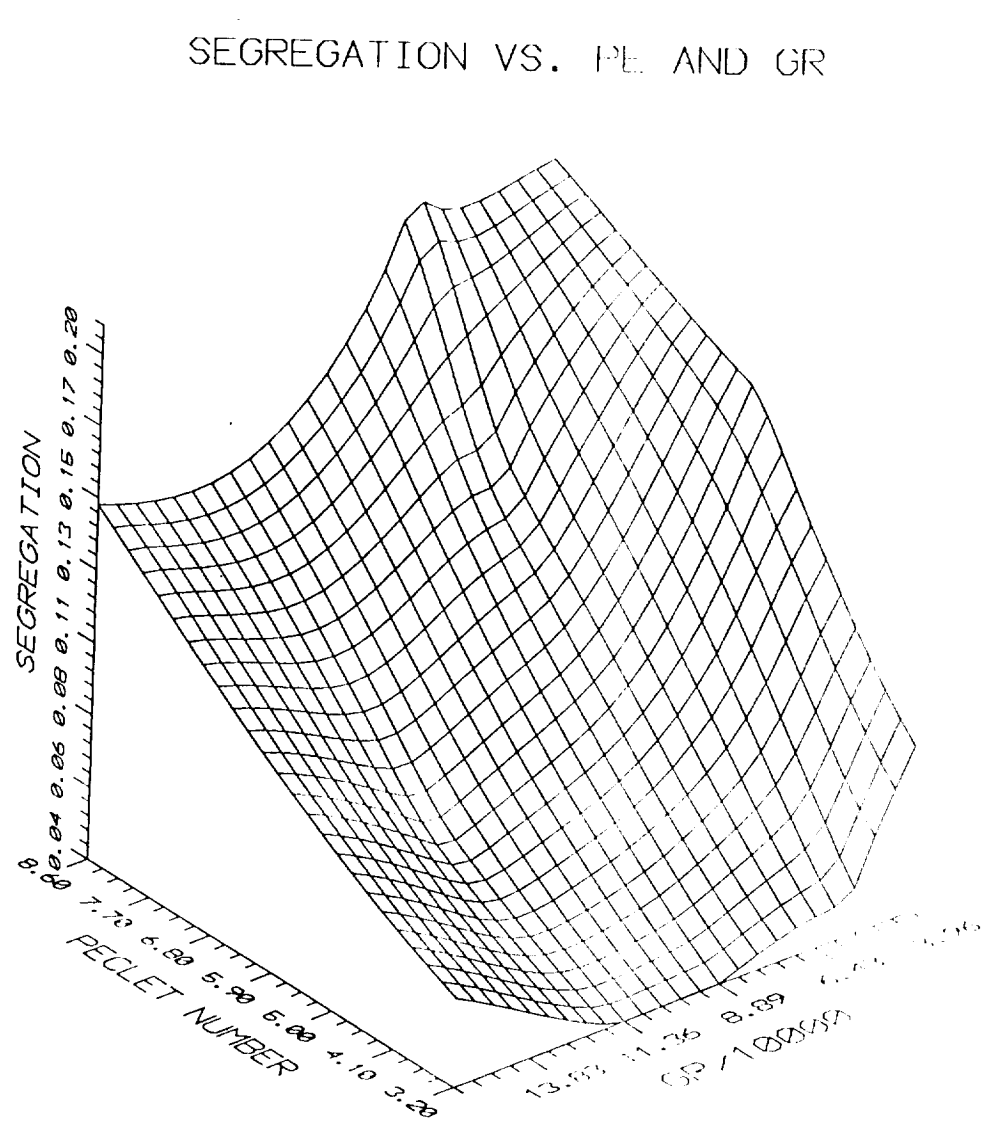

Figure 6.3: Influence of Pe and Gr on radial segregation for destabilized conditions.

indicate that the melt was well-mixed for destabilized conditions. (If the experimental error were ignored and 0.55 is chosen as a nominal value for $C(0.5)/C_o$, Equation 6.5 predicts $k_{eq} = 0.35$. This agrees fairly well with the value $k_{eq} = 0.3$ given by Karl(36). As for crystals 51 and 48, the values of $\frac{C(g)}{C_o}$ at $g = 0.5$ were 0.85 and 1.0 respectively. These two aberrations may have caused by constitutional supercooling.

Figure 6.4 is a plot of the minimum asymmetry index vs. Peclet number and Grashof number for destabilized conditions. Note the similarities between this figure and Figure 6.3 (Radial segregation vs. Pe and Gr). As with radial segregation, asymmetry was greatest when Pe was large and Gr was small. As Pe was decreased and as Gr was increased, asymmetry was reduced. The similarities between Figures 6.3 and 6.4 suggests that radial segregation and the asymmetry of the radial composition profile are related. This is further demonstrated by Figure 6.5. Figure 6.5 is a plot of the minimum asymmetry observed for a given growth condition versus the minimum segregation observed for the same set of conditions. The data in Figure 6.4 are fit fairly well by a straight line (the square of the correlation coefficient, r^2, equals 0.82) with a slope equal to 2.4.

Table 6.4 gives a comparison of the radial segregation measured for the two types of thermal conditions. In all but one case, the values for the segregation and the range of segregation were smaller for destabilized conditions. (The one exception was $Pe = 3.2$ in a destabilized condition. Recall that this was the only case where a discontinuity in radial concentration was observed. If this case is ignored, the range associated with $Pe = 3.2$ for this destabilized condition would be minimal, 0.04 - 0.05.)

Large variations in the amount of segregation and asymmetry index for a given growth condition were often observed. For instance, for a destabilized condition with $Pe = 7.4$ (crystal number 51), composition profiles were measured at two different axial locations for a total of four diameters. The segregation ranged from 14% to 45%. The asymmetry index ranged from 0.13 to 0.68. Under stabilized conditions, even larger variations in radial segregation and the asymmetry index were observed. A plot of the asymmetry index versus Peclet number for stabilized conditions has not been presented here because it would resemble a scatter diagram. The general trend here was that the larger the segregation for

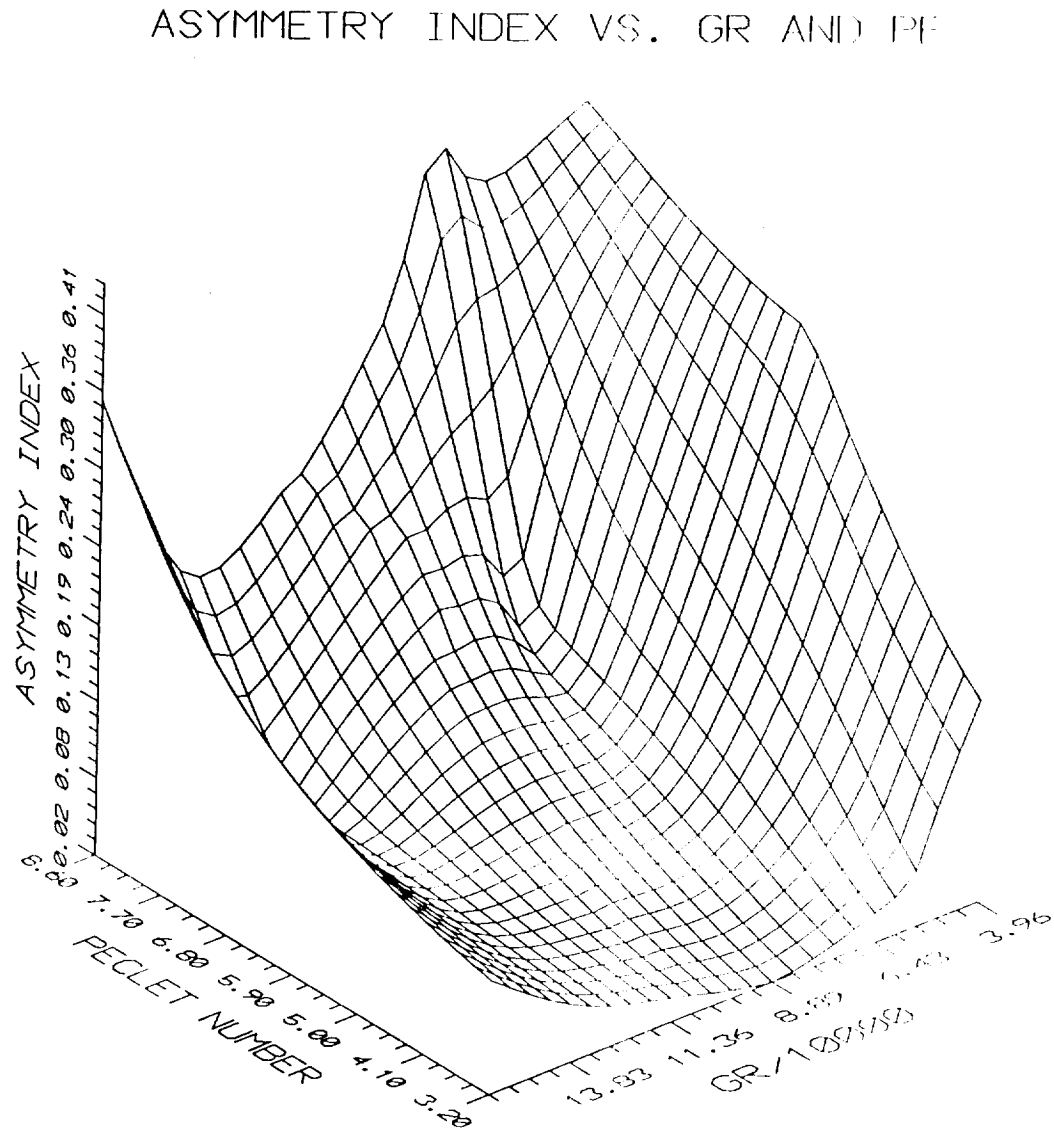

Figure 6.4: Influence of Pe and Gr on asymmetry for destabilized conditions.

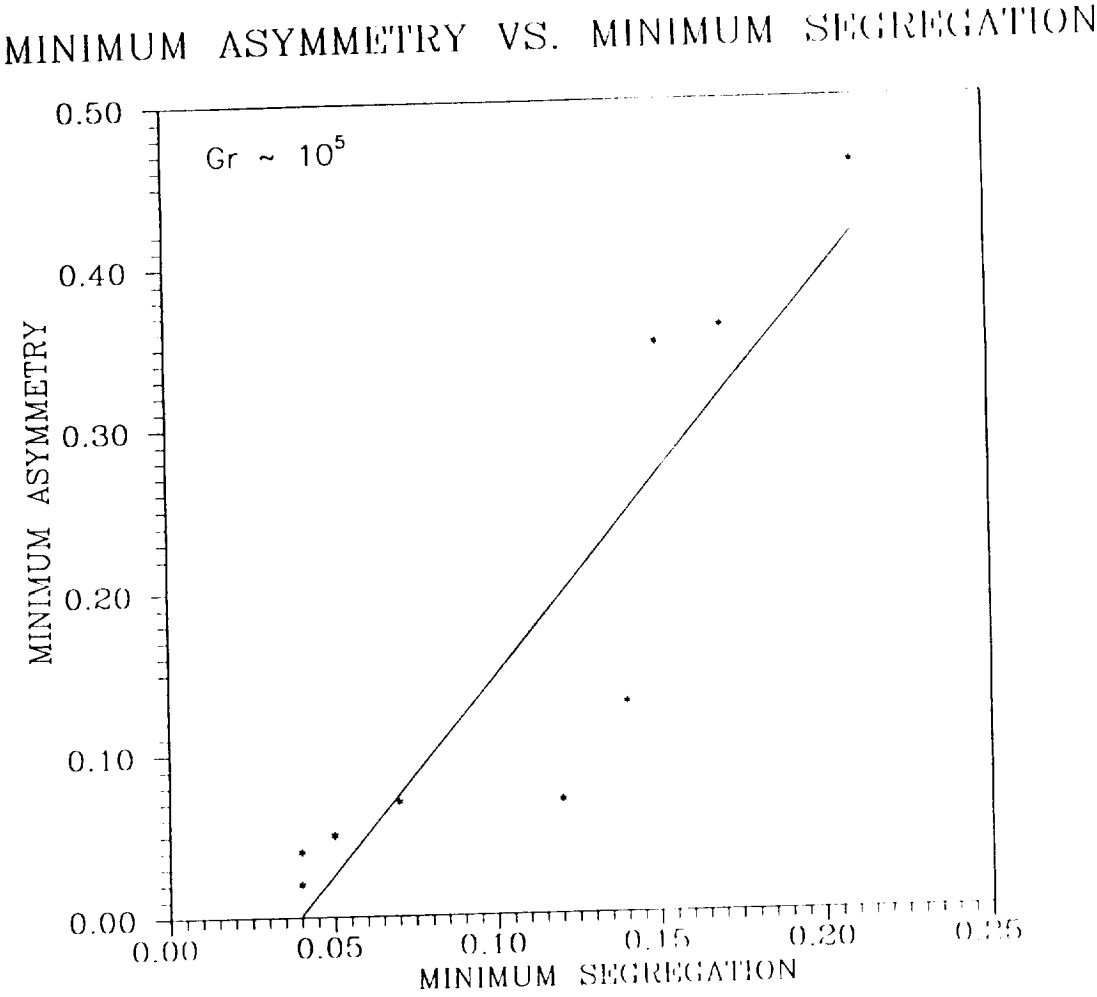

Figure 6.5: Minimum asymmetry index vs. minimum segregation obtained for a given Pe and Gr for destabilized conditions.

a given growth condition, the larger the variation in the results.

The scatter in the results isn't surprising. If a crystal was grown under conditions that radial precluded segregation (low growth rate and intense convection in the melt), the crystals would always be radially homogeneous and consequently the asymmetry index would have to be small. If a crystal was grown at a high growth rate and with little mixing in the melt, nothing would theoretically forbid the crystal from being radially homogeneous. Any number of growth parameters could combine to increase or decrease radial segregation. This is reflected in the scatter of the results when segregation is large.

6.3 Diffusion Controlled Conditions

One reason for using the numerical model described in Section 3 was to calculate the effect of interfacial curvature on radial segregation. Table 6.5 lists the results of the model for the case of an interface with a dimensionless amplitude of 0.25 and $k_{eq} = 0.3$, parameters typical of the experiments. A comparison of Tables 6.5 and 6.4 shows that for destabilized conditions, the convection in the melt reduced the segregation that would have been caused by interfacial curvature. For stabilized conditions, the observed radial segregation was even larger than the segregation predicted by interfacial curvature alone. For this condition the convection in the melt amplified the effect of the interfacial curvature in creating crystals with poor radial homogeneity.

Results from the numerical model are further summarized in Figures 6.6 to 6.8. These figures demonstrate the effects of Peclet number, interfacial amplitude, and segregation coefficient on radial segregation for diffusion controlled conditions. Figure 6.6 is a plot of segregation versus Peclet number and equilibrium constant. For $k_{eq} = 1$ there is no segregation. As k_{eq} is decreased segregation becomes greater, although this effect is greater for larger values of the Peclet number.

Figure 6.7 is a plot of radial segregation vs. interfacial amplitude and Peclet number. By convention the amplitude is negative for a convex melt/solid interface. When the amplitude of the interface is zero (no curvature), there is no segregation. As the magnitude of the amplitude is increased the segregation is increased. Segregation is always greater for a convex interface than for a concave interface of the same amplitude. The difference in segregation becomes greater as the Peclet number is increased.

Figure 6.8 is a plot of segregation and equilibrium constant versus interfacial amplitude. Not surprisingly, there is no segregation for a flat interface or when $k_{eq} = 1$. Again, segregation is always greater for a convex interface than for a concave interface of the same amplitude. This difference in segregation becomes greater as k_{eq} is decreased.

In summary, low crystal growth rates help to create crystals that are radially homogeneous regardless of thermal condition. Efficient mixing of the melt, such as that present in a destabilized condition, also reduces radial segregation and can even eliminate it when

Condition	$Pe = 3.2$	$Pe = 5.6$	$Pe = 7.4$	$Pe = 8.6$
Stabilized condition	.11 - .45	.22 - .49	.29 - .59	.21 - .67
Destabilized condition	.04 - .93	.07 - .17	.12 - .45	.15 - .50

Table 6.4: Observed range of radial segregation as a function of Peclet number. (The cases where the ampoule was rotated and a thermal asymmetry was created were not included.)

Interfacial shape	$Pe = 3.2$	$Pe = 5.6$	$Pe = 7.4$	$Pe = 8.6$
$H(R) = 0.25R^2$	.22	.27	.29	.30
$H(R) = -0.25(R^2 - 1)$	.24	.38	.45	.49

Table 6.5: Calculated radial segregation as a function of interfacial shape and Peclet number with $k_{eq} = 0.3$ for diffusion controlled conditions. The radial segregation was calculated using the model described in Section 3. The parameters used were typical of the azulene/naphthalene system.

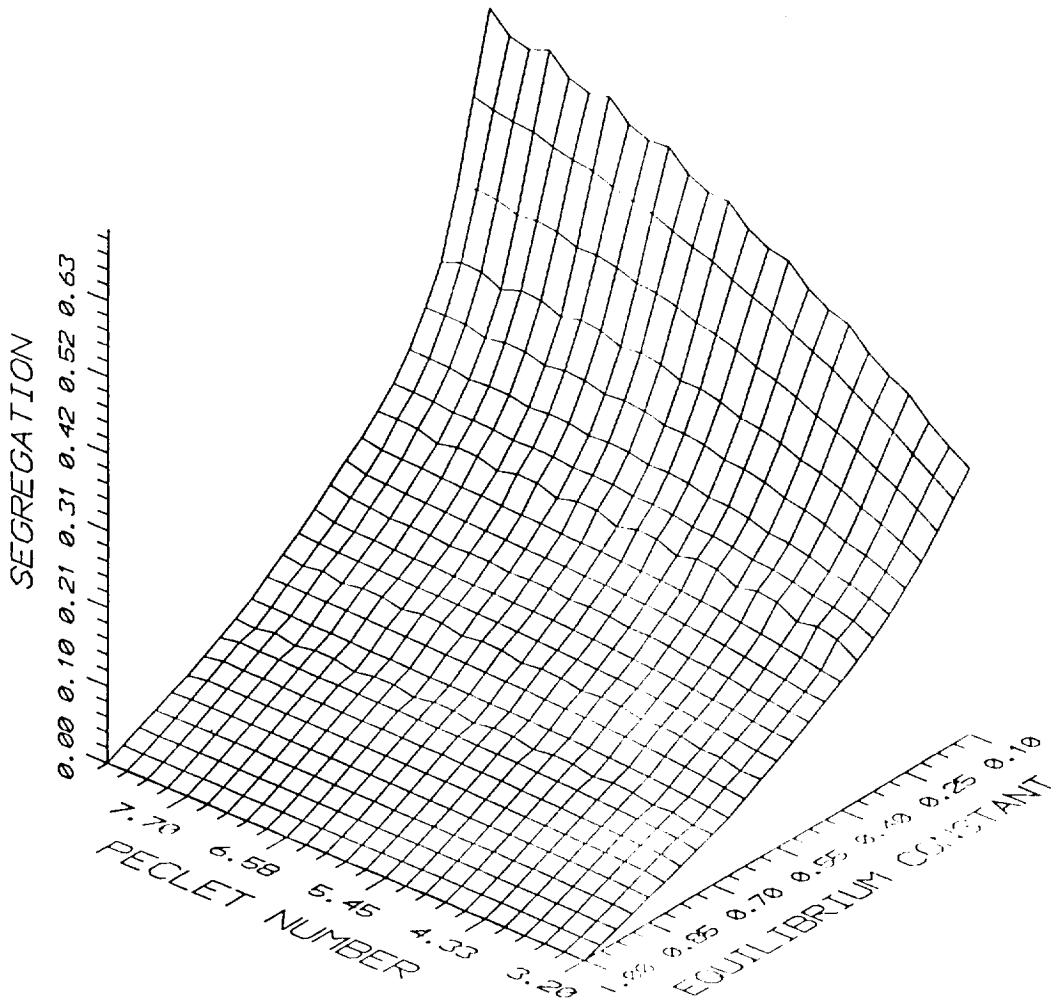

Figure 6.6: Segregation vs. Peclet number and equilibrium constant for diffusion controlled conditions with $H(R) = 0.25R^2$.

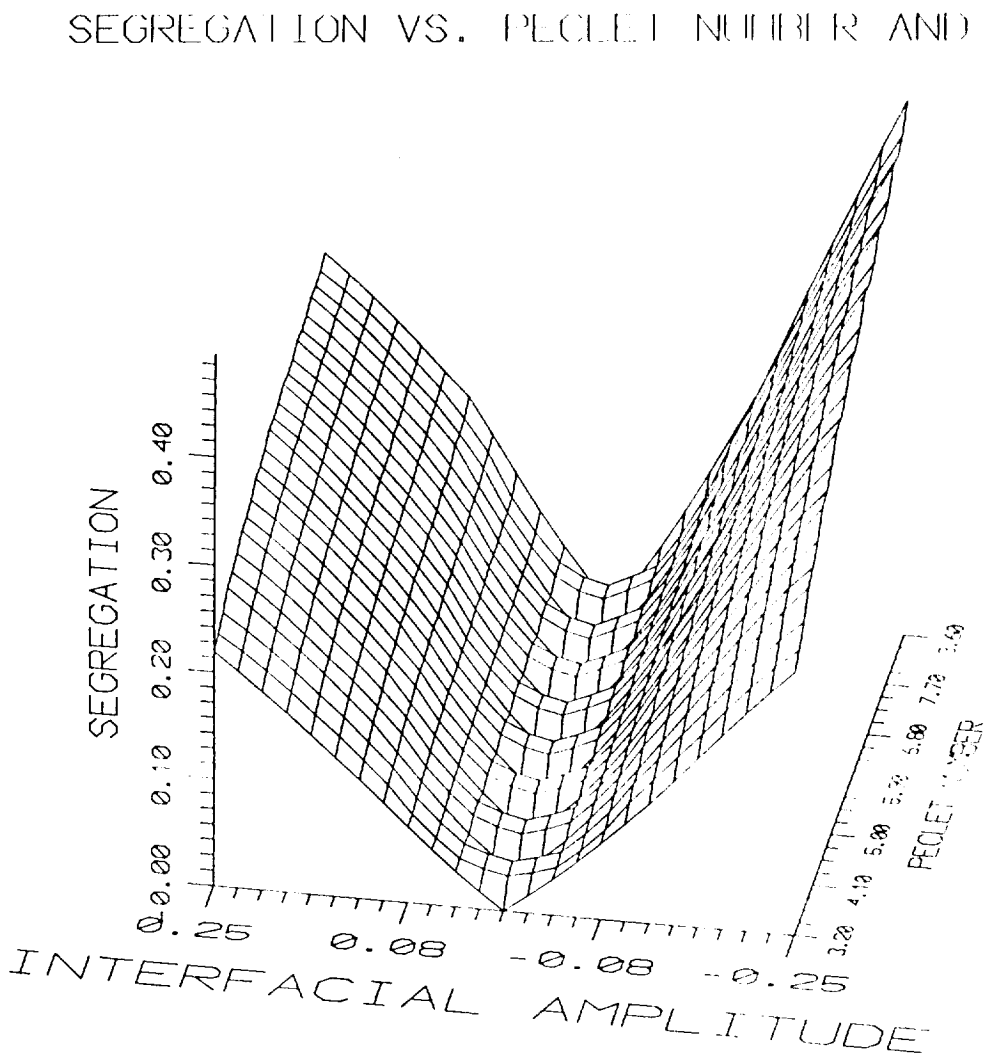

Figure 6.7: Segregation vs. interfacial amplitude and Peclet number for for diffusion controlled conditions with $k_{eq} = 0.3$. By convention, the amplitude of a convex interface is negative.

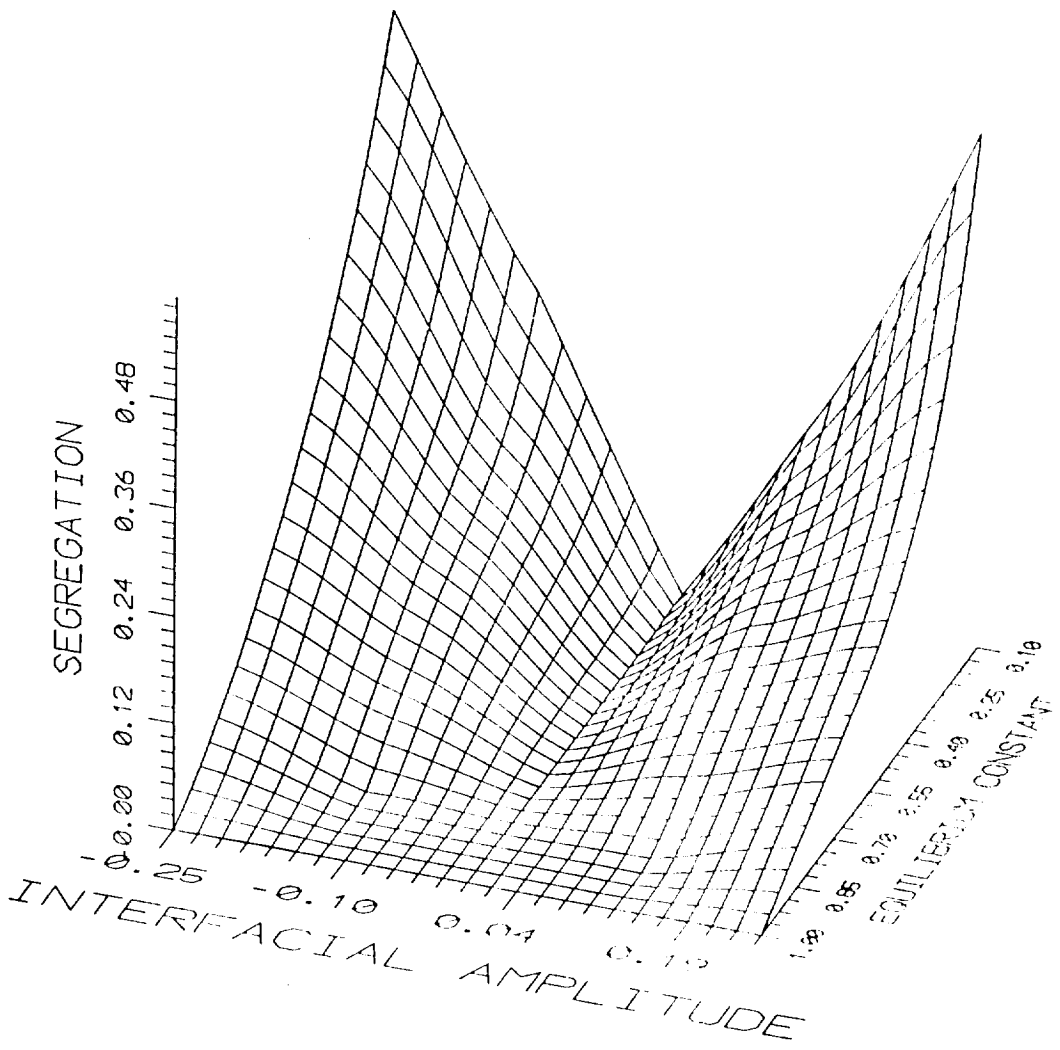

Figure 6.8: Segregation vs. interfacial amplitude and equilibrium constant for diffusion controlled conditions with $Pe = 5.6$. Although it may not be clear from the figure, the range in interfacial amplitude is -0.25 to 0.25.

the growth rate is low. For destabilized conditions, increasing the maximum temperature in the melt improves radial homogeneity in the crystal.

7 Nomenclature

Bi	Biot number, $\frac{hR}{k}$
C	Concentration in the melt
C_o	Initial concentration in the melt
C_p	Heat capacity, J/kg.K
D	Diffusion coefficient, m^2/s
g	Axial position in a crystal in terms of crystal mass fraction
g_e	Gravitational acceleration, m/s^2
Gr	Grashof number, $\frac{R_a^3 g_e \beta \Delta T}{\nu^2}$
h	Heat transfer coefficient, $J/m^2.K.s$
k_{eq}	Equilibrium segregation coefficient
Pe	Peclet number, $\frac{RV}{D}$
Pr	Prandtl number, $\frac{\nu}{\alpha}$
R	Radial position, m
R_a	Inner radius of ampoule, m
Ra_S	Solutal Rayleigh number, $GrSc$
Ra_T	Thermal Rayleigh number, $GrPr$
Sc	Schmidt number, $\frac{\nu}{D}$
T	Temperature, K
T_c	Cooler temperature, K
T_h	Heater temperature, K
ΔT	$T_{max} - T_{top\ of\ melt}$, destabilzed conditions, K
ΔT	$T_{R=1} - T_{R=0}$, stabilzed conditions, K
TE	Truncation error
V	Solidification rate, m/s
x	Mole fraction
Z	Axial position, m
α	Thermal diffusivity, m^2/s
β	Coefficient of thermal expansion, K^{-1}

δ_S	Solutal boundary layer thickness, m
δ_T	Thermal boundary layer thickness, m
δ_V	Momentum boundary layer thickness, m
μ	Dynamic viscosity, kg/m.s
ν	Kinematic viscosity, m^2/s
ρ	Density, kg/m^3